UNIVERSITY OF CALIFORNIA

Los Angeles

Advanced Supercapacitor based on Combination of Graphene Hybrid Materials and Redox-Electrolytes

A dissertation submitted in partial satisfaction of the

requirements for the degree Doctor of Philosophy

in Chemistry

by

Jee Youn Hwang

2016

ABSTRACT OF THE DISSERTATION

Advanced Supercapacitors based on

Combining Graphene Hybrid Materials with Redox-Electrolytes

by

Jee Youn Hwang

Doctor of Philosophy in Chemistry

University of California, Los Angeles, 2016

Professor Richard B. Kaner, Chair

Electrochemical capacitors, also known as supercapacitors, are attractive energy storage devices with the ability to recharge in seconds instead of hours for traditional batteries. They also can be used for up to a million charge/discharge cycles. However, the low energy density of carbon electrodes is the main impediment to realizing the full potential of this technology. State-of-the-art supercapacitors feature activated carbon electrodes impregnated with a non-aqueous electrolyte (typically acetonitrile) that operate at voltages between 2.2-2.7 V. Unfortunately, activated carbons have low specific capacitance in organic electrolytes which severely limits the energy density of commercial systems. In addition, organic solvents are often flammable leading to safety and environmental concerns. Aqueous electrolytes, on the other hand, are safer, cheaper

and have higher ionic conductivity, promising higher capacitance electrodes. This has triggered tremendous research efforts in order to develop new hybrid electrode materials that are capable of providing a huge amount of energy in an aqueous electrolyte. We have used a commercial grade LightScribe DVD burner for the direct synthesis and processing of graphene-metal oxide (RuO_2, Fe_3O_4, MnO_2, V_2O_5, etc.) hybrid electrodes in a single step. By anchoring metal oxide nanoparticles directly onto graphene, the 3-dimensional, highly porous graphene surfaces serve as excellent conductors for fast electron transfer, while metal oxide nanoparticles provide a large electrochemically active surface area for fast and reversible Faradaic reactions.

Although metal oxide and carbon composite active materials are able to improve the capacitance, the energy density cannot be improved significantly if one only relies on the solid active materials comprising the electrode. Adding redox-additives into a traditional aqueous electrolyte has proven to be an efficient route to enhance supercapacitor performance because redox additives can contribute to the capacitance and enhance the energy densities via redox reactions between the electrode and the electrolyte. While carbon hybrid electrodes can only operate at 1.0 V, the addition of a redox mediator extends the decomposition voltage of the electrolyte, resulting in a symmetric supercapacitor with an ultrahigh voltage of 2 V. As both electrode and electrolyte contribute to charge storage simultaneously, an ultrahigh specific capacitance can be obtained. In addition, single-step direct laser writing of hybrid micro-supercapacitors shows great potential for miniaturized electronics. Thus, the current work provides an effective strategy for designing and fabricating aqueous supercapacitors and micro-supercapacitors that hold promise for a sustainable energy future.

The dissertation of Jee Youn Hwang is approved.

Xiangfeng Duan

Yu Huang

Richard B. Kaner, Committee Chair

University of California, Los Angeles

2016

I would like to delicate this dissertation to:

my father, Dr. Woon Bong Hwang, for his continued support and counsel.

my mother, Boyoung Lee, for her unconditional love and unwavering belief.

my sister, Jeehye Hwang, for her endless encouragement.

Without them, this thesis would never have been written.

Thank you for all of your support and for helping to make this dream come true.

I love you all!!

TABLE OF CONTENTS

Chapter 7. Conclusions and Future Work

LIST OF FIGURES

Chapter 1. Introduction

500, 700, and 1000 mV s^{-1} tested at a maximum voltage of 1.8 V. (g) Nyquist plot with a magnified high-frequency region and (h) Bode plots of the LSG/Fe_3O_4 symmetric supercapacitor over a frequency range from 1 MHz to 0.01 Hz. (i) CV curves of a flexible LSG/Fe_3O_4 full cell at different bending radii: (1) 24, (2) 14, (3) 7, and (4) 2.5 mm at a scan rate of 100 mV s^{-1}. Inset is the corresponding digital images of the bending conditions and a glowing red LED in the bent state confirming the electrochemical stability of the device under mechanical stress……..78

Figure 3.4 Electrochemical performance of LSG/Fe_3O_4 electrodes and a symmetric supercapacitor in an [$Fe(CN)_6^{3-}$/$Fe(CN)_6^{4-}$] redox-active electrolyte (a) Illustration of the charge storage mechanism in LSG/Fe_3O_4 supercapacitors using 1.0 M Na_2SO_4 electrolyte (1) in the absence, and (2) in the presence of a redox additive. (b) CV curves collected at increasing concentrations of the redox additive, tested at a scan rate of 50 mV s^{-1}. (c) The corresponding CC curves collected at a current density of 8 mA cm^{-2}. (d) Specific capacitance by area and active material mass vs. current density for an LSG/Fe_3O_4 electrode in 1.0 M Na_2SO_4 containing different concentrations (0, 0.025, 0.050, and 0.100 M) of the redox additive, measured in a three-electrode setup. (e) CV curves at 20 mV s^{-1} for an LSG/Fe_3O_4 electrode tested at different potential regions in order to assess its performance as a positive and negative electrode in a symmetric supercapacitor. (f) Areal capacitance and amount of electric charge calculated at a 10 mV s^{-1} scan rate for the negative and positive electrodes. The figure shows the results obtained in the absence and presence of 0.025 M redox additive. (G-I) The electrochemical performance of a symmetric supercapacitor made of two identical pieces of LSG/ Fe_3O_4 electrodes. (g) CV curves at a scan rate of 50 mV s^{-1}. (h) CC curves at a current density of 12 mA cm^{-2}. (i) Areal

Chapter 4. Next-Generation Activated Carbon Supercapacitors: A Simple Step in Electrode Processing Leads to Remarkable Gains in Energy Density

Figure 4.3 Electrochemical performance of a high voltage supercapacitor (SC) in a [$Fe(CN)_6^{3-}$/$Fe(CN)_6^{4-}$] redox-active aqueous electrolyte (RE). (A) CV curves of the supercapacitor at an increasing voltage window from 1.0 V to 2.0 V in 0.1 M RE at 50 mV s^{-1}. (B) CV curves collected at increasing concentrations of the redox additive, tested at a scan rate of 50 mV s^{-1}, (C) the corresponding CC curves collected at a current density of 11.3 mA cm^{-2}, (D) specific capacitance by area vs. current density for an activated carbon electrode in a 1.0 M Na_2SO_4 electrolyte containing different concentrations (0, 0.025, 0.050, and 0.100 M) of the redox additive. (E) CV profiles of 0.1M RE-SC at different scan rates of 30, 50, 70, 100, 200, and 300 mV s^{-1}. (F) Nyquist plots of the 0.1 M RE aqueous electrolyte and 1.0 M $TEABF_4$ in acetonitrile supercapacitors over a frequency range of 1.0 MHz to 0.1 Hz. All the electrochemical experiments were measured in a CR2032 coin cell. ……...……129

Figure 4.4 Electrochemical performance a supercapacitor combining laser scribed activated carbon (LSAC) electrodes and [$Fe(CN)_6^{3-}$/$Fe(CN)_6^{4-}$] redox-active electrolyte (RE). (A) Illustration of the charge storage mechanism in an LSAC electrode using a 1.0 M Na_2SO_4 electrolyte (1) in the absence, and (2) in the presence of a redox additive. (B) CV profiles comparing the electrochemical performance of activated carbon electrodes before and after laser scribing tested in a traditional 1.0 M acetonitrile electrolyte and in a 0.1 M redox electrolyte with data collected at a scan rate of 50 mV s^{-1}. (C) Evolution of the electrochemical performance of an LSAC supercapacitor using 0.1 M RE at different CV scan rates at 30, 50, 70, 100, 200 and 300 mV s^{-1}, (D) corresponding CC curves at different current densities of 8.5, 11.3, 11.4, 16.9, 19.8,

LIST OF TABLES

ACKNOWLEDGEMENTS

It is a pleasure to thank those who made this thesis possible. First, I would like to express my special appreciation and thanks to my advisor Professor Richard Kaner, for providing the time and equipment to accomplish the work contained herein. I would like to thank you for encouraging my research and for allowing me to grow as a research scientist. His advice on both research as well as on my career have been priceless. I would also like to thank my committee members, Professor Xiangfeng Duan, Professor Yves F. Rubin, and Professor Yu Huang for serving as my committee members. I want to thank you for letting my oral exam be an enjoyable moment, and for brilliant comments and suggestions.

I would also like to extend my appreciation to Dr. Maher El-Kady, who is the mentor for me and helped me get started research in supercapacitor field. Without his mentorship, I would not be able to start and complete this important phase of my career. I have learned much from him throughout his valuable mentorship. He is the person, who always provide good feedbacks that are enriching my research. The valuable skills gained from him will always stay with me, and I will be grateful whenever I apply them in future. Thank you for all of the meetings and chats over the seven years.

I would like to thank my supercapacitor sub-group members. Dr. Lisa Wang, Mengping Li and Haosen Wang were always willing to help and give their best suggestions. It would have been a lonely Ph.D. life without them. Many thanks to Matthew Kowal, Kris Marsh, Chris Turner, Dr. Brain McVerry, Dr. William Huang, and other workers in the Kaner laboratory for helping me collect valuable data. My research would not have been possible without their help.

This journey would not have been possible without the support of my family and friends. Yuree Noh and Chia-Jung Yu have become two of my best friends and closest colleagues in grad school UCLA. We have seen and helped each other through both good and bad times. I will always remember the great conversations we had during UCLA grad school life and I know that we will break bread together many more times. I look forward to the day that all of us having finished our Ph.D. work.

To my family, thank you for encouraging me in all of my pursuits and inspiring me to follow my dreams. Special thanks to the memory of grandfather Dr. Jongheul Hwang who would have been happy to see me follow in his steps as a scientist. Although he was my inspiration to pursue my doctoral degree, he was unable to see my graduation. I am especially grateful to my grandparents (Jongman Lee and Youngja Hong), who supported me emotionally and financially. I want to show my loving gratitude to my parents, Dr. Woonbong Hwang and Boyoung Lee for their unflagging love and unconditional support throughout my life and my studies. You made me live the most special and unique childhood that made me who I am now! I am so proud to be your daughter.

Previous Publications and Contributions of Co-Authors:

Chapter 2 is a version of Jee Y. Hwang, Maher F. El-Kady, Yue Wang, Lisa Wang, Yuanlong Shao, Kristofer Marsh, Jang M. Ko and Richard B. Kaner, "Direct Preparation and Processing of Graphene/RuO_2 Nanocomposite Electrodes for High-Performance Capacitive Energy Storage". J.Y.H., M.F.E. and J.M.K. perceived and designed the research, J.Y.H. built the supercapacitors, performed electrochemical experiments, SEM and thermal analysis, Y.W. collected XRD data, K.M. collected XPS data. J.Y.H. and M.F.E. wrote the manuscript. R.B.K. supervised the project and was involved in discussions and interpretation of data. All authors discussed the results and contributed to the analysis of data and commented on the manuscript. Funding was provided by the Nanotech Energy, Inc. This manuscript has been published in *Nano Energy* in 2015. I appreciate *Nano Energy* for giving me the permission to reproduce the manuscript here.

Chapter 3. is a version of Jee Y. Hwang, Maher F. El-Kady, Mengping Li, Cheng-Wei Lin, Matthew Kowal, Xu Han and Richard B. Kaner, "Boosting the Capacitance and Voltage of Aqueous Supercapacitors via Redox Charge Contribution from both Electrode and Electrolyte". J.Y.H., M.F.E. perceived and designed the research, J.Y.H., M.L, X.H. built the supercapacitors, performed electrochemical experiments, J.Y.H collected SEM, XRD and thermal analysis data, M.K synthesized the graphite oxide and C.W.L. collected HRTEM data. J.Y.H. and M.F.E. wrote the manuscript. R.B.K. supervised the project and was involved in discussions and interpretation of data. All authors discussed the results and contributed to the analysis of data and commented on the manuscript. Funding was provided by the Nanotech Energy, Inc. This manuscript will be submitted soon.

Chapter 4. is a version of Jee Y. Hwang, Mengping Li, Maher F. El-Kady and Richard B. Kaner, “Next-Generation Activated Carbon Supercapacitors: A Simple Step in Electrode Processing Leads to Remarkable Gains in Energy Density”. JYH, ML and MFE conceived and designed the experiments. JYH and ML made the electrodes, did the characterization and performed electrochemical experiments. MFE collected data for optical microscopy. MFE and JYH wrote the manuscript. RBK supervised the project and contributed to the experimental planning and data analysis. All authors discussed the results and commented on the manuscript. Funding was provided by the Nanotech Energy, Inc. Mengping Li would like to thank the China Scholarship Council for a graduate research fellowship This manuscript will be submitted soon.

Chapter 5. is a version of Jee Y. Hwang, Maher F. El-Kady, Lisa Wang and Richard B. Kaner, “Flash converted Graphene/Activated carbon supercapacitors for Potential Industrial Applications”. JYH, LW and MFE conceived and designed the experiments. JYH and LW made the electrodes, did the characterization and performed electrochemical experiments. JYH wrote the manuscript. RBK supervised the project and contributed to the experimental planning and data analysis. All authors discussed the results and commented on the manuscript. Funding was provided by the Nanotech Energy, Inc.

Chapter 6. is a version of Jee Y. Hwang, Maher F. El-Kady, Winn Huynh and Richard B. Kaner, “A comparison of the electrochemical performance of different structures (1D, 2D, and 3D) based on Polyaniline/Graphene Micro-Supercapacitors”. J.Y.H., M.F.E. perceived and designed the research, JYH and W.H. made the electrodes, J.Y.H. built the supercapacitors, performed electrochemical experiments, collected SEM. J.Y.H. and M.F.E. wrote the manuscript.

R.B.K. supervised the project and was involved in discussions and interpretation of data. All authors discussed the results and contributed to the analysis of data and commented on the manuscript. Funding was provided by the Nanotech Energy, Inc. This manuscript will be submitted soon.

VITA

2010	College Honors, UCLA
2012	Outstanding Undergraduate Research Scholarship, UCLA
2012	Departmental High Honors Hypercube Scholarship Award, UCLA
2012	B.S., Chemistry, UCLA
2013-2015	Graduate Dean's Sholar Award, UCLA
2015	Battery Technology Team, Intern, Tesla Motors, Palo Alto, CA
2012-2016	Teaching Assistant Fellowship
	Departement of Chemistry and Biochemistry, UCLA
2012-2016	Research Assistant Fellowship
	Departement of Chemistry and Biochemistry, UCLA

PUBLICATIONS AND SELECTED PRESENTATIONS

J.Y. Hwang, M.F. El-Kady, Y. Wang, L. Wang, Y. Shao, K. Marsh, J. M. Ko, and R.B. Kaner, "Direct preparation and processing of graphene/RuO_2 nanocomposite electrodes for high-performance capacitive energy storage", Nano Energy, 2015 18 57-70

J.Y. Hwang, M.F. El-Kady, M Li, C.W Lin, M. Kowal, X. Han and R.B. Kaner, " Boosting the Capacitance and Voltage of Aqueous Supercapacitors via Redox Charge Contribution from the both Electrode and Electrolyte", *Submitted (under review)*

J.Y. Hwang, M. Li, M.F. El-Kady, and R.B. Kaner, " Enhancing the energy density of commercial activated carbon supercapacitors using a combination of laser scribing technique and redox electrolyte", *Submitted (under review)*

J.Y. Hwang, M.F. El-Kady, W. Huynh, and R.B. Kaner, "A comparison of the electrochemical performance of different structures (1D, 2D, and 3D) based on Polyaniline/Graphene Micro-Supercapacitors", *In-preparation*

J.Y. Hwang, M. Li, and R.B. Kaner, "Integration of porous PVDF piezoelectric nanogenerators for a self-charging supercapacitor", *In-preparation*

M.F. El-Kady, M. Ihns, M. Li, **J.Y. Hwang**, M.F. Mousavi, L. Chaney, A. Lech, and R.B. Kaner, "Engineering Three-Dimensional Hybrid Supercapacitors and Micro-Supercapacitors for High-Performance Integrated Energy Storage", Proceedings of the National Academy of Sciences, 2015 112 (14) 4233-4238

L.J. Wang, M.F. El-Kady, S. Dubin, **J.Y. Hwang**, Y. Shao, K. Marsh, B. McVerry, M. Kowal, M.F. Mousavi, and R.B. Kaner "Flash Converted Graphene for Ultra-High Rate Supercapacitors" , Advanced Energy Materials, 2015 5 (18)

Y. Shao, M. F. El-Kady, C.W. Lin, G. Zhu, K.L. Marsh, **J.Y. Hwang**, Q. Zhang, Y. Li, H. Wang, R.B. Kaner "3D Freeze-casting Cellular Graphene Film for Ultra High Power Density Supercapacitors", Advanced Materials, 2016

P.J. Mackey, M.F. El-Kady, E. Holbert, M.R. Johansen, M.D. Hogue, L. Wang, **J.Y. Hwang**, R.B. Kaner, and C.I. Calle, Contributed Presentation on "Graphene-based Energy Storage Devices for Lunar Applications", to be presented at the 5th International Lunar Surface Applications Workshop, Cocoa Beach, FL, April 14-17 2015

P.J. Mackey, M.F. El-Kady, M.R. Johansen, M.D. Hogue, L. Wang, **J.Y. Hwang** , R.B. Kaner, and C.I. Calle, Contributed Presentation on "Graphene-based Energy Storage Devices for Space Applications", 4th International Symposium on Graphene Devices, Bellevue, WA, September 21-25 2014

R.B. Kaner, M.F. El-Kady, L. Wang, **J.Y. Hwang**, Y.Shao, M. Li, H.Wang, J.M. Ko, M, Mousavi, Contributed Presentation on "Graphene-based supercapacitors", AMN7 Advanced Materials & Nanotechnology, Nelson, New Zealand, February 8-12 2015

PATENT

M.F. El-Kady, R.B. Kaner, **J.Y. Hwang**, POROUS INTERCONNECTED CORRUGATED CARBON-BASED NETWORK (ICCN) COMPOSITE. US Patent 20,160,148,759: 2016

J.Y. Hwang, Mengphing Li, M.F. El-Kady, R.B. Kaner, METHODS, DEVICES AND SYSTEMS FOR ACTIVATED CARBON SUPERCAPACITORS WITH MACROPOROUS ELECTRODES. US Patent:

Chapter 1. Introduction

1.1 Global energy issues and energy storage devices

In the world, there have been ever-increasing concerns regarding the global warming and shortage of fossil fuels (coal, petroleum, and natural gas). As the effects of these problems become of greater concern to people, renewable energy production and the electric car market are fast-growing and will become more accessible in the years ahead. The benefits of reduced greenhouse gas emissions from the sun and wind are limited because the sun does not shine all day while the wind does not continuously blow, limiting the amount of energy that can be harnessed from these sources. Thus, energy storage mechanisms must be combined with energy production systems for full utilization. Besides, as the use of portable electric devices increases in our daily lives, the development of energy storage devices becomes an important issue to almost everyone.

Possible solutions for effectively storing energy includes the rechargeable electrochemical devices – supercapacitors and batteries. Lithium-ion batteries (LIBs) have attracted a lot of attention owing to their demonstrated important role in laptop computer electronics and the electric vehicle market. However, LIB development faces the challenge of low power density, limited cycle life, and safety issues due to the underlying electrochemical mechanism. The power required to run portable electronic devices is predicted to increase 20% per year, while the annual enhancement in the energy density of the lithium-ion battery (LIB) is only 10% per year, leaving a 10% annual gap. Unfortunately, current LIBs have already reached their limit (Fig.1.1).[1]

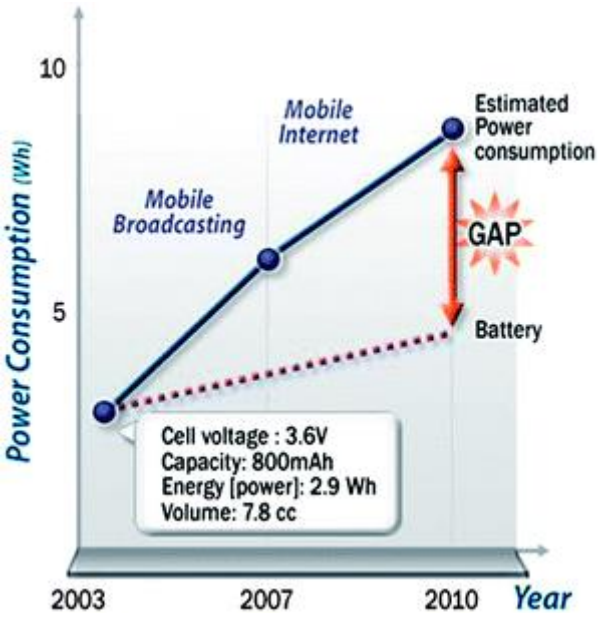

Figure 1.1. Comparison of the increase of power required for mobile electronic devices and the actual increase of battery power.[1]

The global supercapacitor market has been growing steadily and rapidly. Furthermore, supercapacitors have been successfully studied as a promising power source for applications during the last few years and have now become a reality with applications in camera flash, backup power, and regenerative braking.[2] Various companies (Panasonic, NEC Tokin, Seiko Instruments, Cooper Busman, Netscape, Cap-XX, Ioxus, Maxwell Technologies, etc.) have launched supercapacitor products, and their market is growing fast owing to the benefit of high power density and longer cycle life.[3]

1.2 Supercapacitors in Comparison with Batteries

For energy storage devices, energy and power terms are used to characterize the performance of the devices. Power density is used to define the speed of delivering energy to the device, while energy density describes the amount of energy of the device can accommodate. The best energy storage devices should possess both large energy capacity and

power density. Unfortunately, most energy storage devices do not meet these criteria. If we liken energy storage device to a water storage container, then a small water cup represents a capacitor that can store only small amounts of energy, but can deliver high power. In contrast, a large water bottle can represent a battery that store a large amount of energy, but with low power density (Figure 1.2).[4]

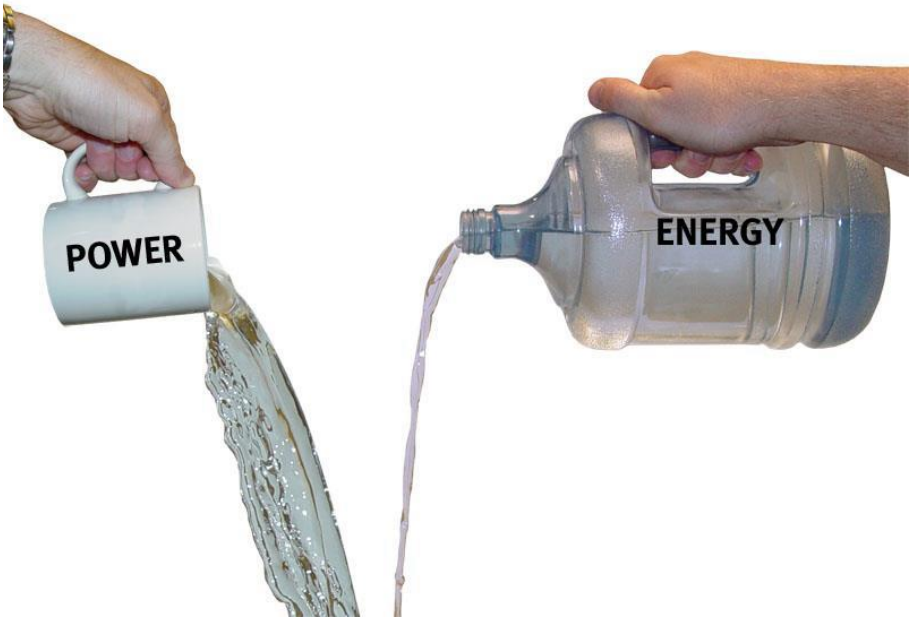

Figure 1.2. Comparison between high power density and energy density [4]

However, a supercapacitor, also referred to as an electrochemical capacitor, has a big power capacity and an enhanced energy capacity, which can fill the gap between batteries and traditional capacitors. As shown in Fig 1.3, different energy storage devices are compared in a Ragone plot. [3]

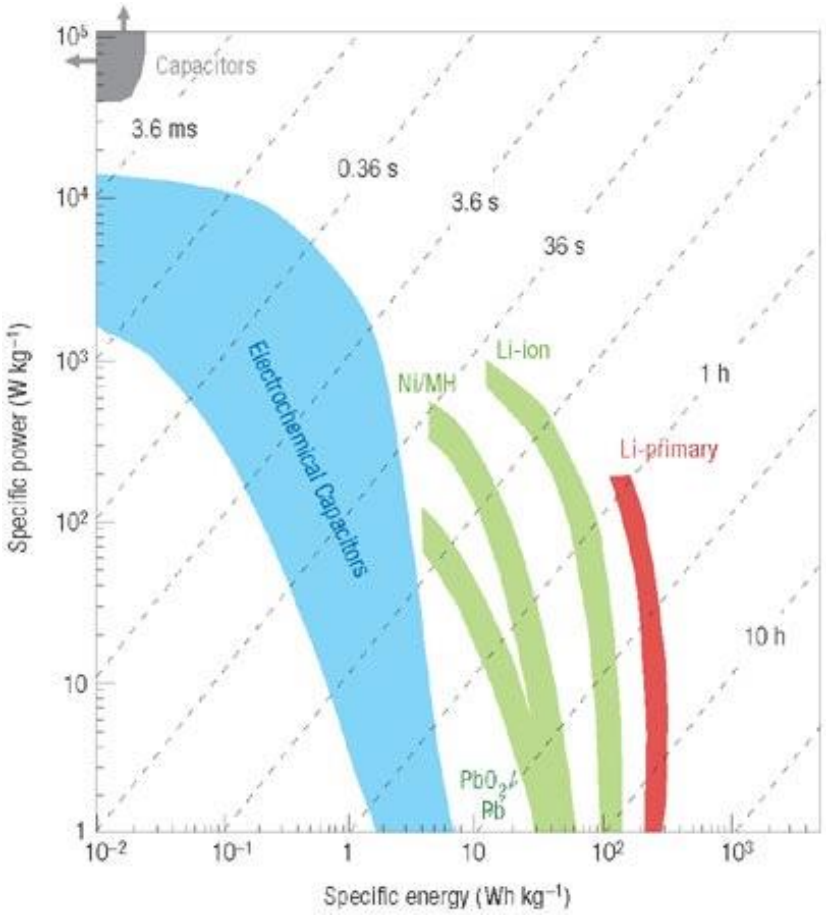

Figure 1.3. Ragone plot of various energy storage devices.[2]

Compared to batteries, supercapacitors give a high power capacity, longer cycle life, and a larger working temperature range. Hence, supercapacitors possess the potential to achieve the power requirements of energy storage devices. While the power capacity of a supercapacitor is larger than a conventional capacitor, it is still lower than that of batteries. Please see Table 1.1 for a comparison of key features. Hence, to fully exploit the potential of supercapacitors, increasing the energy performance without sacrificing the high power is required.

Table 1.1. Comparison of State-of-Art Supercapacitors and Lithium Ion Batteries

Function	Supercapacitors	Lithium Ion Battery
*Charge/discharge time	1 seconds	3-5 minutes
Cycle life	>500,000	<5,000 at 1 C rate
Specific energy (Wh kg-1)	5 (typical)	70-100
Specific power (kW kg-1)	5-10	0.5-1
Cost (Wh)	$10-20/Wh	$1-2/Wh
Cost (kW)	$25-50/kW	$75-150/kW

*Time for discharge and charge of the usable total energy stored in the devices.[5]

1.3 The Mechanisms of Electrochemical Energy Storage Devices

There are three main electrochemical energy storage categories as shown in Fig 1.4: electrical double layer capacitors (EDLCs), pseudo-capacitors, and batteries.[6] EDLCs and pseudo-capacitors are commonly called supercapacitors. Even though batteries and supercapacitors have different working mechanisms, the framework, and underlying systems are the same. Both devices consist of two electrodes, a current collector on every electrode contact, and an electrolyte separated by a separator. If the voltage is applied to a device, the negative ions found in the electrolyte accumulate on the positive electrode, while positive ions present in the electrolyte move to the negative electrode. EDLCs utilize the charge accumulated on the interface between the electrolyte and the surface of the electrode (Figure 1.4a); in contrast, pseudo-capacitors use Faradaic reactions on the surface of the electrode materials (Figure 1.4b), and batteries store charge through electrochemical reactions (Figure 1.4c).

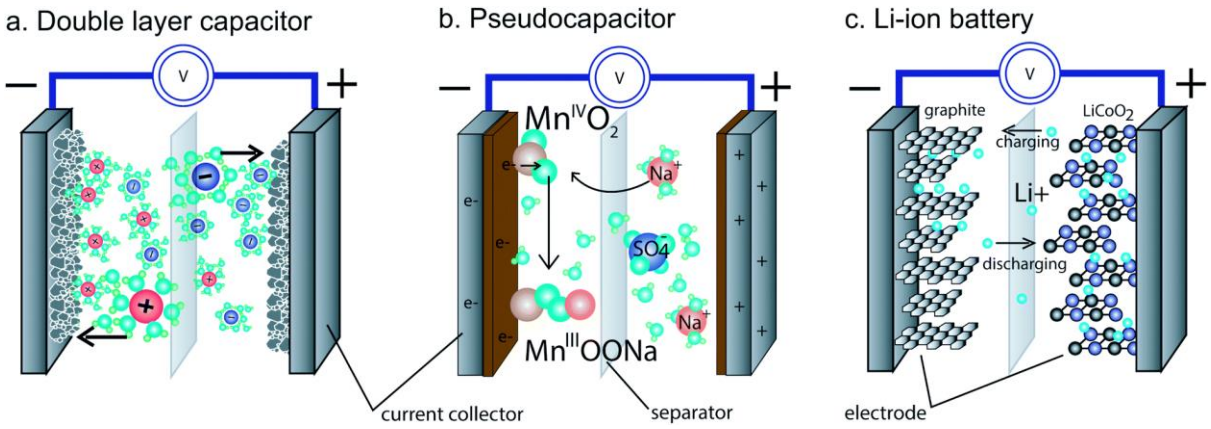

Figure 1.4. Basic mechanistic schematic for (a) double layer capacitor, (b) a pseudo-capacitor and (c) a lithium ion battery.[6]

1.3.1 The Electrical Double-layer Capacitor Mechanism

EDLCs keep the electrostatic charge at the interface between the electrode and electrolyte, where the ions concentrate on the surfaces of the electrodes. The main significant characteristic of an EDLC electrode is a large surface area and high porosity, as the amount of ion concentration is linked to the surface area that is exposed. Porous carbon materials are used as the active material in EDLCs due to their high surface area and low cost. When EDLCs are charging, electron transfer takes place from the positive electrode to the negative electrode via an outside circuit (Fig. 1.5a).[7] As an outcome, cations found in the electrolyte accumulate on the negative electrode and anions accumulate on the positive electrode. At the time of discharge, electrons transfer from the negative electrode to the positive electrode via an outside circuit and electrolyte ions no longer accumulate on the two electrodes. Fig 1.5b demonstrates the Stern model that suggests a mixture of two earlier models (Helmholtz and Gouy-Chapman).

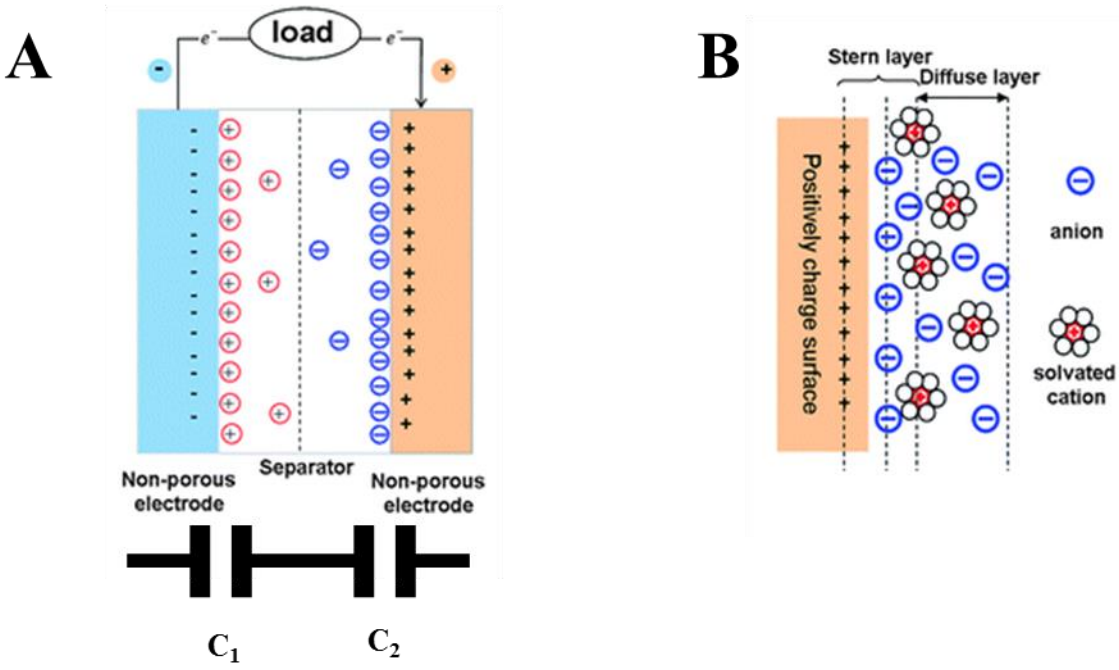

Figure 1.5. Schematic diagrams of (a) a two-cell supercapacitor device and (b) the EDL structure based on a positively charged electrode surface.[7]

In reference to the Stern model, the electrolyte develops a potential between the two layers, the internal Stern layer (the Helmholtz layer) and the diffuse external layer (the Gouy-Chapman layer) leading to the EDL high capacitance. A particular capacitance C (F g^{-1}) for each electrode is provided by:

$$C = \frac{\varepsilon_r \varepsilon_0}{d} A$$

The ε_0 is referred to as permittivity of space (8.854×10^{-12} F m^{-1}), ε_r the corresponding dielectric constant of the interface, A (m^2 g^{-1}) is the specific area of the electrode accessible to the electrolyte charge, and d (m) is the effective thickness of the EDL.

As illustrated in Fig. 1.5A, a supercapacitor may be described as two double capacitors connected in series. The device capacitance (C_T) is calculated as:

$$\frac{1}{C_T} = \frac{1}{C_1} + \frac{1}{C_2}$$

C_1 and C_2 represent the two electrode capacitances, respectively. For example, if a system has a symmetric design ($C_1 = C_2$), the device capacitance would be half of the electrode capacitance. There are many ways of defining specific capacitance, which can be normalized either as the gravimetric specific capacitance (F g^{-1}), a real capacitance (F cm^{-2}) or a volumetric capacitance (F cm^{-3}).

The energy stored and power in a capacitor is given by:

$$E = \frac{1}{2} C (\Delta V)^2$$

$$P = \frac{V^2}{4R_s}$$

In these expressions, C in Farads is referred to as the overall capacitance of the system, V in the expression of the device's total voltage, Rs in ohms is the same as the resistance of the system (ESR), E (Wh) is energy of the device and P (W) is the power of the device. Every factor is important to the total supercapacitor performance. Since energy stored is proportional to voltage squared, a device voltage increase would have a greater contribution to the improvement of the supercapacitor energy density than increasing the capacitance. In general, a higher specific capacitance is achieved with aqueous electrolyte than an organic electrolyte, but organic electrolytes (mostly acetonitrile) are widely used as they can give a high voltage window (up to 2.7 V). Unfortunately, activated carbons have a low specific capacitance in organic electrolytes that limits the energy density. Besides, organic solvents

are flammable which causes safety and environmental concerns. Aqueous electrolytes are safer, cheaper and have higher ionic conductivity, promising higher capacitance electrodes. However, the small voltage window enforced by the low decomposition voltage of water, around 1.23 V, has been challenging.

To enhance the effectiveness of the supercapacitor, in addition to energy density, we also need to consider other important properties (Fig. 1.6).[8]

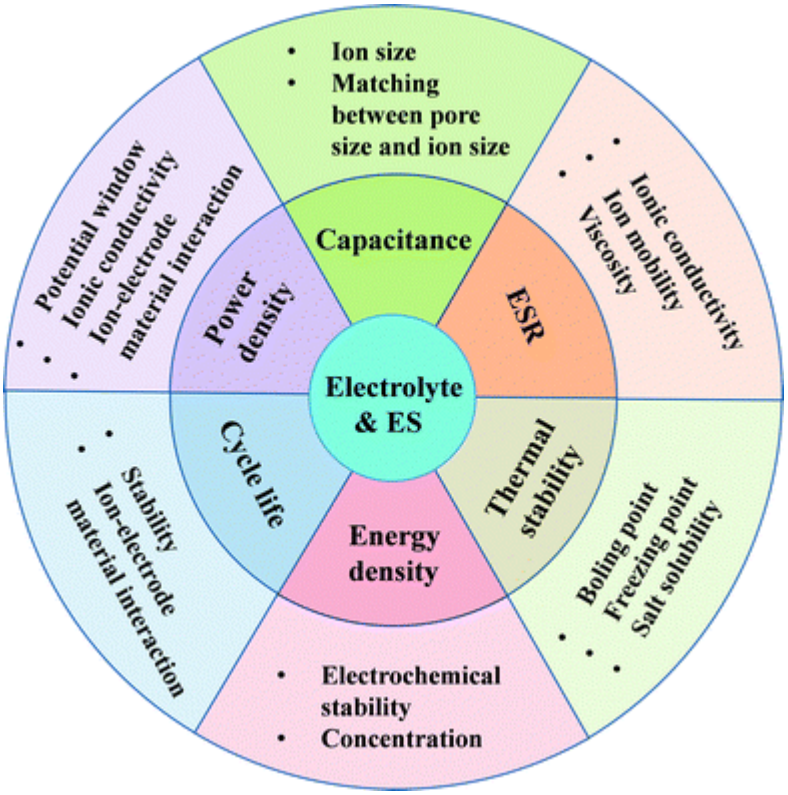

Figure 1.6. Effects of the electrolyte on the ES performance.[8]

The evaluation of supercapacitor performance is based on the following criteria: (1) energy density, (2) power density, (3) internal resistance, (4) cycle ability, (5) rate capability (fast charge/discharge process), (6) self-discharging, (7) operating temperature range, (8) toxicity, (9) safety, and (10) cost.

1.3.2 Pseudo-capacitor Mechanism

Previously, supercapacitors mainly focused on electrostatically charged devices; however, the trend has been moving towards a combination of pseudo-active materials to increase the capacitance. A pseudo-capacitor mechanism involves a redox reaction where the transfer of electrons to the electrode interface takes place. Therefore, in pseudo-capacitive materials, oxidation states undergo change during charge and discharge. To calculate theoretical pseudo-capacitance of metal oxides, the expression below is used:

$$C = \frac{n \times F}{M \times V}$$

In this expression, n is the number of electrons, F stands for Faraday's constant; M refers to the molar mass of the metal oxide, while V is the operating voltage window. Transition metal oxides such as RuO_2, MnO_2, Fe_3O_4, as well as conducting polymers, are the most promising pseudo-capactive materials examined during the past decades because of their very high energy density. The capacitance of a pseudo-capacitor can be 100 times greater than an EDLC. However, pseudo-capacitors suffer from the major drawbacks of having a lack of cycling stability and lower power density compared to an EDLC due to the use of redox reactions. Table 1.2 gives a summary of two types of supercapacitors.

Table 1.2 Summary of Supercapacitor Devices [9]

	EDLC	Pseudo-capacitors
Materials	Carbons (CNT, graphene, activated carbon)	Metal oxides (RuO_2, MnO_2, NiO, Fe_3O_4, V_2O_5)
		Conducting polymers (polyaniline, polypyrrol, polythiophene)
Store mechanism	Electrochemical double layer Physical separation of charges	Faradic reactions (Redox reactions)
Specific capacitance	~200 Fg-1 in aqueous electrolyte ~120 Fg-1 in organic electrolyte	~200-1200 F g^{-1} in aqueous electrolytes
Cycle stability	Up to million cycles	~1000 cycles
Operating voltage	Up to 3 V	~ 1 V
Cost	Inexpensive	Expensive

Much focus is now given to develop a hybrid system where the strength of EDLCs and pseudo-capacitors combine to overcome the shortcomings of each technology. Such hybrid electrochemical capacitors utilize both Faradaic and non-Faradaic mechanisms to accommodate ions, enhance energy and power capacities, in addition to keeping an effective cycling stability. Carbon-metal oxide nanocomposites possessing good electronic conductivities have been of interest as electrodes for amphibious electrochemical capacitors with the proposition that they will profit from the electrical conductivity of carbon and the high capacitance of metal oxides, thus giving devices with both higher energy capacity and higher power density. Carbon not only provides the electrical conductivity, but also plays a role in providing physical help to the metal oxide particles that improves cycling stability.

Several synergistic electrochemical performances could be expected. The attributes of the carbon, metal oxide, and metal oxide-carbon composite electrode are given in Table 1.3.[10]

Table 1.3 Comparison of Carbon, Metal Oxide and Metal Oxide–Carbon Composite Supercapacitor electrodes[10]

Electrode materials	Surface area	Pore size distribution	Specific capacitance	Conductivity	Rate capability	Stability	Cost
Carbon	High	Various way to tailor	Low	High	High	Good	Low
Metal oxide	Normally low	Difficult to tailor	High	Low	Low	Poor	High
Metal oxide-carbon composite	Normally controlled by a carbon support	Various ways to tailor depending on the carbon support	High	Tunable, depending on the carbon support	Good	Good	Moderate

The support structure of carbon should have high conductivity, suitable porosity, and high specific surface area, topped with nanostructured metal oxides to add high energy density. In addition, the composite electrode microstructure is one of the critical factors to achieve high-performance electrodes.

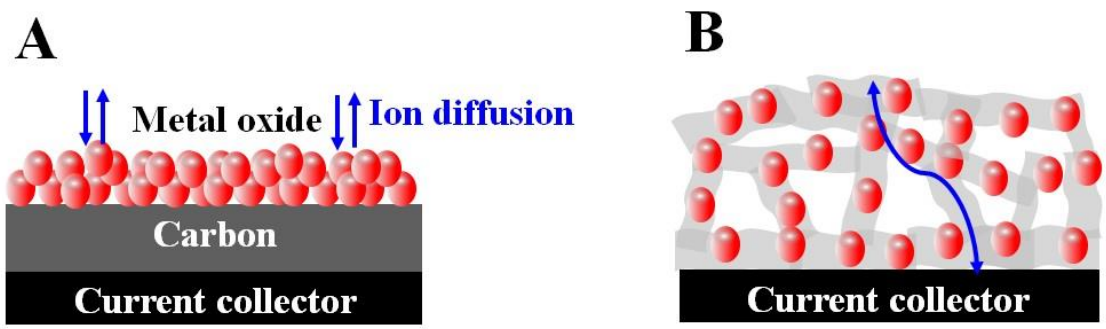

Figure. 1.7 The design of hybrid supercapacitor electrodes showing (A) non-ideal (B) ideal structures.

For example, as can be seen in Figure 1.7a, if a metal oxide is grown on the top of a carbon support, only the metal oxide can be exposed to the electrolyte so that carbon cannot be involved in charge storage. To solve this problem, the carbon substrate should have a macro-porous framework and the metal oxide should be grown to create a structure like Fig. 1.7b. In this structure, the conductive carbon framework provides fast electron charge transfer to the metal oxide and also due to the porous structure, provides short ion diffusion pathways. Besides symmetric composite electrodes, an asymmetric device can use a redox reaction in one electrode, and EDL properties in the other. This type of hybrid supercapacitor can bridge the gap between lithium-ion batteries and supercapacitors (Fig. 1.8). [11]

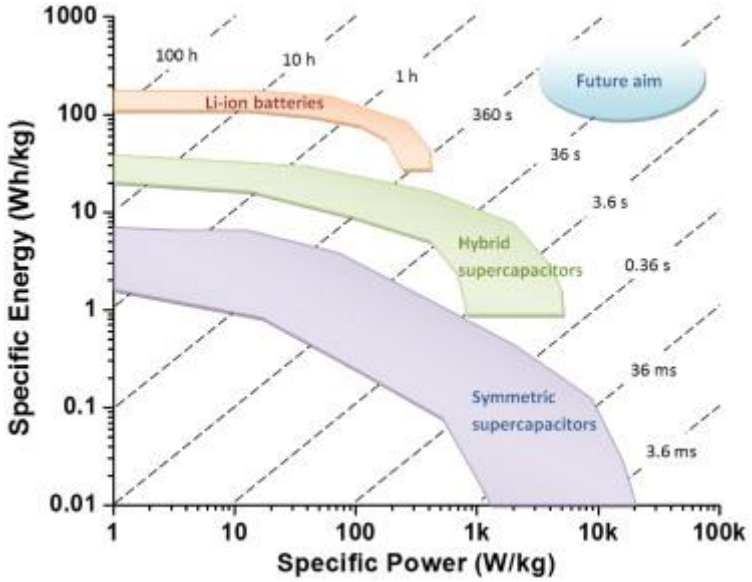

Fig. 1.8 Ragone plot of three major electrochemical energy storage devices. Time constants are shown via dashed lines, by dividing the specific energy by the specific power.[11]

1.4 Electrode Materials for Supercapacitors

1.4.1 EDLC Materials

In supercapacitors activated carbons (ACs) are the most used substances currently because of their high surface area (up to 3033 $m^2 g^{-1}$) and low cost. However, a few micron size particles make an inefficient ion pathway, and inaccessible electrolyte makes significant dead mass, resulting in a low specific capacitance.

Table 1.4 Comparison of Carbon Materials for Supercapacitor Electrodes[7]

Carbon	Specific surface area	Density	Electrical conductivity	Cost	Aqueous electrolyte		Organic electrolyte	
	$m^2 g^{-1}$	$g cm^{-3}$	$S cm^{-1}$		$F g^{-1}$	$F cm^{-3}$	$F g^{-1}$	$F cm^{-3}$
Fullerene	1100-1400	1.72	10^{-8}-10^{-14}	Medium				
CNTs	120-500	0.6	10^4-10^5	High	50-100	<60	<60	<30
Graphene	2630	>1	10^6	High	100-205	>100-205	80-110	>80-110
Graphite	10	2.26	10^4	Low				
ACs	1000-3500	0.4-0.7	0.1-1	Low	<200	<80	<100	<50
Templated carbon	500-3000	0.5-1	0.3-10	High	120-350	<200	60-140	<100
Functionalized carbon	300-2200	0.5-0.9	>300	Medium	150-300	<180	100-150	<90
Activated carbon fibers	1000-3000	0.3-0.8	5-10	Medium	120-370	<150	80-200	<120
Carbon aerogels	400-1000	0.5-0.7	1-10	Low	100-125	<80	<80	<40

Recent developments in carbon beyond three-dimensional (3D) graphite including two-dimensional (2D) graphene, one-dimensional (1D) carbon nanotubes (CNTs) and zero-dimensional (0D) fullerenes, have led to their use in EDLCs because of good electrical conductivity and low dimensional nanostructures. Table 1.4 shows a summary of the properties of the different carbon materials. [7] Graphene is one of the most common materials for such uses, due to its amazingly large surface area, excellent electrical and thermal conductivity, electrochemical stability, and mechanical properties. Graphene-based EDLCs also provide a theoretical capacitance of up to 550 $F g^{-1}$.

1.4.2 Pseudo-Materials

In addition to carbons, a large capacitance is reached by utilizing redox active substances like metal oxides and conducting polymers (Fig 1.9).[7]

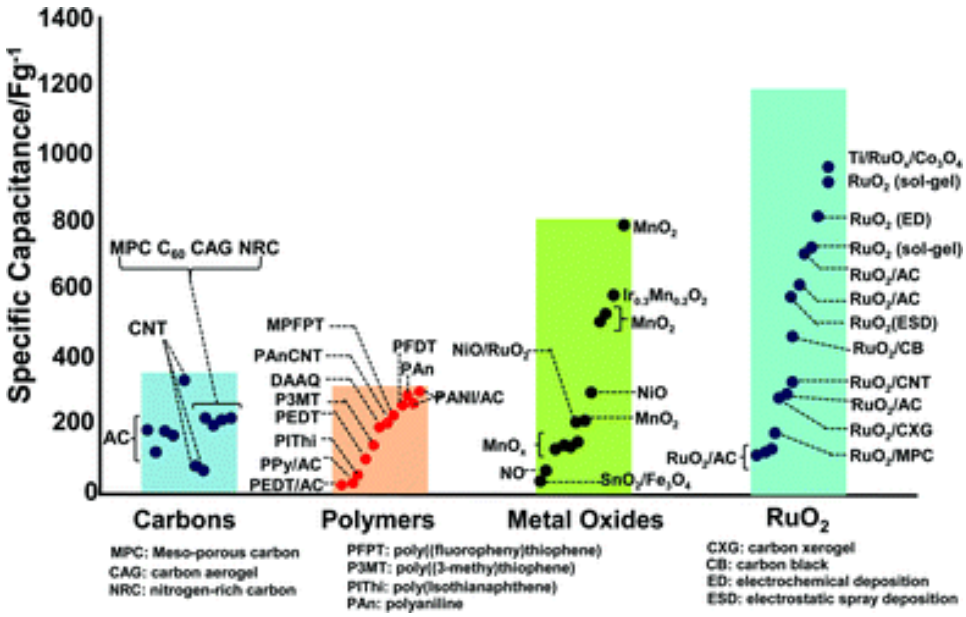

Fig. 1.9 Typical specific capacitances for different supercapacitor materials.[7]

Among all the metal oxides available, RuO_2 has been examined widely as a substance for pseudo-capacitors because of its surprisingly large specific capacitance (1300-2200 F g^{-1}) and highly reversible charge-discharge attributes, wide potential window, and good electrical conductivity (10^5 S cm^{-1}).

The capacitive performance is due to reversible electron transfer at the active redox surfaces of RuO_2, balanced by proton transfer, which leads to the conversion of OH to O_2.

$$RuO_2 + xH^+ + xe^- \leftrightarrow RuO_{2-x}(OH)_x$$

Although RuO_2 has good electrochemical performance, it still has limits for practical applications due to its high price. Less expensive oxides of manganese, iron, vanadium,

nickel and cobalt can replace ruthenium oxide. Particularly, there has been an interest in MnO_2 based electrodes due to the much more affordable cost and low toxicity with a large theoretical special capacitance totaling to 1,380 F g^{-1}. The charge accommodation capacity of MnO_2 is high because of surface absorption of electrolyte cations and redox transitions between Mn(III)/Mn(II), Mn (IV)/Mn(III) and Mn(VI)/Mn(IV) according to the following reaction:

$$MnO_2 + xC^+ + yH^+ + (x+y)e^- \leftrightarrow MnOOC_xH_y$$

MnO_2 shows electrochemical attributes that can be attributed to intrinsic pseudo-capacitive charge storage. The affordable cost, availability, and a large theoretical capacitance make it a very desirable substance for electrochemical capacitors that are based on aqueous electrolytes. The main disadvantage with this material is its poor electronic conductivity (10-13 S cm^{-1}), preventing high areal capacitance at high rates. A recent report showed that ultrathin film of MnO_2 can solve these problems and can achieve above 1000 F g^{-1}, demonstrating that nano-materials can help to improve pseudo-capacitor performance.

Instead of metal oxides, conducting polymer-based pseudo-capacitors are also showing great promise. In addition, polymer electrodes have high electric conductivity up to 10^4 S cm^{-1}. [12] Many studies have been carried out on the synthesis of conducting polymers for energy storage such as for their use in batteries and supercapacitors. To achieve high pseudo-capacitance polyaniline, polypyrrole, and derivatives of polythiophene have been used. However, the disadvantage of these polymers is swelling and shrinking during charging and discharging that can cause long-term degradation.

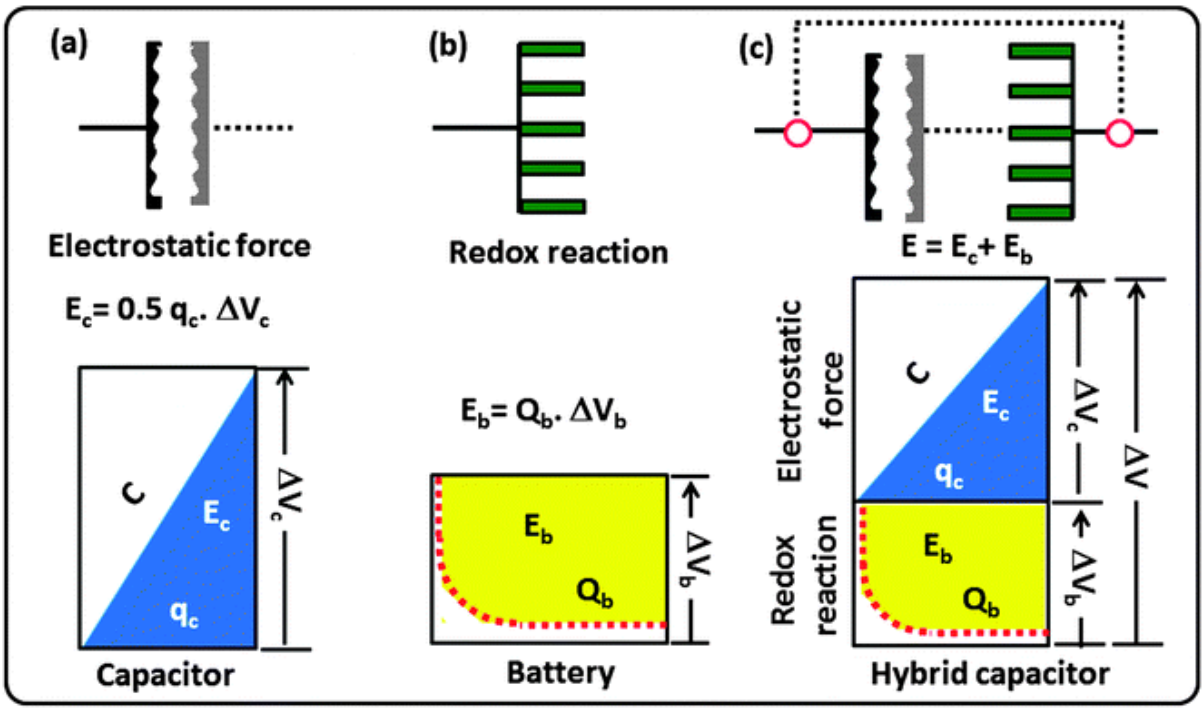

Fig. 1.10 Schematic representations of a (a) supercapacitor electrode, (b) a battery electrode and (c) an asymmetric capacitor system.[13]

Recently, several research reports have focused on hybrid materials to enhance energy density (references?). Dramatic improvements in both capacitance and operating voltage have been achieved with the application of asymmetric systems of various positive and negative electrodes, providing a larger operating voltage. A case in point is a mixture of an EDLC electrode (power source) with a battery-like electrode or a pseudo-capacitor electrode (energy source) in the same cell. This system can provide a high energy density of the battery-like electrode, while the EDLC electrode enables it to deliver high power. Furthermore, an effective electrode mixture can even raise the battery voltage, as shown in Fig 1.10.[13] Consequently, the hybrid asymmetric cell device provides a very good solution for enhanced energy density.

1.5 Applications of Supercapacitors

ECs have several names including supercapacitors and ultracapacitors. The supercapacitor and ultra-capacitor terms were initially introduced by the manufacturers Nippon Electric Company (NEC) and Pinnacle Research Institute (PRI), respectively, in 1978.[14] Since supercapacitors were commercialized by NEC, supercapacitors have become ubiquitous power source devices as a result of their high power density and long cycle life and used in a wide range of applications.

Application 1: Airbus A380

On the Airbus A380, in 2005, the jumbo jets use a supercapacitor to operate the aircraft's heavy doors for emergency opening. The modules can reach 100 F with 2.7 V with supercapacitors connected in series and in parallel. This successful application has proven that supercapacitors are an obviously reliable power source.

Application 2: Toyota Prius

The Toyota TS0040 introduced double supercapacitors for their regenerative braking since their power is several times greater than the former battery design leading to enhanced recovery of energy.[15] In regenerative systems, the power acquisition comes from the braking system and this harnessed power is utilized for increased speed or for the other accessory enhancements. Because this application needs to accommodate energy for a short time, a high power source like supercapacitors provides a good solution for this form of application.

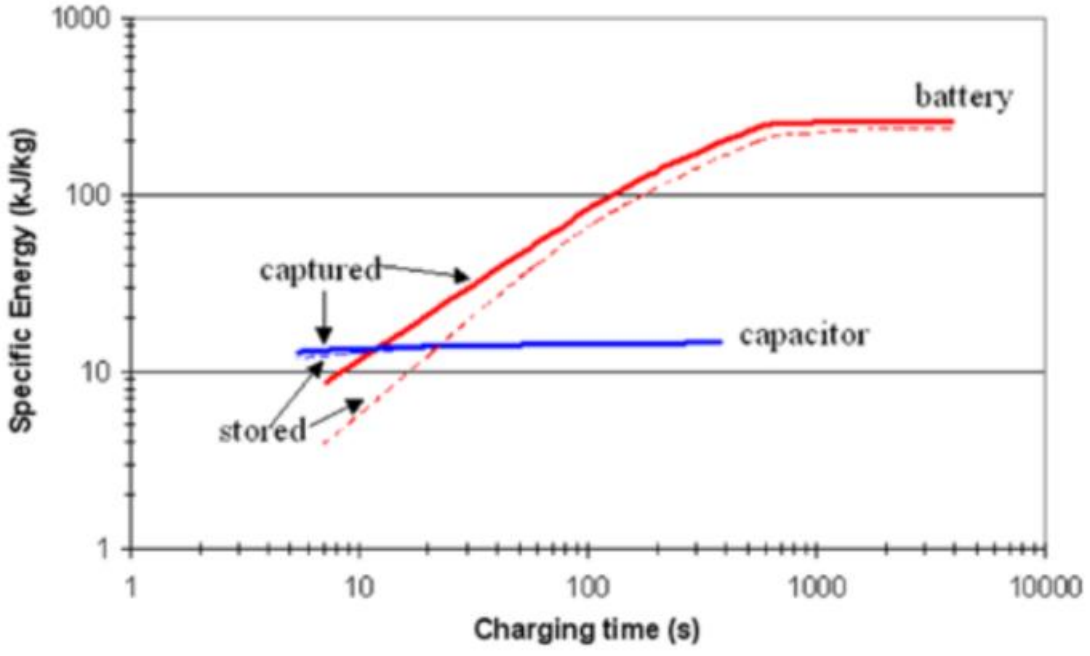

Fig. 1.11 Captured and stored regenerative specific energy for two different energy storage devices (Supercapacitor: 3000 F, 2.7 V and lithium-ion battery: 12 Ah, 2.8 V).[5]

Figure 1.11[5] compares harnessed and stored power for a supercapacitor and a Li-ion battery. During a minimum charging duration (below 10 sec) the capacitor shows higher specific energy than the battery, and for the 10 sec charge time, the captured energy from the two devices is the same. However, the capacitor can store higher energy than the battery. At 20 sec, the amount of energy stored is equal from both devices and after 20 sec battery has higher energy than the supercapacitor. This figure clear shows that a supercapacitor is an excellent energy storage system when charging in a short period is required.

Application 3: Forklifts and Cranes

Many forklift and crane manufacturers are using supercapacitors to capture and store regenerative energy during load lowering and then apply the same power to the next lifting cycle. This operating system can substantially reduce fuel consumption and accompanying emissions. Figure 1.12 is an example of a hybrid diesel-electric gantry crane using supercapacitors for energy storage.

Fig. 1.12 Hybrid diesel/electric rubber tired gantry crane with an electrochemical capacitor energy storage system.[5]

Application 4: Peugeot 308 and Cadillac 2016 sedan

Start-stop systems, which shut down the engine when it comes to a stop and as soon as the drivers depresses the brake pedal, the system automatically restarts the engine, are now entering world car markets in serious numbers to boost fuel efficiency. The Peugeot 308 and several models from Cadillac have selected supercapacitor-based stop-start systems. While we drive, we can experience several stop/start cycles during a day which means this system requires high cycle life. Thus, supercapacitors are better suited for the start-stop system than batteries. Figure 1.13 shows a Peugeot Citroen micro-hybrid system that contains 5 V supercapacitors.[15]

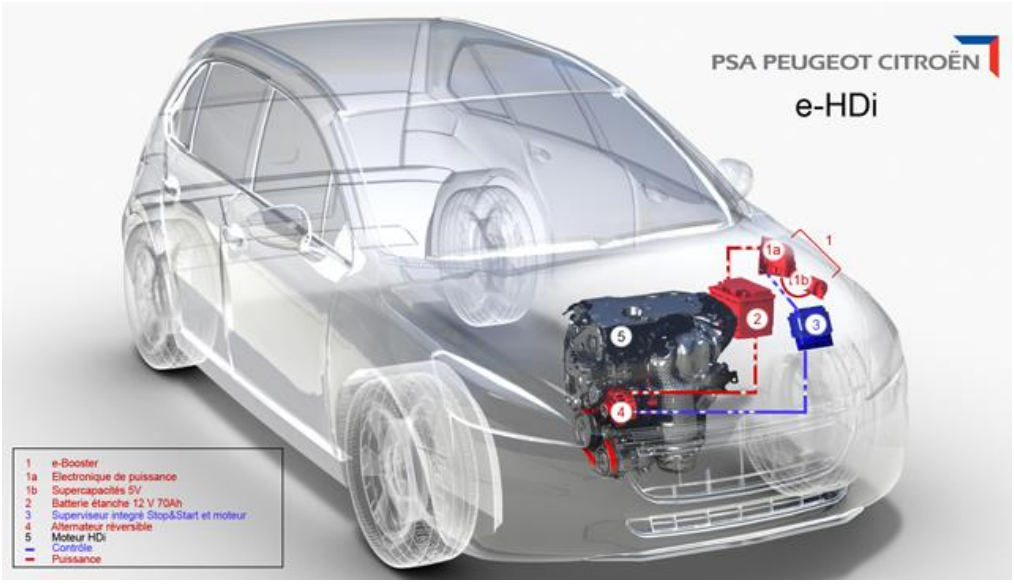

Fig 1.13. PSA Peugeot Citroen in France with their e-HDi microhybrid system contains 5 V supercapacitors.[16]

Application 5: Supercapacitor Buses

Supercapacitors are particularly well suited for city buses that have to stop frequently. Now a Chinese company, AOWEI Science And Technology Co., Ltd has developed a supercapacitor module for city buses, which already have been on the road since 2009.[17] A single charged capacitor can provide enough energy to travel to the next bus stop (5 km) at 44 km h^{-1} and the supercapacitors allow for fast charging during the time passengers need to board or alight from a bus. In addition, the buses have a regenerative braking energy system, which can charge the supercapacitors. Thus, the supercapacitor bus could be the most economical way of powering city buses. A supercapacitor bus in Shanghai is shown in Fig 1.14.

Fig 1.14. A bus that runs entirely on supercapacitors charges up at a bus stop in Shanghai.[17]

Application 6: Power Tools

Coleman introduced a supercapacitor screwdriver that can be fully charged in only 90 sec instead of using batteries which can take 10 minutes or longer. Supercapacitors were selected, rather than batteries because of fast charging performance and longer cycle life, Figure 1.15.

Fig. 1.15. A capacitor powered screwdriver that is fully charged in 90 seconds.[5]

1.6 Objectives of This Thesis

The goal of this thesis is to make and prepare novel carbon-based nanostructures to improve supercapacitor electrochemical performance. A series of metal oxides and conducting polymers are grown on 3-dimensional, highly porous graphene, characterized and evaluated based on the following strategies:

- To look for good electrode substances with high capacitance and good electrical conductivity.

- To optimize the design of composite nanostructures, which can give high energy capacity without compromising power density.
- To enhance cycle life and lower equivalent series resistance of the hybrid electrode.
- To provide for fast charging and discharging.
- To be environmental friendly.

1.7 Structure of the Dissertation

A brief introduction (Chapter 1) will discuss the background and applications of supercapacitors. Chapter 2 will present direct preparation and processing methods for hybrid electrodes using a laser. The produced electrodes demonstrate the highest capacitance reported to date for a RuO_2-based supercapacitor. Also, an asymmetric electrochemical capacitor having an LSG/RuO_2 positive electrode and an active carbon negative electrode shows a very high power density of 55 Wh kg^{-1}, placing it among the best performing hybrid supercapacitors.

Chapter 3 presents a symmetric supercapacitor consisting of magnetite nanoparticles that are carefully hybridized with a three-dimensional form of graphene utilizing a redox mediator [$Fe(CN)_6^{3-}/Fe(CN)_6^{4-}$] with neutral Na_2SO_4 electrolyte. As both electrode and electrolyte contribute to charge storage simultaneously, an ultrahigh specific capacitance of more than 716 F g^{-1} is obtained, which is five times higher than traditional activated carbon electrodes. This symmetric supercapacitor demonstrates excellent electrochemical performance with an energy density of 121 Wh kg^{-1}, placing it among the best performing hybrid supercapacitors.

Chapter 4 discusses two strategies for improving energy density. First, we discuss that laser treatment of activated carbon electrodes results in the formation of micro-channels that can connect the internal pores of activated carbon with the surrounding electrolyte. Second, the capacitance can be further increased via rapid and reversible redox reactions on the surface of the electrode using an active redox electrolyte, enabling the operation of a symmetric device at 2.0 V.

Chapter 5 discusses the composite materials of flash converted graphene and activated carbon to make a novel architectural form that facilitates the rapid transport of the ions and electrons at the same time maintaining the high packing density. Devices made with these composite (FCG/AC) electrodes exhibit improved power, energy density, and rate capability. In addition, this device was made into commercially viable coin cell form that provides an opportunity for a wide scope of uses. Investing in better and more efficient systems of energy will minimize the release of greenhouse gasses associated with traditional sources of energy like fossils fuels.

In Chapter 6, we demonstrate for the first time a simple, yet versatile method for the easy fabrication of high-performance polyaniline micro-pseudo-capacitors. Furthermore, by combining graphene with nano-structured polyaniline several different dimensions (1D, 2D, and 3D) of hybrid supercapacitors can be made; here the energy density and power capacity are compared to dimensionality.

The last chapter (Chapter 7) of this dissertation provides conclusions drawn from the present thesis and suggestions for future work.

1.8 References

(1) Jeong, G.; Kim, Y.-U.; Kim, H.; Kim, Y.-J.; Sohn, H.-J. *Energ. Environ. Sci.* **2011**, *4*, 1986.

(2) Teymourfar, R.; Asaei, B.; Iman-Eini, H.; Nejati fard, R. *Energ. Convers. Manage.* **2012**, *56*, 206.

(3) Simon, P.; Gogotsi, Y. *Nat. Mater.* **2008**, *7*, 845.

(4) http://www.maxwell.com/

(5) Miller, J. R., and Burke. A. F. *Electrochem. Soc. Interface* **Spring 2008,** 53**.**

(6) Jost, K.; Dion, G.; Gogotsi, Y. *Journal of Materials Chemistry A* **2014**, *2*, 10776.

(7) Zhang, L. L.; Zhou, R.; Zhao, X. S. *J. Mater. Chem.* **2010**, *20*, 5983.

(8) Zhong, C.; Deng, Y.; Hu, W.; Qiao, J.; Zhang, L.; Zhang, J. *Chem. Soc. Rev.* **2015**, *44*, 7484.

(9) Liu, C.; Li, F.; Ma, L.-P.; Cheng, H.-M. *Adv. Mater.* **2010**, *22*, E28.

(10) Zhi, M.; Xiang, C.; Li, J.; Li, M.; Wu, N. *Nanoscale* **2013**, *5*, 72.

(11) Li, X.; Wei, B. *Nano Energy* **2013**, *2*, 159.

(12) González, A.; Goikolea, E.; Barrena, J. A.; Mysyk, R. *Renew.Sust. Energ. Rev.* **2016**, *58*, 1189.

(13) Dubal, D. P.; Ayyad, O.; Ruiz, V.; Gomez-Romero, P. *Chem. Soc. Rev.* **2015**, *44*, 1777.

(14) Sharma, P.; Bhatti, T. S. *Energy Convers.Manage.* **2010**, *51*, 2901.

(15) http://gas2.org/2014/06/23/toyota-prius-get-le-mans-supercapacitor-tech/

(16) http://evworld.com/focus.cfm?cid=255

(17) http://www.aowei.com/en/case_view.php?typeid=1&id=4

Chapter 2. Direct Preparation and Processing of Graphene/RuO_2 Nanocomposite Electrodes for High-Performance Capacitive Energy Storage

2.1 Abstract

Carbon materials are widely used in supercapacitors because of their high surface area, controlled porosity and ease of processing into electrodes. The combination of carbon with metal oxides results in hybrid electrodes with higher specific capacitance than pure carbon electrodes, which has so far limited the energy density of supercapacitors currently available commercially. However, the preparation and processing of carbon/metal oxide electrodes into supercapacitors of different structures and configurations, especially for miniaturized electronics, has been challenging. Here, we demonstrate a simple one-step process for the synthesis and processing of laser-scribed graphene/RuO_2 nanocomposites into electrodes that exhibit ultrahigh energy and power densities. Hydrous RuO_2 nanoparticles were successfully anchored to graphene surfaces through a redox reaction of the precursors, graphene oxide, and $RuCl_3$ using a consumer grade LightScribe DVD burner with a 788 nm laser. This binder-free, metal current collector-free graphene/RuO_2 film was then used directly as a hybrid electrochemical capacitor electrode, demonstrating much-improved cycling stability and rate-capability with a specific capacitance up to 1139 F g^{-1}. We employed these hybrid electrodes for building aqueous-based symmetric and asymmetric cells that can deliver energy densities up to 55.3 Wh kg^{-1}, placing them among the best performing hybrid electrochemical capacitors. Furthermore, this technique was used for the direct writing of interdigitated hybrid micro-supercapacitors in a single step for the first time, with great potential for miniaturized electronics. This simple approach provides a general strategy for making a wide range of composite materials for a variety of applications.

2.2 Introduction

The ever-increasing demand for smaller portable electronics has driven the need for efficient energy storage devices with continually shrinking footprints.[1] During the last few years, electrochemical capacitors have been successfully used as a powering medium for a camera flash, back-up power, regenerative braking, and a new generation of electric vehicles. Electrochemical capacitors offer significant advantages compared to conventional storage media, such as batteries and capacitors, [2] providing significantly higher energy densities than conventional capacitors and higher power and longer cycle life than batteries.[3, 4] Electrochemical capacitors can be separated into two general categories: electrical double layer capacitors (EDLCs) and pseudo-capacitors. EDLCs store electrostatic charge at the interface between the electrode and electrolyte, where the charge accumulates on the electrode surface. The most important attributes of an EDLC electrode are high surface area and high porosity, as the amount of charge accumulation is related to the exposed surface area. Recent advances in carbon materials such as carbon nanotubes, [5] graphene, [6] and activated carbon (AC) [7] have led to their use as the active material in EDLCs. Graphene is one of the most attractive materials for such applications, owing to its remarkably high surface area, excellent electrical and thermal conductivity, electrochemical stability, and mechanical properties.[8, 9] Recent studies have reported methods for fabricating 3-dimensional graphene via a laser scribing technique.[10-16] This method is especially advantageous as it allows patterning and fabrication of microsupercapacitors in a very simple fashion, while offering remarkably high electrochemical performance. While graphene-based EDLCs can provide a theoretical capacitance up to 550 F g^{-1}, [11] this falls short for many practical applications, especially when compared to batteries.

Pseudo-capacitors, which are based on redox reactions of the electrode material, can have up to 10 times higher capacitance than EDLCs, yet their wide-spread applications have been limited due to lower power density and poor cycling stability. In pseudo-capacitors, only surfaces and near-surface sites can contribute to charge storage via redox reactions, where the electrode materials are commonly metal oxides[17] or conducting polymers. Among the metal oxides, RuO_2 has been widely studied as a material for pseudo-capacitor applications due to its remarkably high specific capacitance (1300-2200 F g^{-1}), [18-22] highly reversible charge-discharge features, wide potential window, and high electrical conductivity (10^5 S cm^{-1}). For practical applications of RuO_2 as a pseudo-capacitor electrode, power density and cycle life must be improved.

Much attention has been focused on developing a hybrid system where the merits of EDLCs and pseudo-capacitors are combined to overcome the shortcomings of each individual technology. Such hybrid electrochemical capacitors offer improved energy and power densities, as well as improved cycling stability.[23] Carbon-metal oxide nanocomposites with high electronic conductivities have been of interest as electrodes for hybrid electrochemical capacitors with the proposition that they will benefit from the electrical conductivity of carbon and the high capacitance of metal oxides, thus providing systems with both higher energy density and higher power density. While previous studies of carbon-RuO_2 electrochemical capacitors have demonstrated improved overall performances, further improvements in the energy density are still required.[18, 24-30] Another issue is the preparation of these electrochemical capacitors that often require multiple steps including post-processing, thereby limiting the potential of these methods for practical applications. Small-scale supercapacitors, known as micro-supercapacitors, have emerged as promising energy sources for powering microelectronics. Despite the significant progress, graphene/RuO_2

electrodes have been employed only in conventional parallel plate supercapacitors and have not yet been demonstrated in miniature interdigitated supercapacitors. This is because of the difficulty of fabrication and processing of hybrid materials into patterned microelectrodes. These hybrid micro-supercapacitors may, one day, be used to complement or even replace batteries and electrolytic capacitors in a variety of applications.

In this paper we propose a 3-dimensional hybrid electrochemical capacitor based on a carbon-RuO_2 nanocomposite. The nanocomposite is comprised of a 3-dimensional laser-scribed graphene (LSG) framework combined with hydrous RuO_2 nanoparticles via a one-step procedure where graphene oxide (GO)/$RuCl_3$ are simultaneously reduced (GO → LSG) and oxidized ($RuCl_3$ → RuO_2) via a standard laser scribing technique.[11] By anchoring RuO_2 nanoparticles directly onto LSG, the 3-dimensional, highly porous graphene surface serves as an excellent conductor for fast electron transfer, while RuO_2 nanoparticles provide a large electrochemical active surface area for fast and reversible Faradaic reactions. As a result of this unique structure, the LSG/RuO_2 electrodes demonstrate high electrical conductivity (911 Siemens per meter) and ultrahigh specific capacitance of 1139 F g^{-1}, which is nearly 5 times higher than pristine LSG electrodes. We also show that LSG/RuO_2 hybrid electrodes can be integrated into an asymmetric electrochemical capacitor operating at a maximum cell voltage of 1.8 V in an aqueous electrolyte. This asymmetric cell demonstrates a volumetric energy density of 5 mWh cm^{-3}, which is about ten times higher than that of 44 mF/ 2.75 V commercially available activated carbon electrochemical capacitors and comparable to that of a 500 µAh/ 4 V lithium thin-film battery. This excellent electrochemical performance is also superior to other metal oxide based electrochemical capacitors published recently. Unlike previous techniques that can only be used for the preparation of graphene/RuO_2 composites in solution, the technique described here can be used for patterning micro-supercapacitor

electrodes of any arbitrary shape. This has led, for the first time, to the fabrication of hybrid micro-supercapacitors in a single step. These micro-supercapacitors can be made as a single cell or as modules consisting of any number of cells assembled together in series/parallel combinations. This work demonstrates the promise of EDLC/pseudo-capacitor hybrid electrodes for the development of high-performance electrochemical capacitors for future electronics.

2.3 **Results and discussion**

2.3.1 Fabrication of a hydrous LSG/RuO_2 electrode

LSG/RuO_2 was synthesized by the simultaneous reduction of graphene oxide and formation of RuO_2 nanoparticles through *in situ* oxidation of $RuCl_3$. A GO slurry and $RuCl_3$ hydrate powder were first suspended in water to create a well-dispersed suspension of GO/$RuCl_3$ due to the electrostatic attraction between positively charged Ru^{3+} and negatively charged oxygen-containing groups on GO. The presence of hydrophilic oxygen-containing functional groups on the GO surface serves as a surfactant to ruthenium chloride; post-reduction, this well-dispersed ruthenium oxide works as a nanospacer prohibiting the restacking of graphene. Following the standard LightScribe laser etching, the mixed sample undergoes a simultaneous oxidation of Ru^{3+} ($RuCl_3$) to hydrous RuO_2 and reduction of GO to LSG. The Ru loading in the LSG/RuO_2 electrode was estimated to be 45 wt% (by mass) using inductively coupled plasma atomic emission spectroscopy (ICP-AES). These films were used directly as electrodes without any further processing (Fig. 2.1).

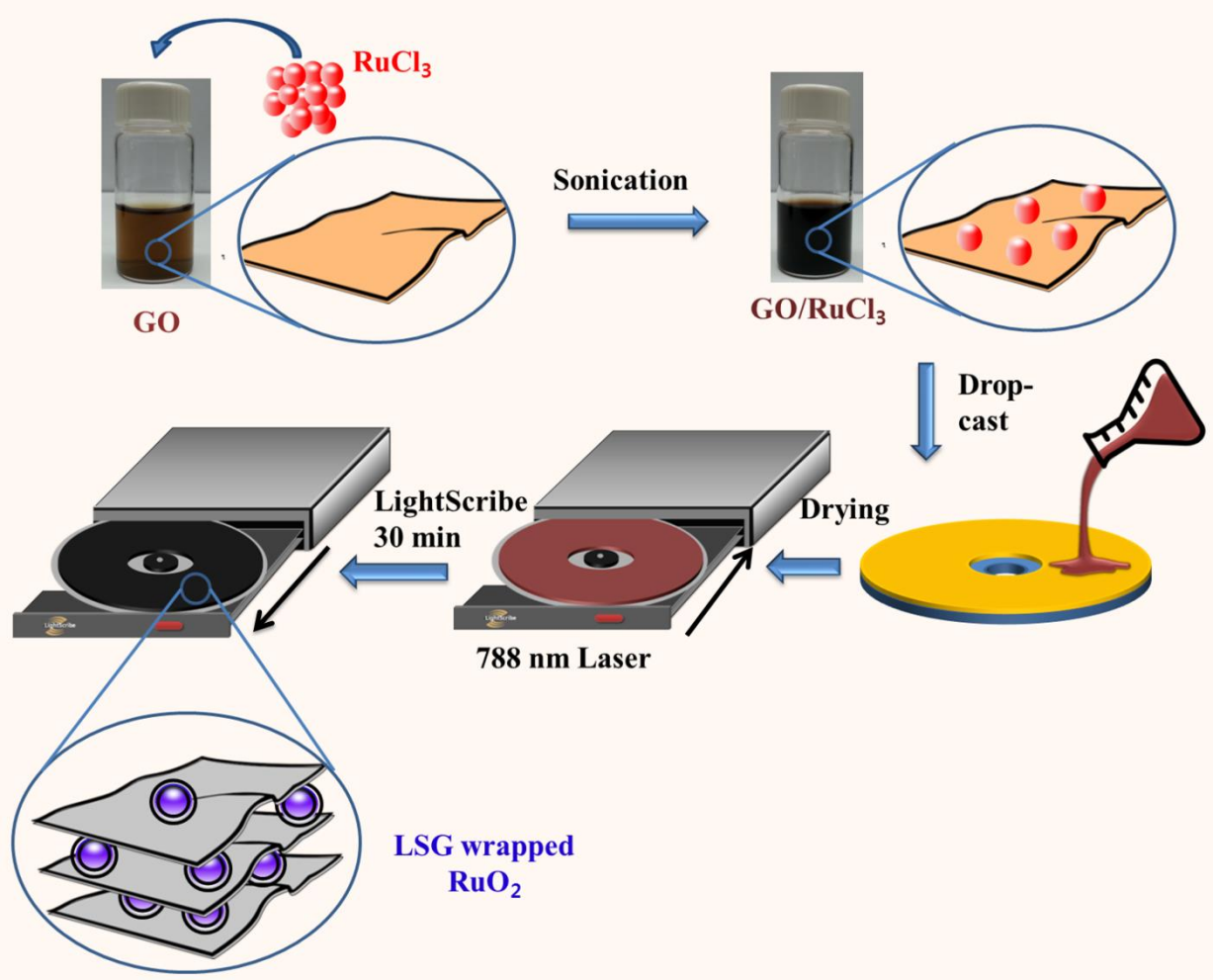

Figure 2.1 Fabrication of LSG/RuO_2 nanocomposites. $RuCl_3$ is mixed with an aqueous dispersion of GO, sonicated, drop-cast onto a compact disc and then exposed to a 788 nm laser in a LightScribe DVD optical drive to create LSG wrapped with RuO_2 nanoparticles.

2.3.2 Characterization of LSG/RuO_2 electrodes

The structure and morphology of LSG/RuO_2 electrodes were investigated by scanning electron microscopy (SEM), transmission electron microscopy (TEM), X-ray photoelectron spectroscopy (XPS) and thermal gravimetric analysis (TGA). Fig. 2.2 a shows an SEM image of the nanocomposite, with RuO_2 nanoparticles uniformly dispersed on the conductive LSG. A TEM image together with a selected area electron diffraction (SAED) pattern of the LSG-

RuO_2 nanocomposite is shown in Fig. 2.2 b. The average RuO_2 particle size was found to be ~20 nm. The relative intensities and positions of the diffraction rings along the dashed line are illustrated in the line-profile in the inset to Fig. 2.2 b. Calculated d-spacings of the peaks are in agreement with the reference data shown in Table 2.1 along with the corresponding Miller indices (<hkl>).

Table 2.1 Crystallographic Index of RuO_2 Nanoparticles

hkl	d-Spacing (nm)	
	Reference	Measured*
101	0.256	0.254
200	0.225	0.225
111	0.222	0.220
210	0.201	0.204
211	0.169	0.169
310	0.142	0.143
202	0.128	0.128
212	0.123	0.122
222	0.111	0.111

*Obtained from the SAED pattern shown in Fig. 2.2b.

Thus, it can be confirmed that the nanoparticles are indeed RuO_2. A high resolution TEM (HRTEM) image of the composite (Fig. 2.2c) reveals that multiple layers of the LSG sheets wrap around each RuO_2 nanoparticle. The spacing between the LSG lamellae is ~0.34 nm (Fig. 2.2d), in agreement with the reported π-π stacking distance of graphitic materials.[31] A HRTEM image of RuO_2 nanoparticles reveals their single crystalline nature, with a <111> d-

spacing of 0.22 nm (Fig. 2.2e). From these electron microscopy studies, it can be concluded that a uniform dispersion of RuO_2 particles has been successfully obtained using the laser scribing method. The unique wrapping configuration of the RuO_2/LSG structure allows several advantages: (i) it prevents the formation of agglomerated RuO_2, promoting low strain and stress that often results from volume changes and may thus improve the cycling performance of RuO_2; (ii) the LSG-wrapped structure allows a strong interaction with individual RuO_2 nanoparticles to induce efficient capacitance collection throughout the conductive LSG; and (iii) RuO_2 nanoparticles serve as nanospacers to help maintain a high surface area, 3-dimensional porous structure within the LSG, allowing the electrolyte to interact with the entire surface of the electrode which in turn facilitates ion transport during redox reactions, as illustrated in Fig. 2.2 f.[28]

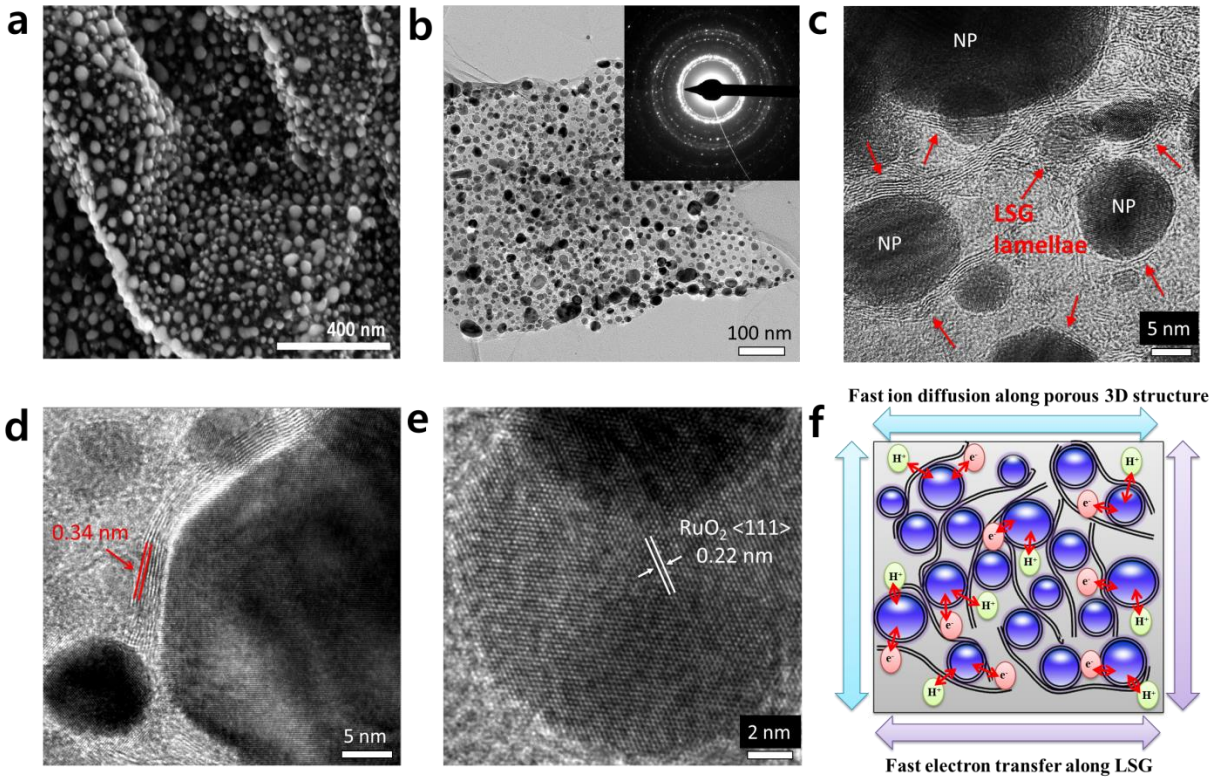

Figure 2.2 Microscopic characterization of LSG/RuO_2 nanocomposites. (a) SEM image showing RuO_2 nanoparticles grown on LSG. (b) TEM image with SAED pattern inset indicating the polycrystalline nature of RuO_2 in the LSG composite. (c) A TEM image under higher magnification illustrating that the RuO_2 nanoparticles (NP) are completely wrapped by the LSG sheets. The arrows point to the LSG lamellae surrounding the nanoparticles. (d) The d-spacing is ~0.34 nm in agreement with previously reported values for reduced GO and graphite. (e) A HRTEM image of a RuO_2 nanoparticle showing the 0.22 nm d-spacing corresponding to the <111> facet of RuO_2. (f) Schematic diagram of the LSG/RuO_2 structure illustrating the origin of fast ion and electron diffusion.

To understand the mechanism of formation of LSG/RuO_2 composite electrodes, we carried out thermogravimetric analysis (TGA) and differential thermal analysis (DTA) for GO, $RuCl_3$ and GO/$RuCl_3$ samples as shown in Fig. S2.2 and illustrated in Fig. 2.3. The thermal deoxygenation of GO is initiated by a small amount of heat (137.7 J g^{-1}) as indicated by an endothermic peak between 50-150 ºC, Fig. S2.2 a. This is followed by a large

exothermic peak at 215 ºC, which corresponds to the energy released during the reduction of GO and is sufficient to propagate and sustain the reduction of GO. This is consistent with differential scanning calorimetry data obtained by F. Kim *et al*. [32] The energy released from the deoxygenation of GO serves as an effective, *in situ,* power source that can drive the oxidation reaction of $RuCl_3$ to RuO_2. This can be illustrated by the amount of heat released during the deoxygenation reaction (-1393.9 J g^{-1}), which is six times the amount of heat required to drive the endothermic $RuCl_3$ to RuO_2 reaction (209.7 J g^{-1} observed at 480-650 ºC, Fig. S2b). When GO is mixed with $RuCl_3$ and heated, we note one exothermic peak at around 215 ºC and no subsequent peaks were observed at higher temperatures, confirming the simultaneous reduction of GO to r-GO and oxidation of $RuCl_3$ to RuO_2, Fig. S2.2c.

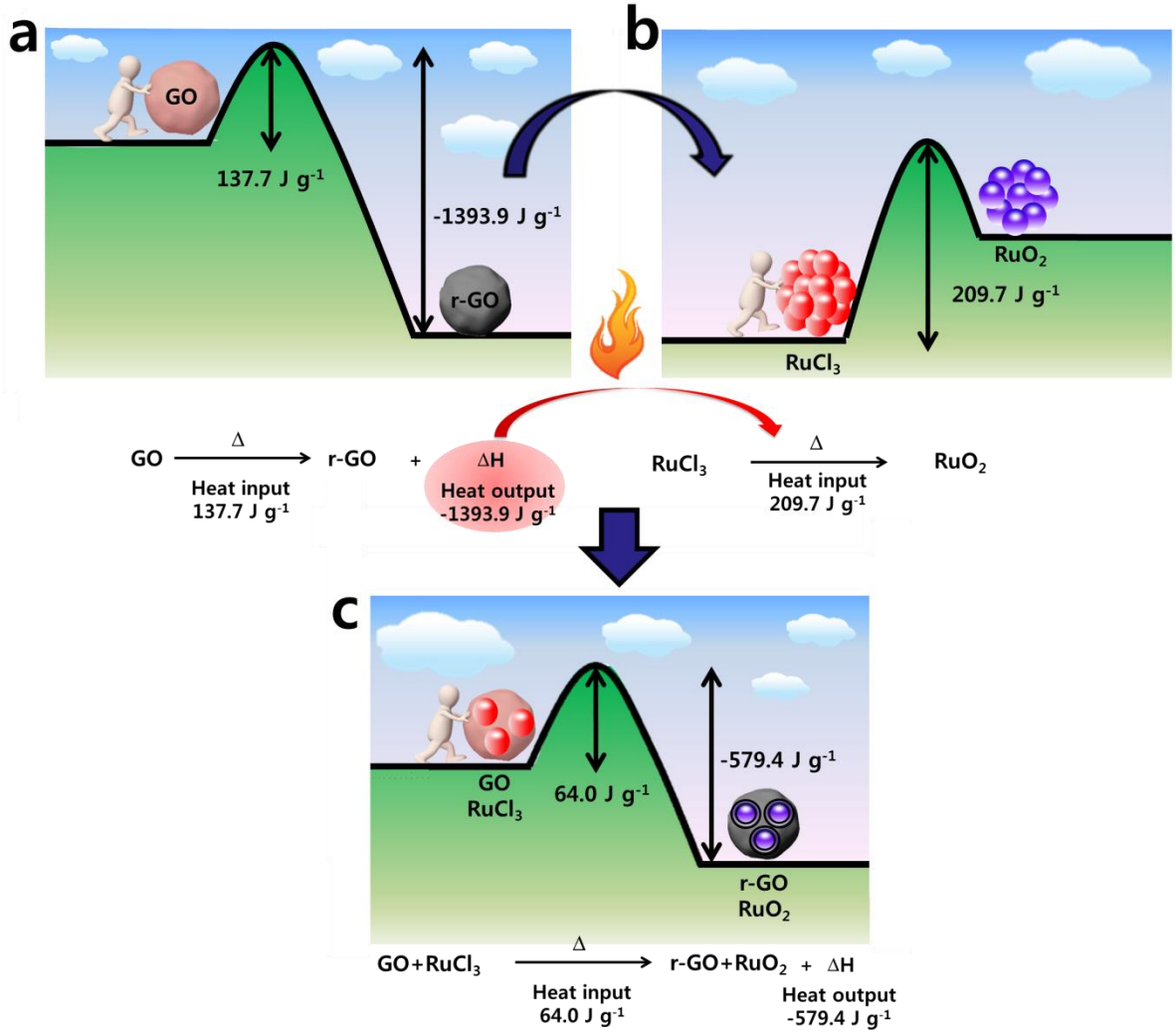

Figure 2.3 Schematic illustration of the thermodynamic mechanism of formation of LSG/RuO_2 composite electrodes (a) Photothermal deoxygenation of GO is associated with the release of a large amount of heat, sufficient to self-sustain the GO reduction reaction. (b) The oxidation of $RuCl_3$ to RuO_2 requires a heat input of 209.7 J g^{-1}, making it an endothermic process. (c) The photothermal reaction of GO and $RuCl_3$ mixture causes the simultaneous reduction of GO to LSG and oxidation of $RuCl_3$ to RuO_2.

The XPS spectra (Fig. 2.4a) of LSG/RuO_2 show Ru $3p_{1/2}$ and $3p_{3/2}$ photoemission peaks at 484.4 and 462.6 eV, respectively, as expected for RuO_2.[33, 34] For as-prepared LSG/RuO_2, a Ru $3d_{5/2}$ peak is observed at a binding energy of 280.7 eV and a C 1*s* peak at 284.8 eV (Fig. 2.4b). In a previous report, [35] the Ru $3d_{5/2}$ photoemission peak of RuO_2 was

observed at 280.7 eV and that of hydrated $RuCl_3$ at 281.6 eV. Thus, it can be concluded that the Ru $3d_{5/2}$ photoemission peak at 280.7 eV corresponds to RuO_2, and the C 1*s* peak corresponds to LSG. The O 1*s* spectra at 531 eV shown in Fig. 2.4c further supports the presence of ruthenium oxide (literature value for RuO_2 = 530.8 eV).[35] The O 1*s* photoemission peak at 532.1 eV can be assigned to the oxygen functional groups remaining from unconverted GO.[36]

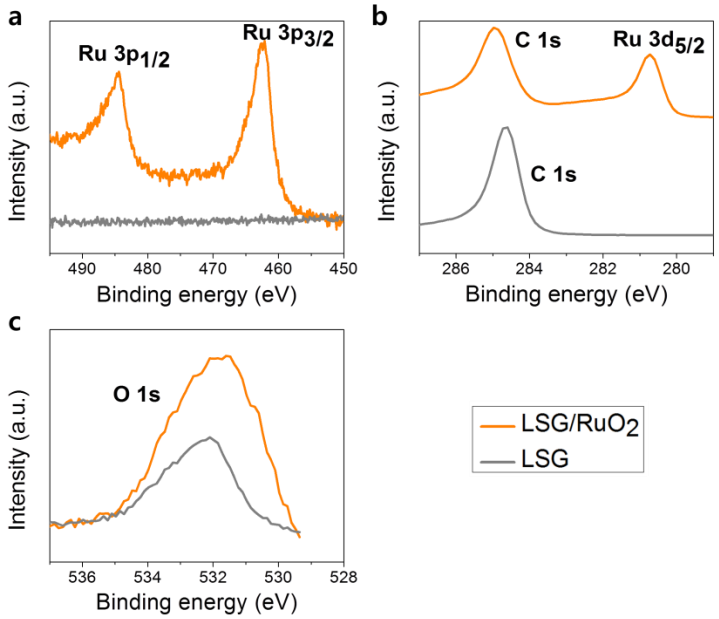

Figure 2.4. XPS spectra comparing LSG to LSG/RuO_2. (a) Ru 3p core spectra show Ru in the composite, but not in the LSG; (b) Ru 3d and C 1s regions; and (C) O 1s spectra.

2.3.3 Electrochemical properties of LSG/RuO_2 hybrid electrodes

We investigated the electrochemical properties of LSG/RuO_2 electrodes in a conventional three-electrode setup utilizing a Pt foil counter electrode and a Ag/AgCl reference electrode and using a mixture of 1 M H_2SO_4 as the electrolyte. Both cyclic voltammetry (CV) and galvanostatic charge/discharge (CC) measurements were performed to gain a good understanding of the charge storage behavior of LSG, RuO_2 and LSG/RuO_2 electrodes. We

observe from the results in Fig. 2.5a that the LSG electrode shows a rectangular and horizontal CV curve, suggesting ideal EDLC behavior. When RuO_2 is loaded onto LSG, a significant increase in the current density is observed; an indication of the improved capacitance resulting from the contribution of RuO_2 to charge storage. In order to understand the role of graphene in this hybrid electrode, a traditional RuO_2 hydrate available from Sigma-Aldrich was mixed with carbon black conductive additive and a polymer binder and coated onto a metal current collector. Apparently, the RuO_2 electrode produces lower current density than the LSG/RuO_2 hybrid electrodes, confirming the key role that graphene plays to achieve this high performance. It is worth noting that the CV profile of the LSG/RuO_2 electrode deviates from the ideal rectangular shape and broad redox peaks appear. This can be attributed to the pseudo-capacitive properties of RuO_2 which stores charge through fast and reversible Faradaic redox reactions according to the following equation:

$$RuO_2 + xH^+ + xe^- \leftrightarrow RuO_{2-x}(OH)_x; 0 \leq x \leq 2$$

Fig. 2.5b further compares the capacitive behavior of the pristine LSG, RuO_2 and hybrid LSG/RuO_2 electrodes at a high current density of 30 A g^{-1}. On the basis of the discharge curve, the specific capacitance of the LSG/RuO_2 electrode was calculated to be 1139 F g^{-1} (158 F cm^{-3}), which is about 5 times larger than the pristine LSG electrode. This remarkable improvement arises from the Faradaic processes at the RuO_2 nanoparticles coupled with the highly conductive LSG framework with large internal surface area and 3-dimensional interconnected porous channels. These channels allow for effective ion migration into RuO_2 active sites, thereby generating fast and reversible redox reactions. The presence of graphene in the LSG/RuO_2 reduces the internal resistance of the electrode as reflected by the lower IR drop observed at the beginning of the discharge curve. Furthermore, this interesting

architecture of the LSG/RuO_2 electrodes offers a unique opportunity for the effective use of the full pseudo-capacitance of RuO_2. For example, when the contribution of the LSG is subtracted from the total capacitance of the LSG/RuO_2 hybrid electrodes, the pseudo-capacitance normalized to RuO_2 is found to be 1523 F g^{-1}, which approaches the theoretical value of 2200 F g^{-1} and represents a clear advancement to previous reports on RuO_2 based electrochemical capacitors (see Supplemental Table S2.1).

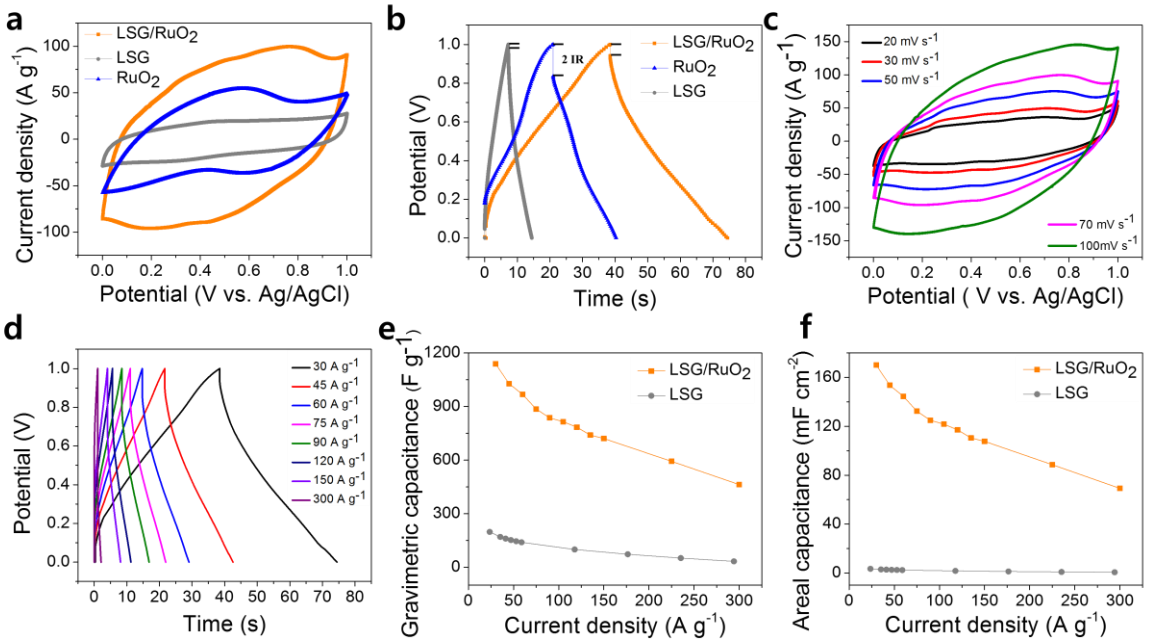

Figure 2.5. Evaluation of the electrochemical performance of LSG/RuO_2 electrodes in a three-electrode setup. (a) Cyclic voltammetry curves of LSG, RuO_2 and LSG/RuO_2 electrodes obtained at 70 mV s^{-1}. (b) Galvanostatic charge/discharge curves of the LSG,RuO_2 and LSG/RuO_2 electrodes measured at a high current density of 30 A g^{-1}. (c) Cyclic voltammetry curves of LSG/RuO_2 electrode at scan rates of 20, 30, 50, 70 and 100 mV s^{-1}. (d) Charge/discharge curves of a LSG/RuO_2 electrode at current densities of 30, 45, 60, 75, 90, 120, 150 and 300 A g^{-1}. (e) The gravimetric capacitance retention of LSG and LSG/RuO_2 electrodes as a function of the applied current density. (f) The areal capacitance retention of LSG and LSG/RuO_2 electrodes as a function of the applied current density.

In addition to its excellent specific capacitance, the LSG/RuO_2 electrodes exhibit reproducible and stable capacitive behavior with increasing scan rates up to 100 mV s^{-1} (Fig.

2.5c). The triangular shape of the charge/discharge curves at increasing current densities provides further evidence for the excellent capacitive behavior of the LSG/RuO_2 hybrid electrodes (Fig. 5d). We also note that the LSG/RuO_2 electrode exhibits very good capacitance retention thanks to rapid internal electron and ion transport (Figs. 2.5 e and f). Even at an ultrahigh current density of 300 A g^{-1}, the hybrid electrode still delivers a high capacitance of 460 F g^{-1} (Fig. 2.5 e) and 70 mF cm^{-2} (Fig. 2.5 f). This is equivalent to running the LSG/RuO_2 hybrid electrodes at a current density 10-100 times higher than conventional electrochemical capacitors. These results imply that LSG/RuO_2 electrodes experience incredibly fast ionic and electronic diffusion thanks to the 3-dimensional and highly porous structure of LSG, which provides much-improved charge transfer pathways for the redox reactions taking place within the RuO_2 nanoparticles.

2.3.4 High voltage asymmetric electrochemical capacitors

Aqueous electrochemical capacitors provide an effective solution for enhanced power density, reduced costs and safer cell chemistries compared to the current EDLCs that capitalize on flammable organic electrolytes for their operation. However, the energy density of aqueous cells is limited by the low decomposition voltage of water. In order to resolve this issue, hybrid electrochemical capacitors with an asymmetric configuration have been widely explored.[37-40] In this configuration, the different stable potential windows of the redox reactions at the positive electrode and the EDL ion adsorption at the negative electrode are used to increase the operating voltage of the cell, thus leading to an obvious improvement in energy density.[41] Taking advantage of the excellent electrochemical behavior of the two materials, we built an asymmetric electrochemical capacitor using LSG/RuO_2 as the positive electrode and activated carbon as the negative electrode as illustrated in Fig. 2.6A. Cyclic

voltammetry was first used to determine the respective capacitance and the stable potential window of each electrode (Fig. 2.6b). Based on these results, the mass ratio between the positive and negative electrodes was adjusted to 5.6 to achieve optimal charge balance between the two electrodes, leading to maximized cell capacitance and voltage. This also ensures that the two electrodes will remain in their respective potential windows for stable operation and improved cycle life.

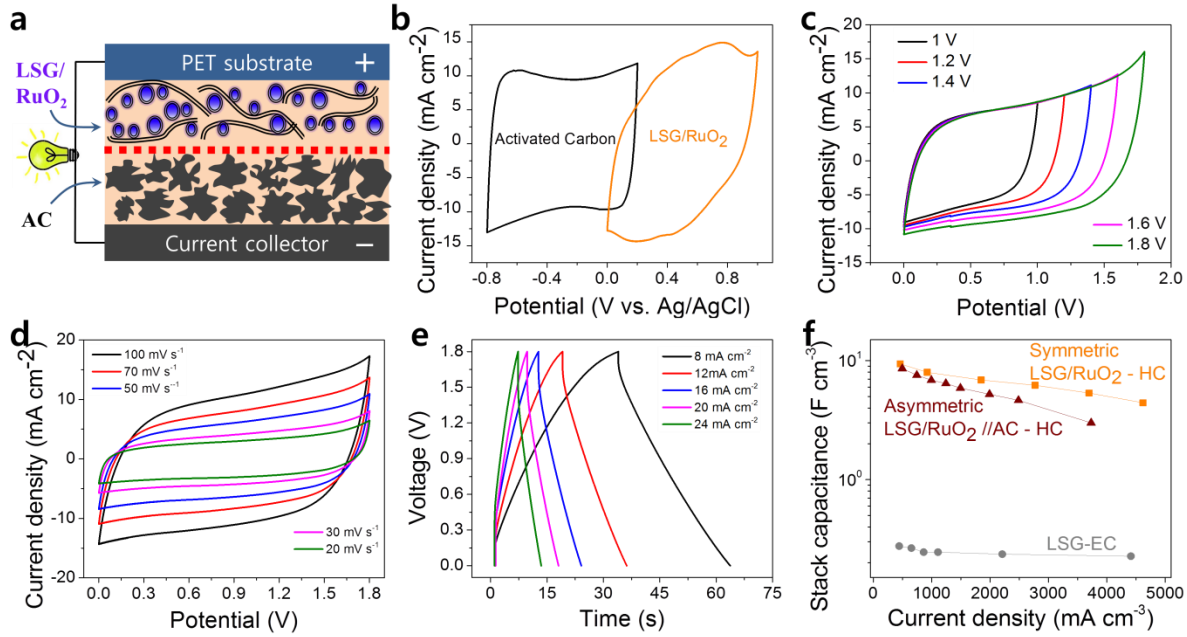

Figure 2.6. Electrochemical performance of an asymmetric LSG/RuO_2//AC supercapacitor. (a) Illustration of the structure of an asymmetric supercapacitor assembled with LSG/RuO_2 positive electrode and activated carbon negative electrode. (b) CV curves comparing the electrochemical properties of the positive and negative electrodes in their stable operating voltage windows, obtained at 70 mV s^{-1}. (c) CV curves of the asymmetric supercapacitor at increasing voltage window from 1.0 V to 2.0 V, all acquired at 70 mV s^{-1}. (d) CV performance of the asymmetric supercapacitor at different scan rates tested at a maximum voltage of 1.8 V. (e) Galvanostatic charge and discharge curves of the asymmetric supercapacitor collected at different current densities. (f) Evolution of the capacitance of the cell stack (including the current collector, active material, electrolyte and separator) as a function of the applied current density for symmetric LSG/RuO_2, asymmetric LSG/RuO_2//AC and LSG supercapacitors.

Figure 2.6c shows the CV profiles of an optimized asymmetric cell acquired at increasing cell voltages. Unlike the symmetric cells, which can only provide a maximum voltage of 1.0 V, the asymmetric cell can be cycled reversibly up to 1.8 V without any obvious distortions. No redox peaks are observed, indicating ideal capacitive behavior. In addition, the cell provides consistent rectangular curves at different scan rates (Fig. 2.6d). We also observe that the device demonstrates symmetric and triangular charge/discharge curves even when operated at a high current density of 24 mA cm^{-2} (Fig. 2.6e), which again confirms the excellent electrochemical performance of the cell. In order to put the performance of this asymmetric electrochemical capacitor in context with other cell configurations, we plot the stack capacitance as a function of the applied current density (Fig. 6f). The stack capacitance was calculated based on the volume of the current collector, the active material, electrolyte and separator. The maximum specific capacitance of the LSG/RuO_2//AC asymmetric cell reaches 8.6 F cm^{-3} at a current density of 500 mA cm^{-3} and still retains 3.0 F cm^{-3} at a higher current density of 3700 mA cm^{-3} (Fig. 2.6f). More importantly, the stack capacitance of the LSG/RuO_2//AC asymmetric cell is about 50 times higher than that of a symmetric LSG electrochemical capacitor. This excellent capacitive behavior can be attributed to the hybrid LSG/RuO_2 electrodes in which both LSG and RuO_2 work synergistically to store the charge more effectively. When compared to the asymmetric cell, the symmetric LSG/RuO_2 electrochemical capacitor can deliver similar capacitance at lower charge/discharge rates, but offers better capacitance retention at higher rates. This verifies that the LSG/RuO_2 electrodes exhibit faster ion and electron transport than conventional activated carbon electrodes.

2.3.5 Direct fabrication of LSG/RuO_2 symmetric micro-supercapacitors

The emergence of miniaturized electronics has driven tremendous research efforts to develop small supercapacitors that can store energy efficiently at the microscale. These micro-supercapacitors are often designed such that the positive and negative electrodes are placed side-by-side in an interdigitated configuration. It is crucial that these micro-supercapacitors can be easily integrated with existing electronic devices and that they have appropriate energy density and power density sufficient for the device which they will power. These micro-supercapacitors have been successfully used for AC line filtering, [42] combined with miniaturized energy harvesters to enable self-powered nano/micro-electronics[43] or even integrated with micro-fluidic analytical devices for standalone portable sensors useful in environmental monitoring.[44] With the rapid progress in the synthesis and manipulation of nanomaterials, researchers have developed various micro-supercapacitors with custom design parameters to enable foldable,[45] stretchable,[46] transparent[47] and even self-healing[48] microscale energy storage devices. These characteristics originate mainly from the properties of the materials used for building the device. Carbon nanomaterials including activated carbon,[49] graphene,[14] carbon nanotubes,[50] and carbon onions[51] have been widely explored. While interesting electrochemical performances have been achieved, the energy density output of these systems is still low and does not meet the requirements of many miniaturized electronics. Alternatively, hybrid materials combining Faradaic and non-Faradaic charge storage have been demonstrated for the fabrication of micro-supercapacitors whose energy densities rival those of lithium thin-film micro-batteries.[52-54] Despite significant progress, the fabrication of micro-supercapacitors, especially those utilizing hybrid materials, is still challenging.[53, 55] It is, thus, essential to develop rapid and inexpensive micro-fabrication

techniques in order to move micro-supercapacitor technology from the laboratory to commercial applications.

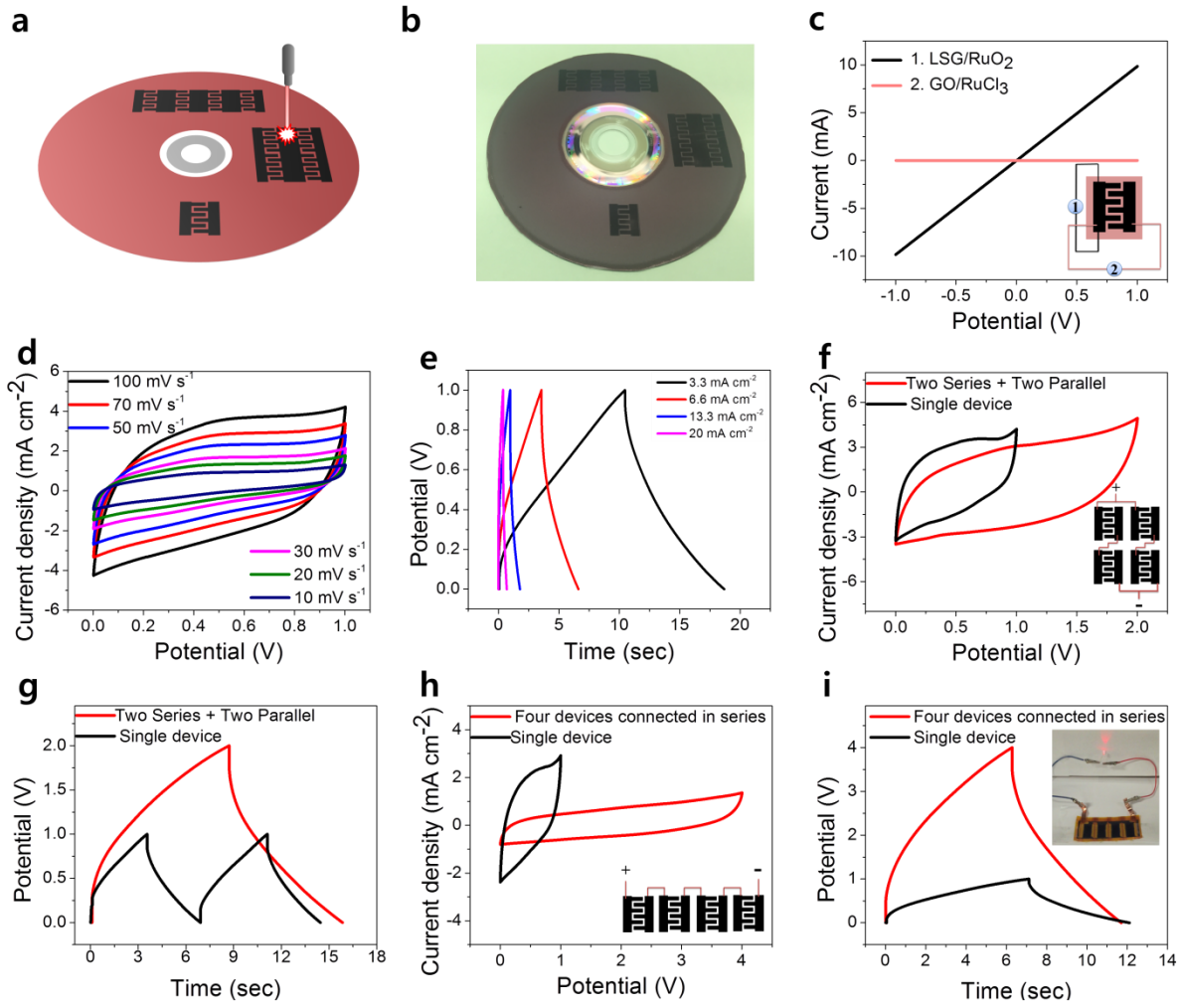

Figure 2.7: Direct laser writing of LSG/RuO_2 interdigitated micro-supercapacitors single cells and modules. (a) Schematic illustration showing the microfabrication process of LSG/RuO_2 hybrid micro-supercapacitors via direct laser writing on a DVD disc using a LightScribe DVD burner. An interdigitated pattern designed on the computer is directly printed on GO/$RuCl_3$ films coated onto DVD discs to produce LSG/RuO_2 micro-electrodes with the appropriate shape and size. (b) A photograph showing micro-supercapacitors obtained after the laser treatment of the DVD disc with the pattern shown on the left. (c) I-V curves measured for the electrically conducting LSG/RuO_2 electrodes and across the positive-negative insulating GO/$RuCl_3$ electrodes. Electrochemical performance of a symmetric LSG/RuO_2 micro-supercapacitor tested by (d) Cycling voltammetry at different scan rates, and (e) Charge/discharge curves at different current densities. (f-g) A micro-supercapacitor module with two cells connected in series and two cells connected in parallel can double both

the voltage and the current output compared to a single cell. (h-i) Compared with a single cell that operates at 1 V, a tandem module consisting of four cells connected in series can provide up to 4 V.

The proposed technique uses a computerized LightScribe laser for the synthesis of electrode materials by illuminating a film of GO/$RuCl_3$ coated onto a CD/DVD disc. With the precision of the laser, this technique can be used for the direct writing of graphene/RuO_2 patterns of any arbitrary shape, thus enabling the fabrication of hybrid micro-supercapacitors in a single step as shown in Figs. 2.7a-b. In this configuration, interdigitated patterns of LSG/RuO_2 are utilized as micro-electrodes with GO/$RuCl_3$ films remaining in between the microelectrodes as the separator. Voltage-current curves confirm the insulating nature of GO/$RuCl_3$, manifesting its adequate electrical properties as a dielectric material to prevent short-circuiting between the positive and the negative microelectrodes, Fig. 2.7c. These micro-supercapacitors show fast and reversible charge and discharge properties as demonstrated by both cyclic voltammetry (Fig. 2.7d) and charge/discharge curves (Fig. 2.7e). Not only is it possible with this technique to make a hybrid micro-supercapacitor in a single step, but also it can be used for the direct writing of a bank of micro-supercapacitors (see Fig. 2.7b). This will enable the design of energy storage modules with any number of cells without the need for complex external wiring needed for micro-supercapacitors made by traditional techniques. Figs. 2.7f-i show the electrochemical performance of the micro-supercapacitor modules printed in Fig. 2.7b. They feature a single micro-supercapacitor, a tandem module with four cells connected in series and a third module with two cells connected in series and two in parallel. The results indicate the feasibility of these micro-supercapacitor modules to achieve the desired operating terminal voltage and current outputs

by combining several cells in series (where each cell adds to the total voltage), in parallel (where each cell adds to the total current) or in combinations of the two.

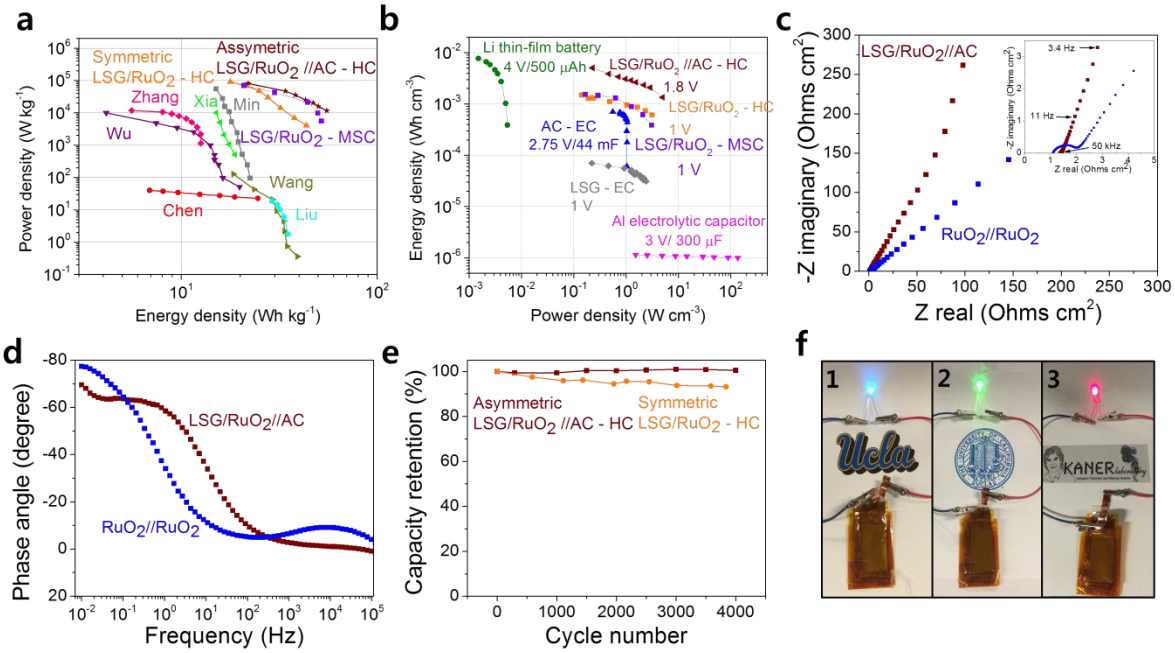

Figure 2.8. Overall performance of LSG/RuO_2 based supercapacitors. (a) Ragone plot comparing gravimetric energy density and power density of LSG/RuO_2 supercapacitors with other RuO_2-based hybrid supercapacitors reported in literature. (b) Ragone plot reproduced based on the volume of the cell instead of mass. The plot compares the volumetric energy density and power density of LSG/RuO_2-based supercapacitors with a number of commercially available energy storage devices. (c) Nyquist and (d) Bode plots of the RuO_2 Symmetric and LSG/RuO_2//AC asymmetric supercapacitors over a frequency range of 100 kHz to 0.01 Hz. (e) long-term cycling stability of LSG/RuO_2 symmetric supercapacitors and LSG/RuO_2//AC asymmetric supercapacitors. (f) Two tandem supercapacitors connected in series can power light emitting diodes of different colors for a long period of time: (1) blue; (2) green; and (3) red LEDs.

A Ragone plot describing the relationship between the energy density and power density of our LSG/RuO_2 based electrochemical capacitors is presented in Fig. 2.8a. This plot was obtained based on the total mass of the active materials in the device. It can be deduced from the plot that the LSG/RuO_2//AC cell can deliver higher energy density than the

LSG/RuO_2 symmetric cell thanks to the ability of the former to run at higher voltages. An LSG/RuO_2//AC electrochemical capacitor can provide an ultrahigh energy density of 55.3 Wh kg^{-1} at a power density of 11.7 kW kg^{-1} owing to its superior properties. Even at a very high power density of 81.4 kW kg^{-1}, our electrochemical capacitor demonstrated an energy density of 22 Wh kg^{-1}, which is much higher than previous published RuO_2 hybrid electrochemical capacitors. Furthermore, the energy density and power density demonstrated here are considerably higher than the values reported from other metal oxide based electrochemical capacitors, including amorphous nickel hydroxide nanospheres (35.7 Wh kg^{-1} at 0.46 kW kg^{-1}),[56] MnO_2-CNT-sponge (at its maximum values of 31 Wh kg^{-1} and 63 kW kg^{-1}),[57] porous MnO_2 nanotubes (22.5 Wh kg^{-1} at ~0.2 kW kg^{-1}) and $NiCo_2O_4$/carbon nanotubes/nickel foam (48.3 Wh kg^{-1} at 0.8 kW kg^{-1}).[58]

The Ragone plot was also produced on a volumetric basis as shown in Fig. 8b. The energy and power density of some commercially available thin-film energy storage devices are presented for comparison. The plot was made using the volume of the entire cell stack including the current collector or the plastic substrate, the active materials, the electrolyte and the separator. The LSG/RuO_2//AC electrochemical capacitor demonstrates a volumetric energy density of 5 mWh cm^{-3}, about tenfold higher than that of a 44 mF/ 2.75 V commercially available activated carbon electrochemical capacitor[11] and comparable to that of a 500 µAh/ 4 V lithium thin-film battery.[51] When compared to other energy storage devices, LSG/RuO_2 hybrid capacitors lie in the upper-right region of the Ragone plot, which demonstrates that both the energy and power performances of the LSG/RuO_2 are outstanding. These results suggest that LSG/RuO_2 hybrid capacitors could be excellent candidates for future energy storage devices.

The superior electrochemical performance of the LSG/RuO_2 based electrochemical capacitors was further confirmed by electrochemical impedance spectroscopy as shown in Figs. 2.8c-d. The Nyquist plot reveals a nearly vertical line in the low-frequency region, which indicates ideal capacitive behavior of the electrode materials. The intercept of the Nyquist plot on the real axis is about 1.4 Ω cm^2, manifesting the good conductivity of the electrolyte and the low internal resistance of the system. Although the LSG/RuO_2 electrodes participate in redox reactions during charge and discharge, the plot shows no semi-circular resistance in the high frequency region (inset of Fig. 2.8c). These results confirm low charge transfer resistance at the electrode/electrolyte interface and suggest favorable ion transport within the 3-dimensional porous LSG/RuO_2 electrodes. This contrasts with the traditional RuO_2 electrode in which a clear semi-circle can be observed, an indication of the large charge transfer resistance of the RuO_2 electrodes. The Bode plot displayed in Fig. 8d provides further evidence for the high rate capability of the LSG/RuO_2//AC electrochemical capacitor. The characteristic frequency f_0 for a phase angle of -45° is 5 Hz. This frequency marks the point at which the resistive and capacitive impedances are equal.[59] The corresponding time constant τ_0 ($= 1/f_0$) equals 0.2 s, showing faster frequency response than RuO_2 (1.9 s) and many conventional activated carbon electrochemical capacitors.[11, 42]

Long-term cycle life is another important parameter for practical electrochemical capacitors. The symmetric LSG/RuO_2 cell exhibits excellent cycling stability, retaining 93% of its initial capacitance after 4000 cycles of continuous charge and discharge at a current density of 11.5 mA cm^{-2} (Fig. 2.8e). The asymmetric cell reveals even better capacitance retention of 99.5% when tested under the same conditions. This superior cycling stability can be explained by the RuO_2 particles wrapped within the LSG structure, the latter of which helps to suppress volume changes and prevent agglomeration of RuO_2 particles during charge

and discharge processes. From a practical point-of-view, when two asymmetric cells are connected in series and charged at a constant voltage of 3.6 V for 3 min, they can be used to run light emitting diodes (LEDs) of various colors as illustrated in Fig. 8f: blue (5 mm, 3.4 V, 30 mA), green (5 mm, 2.6 V, 20 mA) and red (5 mm, 1.9 V, 20 mA). We noticed that the LEDs remained very bright even after 40 min of operation. These results demonstrate the potential of our hybrid electrochemical capacitors for practical applications.

2.4 Material and methods

2.4.1 Fabrication of RuO_2/LSG electrodes and micro-supercapacitors.

The LSG/RuO_2 was prepared using a LightScribe DVD burner. The GO was prepared using a modified Hummers method. Dispersion was carried out by sonicating a mixture of GO (2 mg ml^{-1}) and $RuCl_3$ hydrate (5.7 mg ml^{-1}, Aldrich) in an aqueous solution for 120 min. The homogeneous solution was drop-cast onto a polyethylene terephthalate (PET) substrate attached to a LightScribe DVD disc and dried under ambient conditions for 12 h. The dried film was inserted into a commercial LightScribe DVD optical drive (optimum power output = 5 mW, wavelength = 788 nm) to synthesize LSG/RuO_2 films via laser irradiation. Following irradiation, the LSG/RuO_2 film was washed with deionized water. This binder-free LSG/RuO_2 film on PET was then used directly as an electrode. The electrode density is 0.139 g cm^{-3} and mass loading is 37.33 μg.

2.4.2 Fabrication of RuO_2 electrodes. The RuO_2 electrode was prepared by mixing 60 wt% RuO_2 hydrate (Sigma Aldrich), 20 wt% carbon black and 20% (1:1 CMC/SBR) binder in water. The homogeneous solution was drop-cast onto a gold current collector.

2.4.3 Fabrication of a LSG/RuO_2 hybrid capacitor. Copper tape (3M, US®, 0.005 Ω) and silver paint (SPI Supplies®) were used to establish a close contact between the

LSG/RuO_2 electrodes and the electrochemical workstation. Polyimide tape (Kapton^{TM}) was used to insulate copper tape and silver paint from exposure to the electrolyte. A symmetric LSG/RuO_2 hybrid electrochemical capacitor was constructed based on two identical active areas (0.5 cm × 0.5 cm) of RuO_2/LSG electrodes, with a separator (Celgard® 3501, 25 μm thick) inserted between the two LSG/RuO_2 electrodes. These two electrodes and separator were then assembled by Kapton^{TM} tape after which the electrolyte, consisting of 1 M H_2SO_4 solution, was added. The asymmetric electrochemical capacitor, on the other hand, was assembled using an LSG/RuO_2 positive electrode and an activated carbon negative electrode. The activated carbon was prepared by mixing 86 wt% activated carbon, 10 wt% carbon black and 4% (1:1 CMC/SBR) binder in water. The paste was then coated onto the current collector using a doctor blade. To ensure charge balance between the electrodes, the loading mass was adjusted to 37.3 μg for the positive electrode and 209.5 μg for the negative electrode with an active area of (0.5 cm × 0.5 cm).

2.4.4 Fabrication of a LSG/RuO_2 micro-supercapacitor. The dried film was inserted into a LightScribe DVD drive and an interdigitated pattern scribed onto the film. Copper tape and silver paint were applied along the edges to improve the electrical contacts and Kapton tape was used to cover the copper tape and define the micro-supercapacitor area. An electrolyte was then coated onto the active area of the micro-supercapacitor.

2.4.5 Characterization of the LSG/RuO_2 hybrid capacitor. SEM characterization of the LSG/RuO_2 was performed using a Nova 600 SEM/FIB system. The mass of the active material was measured by a Mettler Toledo MX5, which was found to be 37.33 μg. The effective thickness of the LSG/RuO_2 hybrid capacitor was 86.6 μm including active material (10.8 μm), substrate (20 μm), and separator (25 μm). The TEM images and SAED patterns

were collected on a Tecnai G^2 TF20 TEM (FEI Inc.) operated at 200 kV. The HRTEM and SAED data were analyzed using EMMENU4 and ImageJ software. The d-spacing values extracted from SAED patterns were calibrated with an aluminum standard. The loading percentage of Ru was determined by a plasma atomic emission spectrometer (SHIMADZU ICPE-9000). Thermogravimetric analyses were carried out on a Perkin Elmer Diamond Pyris TGA from 55 °C to 800 °C at a heating rate of 10 °C min^{-1} in air. XPS spectra were recorded using a Kratos Axis Ultra DLD spectrometer equipped with a monochromatic Al Kα X-ray source, and high-resolution spectra were charge-corrected to a peak C 1s binding energy of 284.6 eV. The electrochemical performances of the LSG/RuO_2 electrodes were characterized by cyclic voltammetry (CV) measurements and charge-discharge galvanostatic tests with an electrolyte mixture of 1.0 M H_2SO_4. The LSG/RuO_2 electrode tests were carried out using three electrode cells, with a platinum plate as the counter electrode, and Ag/AgCl as the reference electrode. LSG/RuO_2 symmetric capacitors, asymmetric capacitor and micro-supercapacitors (two-electrode cells) were characterized by CV, electrochemical impedance spectroscopy (EIS), and charge-discharge galvanostatic tests. All electrochemical measurements were carried out in 1.0 M H_2SO_4 except for the asymmetric capacitors which were tested in 1.0 M Na_2SO_4. All electrochemical data were collected using a Biologic VMP3 electrochemical workstation equipped with 10 A current booster (VMP3b-10), USA Science Instrument. EIS experiments were carried out over a frequency range of 1 MHz to 10 mHz with an amplitude of 10 mV at open-circuit potential.

2.5 Conclusions

In summary, we have developed a simple, yet effective, strategy for the direct laser writing of nanocomposite electrodes based on graphene and RuO_2 nanoparticles that can be

directly integrated into high-performance electrochemical capacitors. In this process, LSG/RuO_2 electrodes were synthesized simultaneously from the oxidation of $RuCl_3$ hydrate, while graphene oxide is reduced in a standard LightScribe process. The SEM, HRTEM and SAED studies revealed that these hybrid electrodes are composed of a 3-dimensional porous architecture in which well-dispersed and hydrous RuO_2 nanoparticles are fully wrapped with graphene sheets. This unique structure results in remarkable electron and ion transport within the electrodes, thereby resulting in superior electrochemical performance. Specifically, these electrodes demonstrate an ultrahigh specific capacitance of 1139 F g^{-1} with excellent rate capability up to a current density of 300 A g^{-1}. Furthermore, an asymmetric electrochemical capacitor consisting of an LSG/RuO_2 positive electrode and an activated carbon negative electrode demonstrates an extremely high energy density of 55 Wh kg^{-1} at a power density of 12 kW kg^{-1}, placing it among the best performing hybrid electrochemical capacitors. Using the same technique, we have also developed in-plane hybrid micro-supercapacitors with interesting electrochemical performance. These micro-supercapacitors can be integrated into modules consisting of several cells connected together in series and/or in parallel to increase the voltage and power above that of a single cell. In addition, these devices reveal low internal resistance and excellent long-term cycling life, offering a promising energy storage solution for next generation smart electronics. This approach also paves the way for the direct laser writing of graphene-based devices for electronics, sensors and catalytic applications. [14, 16]

2.6 Appendix to Chapter 2

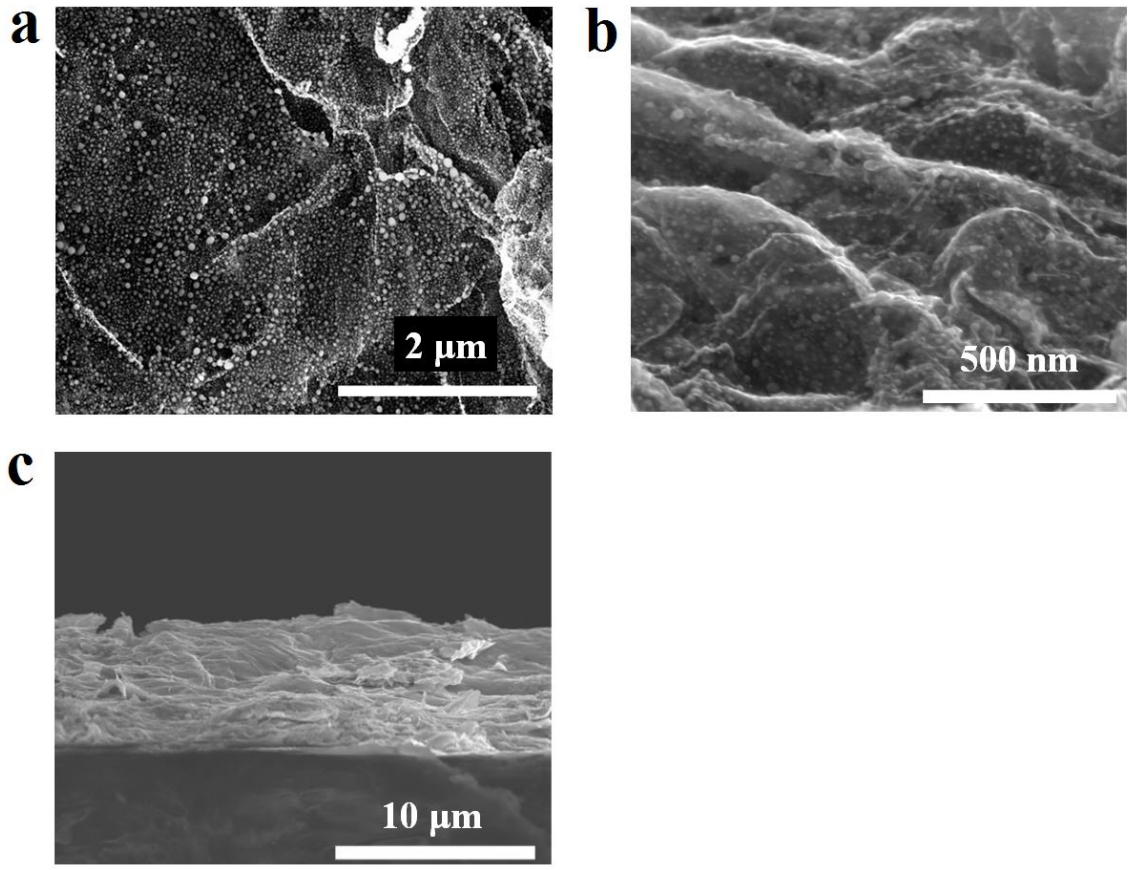

Supplementary Figure S2.1 (a) Overview SEM image of the LSG/RuO_2 composite; (b) Tilted view of the LSG/RuO_2 composite electrode; (c) Cross-sectional SEM image of the LSG/RuO_2 composite electrode.

These SEM images show: (a) well dispersed RuO_2 nanoparticles within LSG framework, (b) Not only does graphene act as a support for RuO_2 nanoparticles but it also acts as a conductive wrap to facilitate electron transport and to suppress the volume changes of the nanoparticles during charge and discharge processes. The image shows also the high surface area of the composite, and (c) a cross-sectional SEM image showing LSG/RuO_2 film on a plastic substrate. The thickness of the LSG/RuO_2 layer is ~10.8 µm.

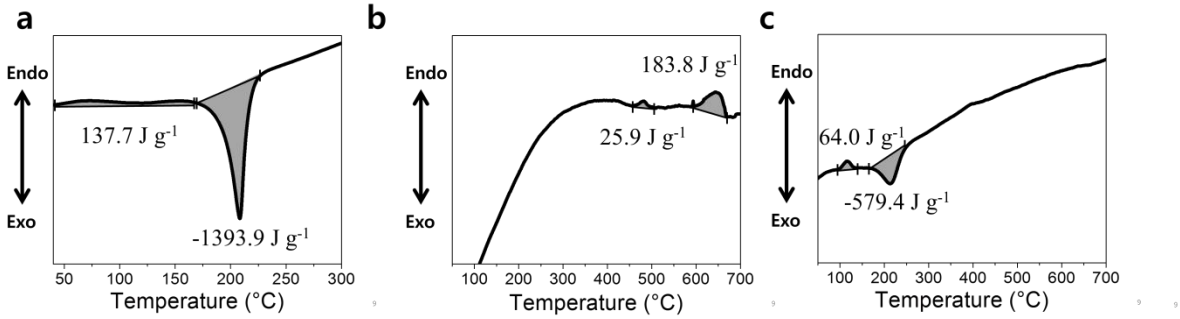

Supplementary Figure S2.2 Differential thermal analysis (DTA) of GO, $RuCl_3$ and a GO/$RuCl_3$ composite. All measurements were performed under an argon atmosphere.

(a) Heat released during the deoxygenation of GO is -1393.9 J g^{-1}, which is much higher than required to initiate the reduction reaction (137.7 J g^{-1}). (b) The formation of RuO_2 from the $RuCl_3$ requires 209.7 J g^{-1} of heat. (c) The thermal induced reaction between GO and $RuCl_3$ mixture results in the simultaneous reduction of GO to r-GO and oxidation of $RuCl_3$ to RuO_2.

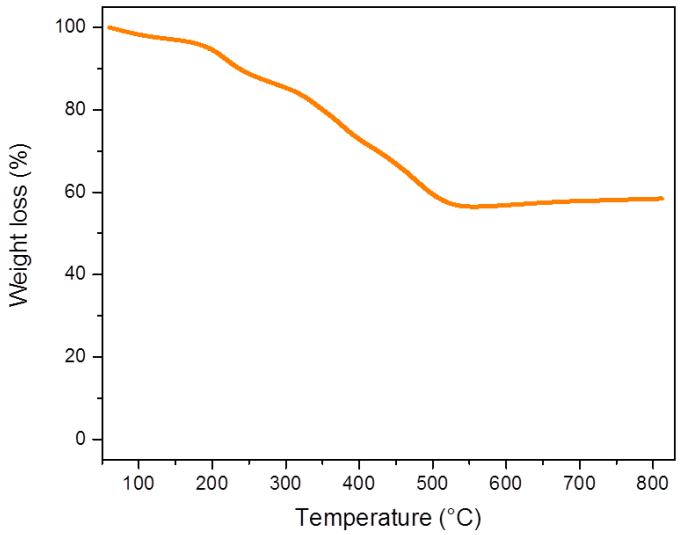

Supplementary Figure S2.3 Thermogravimetric analysis (TGA) curve of the LSG/RuO_2 composite.

Quantitative determination of the amount of RuO_2 anchored onto the surface of the LSG was performed using thermogravimetric analysis (TGA) in the temperature range 60 - 800°C. The TGA plot shows that the overall weight percentage of RuO_2 in the LSG/RuO_2 composite is roughly 58%, which is also consistent the results from ICP-AES. The small mass loss below 170°C is likely due to the evaporation of water from the LSG/RuO_2 surface. The 10% weight loss observed from 175-275°C can be attributed to the loss of chemisorbed and crystalline water from hydrous RuO_2.[24] The drop between 300-550°C represents 28% mass loss which can be ascribed to the decomposition of the LSG. Based on these results, we estimate that the LSG/RuO_2 has a composition of $RuO_2 \cdot 1.27\ H_2O$.

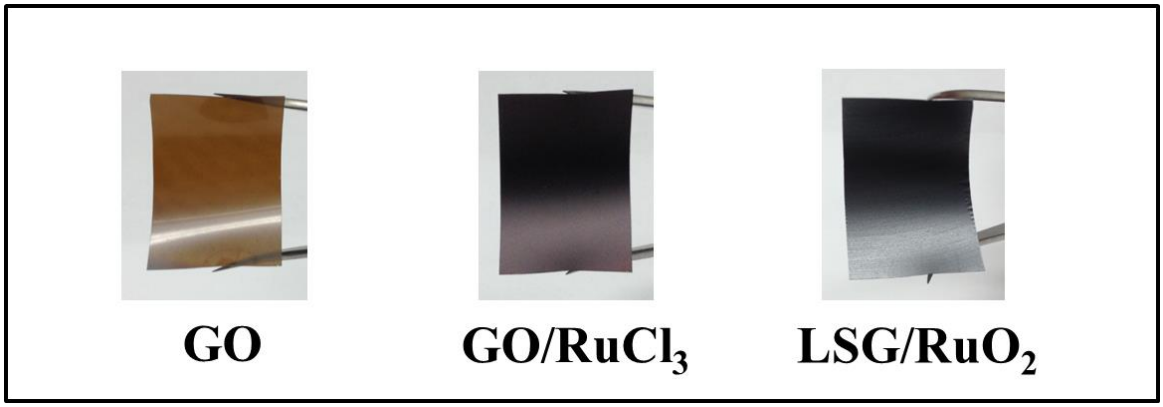

Supplementary Figure S2.4 Photographs of GO, $GO/RuCl_3$, and LSG/RuO_2 films.

Graphene oxide (GO), $GO/RuCl_3$, and LSG/RuO_2 films made on a flexible sheet of plastic (polyethylene terephthalate, PET). These three films show different colors: the GO film is semi-transparent brown, the $GO/RuCl_3$ film looks darker with reddish hues, which turns black after the laser treatment (i.e. LSG/RuO_2).

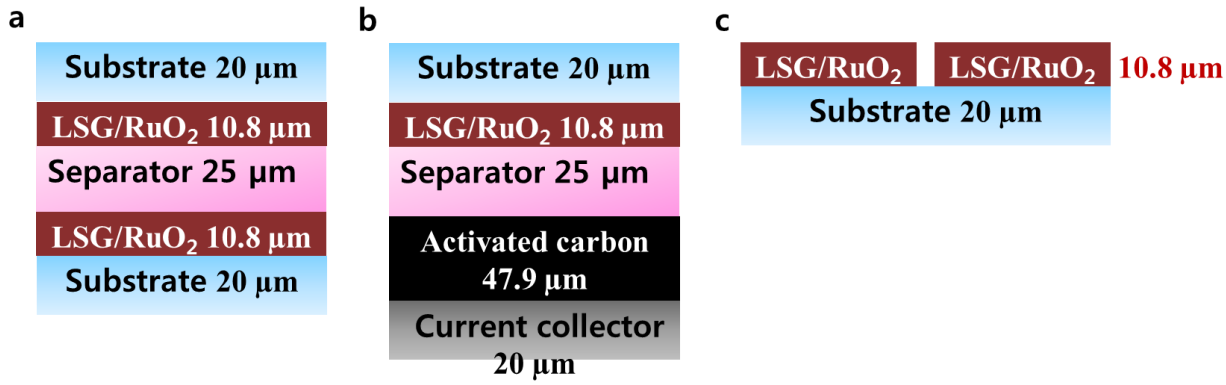

Supplementary Figure S2.5 Cross-section schematics of the LSG/RuO_2 supercapacitors with various arrangements: a) symmetric, b) asymmetric, c) micro supercapators.

(a) Schematic of symmetric LSG/RuO_2 supercapacitor device shows the effective thickness of 86.6 µm. (b) Asymmetric LSG/RuO_2//Activated carbon supercapacitor device thickness is 123.7 µm, slightly thicker than symmetric design. (c) Symmetric LSG/RuO_2 interdigitated pattern microsupercapacitor with a thickness of 30.8 µm.

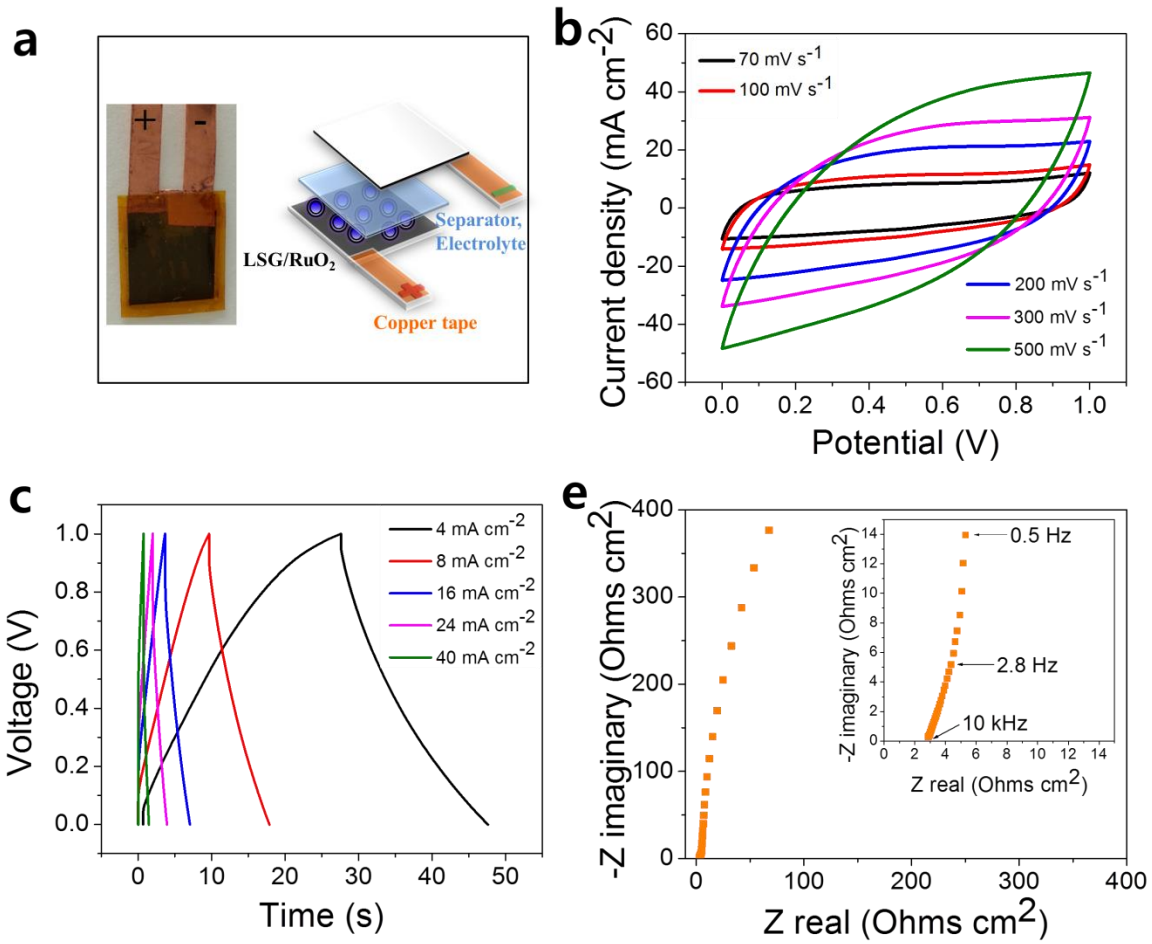

Supplementary Figure S2.6 Electrochemical performance of a symmetric LSG/RuO_2 hybrid electrochemical capacitor (EC). (a) Illustration of the assembly of a symmetric LSG/RuO_2 hybrid EC (right) and a photograph of the final device is also shown (left). (b) Cyclic voltammetry curves of the as-fabricated device at different scan rates of 70, 100, 200, 300 and 500 mV s^{-1}. (c) Charge/discharge curves of the device at different current densities of 4, 8, 16, 24, 40 mA cm^{-2}. (d) Nyquist plot of the electrochemical impedance spectrum of the device, with a magnified high-frequency region.

The LSG/RuO_2 symmetric electrochemical capacitor shows enhanced electrochemical performance with an almost rectangular CV shape at a scan rate of 70 mV s^{-1}, indicating nearly ideal capacitive behavior, thus representing an ultrafast electron transfer to RuO_2 nanoparticles and a similarly fast response to the electrodes. Additionally, the device maintains a semi-rectangular CV shape even at high scan rates of 500 mV s^{-1}. The charge/discharge measurements were conducted over a wide range of applied specific

currents (4 to 40 mA cm^{-2}), as shown in Fig. S2.4 c. The Nyquist impedance plot shown in Fig. S2.4 d reveals the equivalent series resistance of the device to be ~3 Ω cm^2. Although the LSG/RuO_2 device participates in redox reactions during its charge and discharge, the impedance data do not show a semi-circular resistance in the axis. These data confirm low charge transfer resistance of the electrode materials and good ionic conductivity of the electrolyte.

Supplementary Table S2.1 Comparison of LSG/RuO_2 with Other RuO_2 Capacitors.

Material	Method	Capacitance ($F\ g^{-1)}$	Cycle life (Cycles)	Reference
RuO_2 /Graphene	Microwave-hydrothermal process	497	1000	[60]
RuO_2 /Graphene/Carbon nanotube	Sol-gel and dip-coating	502.8	8000	[25]
RuO_2 /Graphene	Sol-gel	570	1000	[24]
RuO_2/Reduced carbon spheres	Sol-gel	614	5000	[26]
RuO_2 /Carbon nanofiber	Sol-gel	645	100	[27]
RuO_2/Layered graphene nanoflakes	Microwave plasma chemical vapor deposition	650	4000	[28]
RuO_2/Carbon nanotube	Hydrothermal	953	2000	[30]
RuO_2/Single-walled carbon nanotube	Electrodeposition	1084		[29]
RuO_2 / Nanoporous gold	Electrodeposition	1450	50	[21]
LSG/RuO_2	LightScribe	1139	4000	This work

A summary of the specific capacitance and cycle life of RuO_2-based nanocomposite hybrid electrochemical capacitors.

Calculations

The capacitance of each electrode was calculated from charge/discharge curves at different current densities using the formula:

$$\text{Specific C}_{\text{electrode}}\,(\text{F g}^{-1}) = \frac{\text{Curent(A)}*\text{Time(sec)}}{Voltage(Volt)*Mass(g)}$$

Mass refers the mass of active materials and time and voltage were measured from the discharge curve

Specific capacitances of the RuO_2 were estimated as follows:

$$\text{Specific } C_{RuO_2\cdot 1.27H_2O}\ (\text{F g}^{-1})$$

$$= \frac{C_{electrode}(F/g)*mass\ of\ LSG\ and\ RuO_2\cdot 1.27H_2O(g) - C_{LSG}(F/g)*mass\ of\ LSG(g)}{mass\ of\ RuO_2\cdot 1.27H_2O(g)}$$

The loading percentage of Ru was determined by inductively coupled plasma atomic emission spectroscopy (ICP-AES). The $RuO_2\cdot 1.27\ H_2O$ weight was determined based on TGA and ICP-AES. LSG mass was determined by deducting the $RuO_2\cdot 1.27\ H_2O$ mass from the total mass of the composite electrode.

The energy density and power density of two electrodes device were calculated from the charge/discharge curves at different current densities.

First, the specific capacitance of the device was calculated, and time and voltage were measured from the discharge curve:

$$\text{Specific C}_{\text{device}}\,(\text{F g}^{-1}) = \frac{\text{Curent (A)}*\text{Time(sec)}}{Voltage\ (V)*\ Mass\ (g)}$$

Mass refers the mass of active materials.

$$\text{Specific C}_{\text{device}}\,(\text{F cm}^{-3}) = \frac{\text{Curent (A)}*\text{Time(sec)}}{Voltage\ (V)*Volume\ (cm^3)}$$

Volume refers the volume of the stack device including active materials, substrates and separator.

Second, the specific energy density of the device was calculated:

$$\text{Specific E}_{\text{device}}\,(\text{Wh kg}^{-1}) = \frac{\text{Specific capacitance}\ (F/g)*\text{Voltage}^2(\text{V}^2)*1000(g/kg)}{2*3600}$$

$$\text{Specific E}_{\text{device}}\,(\text{Wh cm}^{-3}) = \frac{\text{Specific capacitance}\ (F/cm^3)*\text{Voltage}^2(\text{V}^2)}{2*3600}$$

Third, the specific power density of device was calculated:

$$\text{Specific P}_{\text{device}}\,(\text{W kg}^{-1}) = \frac{\text{Energy density}(Wh/kg)}{Time(\text{hr})}$$

$$\text{Specific P}_{\text{device}}\,(\text{W cm}^{-3}) = \frac{\text{Energy density}(Wh/cm^3)}{Time(\text{hr})}$$

2.7 References

(1) Jeong, G.; Kim, Y.-U.; Kim, H.; Kim, Y.-J.; Sohn, H.-J. *Energ. Environ. Sci.* **2011**, *4*, 1986.

(2) Miller, J. R.; Simon, P. *Science* **2008**, *321*, 651.

(3) Simon, P.; Gogotsi, Y. *Nat. Mater.* **2008**, *7*, 845.

(4) Liu, C.; Li, F.; Ma, L.-P.; Cheng, H.-M. *Adv. Mater.* **2010**, *22*, E28.

(5) Zhu, Y.; Li, L.; Zhang, C.; Casillas, G.; Sun, Z.; Yan, Z.; Ruan, G.; Peng, Z.; Raji, A.-R. O.; Kittrell, C.; Hauge, R. H.; Tour, J. M. *Nat. Commun.* **2012**, *3*, 1225.

(6) Chen, P.; Yang, J.-J.; Li, S.-S.; Wang, Z.; Xiao, T.-Y.; Qian, Y.-H.; Yu, S.-H. *Nano Energy* **2013**, *2*, 249.

(7) Wei,L.; Yushin,G. *Nano Energy* **2012**, *1*, 552.

(8) Liu, C.; Yu, Z.; Neff, D.; Zhamu, A.; Jang, B. Z. *Nano Lett.* **2010**, *10*, 4863

(9) Wang, X.; Shi, G. *Energ. Environ. Sci.* **2015**, *8*, 790.

(10) Gao, W.; Singh, N.; Song, L.; Liu, Z.; Reddy, A. L. M.; Ci, L.; Vajtai, R.; Zhang, Q.; Wei, B.; Ajayan, P. M. *Nat. Nano.* **2011**, *6*, 496.

(11) El-Kady, M. F.; Strong, V.; Dubin, S.; Kaner, R. B. *Science* **2012**, *335*, 1326.

(12) Lin, J.; Peng, Z.; Liu, Y.; Ruiz-Zepeda, F.; Ye, R.; Samuel, E. L. G.; Yacaman, M. J.; Yakobson, B. I.; Tour, J. M. *Nat. Commun.* **2014**, *5*.

(13) Peng, Z.; Lin, J.; Ye, R.; Samuel, E. L. G.; Tour, J. M. *Acs. Appl. Mater. Inter.* **2015**, *7*, 3414.

(14) El-Kady, M. F.; Kaner, R. B. *Nat. Commun.* **2013**, *4*, 1475.

(15) Seo, B. H.; Youn, J.; Shim, M. *ACS Nano* **2014**, *8*, 8831.

(16) El-Kady, M. F.; Kaner, R. B. *ACS Nano* **2014**, *8*, 8725.

(17) Zhang, G.; Wang, T.; Yu, X.; Zhang, H.; Duan, H.; Lu, B. *Nano Energy* **2013**, *2*, 586.

(18) Hu, C.-C.; Chen, W.-C. *Electrochim. Acta* **2004**, *49*, 3469.

(19) Hu, C.-C.; Chen, W.-C.; Chang , K.-H. *J. Electrochem. Soc.* **2004**, *151*, A281.

(20) Hu, C.-C.; Chang, K.-H.; Lin, M.-C.; Wu, Y.-T. *Nano Lett.* **2006**, *6*, 2690.

(21) Chen, L. Y.; Hou, Y.; Kang, J. L.; Hirata, A.; Fujita, T.; Chen, M. W. *Adv. Energy Mater.* **2013**, *3*, 851

(22) Zhi, M.; Xiang, C.; Li, J.; Li, M.; Wu, N. *Nanoscale* **2013**, *5*, 72.

(23) Wu, Z.-S.; Zhou, G.; Yin, L.-C.; Ren, W.; Li, F.; Cheng, H.-M. *Nano Energy* **2012**, *1*, 107.

(24) Wu, Z.-S.; Wang, D.-W.; Ren, W.; Zhao, J.; Zhou, G.; Li, F.; Cheng, H.-M. *Adv. Funct. Mater.* **2010**, *20*, 3595.

(25) Wang, W.; Guo, S.; Lee, I.; Ahmed, K.; Zhong, J.; Favors, Z.; Zaera, F.; Ozkan, M.; Ozkan, C. S. *Sci. Rep.* **2014**, *4*.

(26) Zhou, Z.; Zhu, Y.; Wu, Z.; Lu, F.; Jing, M.; Ji, X. *Rsc Adv* **2014**, *4*, 6927.

(27) Vellacheri, R.; Pillai, V. K.; Kurungot, S. *Nanoscale* **2012**, *4*, 890.

(28) Soin, N.; Roy, S. S.; Mitra, S. K.; Thundat, T.; McLaughlin, J. A. *J. Mater.Chem.* **2012**, *22*, 14944.

(29) Das, R. K.; Liu, B.; Reynolds, J. R.; Rinzler, A. G. *Nano Lett.* **2009**, *9*, 677.

(30) Bi, R.-R.; Wu, X.-L.; Cao, F.-F.; Jiang, L.-Y.; Guo, Y.-G.; Wan, L.-J. *J. Phys. Chem. C* **2010**, *114*, 2448.

(31) Xu, Y.; Bai, H.; Lu, G.; Li, C.; Shi, G. *J. Am. Chem. Soc.* **2008**, *130*, 5856.

(32) Kim, F.; Luo, J.; Cruz-Silva, R.; Cote, L. J.; Sohn, K.; Huang, J. *Adv. Funct. Mater.* **2010**, *20*, 2867.

(33) Liu, Z.; Lee, J. Y.; Han, M.; Chen, W.; Gan, L. M. *J. Mater.Chem.* **2002**, *12*, 2453.

(34) Wang, P.; Liu, H.; Tan, Q.; Yang, J. *Rsc Adv* **2014**, *4*, 42839.

(35) Shen, J. Y.; Adnot, A.; Kaliaguine, S. *Appl. Surf. Sci.* **1991**, *51*, 47.

(36) Hawaldar, R.; Merino, P.; Correia, M. R.; Bdikin, I.; Gracio, J.; Mendez, J.; Martin-Gago, J. A.; Singh, M. K. *Sci. Rep.* **2012**, *2*, 682.

(37) Long, J. W.; Bélanger, D.; Brousse, T.; Sugimoto, W.; Sassin, M. B.; Crosnier, O. *MRS Bull.* **2011**, *36*, 513.

(38) Wang, F.; Xiao, S.; Hou, Y.; Hu, C.; Liu, L.; Wu, Y. *Rsc. Adv.* **2013**, *3*, 13059.

(39) Xu, J.; Wang, Q.; Wang, X.; Xiang, Q.; Liang, B.; Chen, D.; Shen, G. *ACS Nano* **2013**, *7*, 5453.

(40) Ji, J.; Zhang, L. L.; Ji, H.; Li, Y.; Zhao, X.; Bai, X.; Fan, X.; Zhang, F.; Ruoff, R. S. *ACS Nano* **2013**, *7*, 6237.

(41) Wang, G.; Zhang, L.; Zhang, J. *Chem. Soc. Rev.* **2012**, *41*, 797.

(42) Miller, J. R.; Outlaw, R. A.; Holloway, B. C. *Science* **2010**, *329*, 1637.

(43) Yuan, L.; Xiao, X.; Ding, T.; Zhong, J.; Zhang, X.; Shen, Y.; Hu, B.; Huang, Y.; Zhou, J.; Wang, Z. L. *Angew.Chem. Int. Ed.* **2012**, *51*, 4934.

(44) Ge, L.; Wang, P.; Ge, S.; Li, N.; Yu, J.; Yan, M.; Huang, J. *Anal. Chem.* **2013**, *85*, 3961.

(45) Peng, L.; Peng, X.; Liu, B.; Wu, C.; Xie, Y.; Yu, G. *Nano Letters* **2013**, *13*, 2151.

(46) Kim, D.; Shin, G.; Kang, Y. J.; Kim, W.; Ha, J. S. *ACS Nano* **2013**, *7*, 7975.

(47) Cao, L.; Yang, S.; Gao, W.; Liu, Z.; Gong, Y.; Ma, L.; Shi, G.; Lei, S.; Zhang, Y.; Zhang, S.; Vajtai, R.; Ajayan, P. M. *Small* **2013**, *9*, 2905.

(48) Wang, H.; Zhu, B.; Jiang, W.; Yang, Y.; Leow, W. R.; Wang, H.; Chen, X. *Adv. Mater.* **2014**, *26*, 3638.

(49) Pech, D.; Brunet, M.; Taberna, P.-L.; Simon, P.; Fabre, N.; Mesnilgrente, F.; Conédéra, V.; Durou, H. *J. Power Sources* **2010**, *195*, 1266.

(50) Meng, Q.; Wu, H.; Meng, Y.; Xie, K.; Wei, Z.; Guo, Z. *Adv. Mater.* **2014**, *26*, 4100.

(51) Pech, D.; Brunet, M.; Durou, H.; Huang, P.; Mochalin, V.; Gogotsi, Y.; Taberna, P.-L.; Simon, P. *Nat. Nano.* **2010**, *5*, 651.

(52) El-Kady, M. F.; Ihns, M.; Li, M.; Hwang, J. Y.; Mousavi, M. F.; Chaney, L.; Lech, A. T.; Kaner, R. B. *Proc.Natl. Acad. Sci. U.S.A* **2015**, *112*, 4233.

(53) Dinh, T. M.; Achour, A.; Vizireanu, S.; Dinescu, G.; Nistor, L.; Armstrong, K.; Guay, D.; Pech, D. *Nano Energy* **2014**, *10*, 288.

(54) Yu, D.; Goh, K.; Wang, H.; Wei, L.; Jiang, W.; Zhang, Q.; Dai, L.; Chen, Y. *Nat. Nano.* **2014**, *9*, 555.

(55) Yuan, L.; Lu, X.-H.; Xiao, X.; Zhai, T.; Dai, J.; Zhang, F.; Hu, B.; Wang, X.; Gong, L.; Chen, J.; Hu, C.; Tong, Y.; Zhou, J.; Wang, Z. L. *ACS Nano* **2012**, *6*, 656.

(56) Li, H. B.; Yu, M. H.; Wang, F. X.; Liu, P.; Liang, Y.; Xiao, J.; Wang, C. X.; Tong, Y. X.; Yang, G. W. *Nat. Commun.* **2013**, *4*, 1894.

(57) Chen, W.; Rakhi, R. B.; Hu, L.; Xie, X.; Cui, Y.; Alshareef, H. N. *Nano Letters* **2011**, *11*, 5165.

(58) Li, X.; Sun, W.; Wang, L.; Qi, Y.; Guo, T.; Zhao, X.; Yan, X. *Rsc Adv* **2015**, *5*, 7976.

(59) Taberna, P. L.; Simon, P.; Fauvarque , J. F. *J. Electrochem. Soc.* **2003**, *150*, A292.

(60) Kim, J.-Y.; Kim, K.-H.; Yoon, S.-B.; Kim, H.-K.; Park, S.-H.; Kim, K.-B. *Nanoscale* **2013**, *5*, 6804.

Chapter 3. Boosting the Capacitance and Voltage of Aqueous Supercapacitors via Redox Charge Contribution from both Electrode and Electrolyte

3.1 Abstract

Supercapacitors are evolving into an important component in energy storage technology with the capability for storing and discharging energy very quickly and effectively. State-of-the-art supercapacitors feature activated carbon electrodes impregnated with a non-aqueous electrolyte (typically acetonitrile) that operate at voltages between 2.2-2.7 V. Unfortunately, activated carbons have low specific capacitance (100-120 F g^{-1}) in organic electrolytes, which severely limits the energy density of supercapacitors. In addition, organic solvents are often flammable leading to safety and environmental concerns. Aqueous electrolytes, on the other hand, are safer, cheaper and have higher ionic conductivity, promising higher capacitance electrodes. However, the low voltage window enforced by the low decomposition voltage of water around 1.23 V is a major challenge. Here, we have demonstrate symmetric supercapacitors operating at an ultrahigh voltage of 1.8 V that can provide specific capacitances up to 716 F g^{-1}, which is higher than traditional activated carbon electrodes. This is possible through designing both the electrode and electrolyte to work synergistically towards improving not only the capacitance of the electrodes, but also the voltage and cycling stability of the supercapacitor. We also demonstrate by using a simple laser technique the possibility of fabricating micro-supercapacitors with great potential for miniaturized electronics. This work provides an effective strategy for designing and fabricating aqueous supercapacitors that hold promise for a sustainable energy future.

3.2 Introduction

In recent years, the rapidly growing portable electronics market has evoked high demand for better energy storage devices with high power density.[1, 2] Supercapacitors (also known as electrochemical capacitors) have long been considered a promising power source that have now been brought into reality with applications for camera flash, backup power, and regenerative braking.[3] In spite of the great advantages of high specific power and long cycle life, their relatively low energy density limits their future applications.[4] At present, many research groups are investigating new electrode materials and electrolytes, and unconventional device architectures in order to improve the energy density of supercapacitors.[5] The energy density of a supercapacitor can be increased by two approaches, either by enhancing the specific capacitance or by extending the voltage window of the device. To improve the specific capacitance, various supercapacitors materials have been proposed by incorporating pseudo-capacitive or faradaic materials[6] (RuO_2[7], NiO[8], Fe_3O_4[9], MnO_2[10], Co_3O_4[11], V_2O_5[12], polyaniline[13], etc.) onto carbon-based materials (activated carbon[14], carbon nanotubes (CNTs)[15], graphene[16], etc.) as hybrid electrodes.[17, 18] In our previous work, we successfully made a laser-scribed graphene (LSG)/RuO_2 electrode via a one-step procedure where graphene oxide (GO)/$RuCl_3$ was simultaneously reduced (GO → LSG) and oxidized ($RuCl_3$ → RuO_2) via standard laser scribing.[19] Despite the simple inexpensive one-step laser process, the high cost of ruthenium limits the commercial potential of this device. Therefore, we searched for less expensive pseudo-capacitive materials that can be substituted for RuO_2 while maintaining our simple one-step laser processing. In this regard, magnetite (Fe_3O_4) has emerged as a promising pseudo-capacitive material owing to its low cost, metallic-like electrical conductivity (10^2–10^3 S cm^{-1})[20], variable oxidation states, low toxicity, and environmentally friendliness. Recently, various research efforts have been

made with the synthesis of iron oxide and carbon nanocomposite materials for supercapacitor electrodes. Qu and co-workers reported[21] the use of a 2-dimensional sandwich-like FeOOH nanorod/graphene as a negative electrode with a specific capacitance of 326 F g^{-1} with good rate capability, but further improvements in the capacitance are still required. Wang *et al.* suggested[22] a single-crystalline Fe_2O_3/graphene hydrogel with a specific capacitance of 908 F g^{-1}. Quan and coworkers synthesized[23] Fe_2O_3 nanoplate-reduced graphene oxide composites, which showed a specific capacitance of 903 F g^{-1}. However, all the work so far has only been focused on the negative electrode employing a three-electrode setup, even though the voltage window for the full cell is a critical factor in determining the energy density of a supercapacitor. In addition, the hybrid supercapacitors must demonstrate good cycle life.

Although metal oxide and carbon composite active materials are able to improve the capacitance, the energy density cannot be improved significantly if one only relies on the solid active materials comprising the electrode. Another important deciding factor for the performance of a supercapacitor is the electrolyte. Adding redox-additives into a traditional aqueous electrolyte has proven to be an efficient route to enhance supercapacitor performance because redox additives can contribute to the capacitance and enhance the energy densities via redox reactions between the electrode and the electrolyte.[24] For example, Roldan *et al.* reported[25] an increase in energy density from 10.1 Wh kg^{-1} (1 M H_2SO_4) to 30.6 Wh kg^{-1} by adding hydroquinone (HQ) in an H_2SO_4 electrolyte. Recently, Chun *et al.* added[26] methyl viologen (MV) in a bromide electrolyte of a supercapacitor with an activated carbon electrode and improved the specific energy of the device up to 14 Wh kg^{-1}. Similarly, many other groups have studied various redox electrolytes (such as methylene blue[27], *p*-phenylenediamine[28], ferrocyanide[29], etc.), significantly enhancing the supercapacitor

performance from plain carbon electrodes. Although much attention has focused on investigating pseudo-capacitive or faradaic materials, most studies only rely on improving either the electrode or the electrolyte. Just a few studies have improved the energy density using both the pseudo-capacitive electrode and the redox-electrolyte simultaneously. For example, Su *et al.* reported[30] an improvement in the specific capacitance up to 712 F g^{-1} using a Co-Al layered double hydroxide by adding $K_3Fe(CN)_6$ into 1.0 M KOH. Zhao and co-workers reported[29] a $Co(OH)_2$/graphene electrode with a $K_3Fe(CN)_6$/KOH system and showed an ultrahigh specific capacitance of 7514 F g^{-1}. The enhancement of capacitance is very impressive, but this value was measured only in a three-electrode system and the capacitive results only include the behavior of an electrode/electrolyte interface, not the real performance of a supercapacitor. Supercapacitors store energy at the interface between two electrodes with the same electrolyte, so when we use a redox-active electrolyte during charging, the positive electrode must be oxidized, while the negative electrode must be reduced. We have observed that the three-electrode and two-electrode systems will give very different electrochemical performances with redox active electrolytes. Therefore, it is very important to study two-electrode systems when using redox-electrolytes.

To the best of our knowledge, the combination of redox materials on both electrode and electrolyte with full cell device studies has not yet been reported. Here, we propose a redox mediator [$Fe(CN)_6^{3-}$/$Fe(CN)_6^{4-}$] added into 1.0 M Na_2SO_4 aqueous electrolyte with a symmetric graphene/Fe_3O_4 electrode supercapacitor. The unique nanocomposite structure of a 3D interconnected porous LSG framework with an approximately 6-nm Fe_3O_4 nanoparticle electrode leads to a high 1.8 V operational voltage window. The combination of the redox-electrolyte with the LSG/Fe_3O_4 electrode exhibits an ultrahigh specific capacitance of 716 F

g^{-1}, which is nearly three times higher than pristine LSG electrodes using 1.0 M Na_2SO_4. Furthermore, the redox-active electrolyte helps to improve the cycle performance at 1.8 V with 90% capacity retention after 5000 cycles. In our system, the energy density of the supercapacitor was increased simultaneously by the high specific capacitance and the 1.8 V cell voltage of the device. Therefore, the symmetric 1.8 V neutral aqueous electrolyte supercapacitor with excellent electrochemical performance (121 Wh kg^{-1}, 67.2 mAh g^{-1}) is superior to other recently published electrochemical capacitors.[21, 22, 31-36] Not only does our supercapacitor demonstrate superior electrochemical performance, but the simple laser technique described here can also be used to fabricate micro-supercapacitors in a single step.

3.3 Results and discussion

An LSG/Fe_3O_4 electrode was fabricated by the *in situ* reduction of graphene oxide and oxidation of $FeCl_3$. A GO slurry and $FeCl_3$ particles were well dispersed in water; due to the electrostatic effect, Fe^{3+} will be absorbed on the negatively charged part of the hydrophilic oxygen functional groups of GO. After about 30 min of sonication, GO-wrapped Fe^{3+} cation particles were obtained. Following the CO_2 laser etching, the mixed sample undergoes a simultaneous oxidation of Fe^{3+} ($FeCl_3$) to Fe_3O_4 and reduction of GO to LSG, and LSG-wrapped Fe_3O_4 was successfully synthesized. These films were utilized as hybrid electrodes and used directly in the assembly of our supercapacitors (Figure. 3.1).

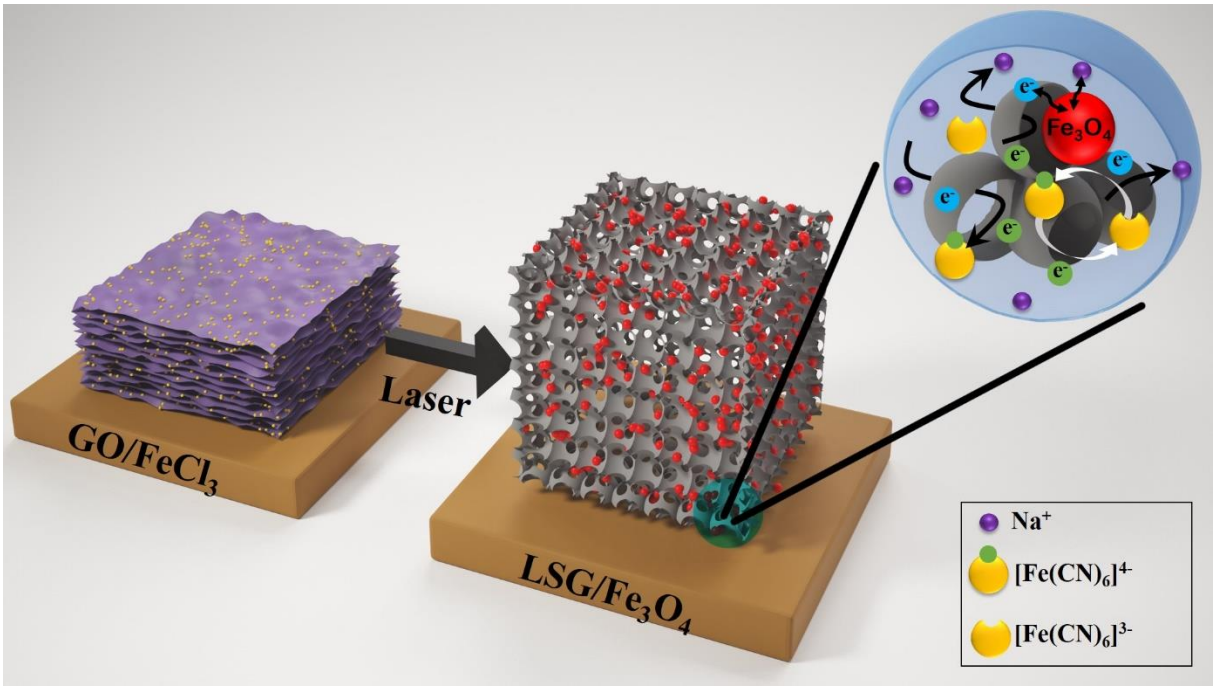

Figure 3.1. Schematic illustration showing the fabrication process for LSG/Fe_3O_4 nanocomposite electrodes along with an explanation of the underlying mechanism for charge storage. A GO/$FeCl_3$ film is exposed to a 7 W CO_2 laser to create an electrode of LSG wrapped with Fe_3O_4 nanoparticles. This photo-thermal process is extremely fast and readily controllable producing electrodes in minutes. The resulting LSG/Fe_3O_4 can be used in combination with a redox active electrolyte containing the [$Fe(CN)_6^{3-}$/$Fe(CN)_6^{4-}$] redox couple in order to produce effective supercapacitors. This system stores charge both through reversible redox reactions on the electrode side (pseudo-capacitive Fe_3O_4 nanoparticles) and the electrolyte side (redox additive).

For a better understanding of the mechanism of formation of LSG/Fe_3O_4 electrodes, we studied TGA/DTA for GO, $FeCl_3$, and GO/$FeCl_3$ samples, as shown in (Figure S3.1, Supporting Information). During the thermal de-oxygenation of GO, a large exothermic peak (-1043 J g^{-1}) was observed at 210 °C (Figure S3.1a). The energy released from the de-oxygenation of GO works as an *in situ* power source that can drive the new oxidation reaction of $FeCl_3$. The heat required to drive the oxidation reaction of $FeCl_3$ to iron oxide is only 269.6 J g^{-1} (Figure S3.1b), which is only one-fourth the amount of heat released during the

reduction of GO. In Figure S3.1c, the GO/$FeCl_3$ mixture shows an exothermic peak (-471.6 J g^{-1}) at 205 °C, confirming that the *in situ* reduction of GO to r-GO and the oxidation of $FeCl_3$ to iron oxide were spontaneous redox reactions. To initiate the reaction of the GO/$FeCl_3$ mixture, a small amount of heat (50.9 J g^{-1}) is required, as indicated by an endothermic peak at 100 °C (Figure S3.1c). This reaction can be initiated with a 7 W CO_2 laser.

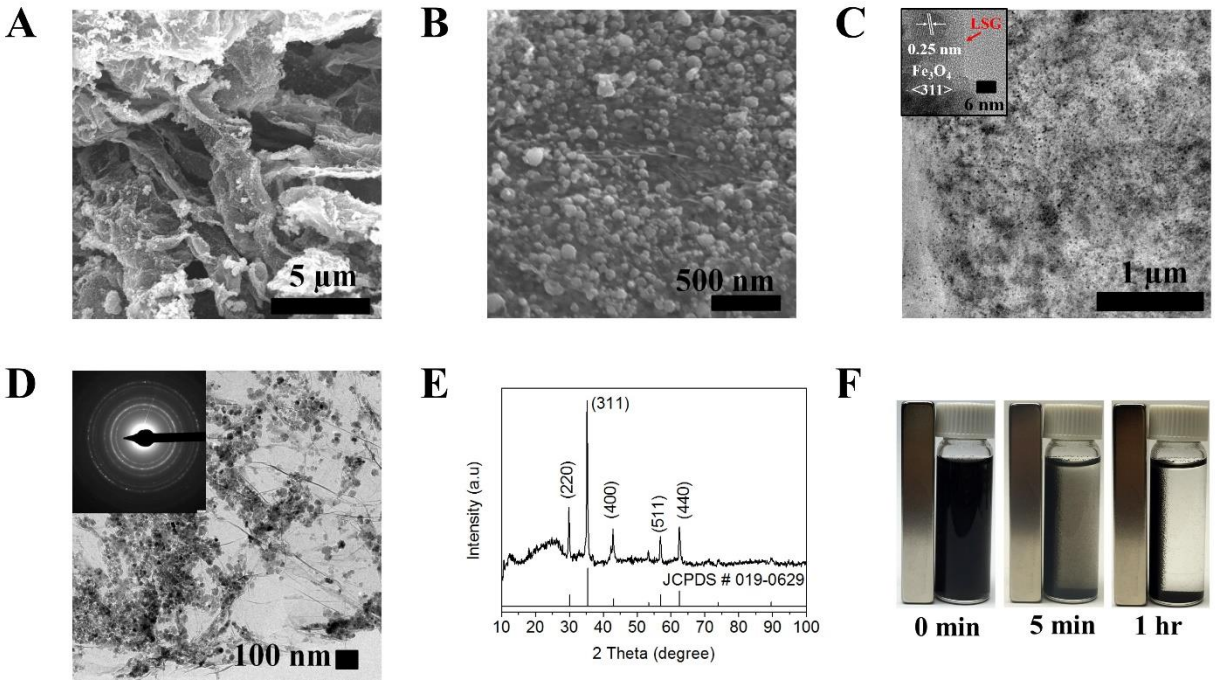

Figure 3.2. Physical characterization of LSG/Fe_3O_4 nanocomposites. (a) An overview SEM image showing Fe_3O_4 nanoparticles grown on LSG. (b) SEM image of LSG/Fe_3O_4 under higher magnification. (c) A TEM image of an LSG/Fe_3O_4 nanocomposite. Inset is the HRTEM image showing the 0.25 nm d-spacing corresponding to the <311> facet of Fe_3O_4. (d) HRTEM image with SAED pattern inset indicating the polycrystalline nature of Fe_3O_4 in the LSG composite. (e) XRD pattern of an LSG/Fe_3O_4 nanocomposite plotted with the Fe_3O_4 JCPDS data file no. 019-0629. (f) Digital photos of an LSG/Fe_3O_4 nanocomposite dispersed in an aqueous solution without and with an external magnetic field (after 5 min and 1 h).

The structure and morphology of the LSG/Fe_3O_4 electrodes were characterized by SEM, TEM, XRD, and TGA. Figure 3.2a shows a typical SEM image of an LSG/Fe_3O_4 nanocomposite, indicating that the iron oxide nanoparticles are well dispersed across the conductive LSG framework. In addition, the image shows the three-dimensional nature of the electrode whose macro-porous network provides large internal surface areas for charge storage. This 3D structure is also supported by the iron oxide nanoparticles that act as nano-spacers for the LSG network and provide enough space for the electrolyte ions to interact with the entire electroactive surface of the electrode, allowing for more efficient charge storage. Not only does graphene act as a support for the iron oxide particles, but it also shows a very strong (i.e. close) connection between each iron oxide nanoparticle, helping to prevent aggregation of the iron oxide nanoparticles, and resolving the restacking problem of the graphene layers, which can enhance electron transport and stability during cycling processes (Figure 3.2b). In Figure 3.2c, the TEM image also shows that a uniform dispersion of iron oxide nanoparticles tightly bonded to the LSG has been successfully synthesized with this laser technique. High-resolution TEM (HRTEM) images of the samples show that the iron oxide nanoparticles are crystalline in nature, as seen from the inset in Figure 3.2c, with a d-spacing of 0.25 nm which is in good agreement with the <311> planes of Fe_3O_4 crystals. The HRTEM image also shows that LSG sheets are wrapped around each 6 - 10 nm sized Fe_3O_4 nanoparticle. This unique LSG-wrapped structure provides an efficient pathway to capture the redox capacitance from Fe_3O_4 nanoparticles throughout the conductive LSG network. A TEM image with an SAED pattern of the LSG/Fe_3O_4 nanocomposite is shown in Figure 3.2d. The d-spacings of the peaks are calculated from the positions of the diffraction rings in the inset of Figure 3.2d. These calculated peaks are in good agreement with reference data for Fe_3O_4 shown in Table S3.1. The crystal structure of iron oxide was further characterized by

its XRD patterns (Figure 3.2e), in which the diffraction peaks are perfectly indexed to Fe_3O_4 (JCPDS 019–0629). These data confirm that the iron oxide nanoparticles are indeed Fe_3O_4. The LSG exhibits a weak broad peak around 25° and very tiny unconverted GO peaks appear around 11°. These XRD results suggest that the material of the electrode nanocomposite is mainly LSG and Fe_3O_4. The Fe_3O_4 content of the electrode was 41 wt%, which was measured by TGA analysis (Figure S3.3, Supporting Information). In addition, Figure 3.2f shows photos of the magnetism of the LSG/Fe_3O_4 nanoparticles dispersed in aqueous solutions without a magnet and with a magnet after 5 min and 1 h. The LSG/Fe_3O_4 nanoparticles in aqueous solution can show oriented movement and be separated from the solution under an external magnet. Through this experiment, we can conclude that the LSG/Fe_3O_4 nanoparticles possess excellent magnetic properties.

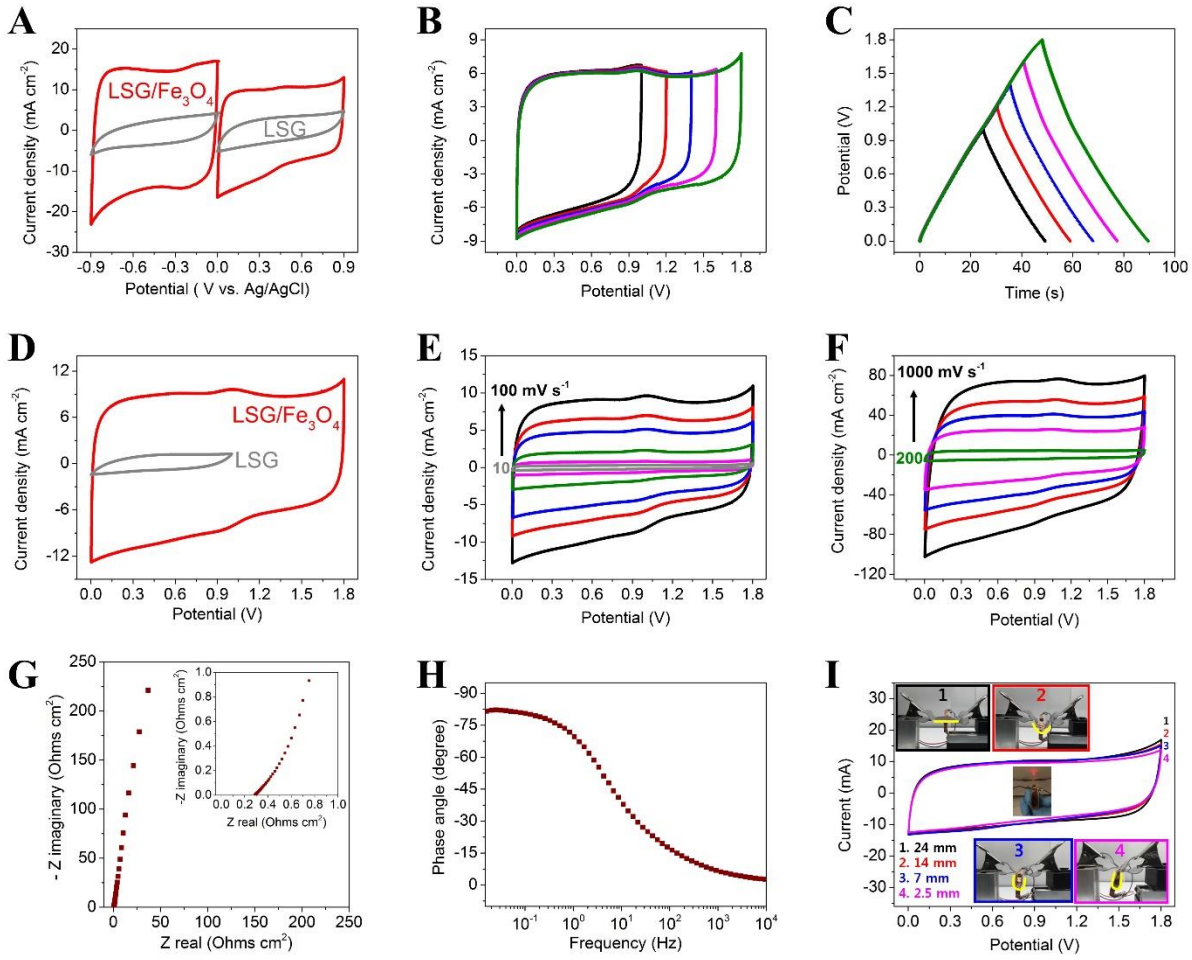

Figure 3.3. Evaluation of the electrochemical performance of LSG/Fe_3O_4 electrodes and a symmetric LSG/Fe_3O_4 supercapacitor in a traditional 1.0 M Na_2SO_4 electrolyte. (a) Cyclic voltammetry (CV) curves of LSG and LSG/Fe_3O_4 electrodes, comparing the electrochemical properties of the positive and negative electrodes in their stable operating voltage windows, obtained at 50 mV s^{-1} with a three-electrode set up. (b) CV curves at 70 mV s^{-1}. (c) Galvanostatic charge/discharge (CC) curves at a current density of 4 mA cm^{-2} for the symmetric LSG/Fe_3O_4 supercapacitor at an increasing voltage window from 1.0 V to 1.8 V. (d) CV curves of an LSG and an LSG/Fe_3O_4 supercapacitor obtained at 100 mV s^{-1}. CV profiles of an LSG/Fe_3O_4 supercapacitor at different scan rates of (e) 10, 20, 30, 50, 70, and 100 mV s^{-1}, and (f) 200, 300, 500, 700, and 1000 mV s^{-1} tested at a maximum voltage of 1.8 V. (g) Nyquist plot with a magnified high-frequency region and (h) Bode plots of the LSG/Fe_3O_4 symmetric supercapacitor over a frequency range from 1 MHz to 0.01 Hz. (i) CV curves of a flexible LSG/Fe_3O_4 full cell at different bending radii: (1) 24, (2) 14, (3) 7, and (4) 2.5 mm at a scan rate of 100 mV s^{-1}. Inset is the corresponding digital images of the bending conditions and a glowing red LED in the bent state confirming the electrochemical stability of the device under mechanical stress.

The electrochemical properties of LSG/Fe_3O_4 electrodes were assessed in both conventional three-electrode cell and two-electrode symmetric supercapacitor pouch cells with 1.0 M Na_2SO_4 as the electrolyte. Figure 3.3a shows the cyclic voltammetry (CV) of the bare LSG and LSG/Fe_3O_4 electrodes in both negative and positive voltage windows, tested at a relatively fast scan rate of 50 mV s^{-1}. The CV of the LSG/Fe_3O_4 electrode exhibits a rectangular shape in both the negative and positive voltage windows with a significant increase in the capacitance compared to that of bare LSG, indicating that iron oxide contributes to the charge storage through reversible redox reactions. The rectangular shapes of the CV curves indicate that Fe_3O_4 stores charge via adsorption pseudo-capacitance rather than intercalation faradaic reaction.[6] This effect can be attributed to the ultra-small particle size of the Fe_3O_4 nanoparticles (6 nm), which limits redox reactions to the surfaces. During the Faradaic processes at the iron oxide nanoparticles, electrons coupled with the highly conductive macro-porous LSG framework enables higher energy density without sacrificing the power density. Another interesting property of the combination of LSG/Fe_3O_4 electrode with the 1.0 M Na_2SO_4 electrolyte is that both positive and negative voltage windows reveal ideal CV shapes without a significant increase in the cathodic or anodic current. This signifies that neither H_2 on the negative electrode nor O_2 on the positive electrode are produced, indicating that the electrolyte decomposition voltage is higher than the thermodynamic value of 1.23 V. This can be attributed to the strong solvation energy of the sodium cations as well as sulfate anions, which provide strong bonds in the solvation shell and prevent water decomposition up to 1.8 V. In this potential range, energy is consumed to break bonds in the solvation shell instead of causing the decomposition of water.[37] The CVs retain their rectangular shapes with increasing scan rates up to 100 mV s^{-1}, and an ideal triangular shape is observed in the charge/discharge (CC) curves at different current densities,

which indicate the high rate capability of the electrode in both positive (0 V to 0.8 V vs. Ag/AgCl) and negative (0 V to -1.0 V vs. Ag/AgCl) voltage windows (Figure S3.4). The areal specific capacitances of the LSG/Fe_3O_4 electrode in the negative and positive voltage windows are 264 mF cm^{-2} (691 F g^{-1}) and 137 mF cm^{-2} (357 F g^{-1}) at a scan rate of 20 mV s^{-1}, respectively. While the two electrodes have the same chemical composition (Fe_3O_4 nanoparticles on 3D porous graphene framework), some components store more charge than others depending on the polarity of the electrode. Specifically, capacitance of the negative electrode arises mainly from Fe_3O_4 nanoparticles whereas graphene dominates charge storage in the positive electrode. In the negative electrode, the conducting LSG network acts as a 3D current collector to provide electron "superhighways" for charge storage and delivery, while the nanostructured Fe_3O_4 enables fast and reversible Faradaic reactions with short ionic diffusion pathways. The 3D porous structure of the electrode allows for the full utilization of the capacitive properties of Fe_3O_4 and explains the ultrahigh capacitance of the negative electrode. Since the positive electrode stores less charge, the electrical charge of the positive and negative electrodes can be balanced by using a redox active electrolyte, the details of which are shown in Figure 3.4 and discussed in the following section. Based on the operating voltage window determined by the three-electrode cell results, a symmetric LSG/Fe_3O_4 supercapacitor can be expected to have a 1.8 V working voltage in the 1.0 M Na_2SO_4 aqueous electrolyte. To confirm our assumption, a symmetric LSG/Fe_3O_4 supercapacitor was assembled with two identical LSG/Fe_3O_4 electrodes separated by an ion porous separator. Both CV and CC were collected at an increasing voltage window starting from 0.8 V and increased up to 1.8 V with voltage intervals of 0.2 V for each scan, all tested at a scan rate of 70 mV s^{-1} for CV curves and a current density of 4 mA cm^{-2} for CC curves. The results presented in Figures. 3.3b,c indicate that by increasing the potential window up to 1.8 V, the

cell exhibits ideal capacitive behavior with a nearly rectangular CV shape without showing any significant increase of anodic current even at 1.8 V. This signifies that any decomposition of the aqueous electrolyte with hydrogen or oxygen evolution was not observed. In addition, the ideal triangular shape CC curves shown in Figure 3.3c with very small IR drops and high capacitance were maintained with the increasing voltage window up to 1.8 V, verifying that the electrolyte is stable and does not decompose. Figure 3.3d further compares the performance with a bare LSG symmetric supercapacitor and an LSG/Fe_3O_4 symmetric supercapacitor at a scan rate 100 mV s^{-1}. Even at a high operating voltage of 1.8 V, the specific capacitance of an LSG/Fe_3O_4 supercapacitor is about 10 times larger than the bare LSG. These results suggest that the operational voltage window for a symmetric LSG/Fe_3O_4 supercapacitor with 1.8 V is feasible. For comparison, a bare LSG symmetric supercapacitor and a pristine iron oxide symmetric supercapacitor were tested at 1.8 V with a current density of 100 mV s^{-1} (Figures S3.5a and b). The CV curves show that both supercapacitors obviously suffer from decomposition of the aqueous electrolyte above 1.2 V. These results indicate the remarkable improvement of the extended operational voltage and capacitance that arises from the combination of the special architectural form of the LSG/Fe_3O_4 electrode with a 1.0 M Na_2SO_4 electrolyte. Although we have a symmetric supercapacitor in terms of electrode composition and loading mass, it functions like an asymmetric device. In this case, most of the charge stored in the negative electrode comes from Fe_3O_4 whereas graphene offers more charge stroage in the positive electrode. This asymmetric charge storage mechanism is the main reason for stretching the voltage window of this aqueous supercapacitor up to 1.8 V. In addition to its higher voltage window, Figures 3.3 e,f show the rectangular CV shape of the LSG/Fe_3O_4 with the potential window of 1.8 V under different scan rates from 10 to 1000 mV s^{-1}. The rectangular shape is retained at very high scan rates

including 1000 mVs^{-1} and even at 10,000 mV s^{-1} the CV retains a quasi-rectangular shape (Figure S3.6a), suggesting that the symmetric supercapacitor based on LSG/Fe_3O_4 performs near ideal capacitive behavior with a high rate capability at 1.8 V. The ideal triangular shape of the CC curves under different current densities from 4 mA cm^{-2} to 400 mA cm^{-2} provides further evidence for the ideal supercapacitor behavior of the LSG/Fe_3O_4 supercapacitors (Figures S3.6b, c, d). The specific capacitance of the LSG/Fe_3O_4 was calculated through the discharge curve from the two-electrode setup and was calculated to be 460 F g^{-1} (176 mF cm^{-2}) per electrode at a scan rate of 20 mV S^{-1}.We also calculated the specific capacitance per electrode, the areal capacitance for the device, and the entire stack capacitance for the supercapacitor (including current collector and separator) under different current densities (Figure S3.6e,f). Even at an ultrahigh current density of 1300 A g^{-1}, the LSG/Fe_3O_4 supercapacitor can deliver 335 F g^{-1}. These results imply that the LSG/Fe_3O_4 supercapacitor exhibits excellent rate capability through the special three-dimensional architectural form of the LSG/Fe_3O_4. The special structure of LSG/Fe_3O_4 enables fast ionic and electronic diffusion within the electrode. In addition, the highly conductive and porous structure of LSG provides a very efficient way for charge transfer to iron oxide nanoparticles during redox reactions. This statement can also be verified from the x-intercept of the Nyquist plot (Figure 3.3g), which is about 0.35 Ω cm^2. This value represents a very low equivalent series resistance (ESR) for the device. No semicircles are detected, indicating no charge transfer resistance, while the vertical straight up line at low frequency in the Nyqist plot also confirms the fast ionic diffusion to the electrode and fast electron transfer during the redox reactions. A Bode plot (Figure 3.3h) was made to determine the maximum phase angle and frequency response time. The phase angle of the LSG/Fe_3O_4 supercapacitor is -82°, close to the -90° for ideal capacitors. In addition, the corresponding time constant τ_0 is 0.14 s (the inverse of the

characteristic frequency f_0 (7 Hz) at a phase angle of -45° in the Bode phase plot), showing a much faster response time than many conventional activated carbon electrochemical capacitors.[18, 38] This rapid frequency response of the LSG/Fe_3O_4 can be accounted for by the excellent three-dimensional architecture whose interconnected structure allows for strong interaction between LSG and the Fe_3O_4 nanoparticles. This electrode structure enables ions to easily access the macro-porous LSG and provide fast charge transfer to iron oxide during the Faradaic reactions. To pursue a highly flexible energy storage device, all-solid-state supercapacitors were made with two LSG/Fe_3O_4 electrodes sandwiched with a PVA-Na_2SO_4 gel-like electrolyte. To study the electrochemical properties under bending conditions (with radii of curvature corresponding to flat, 14, 7 and 2.5 mm), CV curves were plotted in Figure 3.3i at 100 mV s^{-1}. Even under a highly bent condition of 2.5 mm, the CV shape change is almost negligible compared to that of the flat state. These results imply that mechanical bending does not influence any ionic and electronic diffusion between the gel electrolyte and the LSG/Fe_3O_4 electrode, thanks to the large porous space from the three-dimensional interconnected LSG framework, which can accommodate the deformation of the electrode. Insets in Figure 3.3i show the flexible supercapacitor as it is turning on a light emitting diode (LED) while in the bent state, indicating excellent capacitive performance even under harsh mechanical stress.

Pseudo-capacitor research is commonly focused on the reversible redox reactions from the electrode materials, like metal oxides or conducting polymers, but there is a limited improvement of the pseudo-capacitance if we only rely on solid electrode materials. One simple strategy to improve capacitance is utilization of a redox-active electrolyte (RE). We explore the enhancement of capacitance from both LSG/Fe_3O_4 electrode materials and

ferricyanide/ferrocyanide RE. Our results show that the redox pair of the [$Fe(CN)_6^{3-}$/$Fe(CN)_6^{4-}$] electrolyte contributes to the capacitance and stabilizes the cycle life at 1.8 V. We used exactly the same materials (same chemical composition and loading mass) for both positive and negative electrodes and balanced the charge with the redox electrolyte. On the negative side, the capacitance originates from the active materials on the electrode (LSG/Fe_3O_4) while on the positive side, the solid electrode contributes to charge storage but the capacitance comes mainly from the redox electrolyte. This combination of Faradaic charge storage materials on the electrode and redox electrolyte to widen the operating voltage window is novel and is being reported here for the first time. We propose a new concept for the asymmetric capacitor mechanism, which effectively utilizes pseudo-capacitance from the solid electrode and the faradaic reaction from the liquid electrolyte. In order to understand the mechanism, we need a more distinct characteristic Fe_3O_4 peak from the LSG/Fe_3O_4 electrode, so we specially synthesized an electrode containing a high percentage of Fe_3O_4 (~82%). With this electrode, CV measurements were performed both before and after adding [$Fe(CN)_6^{3-}$/$Fe(CN)_6^{4-}$] into a 1.0 M Na_2SO_4 electrolyte. Figure. S3.7 shows the CVs with two different systems in the same potential range from 0 to 0.8 V at 5 mV s^{-1}. The black CV curve is shown before adding the RE and the red CV curve is shown after 0.005 M RE was added. From the solid LSG/Fe_3O_4 electrode, iron oxide particles exhibit pseudo-capacitive properties through reversible charge-transfer processes, according to the following equation:

$$Fe^{Z+} \rightleftharpoons Fe^{(Z+N)+} + Ne^-; 0 \leq Z \leq 2, 1 \leq N \leq 3 \quad (2)$$

The oxidation and reduction peaks appear at 0.4 V and 0.28 V, respectively (Figure S3.7 black curve). The charging process entails an oxidation process from Fe^{2+} to Fe^{3+}, while the discharging process comprises a reduction process from Fe^{3+} to Fe^{2+}.

From the RE side, the oxidation and reduction attributed to the Faradaic reaction shown in the following equation:

$$Fe(CN)_6^{4-} \leftrightharpoons Fe(CN)_6^{3-} + e^- \quad (3)$$

In Figure S3.7 the red CV shows two independent oxidation peaks at 0.22 V and 0.4 V. We can observe that 0.4 V broad oxidation peak is superimposed with a black oxidation peak, indicating that this oxidation peak is from the LSG/Fe_3O_4 electrode and the 0.22 V peak is from the RE. These results indicate that the redox reaction of the LSG/Fe_3O_4 electrode and the RE occur independently and simultaneously, with the mechanism depicted in Figure 3.4a. In this RE system, when the supercapacitor is charged, both electrode and electrolyte materials will be oxidized, and when the supercapacitor is discharged, both the electrode and the electrolyte will be reduced simultaneously. In order to compare redox reactions for different concentrations of [$Fe(CN)_6^{3-}$/$Fe(CN)_6^{4-}$] in the 1.0 M Na_2SO_4 electrolyte, the CVs, CCs, and EIS measurements were performed in a three-electrode system (Figure 3.4 b,c and S 3.8). A very sharp reversible redox peak is observed in Figure 3.4 b, indicating that the [$Fe(CN)_6^{3-}$/$Fe(CN)_6^{4-}$] ions are highly electrochemically active. Moreover, Figure 3.4b shows the CV curves with various concentrations of RE ions of 0, 0.025, 0.050, and 0.100 M in 1.0 M Na_2SO_4 at a scan rate of 50 mV s^{-1}. As the RE ion concentration is increased, the characteristic redox peak obviously increases, indicating that the capacitance contributed by the RE ions increase. As the RE ions concentration increases in the electrolyte, more RE ions contribute to the Faradaic-capacitance and extra electrons work as an electron shuttle to the electrode promoting the high activity of the LSG/Fe_3O_4 electrode. Figure 3.4c shows the CC curves with different concentrations of redox-ions in the electrolyte at a current density of 8 mA cm^{-2}. On the basis of the discharge time in the CC curves, the specific capacitances of the

electrode were calculated at various current densities (Figure 3.4d). The LSG/Fe_3O_4 electrode and the 0.1 M RE system shows an ultrahigh specific capacitance of 1489 F g^{-1} (570 mF cm^{-2}) at 8 mA cm^{-2}, which is about four times larger than the pristine 1.0 M Na_2SO_4 electrolyte. This remarkable improvement arises from the Faradaic processes at the solid iron oxide nanoparticles coupled with the RE and promoting the electron transfer between the LSG/Fe_3O_4 electrodes. This promising result was further confirmed by the Nyquist plot, as shown in Figure S3.8. As the redox-ion concentration is increased, the intercept of the Nyquist plot values decreases. These results confirm that as the redox-ions concentration is increased, low charge transfer resistance at the electrode-electrolyte interface is observed.

For practical applications, the RE electrolyte in a two-electrode system was assessed. In the two-electrode system, the positive and negative electrodes of the redox states should be stable in the same RE with the separator. Interestingly, compared to the three-electrode setup, the two-electrode system exhibits very different performance with a higher concentration of RE. The reason is for a full supercapacitor, the balance of the electric charge between positive and negative electrodes is critical to obtain a satisfactory capacitive performance. The charge balance between the two electrodes should follow the relationship $Q_+ = Q_-$. To balance the positive and negative electrical charge, CV measurements were performed in both negative potential window (0 to -1 V) and positive potential window (-0.2 to 0.8 V) at different scan rates. Figure 4e shows a CV at 20 mV s^{-1} without RE and with 0.025 M RE in both positive and negative windows with the same electrode, measured with a 3-electrode setup. According to the analysis of the electric charge values for both negative and positive voltage windows in different concentrations of RE, the optimal RE concentration was determined to be 0.025 M for the symmetric LSG/Fe_3O_4 supercapacitor (Figure 3.4f).

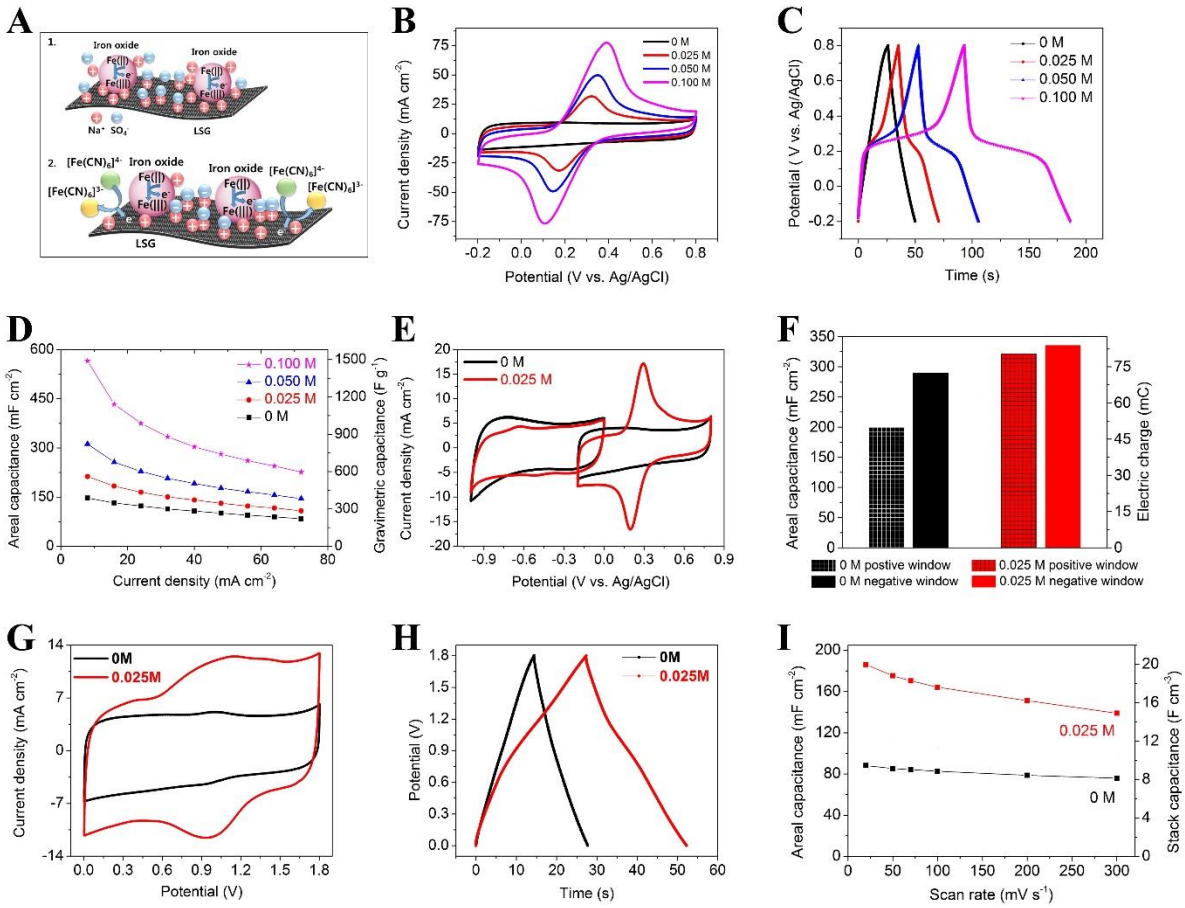

Figure 3.4. Electrochemical performance of LSG/Fe_3O_4 electrodes and a symmetric supercapacitor in an [$Fe(CN)_6^{3-}$/$Fe(CN)_6^{4-}$] redox-active electrolyte (a) Illustration of the charge storage mechanism in LSG/Fe_3O_4 supercapacitors using 1.0 M Na_2SO_4 electrolyte (1) in the absence, and (2) in the presence of a redox additive. (b) CV curves collected at increasing concentrations of the redox additive, tested at a scan rate of 50 mV s^{-1}. (c) The corresponding CC curves collected at a current density of 8 mA cm^{-2}. (d) Specific capacitance by area and active material mass vs. current density for an LSG/Fe_3O_4 electrode in 1.0 M Na_2SO_4 containing different concentrations (0, 0.025, 0.050, and 0.100 M) of the redox additive, measured in a three-electrode setup. (e) CV curves at 20 mV s^{-1} for an LSG/Fe_3O_4 electrode tested at different potential regions in order to assess its performance as a positive and negative electrode in a symmetric supercapacitor. (f) Areal capacitance and amount of electric charge calculated at a 10 mV s^{-1} scan rate for the negative and positive electrodes. The figure shows the results obtained in the absence and presence of 0.025 M redox additive. (G-I) The electrochemical performance of a symmetric supercapacitor made of two identical pieces of LSG/ Fe_3O_4 electrodes. (g) CV curves at a scan rate of 50 mV s^{-1}. (h) CC curves at a current density of 12 mA cm^{-2}. (i) Areal capacitance and stack capacitance (including the current collector, active material, electrolyte, and separator) as a function of

the applied current density. The results show the performance of the supercapacitor in the absence and in the presence of a 0.025 M redox additive.

With an increasing RE ion concentration, only the positive electrode's capacitance increases, while the negative electrode capacitance stays essentially the same. Therefore, the increase in the concentration of RE in the electrolyte is no longer correlated to an increase in capacitance in the two-electrode system. This occurs because under a high concentration, the positive and negative charges are not balanced and part of the positive charges are used for the decomposition of the electrolyte instead of charge storage between the negative and positive electrodes (Figure S3.9b, Supporting Information). This is also the reason for the low Coulombic efficiency at high concentrations of RE. We can conclude that in the two-electrode system, an electrolyte concentration of 0.025 M is safe to use to increase the capacitance without any decomposition of the electrolyte. Figure 3.4g, h show the CV and CC curves of the two-electrode cells before and after the addition of 0.025 M RE. Both CV and CC curves with the 0.025 M RE with the two-electrode system show ideal behavior. In Figure 3.4g, the CV curve with the RE shows that the area under the curve increases by a factor of two compared to the normal electrolyte and also shows characteristic redox peaks (at 1.1 V and 0.9 V) of the RE. The shape of the CC curves (Figure 3.4h) also follows the 1.1 V and 0.9 V redox peaks that appear in the CV curves associated with a doubling of the discharge time compared with the normal electrolyte. We also note in Figure S3.10 (Supporting Information) that this device exhibits a very distinct redox peak, even under a high scan rate (1000 mV s^{-1}) and high current density (80 mA cm^{-2}). These results imply that the RE electrolyte experiences incredibly fast electron transfer due to the unique properties of the LSG/Fe_3O_4 electrodes. We also plotted the areal capacitance and stack capacitance as a

function of the applied current density (Figure 3.4i). The stack capacitance was calculated based on the volume of the current collector, the active materials, electrolyte, and separator. The maximum stack capacitance of the 0.025 M RE reached 25.6 F cm^{-3} (716 F $g^{-1}_{electrode}$) at a scan rate of 20 mV s^{-1} and still retained 19.2 F cm^{-3} (535 F $g^{-1}_{electrode}$) at a high scan rate of 300 mV s^{-1} (Figure 3.4i). More importantly, the stack capacitance with the 0.025 M RE is about double that of a bare 1.0 M Na_2SO_4 electrolyte. This excellent capacitive behavior can be attributed to the hybrid LSG/Fe_3O_4 electrodes in which both the solid electrode and the RE work synergistically to store charge more effectively.

One of the main concerns of supercapacitors is the rate of self-dischage or how fast the cell loses charge under open circuit conditions. The self-discharge curves obtained after charging up to 1.8 V for 2 hr are shown in Figure S3.11 (Supporting Information). The voltage was measured on an open circuit as a function of time. We collected results for two different concentrations of the RE to study its effect on the self-discharge rate of the supercapacitor. Results indicate that the higher the concentration of the redox electrolyte, the faster the self-discharge rate. Specifically, capacitors with 0.025 M RE self-discharge to 1/2 V_{max} (0.9 V) in 120 h whereas 0.05 M of RE self-discharge to 0.9 V in 40 h, which is superior to a commercial Cellergy capacitor ($t_{1/2}V_{max}$=2hr).[26] In other words, the value of the leakage current is 0.00368 mA which is required to maintain the 1.8 V after holding the voltage steady for 12 hours. This superior self-discharge performance shows the promise of LSG/Fe_3O_4 supercapacitors.

3.3.1 Direct fabrication of LSG/Fe_3O_4 *interdigitated micro-supercapacitors* (MSCs)

The recent trend in miniaturized portable electronic devices has raised the demand for developing new types of miniaturized energy storage devices. It is also very important to design energy storage devices that can be easily integrated into an electronic circuit.[39, 40]

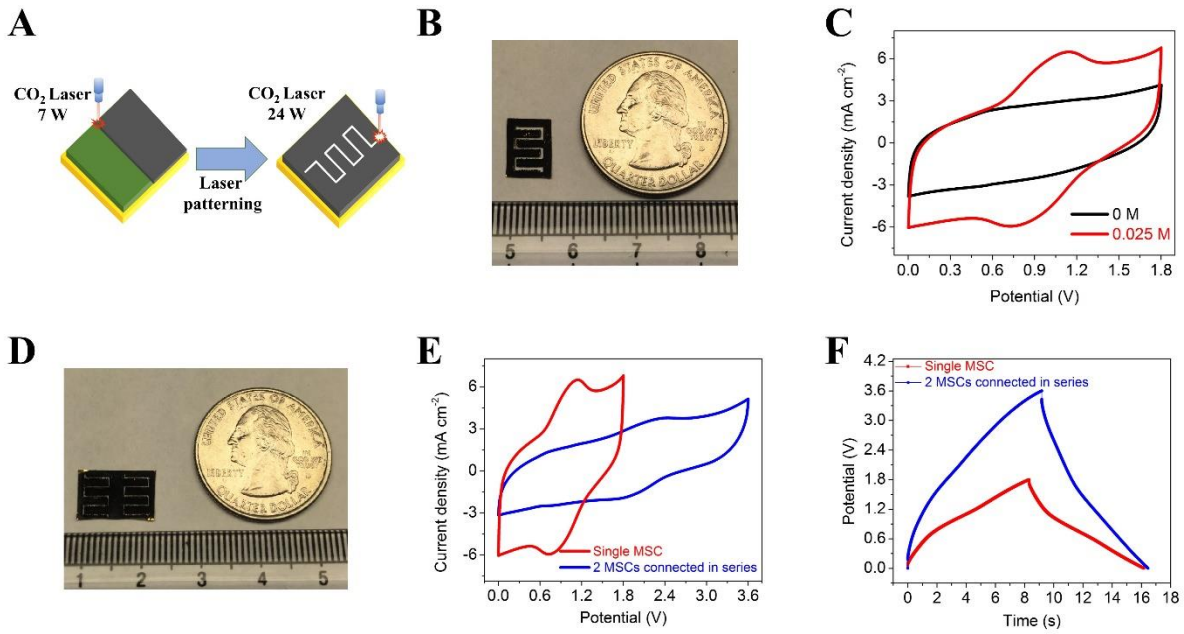

Figure 3.5. Direct laser writing of LSG/Fe_3O_4 interdigitated micro-supercapacitors both as individual cells and in modules (a) Schematic illustration showing the microfabrication process of an LSG/Fe_3O_4 hybrid micro-supercapacitor created by forming LSG/Fe_3O_4 plain electrodes via laser irradiation at low power (7 W CO_2 laser) followed by defining the interdigitated pattern by increasing the laser power to 24 W. (b) A photograph showing micro-supercapacitors obtained after the 24 W laser treatment with the interdigitated pattern. (c) Electrochemical performance of a symmetric LSG/Fe_3O_4 micro-supercapacitor tested by CV at a scan rate 100 mV s^{-1}. (d) A photograph of a micro-supercapacitor module consisting of two cells connected in series, made in a single step. (e) CV curves and (f) CC curves of two micro-supercapacitors connected in series that can extend the voltage window to 3.6 V in contrast to 1.8 V for the individual cells.

Unlike previous techniques that require multiple complex steps, the laser technique described here can be used for the direct patterning of MSCs of any shape and size within minutes. This technique is illustrated in Figure 3.5a. The LSG/Fe_3O_4 electrode film is fabricated in the same way under a 7 W CO_2 laser. Once the starting material ($FeCl_3$ + GO) has changed to the LSG/Fe_3O_4 electrode, we use a 24 W CO_2 laser to make interdigitated finger patterned electrodes. Under the high-power laser, all the active materials and current collector are etched away and work as separators. Therefore, we take advantage of this laser patterning technique to define the MSC pattern of choice. In this case, the photograph shown in Figure 3.5b features a micro-supercapacitor with three micro-electrodes for the positive side and three micro-electrodes for the negative side of the device. The pattern is well defined without any overlap or short circuits between the positive and negative micro-electrodes. These MSCs show an ideal CV rectangular shape with simply a 1.0 M Na_2SO_4 electrolyte even when operated at 1.8 V under 100 mV s^{-1} (Figure 3.5c). Adding 0.025 M of RE, very distinct characteristic redox peaks are observed. Those redox peaks also appear in the CC curves (Figure S3.12a, Supporting Information) with a 2.1 times increased capacitance when using a RE. These MSCs with 0.025 M RE show fast and reversible charge and discharge properties, as demonstrated by both variable scan rates of CV (Figure S3.12b) and variable current densities of CC curves (Figure S3.12c). Not only can this laser technique make micro-supercapacitors in one simple step, but it also enables the fabrication of several cells connected together in series and in parallel for energy modules. These MSC modules can be prepared in a facile way and are suitable for on-chip integration into electronic circuits without any further processing. Figure 3.5d shows a photograph of a tandem model with two cells connected in series whose electrochemical performance is shown in Figures 3.5e,f. As expected, the voltage of the module adds up to work at 3.6 V compared to 1.8 V for a single

cell. In Figure 3.5i, the CC curve for the tandem device shows a very low voltage drop as well, indicating an excellent performance with low internal resistance when connecting these MSCs in series. This confirms the feasibility of the MSC modules for real applications.

Furthermore, when compared to other reported iron oxide supercapacitors (Figure 3.6a), LSG/Fe_3O_4 is the only symmetric supercapacitor that works at 1.8 V in an aqueous electrolyte. The LSG/Fe_3O_4 supercapacitor-redox electrolyte (SC-RE) system can deliver a specific capacitance up to 716 F g^{-1} a value that is approximately 1.5 times higher than that of the traditional 1.0 M Na_2SO_4 electrolyte LSG/Fe_3O_4 supercapacitor cell system. These results indicate that the combination of an LSG/Fe_3O_4 electrode with a redox active electrolyte can dramatically improve both the operational voltage and the capacitance.

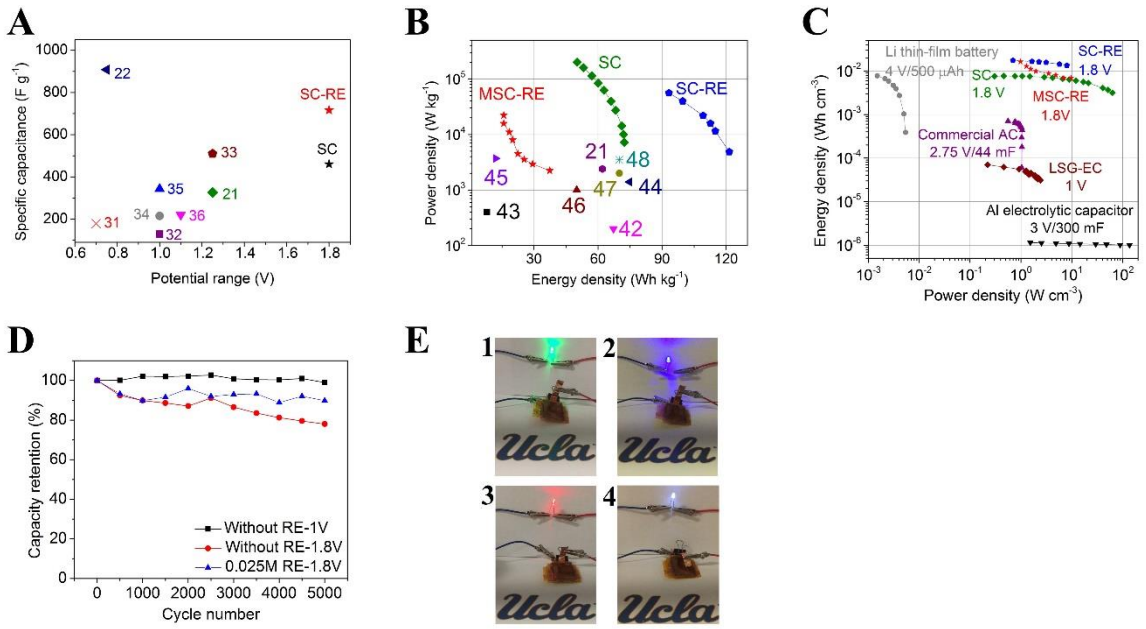

Figure 3.6. Overall performance of LSG/Fe_3O_4 based supercapacitors. (a) The potential range and specific capacitances of iron oxide based electrodes reported in literature vs. our symmetric LSG/Fe_3O_4 supercapacitors without (SC) and with a redox additive (SC-RE). [21, 22, 31-36] (b) A Ragone plot of SC, SC-RE and a micro-supercapacitor (MSC). The plot also shows results for the gravimetric energy density and power density of other iron oxide-based hybrid asymmetric supercapacitors reported in the literature.[21, 42-48] (c) A Ragone plot comparing the volumetric energy density and power density of the supercapacitors developed in this work with commercially available energy storage devices. (d) Long-term cycling stability of an LSG/Fe_3O_4 supercapacitor compared at 1.0 V and 1.8 V voltage windows, with and without a redox-additive. (e) Digital photographs demonstrating that two tandem symmetric LSG/Fe_3O_4 supercapacitors connected in series can power light emitting diodes of different colors for a long period of time: (1) green; (2) blue; (3) red; and (4) white LEDs.

A Ragone plot describing the relationship between the energy density and power density of our LSG/Fe_3O_4 based electrochemical capacitors is presented in Figure 3.6b. This plot was obtained based on the total mass of the active materials in each device. The SC-RE system can deliver energy densities up to 157.9 Wh kg^{-1}. Even at a very high power density of 55.9 kW kg^{-1}, our SC-RE exhibited an energy density of 93.2 Wh kg^{-1}. The maximum power density of this supercapacitor is 201 kW kg^{-1}, which is two-orders of magnitude higher

than previously published iron oxide hybrid supercapacitors. Since we used a RE sytem, the mass of the redox mediator was included in all calculation.

Another Ragone plot was created based on the volume of the full device that includes the active material, current collector, separator, and electrolyte. To compare our LSG/Fe_3O_4 supercapacitors with current technology, we plot data for a commercially available lithium thin film battery, a carbon based supercapacitor, and an aluminum electrolytic capacitor together in Figure. 3.6c, along with data for traditional sandwich-type and interdigitated-MSCs. The energy density of an SC-RE is 17.4 mWh cm^{-3}, which is about 15 times higher than a commercially available activated carbon electrochemical capacitor and 1.5 times higher than a lithium thin film battery. Furthermore, the SC can provide power densities up to 63 W cm^{-3}, which is 10,000 times faster than a lithium thin-film battery. Therefore, LSG/Fe_3O_4 devices in combination with a redox electrolyte could be excellent candidates for future energy storage devices.

A long cycle life is another important parameter for practical energy storage devices. The combination of a redox-electrolyte and LSG/Fe_3O_4 not only increases the capacitance, but also stabilizes the device cycle life at a high operating voltage. Figure 3.6d shows the cycle performance of the symmetric LSG/Fe_3O_4 supercapacitor with and without redox electrolyte charged and discharged at a current density of 12 mA cm^{-2} for 5000 cycles. As mentioned above, the symmetric LSG/Fe_3O_4 supercapacitor can operate at 1.8 V in aqueous 1.0 M Na_2SO_4 electrolyte. Even though the device shows excellent power and energy performance at 1.8 V, the cycle life performance was slightly degraded compared to operation at 1 V. The decrease of the capacitance is probably due to electrolyte decomposition forming gas (H_2 or O_2), and these gases in turn affect the active material

leading to detachment from the current collector. By adding 0.025 M of the RE into 1.0 M Na_2SO_4, we can see that the cycle life is improved to 90% capacity retention for 5000 cycles. In RE-SC system, the redox mediator plays a major role during charge and discharge. Without the redox mediator, the positive and negative electrodes are not charge balanced, meaning that the negative electrode will experience more degradation in cycling stability than the positive electrode, resulting in a supercapacitor with low cycling stability. However, after the redox mediator is added into the electrolyte, the positive and negative electrodes are balanced and a better cycle life is expected. From a practical point-of-view, supercapacitors are often packed in series to build up modules with operating voltages sufficient for the application. Therefore, the performance of two LSG/Fe_3O_4 supercapacitor in series was evaluated. When two LSG/Fe_3O_4 supercapacitors in series were charged for 3 min at 3.6 V, they can light up several LEDs of different colors. We found that the green (5 mm, 2.6 V, 20 mA), blue (5 mm, 3.4 V, 20 mA), red (5 mm, 1.9 V, 20 mA), and white (5 mm, 3.6 V, 20 mA) LEDs remained very bright even after 1 h of operation (Figure. 3.6e). These results demonstrate the potential of the LSG/Fe_3O_4 supercapacitors for practical applications.

3.4 Experimental

3.4.1 Synthesis of LSG/Fe_3O_4 *electrodes*

Graphene oxide was synthesized from graphite flakes using a modified Hummers method.[41] In a typical experiment, 100 mg of $FeCl_3 \cdot 6H_2O$ (Aldrich) powder was slowly added to 20 mL of a graphene oxide dispersion in water (2 mg ml^{-1}) under continuous stirring followed by sonication for 30 minutes. The homogeneous solution was drop-cast onto a gold-sputtered polyimide sheet (Astral Technology Unlimited) and dried for 12 h under ambient conditions.

The dried film was exposed to a 7 W CO_2 laser (Full Spectrum Laser H-series) to synthesize the LSG/Fe_3O_4 film. After being exposed to the laser, the LSG/Fe_3O_4 film was washed with deionized water and directly used as a supercapacitor electrode. To make the micro-structured electrode, the active material (LSG/Fe_3O_4) and the current collector were cut out of a six interdigitated-electrode pattern using a 24-W CO_2 laser (Full Spectrum Laser H-series).

3.4.2 Fabrication of a LSG/Fe_3O_4 supercapacitor and micro-supercapacitor

The electrodes were extended by connecting copper tape (3 M, US®, 0.005 Ω) and gold-sputtered polyimide as the current collector. These extended electrodes were connected to a Biologic VMP3 workstation (Biologic) for electrochemical characterization. Polyimide tape (Kapton™) was used to insulate the copper tape from exposure to the electrolyte. A symmetric LSG/Fe_3O_4 supercapacitor was constructed from two identical pieces (0.5 cm × 0.5 cm) of LSG/ Fe_3O_4 electrodes, separated by an ion-porous membrane (polypropylene separator, NKK MPF30AC100, 25 μm thick). These two electrodes and separator were then assembled using Kapton™ tape after the electrolyte (8 μL) was added. In addition, the symmetric micro-supercapacitor electrodes were extended with copper tape along the edges to improve the connection between the electrodes and the workstation. Kapton tape was used to cover the copper tape and define the micro-supercapacitor area (0.7 cm × 0.9 cm). An electrolyte was coated onto the active area of the micro-supercapacitor.

3.4.3 Assembly of all-solid-state supercapacitors

A gel electrolyte was fabricated by mixing equal amounts of Na_2SO_4 (1 g) and polyvinyl alcohol (1 g) in deionized water (10 mL) and then stirring for 1 h at 80 °C. The resulting gel electrolyte was applied to the electrodes and left for 60 min in order to ensure complete

wetting of the electrode surfaces. The two electrolyte-filled electrodes were assembled and dried for 12 h at room temperature until fully solidified.

3.4.4 Materials characterization and electrochemical measurements

Scanning electron microscopy (SEM) characterization of the LSG/Fe_3O_4 was performed using a Nova 600 SEM/FIB system. The mass of the active material was measured by a Mettler Toledo MX5 microbalance, which was found to be 382.4 μg cm^{-2}. The effective thickness of the LSG/Fe_3O_4 hybrid capacitor was 72.6 μm, including the active material, substrate (23.8 μm) and separator (25 μm). The transmission electron microscopy (TEM) images and selected electron area diffraction (SAED) patterns were collected on a Tecnai G^2 TF20 TEM (FEI Inc.) operated at 200 kV. The HRTEM and SAED data were analyzed using EMMENU4 and ImageJ software. Thermogravimetric analysis (TGA) and differential thermal analysis (DTA) were carried out on a Perkin Elmer Diamond Pyris TGA at a heating rate of 10 °C min^{-1} in air. X-ray powder diffraction (XRD) spectra were recorded on a Panalytical X'Pert Pro X-ray powder diffractometer using Cu Kα radiation with a wavelength of 0.154 nm. The electrochemical performances of the LSG/Fe_3O_4 electrodes were characterized by cyclic voltammetry (CV), galvanostatic charge-discharge (CC), and electrochemical impedance spectroscopy (EIS) measurements with various electrolytes. The LSG/Fe_3O_4 electrode tests were carried out using three-electrode cells, with a platinum plate (Aldrich) as the counter-electrode, and Ag/AgCl as the reference electrode. The LSG/Fe_3O_4 symmetric capacitors and micro-supercapacitors (two-electrode cells) were characterized using CV, CC, and EIS experiments. The EIS measurements were performed at open circuit potential with a sinusoidal signal over a frequency range from 1 MHz to 10 mHz and an amplitude of 10 mV. All electrochemical data were collected using a Biologic VMP3

electrochemical workstation equipped with a 10-A current booster (VMP3b-10, USA Science Instrument).

3.5 Conclusions

A [$Fe(CN)_6^{3-}/Fe(CN)_6^{4-}$] RE was introduced into LSG/Fe_3O_4 composite electrodes for the first time to create hybrid supercapacitors. As both electrode and electrolyte contribute to the Faradaic reaction simultaneously, an ultrahigh specific capacitance has been obtained. This represents a most promising approach to boost the specific capacitance of hybrid supercapacitors. At the same time, the cell voltage was increased to 1.8 V in an aqueous electrolyte, which produces an extremely high energy density of 121 Wh kg^{-1}, placing it among the best-performing hybrid electrochemical capacitors. Considerable enhancement of the electrochemical performance of LSG/Fe_3O_4 supercapacitors has been achieved, owing to the improved electrolyte conductivity and the feasibility of this unique new interface chemistry mechanism. Not only do these supercapacitors exhibit excellent electrochemical performances, but they represent a simple yet effective strategy for laser scribed nanocomposite synthesis. This investigation opens up a promising route to high-performance hybrid supercapacitors for energy storage applications.

3.6 Appendix to Chapter 3

Thermodynamic Analysis of LSG/Fe_3O_4 Synthesis

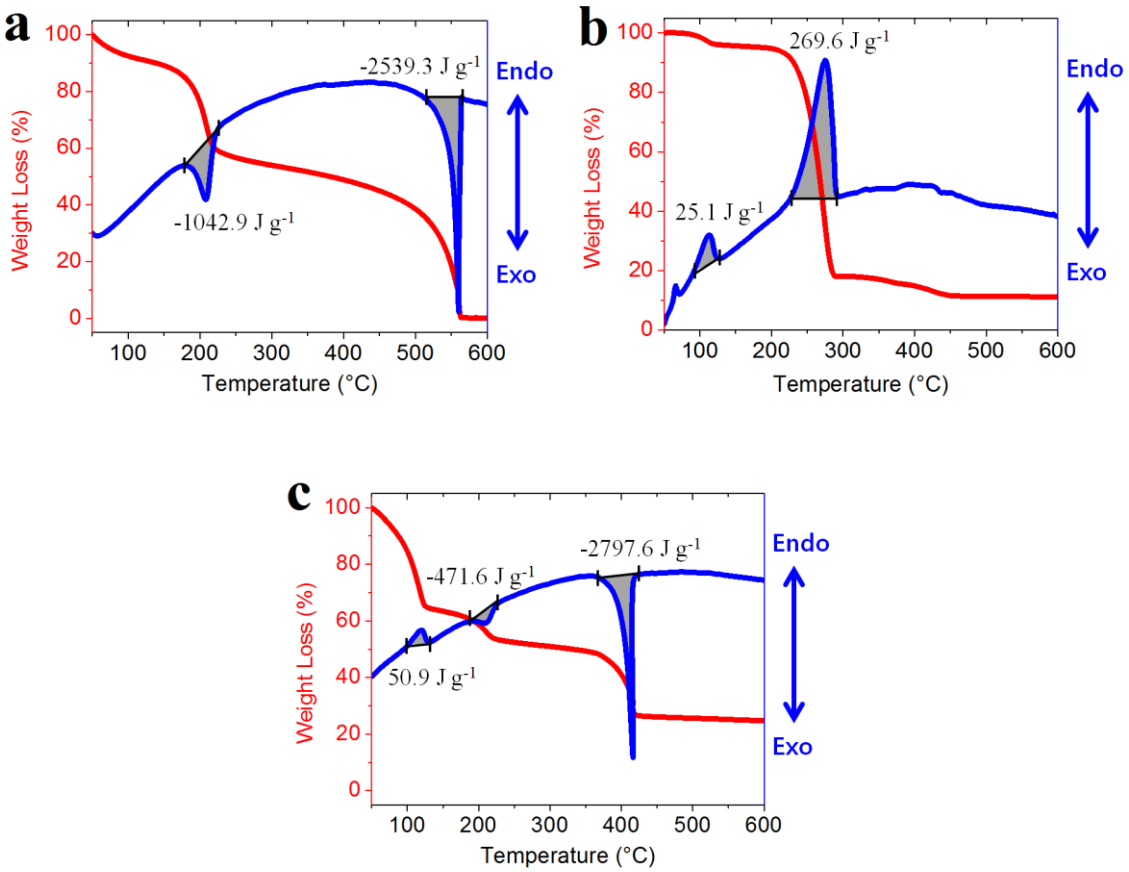

Supplementary Figure S3.1**:** Thermo-gravimetric analysis (TGA, red) and differential thermal analysis (DTA, blue) of GO, $FeCl_3$ and a GO/$FeCl_3$ composite. All measurements were performed under air. (a) The heat released during the deoxygenation of GO is -1042.9 J g^{-1} at 210 ºC and around 550 ºC the graphitic carbon oxidizes to produce CO_2 (b) The formation of iron oxide from the $FeCl_3$ requires 269.6 J g^{-1} of heat, which is much lower than the heat released during the deoxygenation. (c) The thermal induced reaction between the GO and the $FeCl_3$ mixture results in an exothermic reaction (-471.6 J g^{-1}), making the formation of LSG/Fe_3O_4 a spontaneous process, i.e. simultaneous reduction of GO to r-GO and oxidation of $FeCl_3$ to iron oxide.

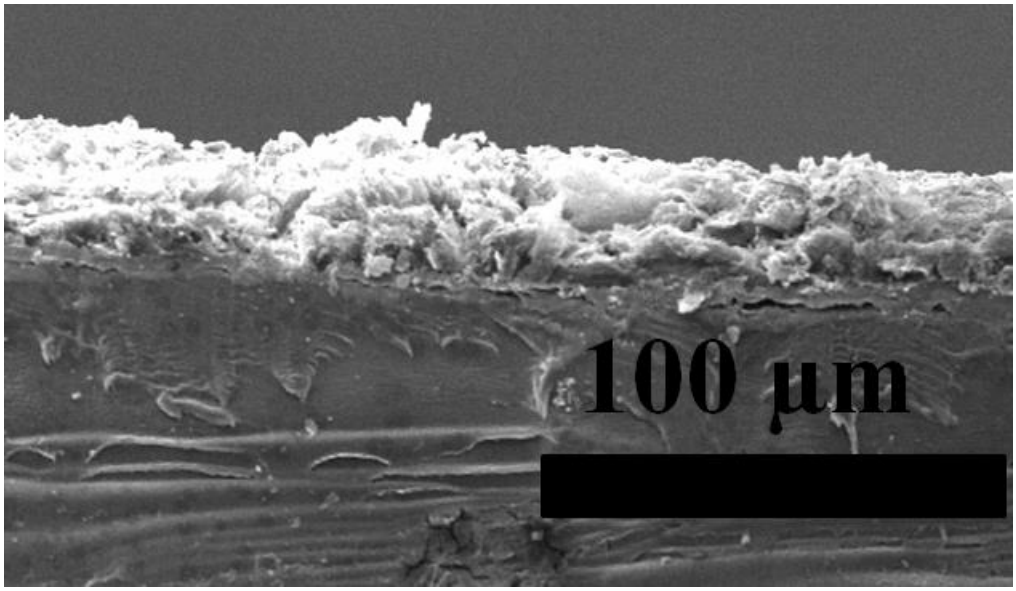

Supplementary Figure S3.2**:** A cross-sectional SEM image showing an LSG/Fe_3O_4 film on a plastic substrate. The thickness of the LSG/Fe_3O_4 film is 18.4 µm.

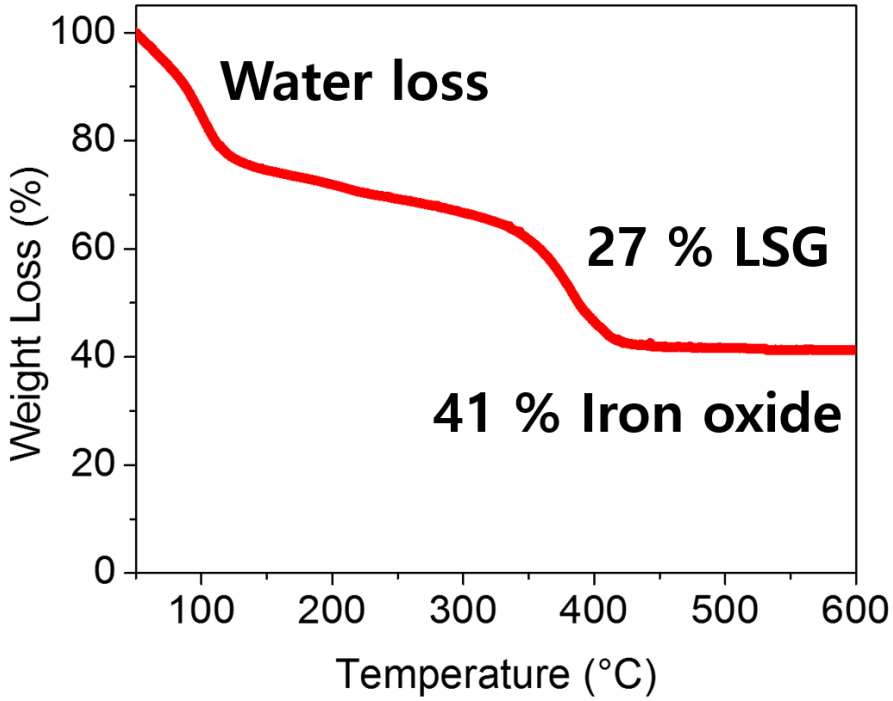

Supplementary Figure S3.3: TGA results of the LSG/Fe_3O_4 nanocomposite.

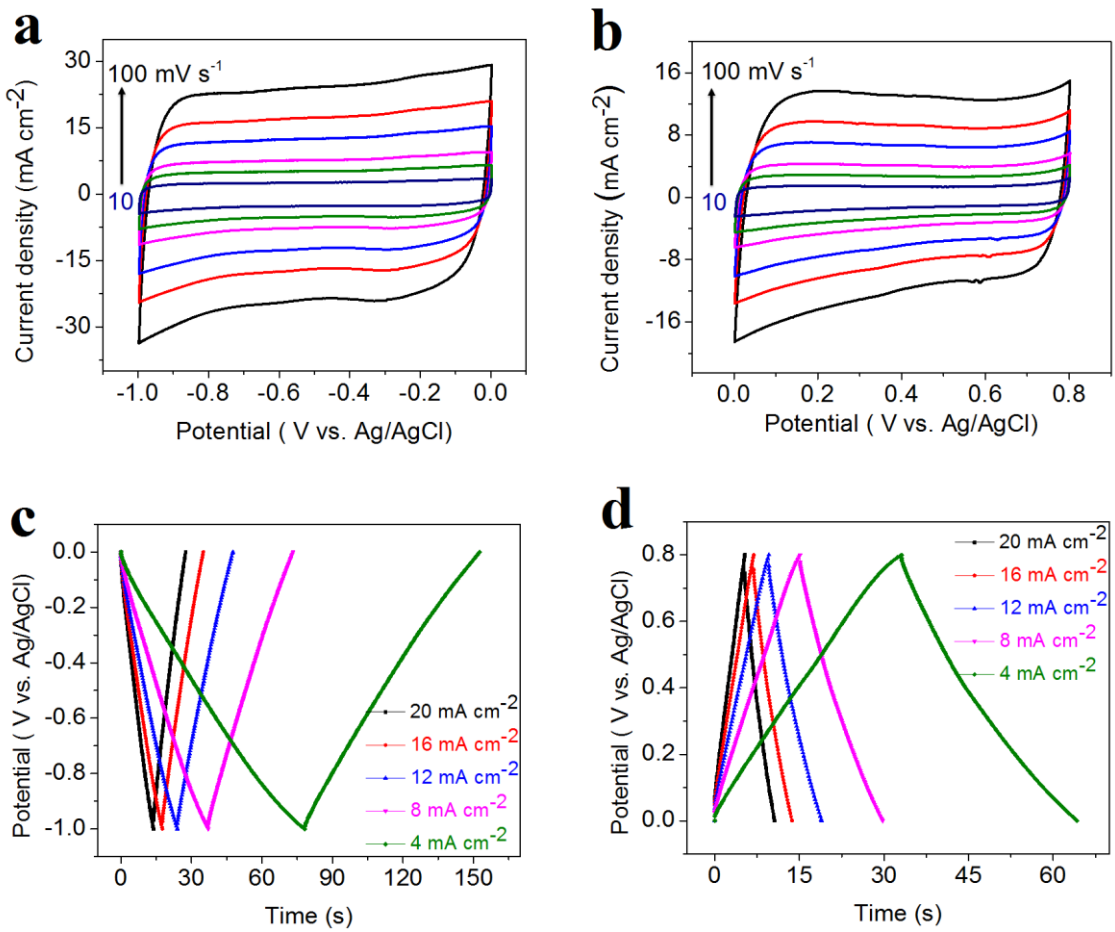

Supplementary Figure S3.4: Electrochemical performance of an LSG/Fe_3O_4 electrode in 1.0 M Na_2SO_4 measured with a three-electrode system. Cyclic voltammetry (CV) curves of (a) the negative voltage window (0 V to -1.0 V vs. Ag/AgCl) and (b) the positive voltage window (0 V to 0.8 V vs. Ag/AgCl) at different scan rates of 10, 20, 30, 50, 70 and 100 mV s^{-1}. Charge/discharge (CC) curves of (c) the negative voltage window (0 V to -1.0 V vs. Ag/AgCl), and (d) the positive voltage window (0 V to 0.8 V vs. Ag/AgCl) at different current densities.

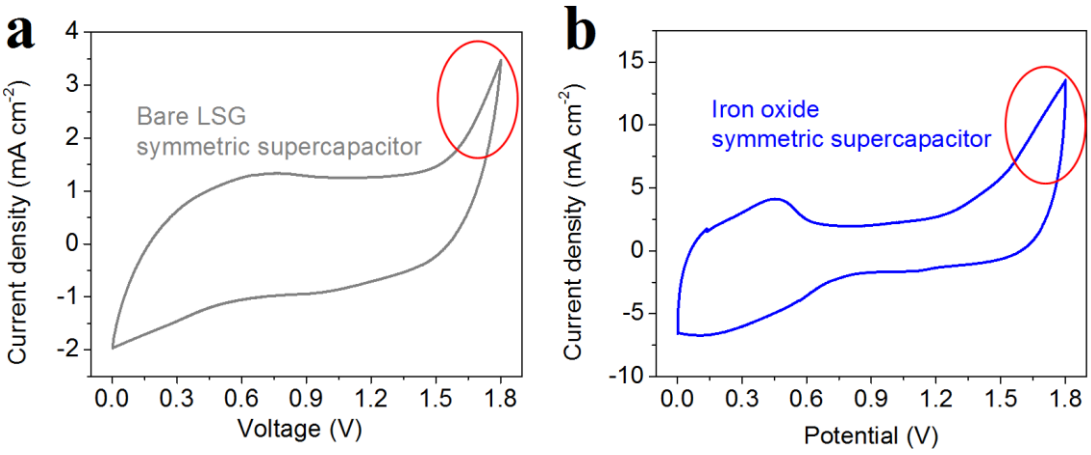

Supplementary Figure S3.5: CV curves of the symmetric (a) LSG supercapacitor and (b) Fe_3O_4 supercapacitor measured to 1.8 V with 1.0 M Na_2SO_4 aqueous electrolyte at a scan rate of 100 mV s^{-1}.

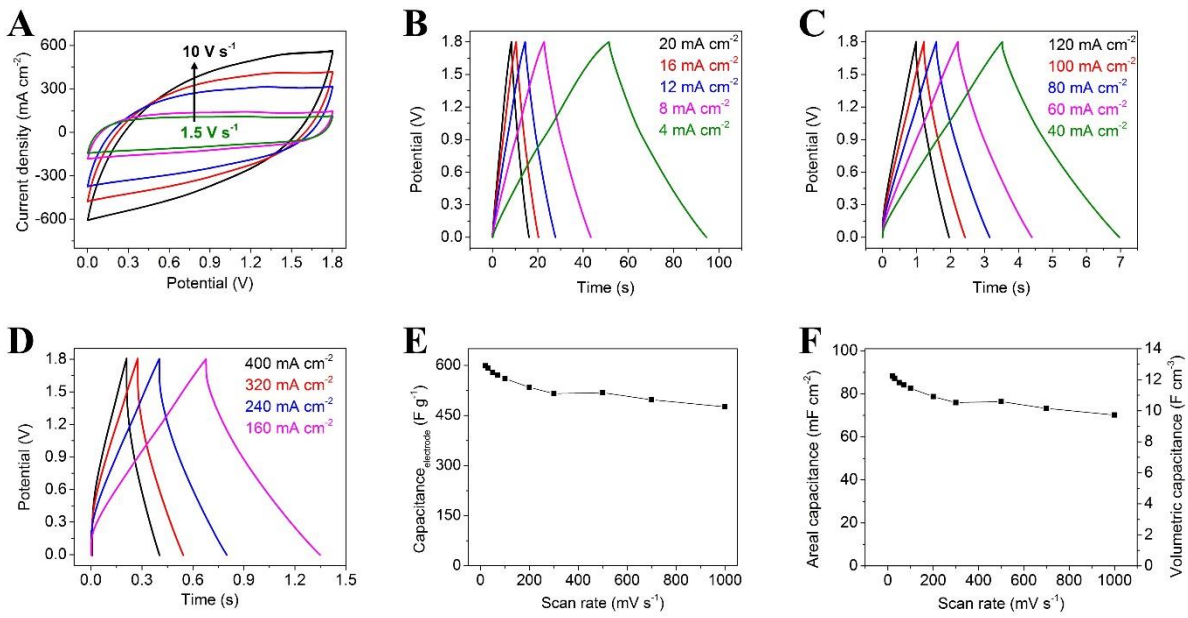

Supplementary Figure S3.6: Electrochemical performance of a symmetric LSG/Fe_3O_4 supercapacitor. (A) CV curves at different scan rates of 1.5, 2.0, 5.0, 7.0 and 10 V s^{-1}. CC curves at different current densities (B) 4, 8, 12, 16, 20, (C) 40, 60, 80, 100, 120 and (D) 160, 240, 320 and 400 mA cm^{-2}. (E) Specific capacitance of the electrode by active materials mass only, (F) specific capacitance of the full cell by areal and volume of the stack (active materials, separator and current collector) vs. Scan rate for the symmetric LSG/Fe_3O_4 supercapacitor. All values were calculated from full cell measurements.

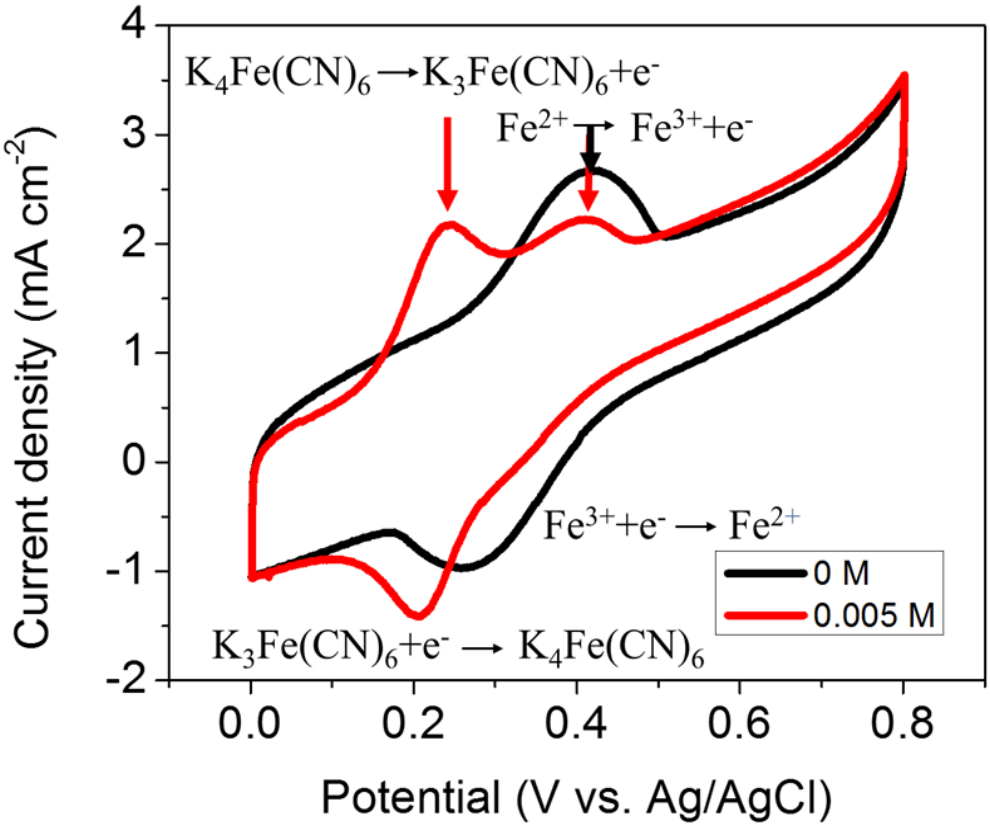

Supplementary Figure S3.7: CV curves of an LSG/Fe_3O_4 electrode measured in a three-electrode system at 5 mV s^{-1} with 1.0 M Na_2SO_4 electrolyte (black) and 1.0 M Na_2SO_4 + 0.005 M [$Fe(CN)_6^{3-}$/$Fe(CN)_6^{4-}$] redox-active electrolyte (red).

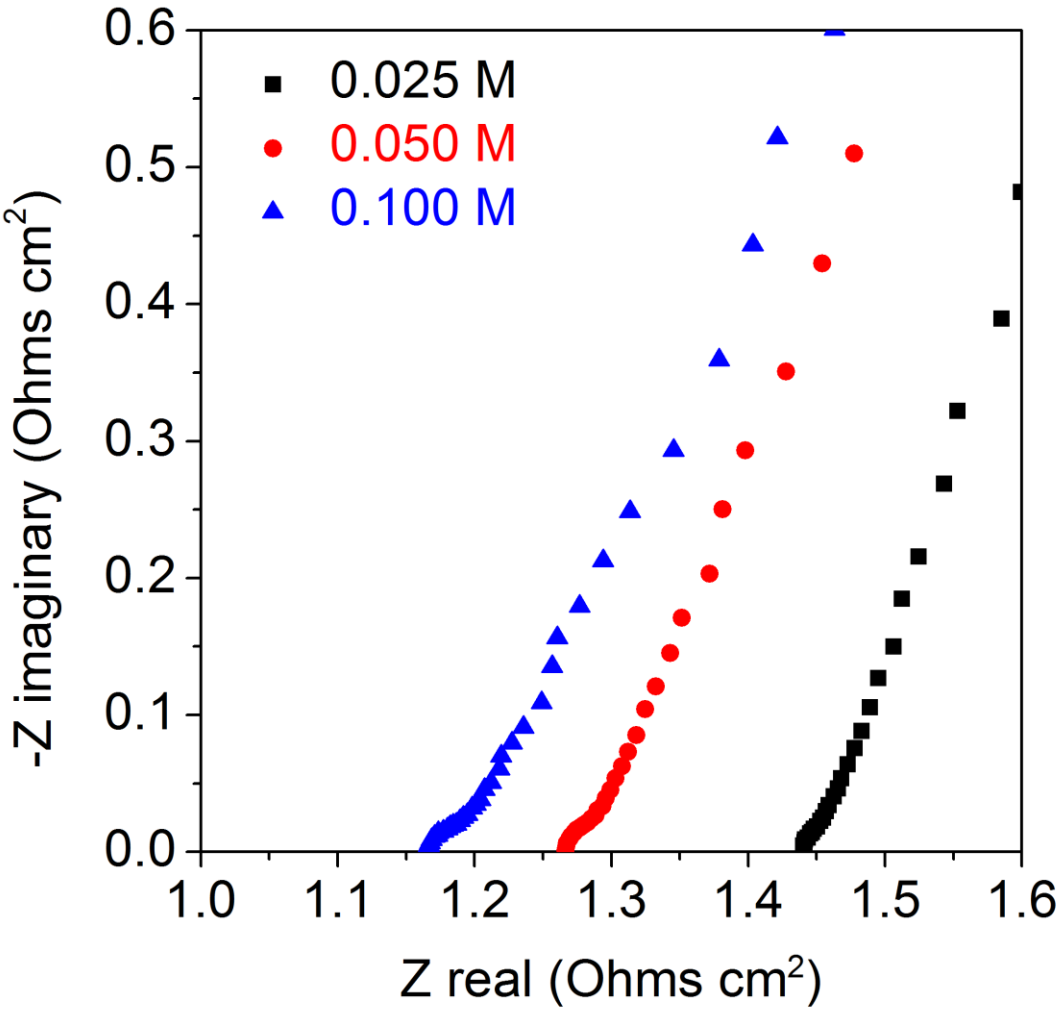

Supplementary Figure S3.8: Nyquist plot of the electrochemical impedance spectrum of the LSG/Fe_3O_4 electrode, with 0.025 M (black), 0.050 M (red) and 0.100 M (blue) of [$Fe(CN)_6^{3-}$/$Fe(CN)_6^{4-}$] redox-active electrolyte in 1.0 M Na_2SO_4 electrolyte.

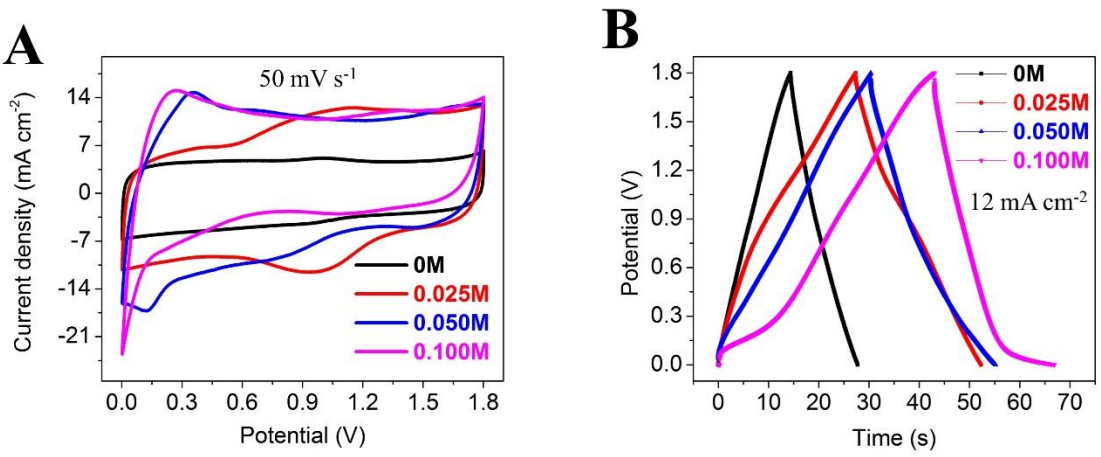

C

Concentration of $Fe(CN)_6^{3-}/Fe(CN)_6^{4-}$ (M)	Areal Capacitance (mF cm^{-2})	Coulombic Efficiency (%)
0	89.4	92.8
0.025	168.6	90.8
0.050	169.0	81.7
0.100	162.9	30.1

Supplementary Figure S3.9: (a) CV curves at 50 mV s^{-1} and (b) CC curves at 12 mA cm^{-2} of the symmetric LSG/Fe_3O_4 supercapacitor without (black) and with 0.025 M (red), 0.050 M (blue) and 0.100 M (pink) redox-active electrolyte [$Fe(CN)_6^{3-}/Fe(CN)_6^{4-}$] in 1.0 M Na_2SO_4 electrolyte. (c) The areal capacitance and Coulombic efficiency at different concentrations of redox-active electrolyte are listed. Values are calculated based on the CC results.

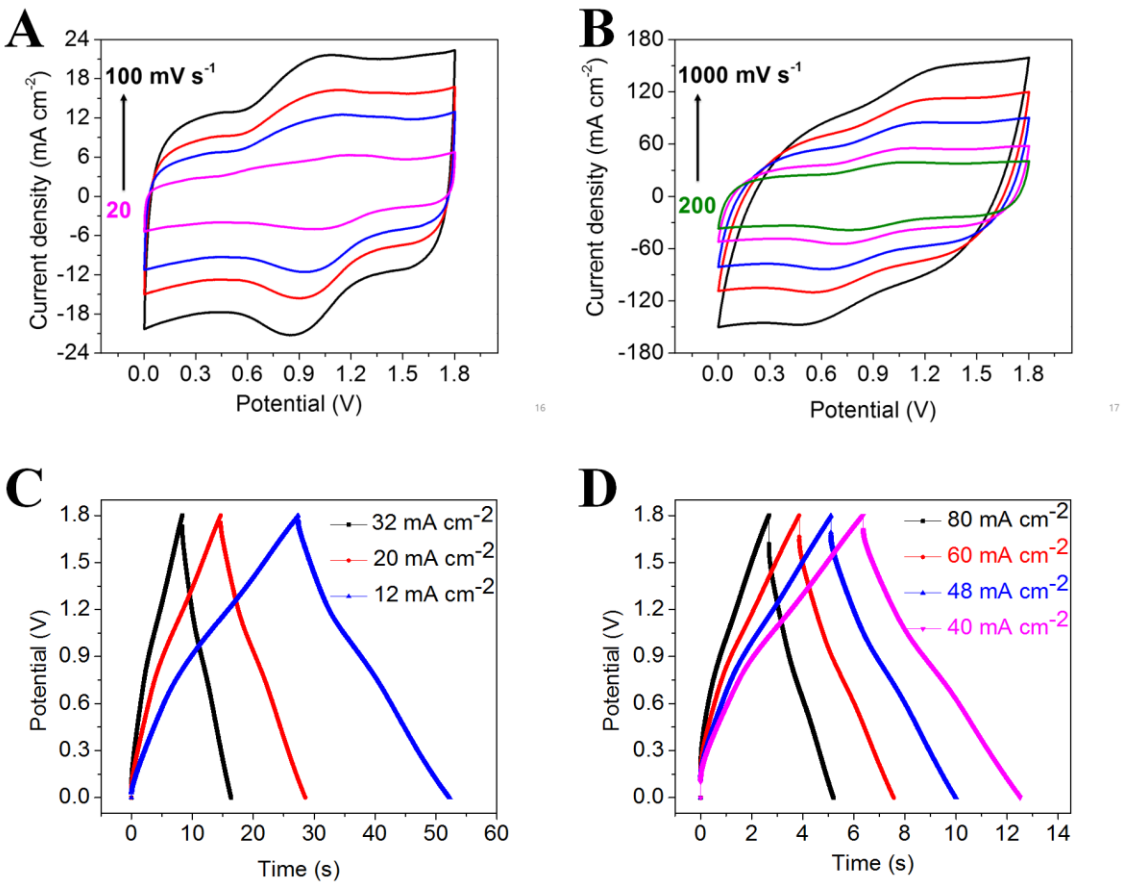

Supplementary Figure S3.10: CV curves of the symmetric LSG/Fe_3O_4 supercapacitor with 0.025 M RE at different scan rates of (a) 20, 50 70, and 100 mV s^{-1}, (b) 200, 300, 500, 700, and 1000 mV s^{-1}. CC curves at current densities of (c) 12, 20, and 32 mA cm^{-2}, (d) 40, 48, and 80 mA cm^{-2} for the symmetric LSG/Fe_3O_4 supercapacitor with 0.025 M RE.

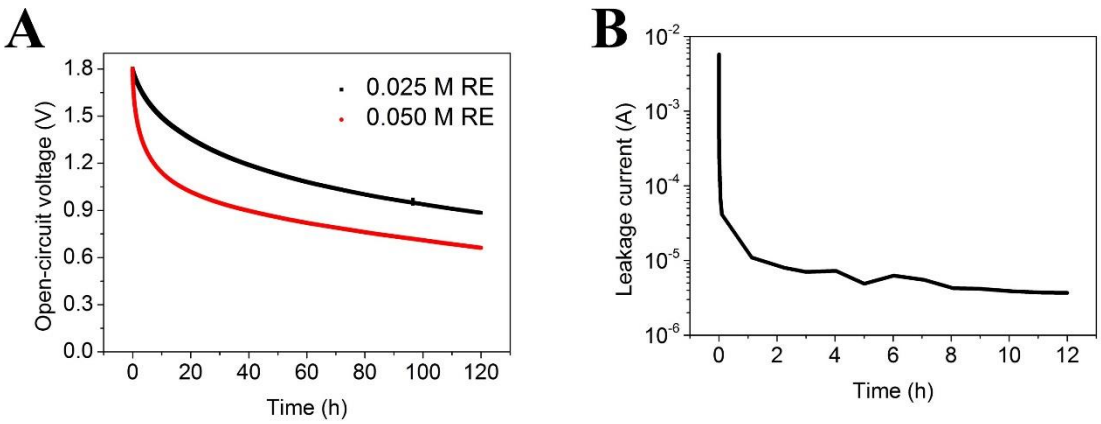

Supplementary Figure S3.11: (A) Testing the self-discharge curves of LSG/Fe_3O_4 supercapacitor with 0.025 M (black) and 0.050 M (red) redox electrolyte [$Fe(CN)_6^{3-}$/$Fe(CN)_6^{4-}$] in 1.0 M Na_2SO_4 electrolyte (B) Leakage current measurement of an LSG/Fe_3O_4 supercapacitor with 0.025 M redox electrolyte

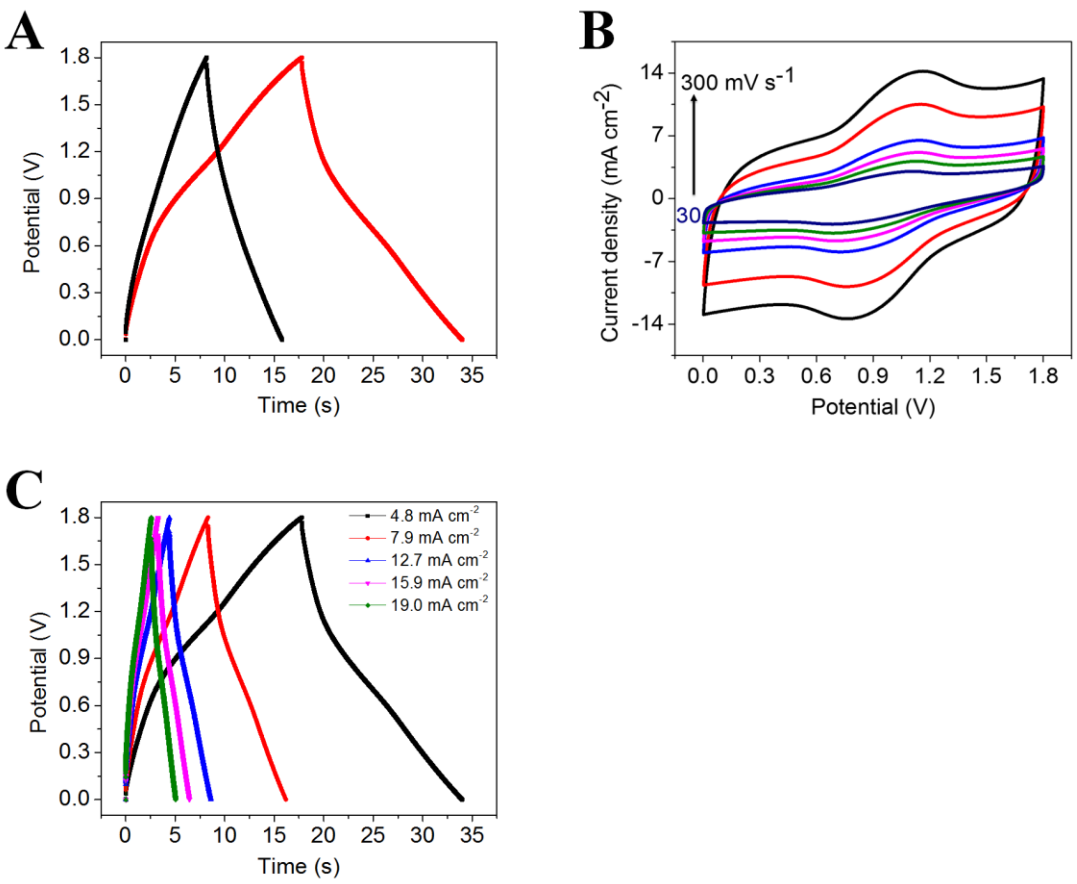

Supplementary Figure S3.12: (a) CC curves for an LSG/Fe_3O_4 micro-supercapacitor at a current density of 4.8 mA cm^{-2} with 0.025 M RE (red) and without RE (black). (b) CV curves at different scan rates and (c) CC curves at different current densities for an LSG/Fe_3O_4 micro-supercapacitor using a mixture of 1.0 M Na_2SO_4 and 0.025 M RE electrolyte.

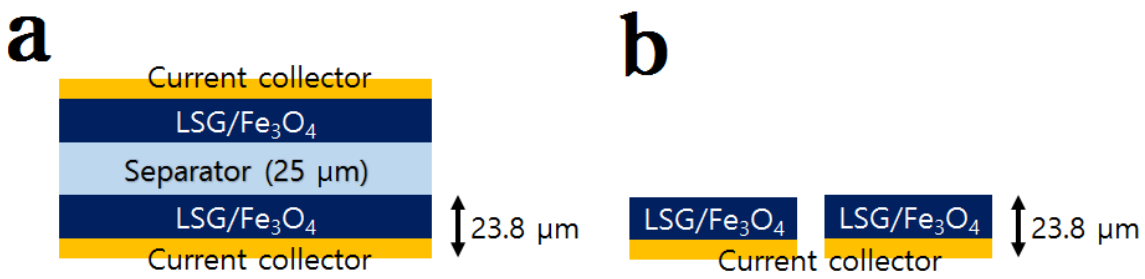

Supplementary Figure S3.13: Schematic illustrations of the cross-section of LSG/Fe_3O_4 supercapacitors with various arrangements: a) sandwich type supercapacitors, and b) interdigitated micro-supercapacitors. As can be seen, the effective thickness of the sandwich type device is 72.6 µm compared to only 23.8 µm for the planar device.

Supplementary Table S3.1 Crystallographic index of Fe_3O_4 nanoparticles

hkl	d-spacing (nm)	
	Reference	Measured*
220	0.296	0.297
311	0.253	0.253
400	0.210	0.210
422	0.171	0.171
511	0.161	0.161
440	0.148	0.148

*Obtained from the SAED pattern shown in Fig. 3.2d.

Supplementary Table S3.2: Comparison of the Performance of LSG/Fe_3O_4, 0.025 M Redox-Electrolyte LSG/Fe_3O_4 and 0.025 M Redox-Electrolyte LSG/Fe_3O_4 Micro-supercapacitors[a]

	Capacitance (20 mV s^{-1})			Energy density (20 mV s^{-1})		Power density (300 mV s^{-1})	
Device	F g^{-1}	mF cm^{-2}	F cm^{-3}	Wh kg^{-1}	Wh cm^{-3}	kW kg^{-1}	W cm^{-3}
LSG/Fe_3O_4	114	87.2	12.0	72.5	0.00765	39.6	4.18
Redox-electrolyte LSG/Fe_3O_4	178.9	186.1	25.6	121.5	0.0174	55.9	8.03
Redox-electrolyte LSG/Fe_3O_4 Mircro-supercap	151.9	62.7	26.3	37.3	0.0164	11.1	4.83

[a]A summary of the specific capacitance, energy density and power density of a symmetric LSG/Fe_3O_4 supercapacitor with 1.0 M Na_2SO_4, LSG/Fe_3O_4 supercapacitor with 0.025 M [$Fe(CN)_6^{3-}$/$Fe(CN)_6^{4-}$] in 1.0 M Na_2SO_4 and an LSG/Fe_3O_4 micro-supercapacitor with 0.025 M [$Fe(CN)_6^{3-}$/$Fe(CN)_6^{4-}$] in 1.0 M Na_2SO_4. All values reported in Table S2 are based on two electrode full cells, normalized by the two electrode active materials (LSG/Fe_3O_4) and 0.025 M redox additive. The volume is calculated based on the whole device (current collector, active materials, electrolyte and separator), no packaging.

Calculations

The capacitance of each electrode (measured in three-electrode system) was calculated from charge/discharge (CC) curves at different current densities using the formula:

$$\text{Specific C}_{\text{electrode}}\,(\text{F g}^{-1}) = \frac{2*\text{Curent(A)}*\int U(\text{Volt})\text{dt(sec)}}{U^2*Mass(g)}$$

Mass refers to the mass of LSG/Fe_3O_4 active materials while time and U voltage were obtained from the discharge curve.

The specific capacitance, energy density and power density of the full device were also were calculated based on both cyclic voltammetry (CV) profiles and Galvano static charge/discharge curves (CC).

For the CV technique, the capacitance was calculated by integrating the discharge current vs. potential plots using the following equation:

$$\text{Specific C}_{\text{device}}\,(\text{F g}^{-1}) = \frac{\int i\text{dV(A)(V)}}{\nu\left(\frac{V}{s}\right)U(V)*Mass(g)}$$

Where i is current (A), V is potential, ν is the scan rate (V/s) and U is the operating potential window. Mass refers the mass of active materials (2 electrodes of LSG/Fe_3O_4 and 0.025 M redox additive).

$$\text{Specific C}_{\text{device}}\,(\text{F cm}^{-3}) = \frac{\int i\text{dV(A)(V)}}{\nu\left(\frac{V}{s}\right)U(V)*Volume(cm^3)}$$

Volume is calculated based on the whole device (current collector, active materials, electrolyte and separator), no packaging.

The specific capacitance of the electrode was calculated from the full cell.

Specific $C_{electrode}$ (F g^{-1}) = 4*C_{device} (F g^{-1})

The specific energy density of the device was calculated through discharge curve from CC:

$$\text{Specific } E_{device} \text{ (Wh kg}^{-1}\text{)} = \frac{\text{I(A)} \int U(\text{t})\text{dt(Volt)(hr)}}{Mass(kg)}$$

$$\text{Specific Capacity (mAh g}^{-1}\text{)} = \frac{\text{E device (Wh } kg^{-1}\text{)}}{Voltage\ (V)} * \frac{1000\ (mA)}{(A)} * \frac{(kg)}{1000(g)}$$

$$\text{Specific } E_{device} \text{ (Wh cm}^{-3}\text{)} = \frac{\text{I(A)} \int U(\text{t})\text{dt(Volt)(hr)}}{volume(cm^3)}$$

Fourth, the specific power density of device was calculated:

$$\text{Specific } P_{device} \text{ (W kg}^{-1}\text{)} = \frac{\text{Energy density}(Wh/kg)}{Time(\text{hr})}$$

$$\text{Specific } P_{device} \text{ (W cm}^{-3}\text{)} = \frac{\text{Energy density}(Wh/cm^3)}{Time(\text{hr})}$$

3.7 References

(1) Simon, P.; Gogotsi, Y. *Nat. Mater.* **2008**, *7*, 845.

(2) Etacheri, V.; Marom, R.; Elazari, R.; Salitra, G.; Aurbach, D. *Energ. Environ. Sci.* **2011**, *4*, 3243.

(3) Wang, X.; Lu, X.; Liu, B.; Chen, D.; Tong, Y.; Shen, G. *Adv. Mater.* **2014**, *26*, 4763.

(4) Dunn, B.; Kamath, H.; Tarascon, J.-M. *Science* **2011**, *334*, 928.

(5) Yu, Z.; Tetard, L.; Zhai, L.; Thomas, J. *Energ. Environ. Sci.* **2015**, *8*, 702.

(6) Augustyn, V.; Simon, P.; Dunn, B. *Energ. Environ. Sci.* **2014**, *7*, 1597.

(7) Liu, X.; Pickup, P. G. *Energ. Environ. Sci.* **2008**, *1*, 494.

(8) Zhou, W.; Cao, X.; Zeng, Z.; Shi, W.; Zhu, Y.; Yan, Q.; Liu, H.; Wang, J.; Zhang, H. *Energ. Environ. Sci.* **2013**, *6*, 2216.

(9) Wang, H.; Tan, H. T.; Yi, H.; Zhang, Y.; Guo, G.; Wang, X.; Madhavi, S.; Yan, Q. *RSC Adv.* **2015**, *5*, 88191.

(10) Su, Z.; Yang, C.; Xie, B.; Lin, Z.; Zhang, Z.; Liu, J.; Li, B.; Kang, F.; Wong, C. P. *Energ. Environ. Sci.* **2014**, *7*, 2652.

(11) Meher, S. K.; Rao, G. R. *J. Phys. Chem. C*. **2011**, *115*, 1564.

(12) Nagaraju, D. H.; Wang, Q.; Beaujuge, P.; Alshareef, H. N. *J. Mater.Chem. A* **2014**, *2*, 17146.

(13) Cong, H.-P.; Ren, X.-C.; Wang, P.; Yu, S.-H. *Energ. Environ. Sci.* **2013**, *6*, 1185.

(14) Zhi, M.; Yang, F.; Meng, F.; Li, M.; Manivannan, A.; Wu, N. *ACS Sustain. Chem. Eng.* **2014**, *2*, 1592.

(15) Rangom, Y.; Tang, X.; Nazar, L. F. *ACS Nano* **2015**, *9*, 7248.

(16) Wang, L. J.; El-Kady, M. F.; Dubin, S.; Hwang, J. Y.; Shao, Y.; Marsh, K.; McVerry, B.; Kowal, M. D.; Mousavi, M. F.; Kaner, R. B. *Adv. Energ. Mater.* **2015**, *5*.

(17) Lota, G.; Fic, K.; Frackowiak, E. *Energ. Environ. Sci.* **2011**, *4*, 1592.

(18) El-Kady, M. F.; Ihns, M.; Li, M.; Hwang, J. Y.; Mousavi, M. F.; Chaney, L.; Lech, A. T.; Kaner, R. B. *Proc. Natl. Acad. Sci. U.S.A.* **2015**, *112*, 4233.

(19) Hwang, J. Y.; El-Kady, M. F.; Wang, Y.; Wang, L.; Shao, Y.; Marsh, K.; Ko, J. M.; Kaner, R. B. *Nano Energy* **2015**, *18*, 57.

(20) Reisinger, D.; Majewski, P.; Opel, M.; Alff, L.; Gross, R. *Appl. Phys. Lett.* **2004**, *85*, 4980.

(21) Qu, Q.; Yang, S.; Feng, X. *Adv. Mater.***2011**, *23*, 5574.

(22) Wang, H.; Xu, Z.; Yi, H.; Wei, H.; Guo, Z.; Wang, X. *Nano Energy* **2014**, *7*, 86.

(23) Quan, H.; Cheng, B.; Xiao, Y.; Lei, S. *Chem. Eng. J.* **2016**, *286*, 165.

(24) Akinwolemiwa, B.; Peng, C.; Chen, G. Z. *J. Electrochem. Soc.* **2015**, *162*, A5054.

(25) Roldán, S.; Granda, M.; Menéndez, R.; Santamaría, R.; Blanco, C. *J. Phys. Chem. C* **2011**, *115*, 17606.

(26) Chun, S.-E.; Evanko, B.; Wang, X.; Vonlanthen, D.; Ji, X.; Stucky, G. D.; Boettcher, S. W. *Nat. Commun.* **2015**, *6*.

(27) Roldán, S.; Granda, M.; Menéndez, R.; Santamaría, R.; Blanco, C. *Electrochim. Acta* **2012**, *83*, 241.

(28) Wu, J.; Yu, H.; Fan, L.; Luo, G.; Lin, J.; Huang, M. *J. Mater. Chem.* **2012**, *22*, 19025.

(29) Zhao, C.; Zheng, W.; Wang, X.; Zhang, H.; Cui, X.; Wang, H. *Sci. Rep.* **2013**, *3*, 2986.

(30) Su, L.-H.; Zhang, X.-G.; Mi, C.-H.; Gao, B.; Liu, Y. *Phys. Chem. Chem. Phys.* **2009**, *11*, 2195.

(31) Kulal, P. M.; Dubal, D. P.; Lokhande, C. D.; Fulari, V. J. *J. Alloys.Compd.* **2011**, *509*, 2567.

(32) Guan, D.; Gao, Z.; Yang, W.; Wang, J.; Yuan, Y.; Wang, B.; Zhang, M.; Liu, L. *Mater. Sci. Eng-B* **2013**, *178*, 736.

(33) Wu, N.-L.; Wang, S.-Y.; Han, C.-Y.; Wu, D.-S.; Shiue, L.-R. *J. Power Sources* **2003**, *113*, 173.

(34) Lee, K. K.; Deng, S.; Fan, H. M.; Mhaisalkar, S.; Tan, H. R.; Tok, E. S.; Loh, K. P.; Chin, W. S.; Sow, C. H. *Nanoscale* **2012**, *4*, 2958.

(35) Sassin, M. B.; Mansour, A. N.; Pettigrew, K. A.; Rolison, D. R.; Long, J. W. *ACS Nano* **2010**, *4*, 4505.

(36) Wang, Q.; Jiao, L.; Du, H.; Wang, Y.; Yuan, H. *J. Power Sources* **2014**, *245*, 101.

(37) Fic, K.; Lota, G.; Meller, M.; Frackowiak, E. *Energ. Environ. Sci.* **2012**, *5*, 5842.

(38) Miller, J. R.; Outlaw, R. A.; Holloway, B. C. *Science* **2010**, *329*, 1637.

(39) El-Kady, M. F.; Kaner, R. B. *Nat. Commun* **2013**, *4*, 1475.

(40) Beidaghi, M.; Gogotsi, Y. *Energ. Environ. Sci.* **2014**, *7*, 867.

(41) Hummers, W. S.; Offeman, R. E. *J. Am. Chem. Soc.* **1958**, *80*, 1339.

(42) Li, J.-J.; Liu, M.-C.; Kong, L.-B.; Wang, D.; Hu, Y.-M.; Han, W.; Kang, L. *RSC Adv.* **2015**, *5*, 41721.

(43) Brousse, T.; Bélanger, D. *Electrochem. Solid-State. Lett.* **2003**, *6*, A244.

(44) Guan, C.; Liu, J.; Wang, Y.; Mao, L.; Fan, Z.; Shen, Z.; Zhang, H.; Wang, J. *ACS Nano* **2015**, *9*, 5198.

(45) Jin, W.-H.; Cao, G.-T.; Sun, J.-Y. *J. Power Sources* **2008**, *175*, 686.

(46) Zhao, X.; Johnston, C.; Grant, P. S. *J. Mater. Chem.* **2009**, *19*, 8755.

(47) Lin, T.-W.; Dai, C.-S.; Hung, K.-C. *Sci. Rep.* **2014**, *4*, 7274.

(48) Saha, S.; Jana, M.; Khanra, P.; Samanta, P.; Koo, H.; Chandra Murmu, N.; Kuila, T. *RSC Adv.* **2016**, *6*, 1380.

Chapter 4. Next-Generation Activated Carbon Supercapacitors: A Simple Step in Electrode Processing Leads to Remarkable Gains in Energy Density

4.1 Abstract

The global electric double layer capacitor (supercapacitor) market has been growing rapidly during the past decade. Today, virtually all commercial devices use activated carbon film derived from coconut shells as the active material. This is due to its large specific surface area, low-cost and wide pore size distribution in addition to processability from a wide range of solvents. In this work, we show that laser treatment of activated carbon electrodes result in the formation of micro-channels that can connect the internal pores of activated carbon with the surrounding electrolyte. These micro-channels serve as electrolyte reservoirs that in turn shorten the ion diffusion distance and enable better interaction between the electrode surfaces and electrolyte ions. As a result, the laser treated electrodes demonstrate both higher capacitance and lower internal resistance. The capacitance can be further increased through fast and reversible redox reactions on the electrode surface using a redox active electrolyte, enabling the operation of a symmetric device at 2.0 V, much higher than the thermodynamic decompostion voltage of water (1.23 V). This simple approach can effectively alleviate the low energy density of carbon supercapacitors that has so far limited the widespread use of this technology. This work represents a clear advancement in the processing of activated carbon electrodes towards the next-generation of low-cost supercapacitors.

4.2 Introduction

The need for higher energy density storage devices has increased rapidly due to the burgeoning market for portable electronic devices.[1] Besides battery, electrochemical capacitors (ECs) have garnered a great deal of attention due to their high power density, excellent low temperature performance and essentially unlimited charge/discharge cycles. Today, virtually all ECs use activated carbon derived from coconut-shells as the active material, aluminum current collectors and tetraethylammonium tetrafluoroborate in acetonitrile as the electrolyte.[2] While these carbon supercapacitors demonstrate excellent electrochemical performance, the high cost per kWh has limited the wide-spread adoption of this technology. Compared to lithium ion batteries, supercapacitors provide energy at 10 times higher cost per kWh.[3] This not only is a major concern for capacitive energy storage, but also it prevents supercapacitors from replacing batteries in many applications. Here, we suggest two strategies for solving this problem. The first involves increasing the capacitance of carbon electrodes through a simple yet effective step in the electrode processing currently used in the manufacture of supercapacitors. The second strategy focuses on the use of redox active electrolytes, increasing capacitance and reducing cost of fabrication relative to the currently used more expensive organic electrolytes. Increasing the capacitance of carbon electrodes will reduce the cost of storing energy in supercapacitors.

Although other forms of carbon such as carbon aerogels, carbon nanotubes and graphene have been developed, activated carbon is still attractive because of its low cost and well-established electrochemical properties. In addition, activated carbons can be solution processed and thus provide an effective means for the manufacture of supercapacitors using standard industrial processes from slurry preparation, coating and drying, calendering,

slitting, welding, electrolyte filling and packaging. Here, we discovered that laser irradiation of the carbon coated electrodes results in the formation of microscale trenches that provide better means for storing electrolyte for effective charging and discharging. Laser scribed activated carbon (LSAC) can also reduce the distance over which the ions will have to move during charge and discharge processes. As a result, laser scribed carbon electrodes demonstrate both higher capacitance and lower internal resistance. This method provides an effective strategy for the design and fabrication of high-energy carbon electrodes with only one simple additive to the electrode processing techniques that are currently utilized for the industrial production of supercapacitors.

Another way for reducing the cost of carbon supercapacitors is to replace the expensive components in the current technology with inexpensive alternatives without compromising the cell performance. For example, a cost breakdown of a supercapacitor cell shows that the greatest cost driver is the organic salt used for making the electrolyte.[4] These electrolytes are generally made by dissolving tetraethylammonium tetrafluoroborate salt in acetonitrile or propylene carbonate. While this allows the operation of ECs at a relatively high voltage of 2.7 V, this electrolyte is flammable and has a fairly low ionic conductivity. Therefore, in order to reduce the cost and improve safety of carbon supercapacitors, it is imperative to replace the organic electrolyte with a less expensive and safer alternative. A good choice maybe aqueous electrolytes due to their low cost and environmentally friendly energy storage applications.[5] Because of their high ionic conductivity, aqueous electrolytes have the capability to not only increase the capacitance, but also enhance the power density of carbon-based supercapacitors. The major disadvantage of an aqueous electrolyte is the low operating voltage window dictated by the thermodynamic decomposition of water at 1.23 V.[6]

Recently, a number of aqueous supercapacitors have demonstrated higher voltages by utilizing asymmetric designs instead of conventional two symmetric carbon electrodes. This configuration takes advantage of the large hydrogen evolution overpotential of carbon negative electrodes and the large specific capacitance of metal oxide positive electrodes for extending the operating voltage window beyond the thermodynamic breakdown voltage of water. This has enabled aqueous supercapacitors that can store and deliver the charge at voltages as high as 2.0 V.[7, 8] However, this system has several drawbacks. First, the charge of the positive and negative electrodes (Q) must be balanced to ensure maximum cycling stability. Second, carbon-metal oxide composites often require complicated synthetic procedures that adds to the cost. Third, unlike traditional carbon supercapacitors which can be used for millions of cycles, asymmetric devices often suffer from stability issues resulting from the rapid degradation of metal oxide-based electrodes.

Instead of using an asymmetric design, the voltage of symmetric aqueous-based ECs can be increased by modifying the physicochemical properties of the electrolyte or surface chemistry of the electrode materials. In this way, the overpotential for hydrogen and oxygen evolution can be tuned to avoid the decomposition of water at low voltages.[6] Several examples from the recent literature demonstrate the feasibility of this approach. For instance, Boettcher, Stucky and co-workers discovered a unique redox electrolyte based on methyl viologen that not only increases the voltage window of an activated carbon supercapacitor, but also its specific capacitance.[9] This system, however, is limited to 1.4 V, so that further improvements are still needed. Fic and co-workers extended the voltage of symmetric carbon supercapacitors up to 2.2 V, using a 1.0 M Li_2SO_4 aqueous electrolyte.[10] However, such an impressive voltage was obtained using expensive gold current collectors, whereas practical

systems use aluminum in which parasitic and corrosion reactions are difficult to avoid. Besides, this set-up can only store charge in electric double layers, whose limited specific capacitance is the reason behind the low energy density of carbon-based supercapacitors.

Herein, we demonstrate that laser scribing of standard activated carbon electrodes results in the formation of macroporous electrodes, allowing for a new generation of carbon supercapacitors with improved power density. Furthermore, the introduction of a 0.1 M ferricyanide/ferrocyanide redox couple into the electrolyte enables supercapacitors with an 8-fold increase in capacitance compared with a control supercapacitor without the redox electrolyte. In addition, the redox electrolyte enables the operation of the supercapacitor at an enhanced voltage of 2.0 V. We also note that the micro-channels formed in the electrode can facilitate charge transport and enable charge storage at high rates. The combination of this unique architecture with a redox electrolyte leads to synergetic effects and produces high areal capacitance (up to 379 mF cm^{-2}), specific power (up to 5.26 W cm^{-3}), specific energy (up to 9.05 mWh cm^{-3}) and low ESR (0.9 Ω). Note that these supercapacitor cells can be assembled in air without using any special dry rooms or glove boxes. In addition, the laser irradiation was performed using standard laser cutting tools that are widely utilized in industry. [11, 12] This unprecedented performance was achieved with industrial grade active materials, current collectors and separators and may, thus, have potential for real-world applications.

4.3 Results and Discussion

4.3.1 Fabrication of laser scribed activated carbon (LSAC) electrodes

Today, activated carbons are the most popular materials used for the manufacturing of supercapacitors due to their high surface area (up to 3033 $m^2 g^{-1}$),[13] low cost and high packing density (0.5-0.8 g/cm^3). However, activated carbons contain some micrometer size particles with complex porosity that leads to slow ion diffusion and low power density. Additionally, most of the surface area resides within small micropores that are inaccessible to the electrolyte ions, leading to significant dead mass and low specific capacitance. To overcome these problems, researchers have suggested graphene as an alternative electrode material because of its outstanding surface area that is readily accessible to the electrolyte ions. Graphene electrodes with very high gravimetric capacitance (~300 F g^{-1}) have already been demonstrated, but low packing density values (~0.1 g cm^{-3}) have limited the performance of these devices when considering the mass of a fully packaged cell.[14] There have been some efforts made to increase the packing density of garphene electrodes,[15] however, this approach is very challenging because of the tendency of graphene sheets to restack. This suggests that low packing density materials like graphene and other forms of nanocarbons may not be sufficient for commercial applications. Therefore, here we undertake a unique approach to improve the power density of activated carbon while keeping the high electrode packing density needed for practical devices.

High packing density (0.60 g cm^{-3}) activated carbon electrodes were fabricated on carbon coated aluminum current collectors using a standard doctor blade coating technique. Exposure of the electrodes to a CO_2 laser results in the formation of microscale size trenches

as illustrated in Figure 4.1A. Figures 1B and C show obvious changes to the microstructure of the electrode before and after laser irradiation. Zooming in on the laser treated electrode reveals its macroporous nature, Figure 4.1D. These results are further confirmed from optical microscopy indicating the appearance of macropores in the structure of the electrode following laser irradiation, Fig. S4.1. Similar results were obtained when processing the electrodes from an organic system with a PVDF binder and an aqueous system with a CMC/SBR binder.

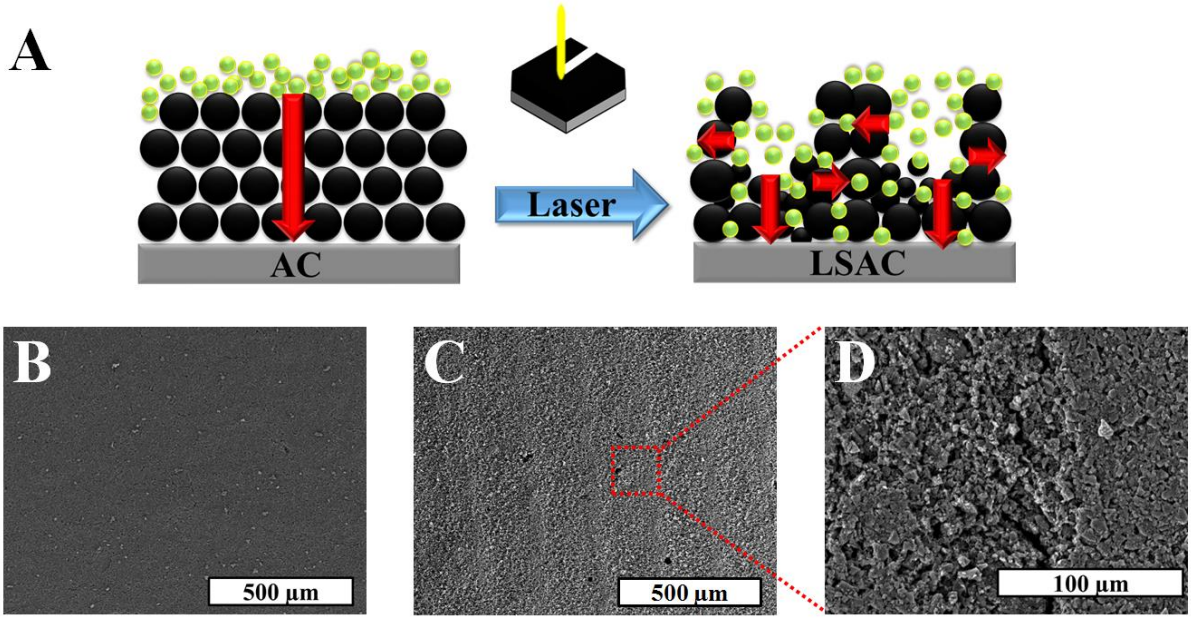

Figure 4.1. Design, structure and characterization of the laser scribed activated carbon (LSAC) electrodes. (A) Schematic illustration showing the fabrication process of laser scribed activated carbon (LSAC) electrodes. The laser treated electrodes contain trenches that serve as electrolyte reservoirs, enabling better interaction between the electrolyte ions and the electrode surfaces. (B) An overview SEM image showing activated carbon before exposure to the laser. (C) SEM image showing an activated carbon electrode after exposure to 7-W laser. (D) A magnified view illustrating the macroporous structure created by laser etching of the activated carbon.

This unique electrode architecture makes a high surface area and porous structure, allowing the electrolyte to interact with the entire surface of the activated materials. In addition, microscale trenches allow for the rapid transport of ions and provide ionic connections between the interior pores of the activated carbon particles and the external electrolyte. These trenches can also reduce the distance over which the ions must move during charge and discharge processes. An additional advantage of this technique is that the electrode maintains its high packing density after laser irradiation (0.54 g cm^{-3}). Therefore, the laser irradiation technique demonstrated in this work enables the direct fabrication of high power/high energy density activated carbon electrodes without compromising their outstanding volumetric performance. In addition, the microscale trenches may help alleviate the stress and strain between particles during charge and dishcarge and leading to improved cycling stability of the supercapacitor.

4.3.2 Electrochemical properties of LSAC electrodes in traditional acetonitrile electrolyte

We investigated the electrochemical properties of the laser scribed activated carbon (LSAC) electrodes in CR2032 coin cell devices using 1.0 M tetraethylammonium tetrafluoroborate ($TEABF_4$) in acetonitrile as the electrolyte. Fig. 4.2A shows the cyclic voltammetry (CV) of the electrode before and after laser irradiation. In comparison with a non-scribed electrode, the LSAC shows an enhanced capacitance with a nearly textbook rectangular CV curve at 50 mV s^{-1}, suggesting a nearly textbook electric double layer capacitance behavior. This nearly textbook rectangular CV shape of the LSAC supercapacitor is retained even when tested at high scan rates up to 300 mV s^{-1} (Fig. 4.2B). In addition, Fig 4.2C shows nearly textbook triangular charge/discharge (CC) curves that can be maintained

with a very small IR drop at increasing current densities. Based on these measurements, we calculated the areal capacitances (Fig. 4.2D) and gravimetric capacitances (Fig. 4.2E) of the electrode at different current densities. Although some active materials were lost during the laser scribing of the microscale trenches, LSAC shows improved capacitance on both a high gravimetric and an areal basis. In addition, LSAC exhibits excellent rate capability with high capacitance retention up to a current density of 25 A g^{-1} at which point the LSAC electrode delivers a 6 times larger capacitance compared to the non-scribed electrode.

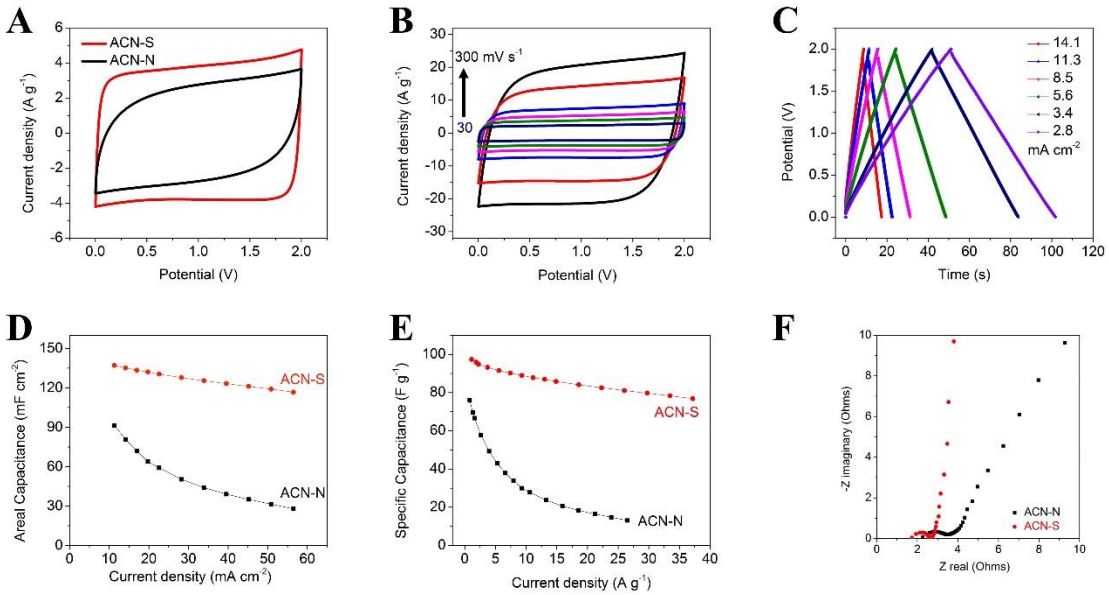

Figure 4.2. Evaluation of the electrochemical performance of laser scribed activated carbon (LSAC) supercapacitors in a traditional 1.0 M tetraethylammonium tetrafluoroborate ($TEABF_4$) in acetonitrile (ACN) electrolyte. (A) Cyclic voltammetry (CV) curves of supercapacitors before (black) and after (red) laser treatment, obtained at a scan rate of 50 mV s^{-1}. (B) CV profiles of an LSAC supercapacitor at different scan rates of 30, 50, 70, 100, 200, and 300 mV s^{-1}. (C) Charge/discharge (CC) curves at different current densities of 1.7, 2.8, 3.4, 5.6, 8.5, 11.3, 14.1 and 16.9 mA cm^{-2}. (D) The areal capacitance retention and (E) gravimetric capacitance retention before (black) and after (red) laser treatment as a function of the applied current density. All the values were measure from the full cell and calculated based on the electrode. (F) Nyquist plots of the LSAC supercapacitor (red) and non-scribed (black) supercapacitor over a frequency range of 1.0 MHz to 0.1 Hz.

Excellent rate capability of LSAC electrodes was further verified from electrochemical impedance measurements. The results indicate that the LSAC electrode show lower equivalent series resistance (ESR) as small as 1.66 Ω, as obtained from the intercept of the Nyquist plot (Fig. 4.2F) on the real axis. In addition, the Nyquist plot of the LSAC electrode is nearly a straight vertical line in the low frequency region, indicating essentially ideal capacitive behavior. These results imply low charge transfer resistance at the electrode/electrolyte interface and suggest rapid electron and ion transport within the LSAC electrode. This can be ascribed to the large macroporous surfaces of the electrode that are easily accessible to the electrolyte ions.

4.3.3 Role of the redox active electrolyte (RE)

While traditional supercapacitors consist of activated carbons as the only electrochemically active material in the cell, redox supercapacitors have now shifted this paradigm. In addition to the active electrode material, more charge can be added by using redox active electrolytes and may, thus, increase the overall capacitance of the cell. For example, Wu *et al.* [16] reported an increase in capacitance of about 4 times by adding p-phenylenediamine (PPD) into a KOH electrolyte; however, this system runs at 1.0 V necessitating further improvements for real world applications. Similarly, Mai *et al.*[17] added cupric chloride ($CuCl_2$) into a HNO_3 electrolyte to increase the capacitance from 440 F g^{-1} to 4700 F g^{-1}. However, such an impressive value was measured in a three-electrode system using a very limited voltage window (-0.1 V to 0.4 V). Integration of this electrode into an asymmetric cell (1.35 V) is associated with a huge reduction of the capacitance down to 294 F g^{-1}, likely because of the charge imbalance between the positive and negative electrodes. Here, we propose a ferricyanide/ferrocyanide electrolyte, which adds more capacitance to the

cell while at the same time enabling the operation of the cell at a high voltage of up to 2.0 V in an aqueous electrolyte. Unlike most aqueous supercapacitors that use precious metal current collectors (gold, platinum, etc.), this redox supercapacitor employs aluminum current collectors which are widely used today in the manufacturing of supercapacitors and lithium ion batteries.

Aluminum is the preferred current collector in industry because of its high conductivity, light weight and low cost. In addition, it has excellent electrochemical stability in organic electrolytes, but often experiences corrosion in aqueous systems. To confirm that aluminum current collectors are safe to use in our redox electrolyte system, we first built a supercapacitor coin cell consisting of activated carbon electrodes coated on Al using an aqueous 1.0 M Na_2SO_4 electrolyte without any redox additives. Electrochemical testing acquired in this system (Fig S4.2) shows rapidly changing CV profiles associated with an increase of the ESR after each cycle, which suggests that corrosion of aluminum occurs in the 1.0 M Na_2SO_4. However, surprisingly after we introduce the [$Fe(CN)_6^{3-}$/$Fe(CN)_6^{4-}$] Redox electrolyte (RE) into 1.0 M Na_2SO_4, the electrochemical performance is very stable even at the higher voltage of 2.0 V. A possible explanation is that [$Fe(CN)_6^{3-}$/$Fe(CN)_6^{4-}$] works as a solution buffer and maintains a neutral pH (7.1) while charging and discharging. Note that 1.0 M Na_2SO_4 has a pH of 6. It is also possible that the redox additive acts as a sacrificial anode and thus protects Al from corrosion.

Figure 4.3 shows the electrochemical performance of coin cell supercapacitors containing activated carbon tested at different concentration of the redox additive in 1.0 M Na_2SO_4, denoted as *x* M RE, where *x* is the molar concentration of the additive. Fig 4.3a present CV profiles collected with 0.1 M RE at an increasing voltage window from 1 V to 2 V with an interval of 0.2 V and a scan rate 50 mV s^{-1}. The CV profiles show no significant

increase in the current especially in the high voltage end, which signifies that there is no decomposition of the electrolyte and suggests that 2.0 V can be safely applied for a supercapacitor operating in this electrolyte. It was reported that both Na^+ and SO_4^{2-} ions have strong solvation energy which stems from the fact that sulfate ions can be surrounded by 12-16 molecules of water.[10] Therefore, it is possible to assume that the energy that causes the decomposition of water in traditional aqueous electrolytes is now used to break the bonds in the solvation shell of Na^+ and SO_4^{2-} ions or even to drive redox reactions of the redox electrolyte. Therefore, we believe that the combination of the ferrocyanide/ferricyanide redox couple with an electrolyte possessing high solvation energy is the reason behind the electrochemical stability of the supercapacitor even when tested at 2.0 V where water molecules would normally decompose.

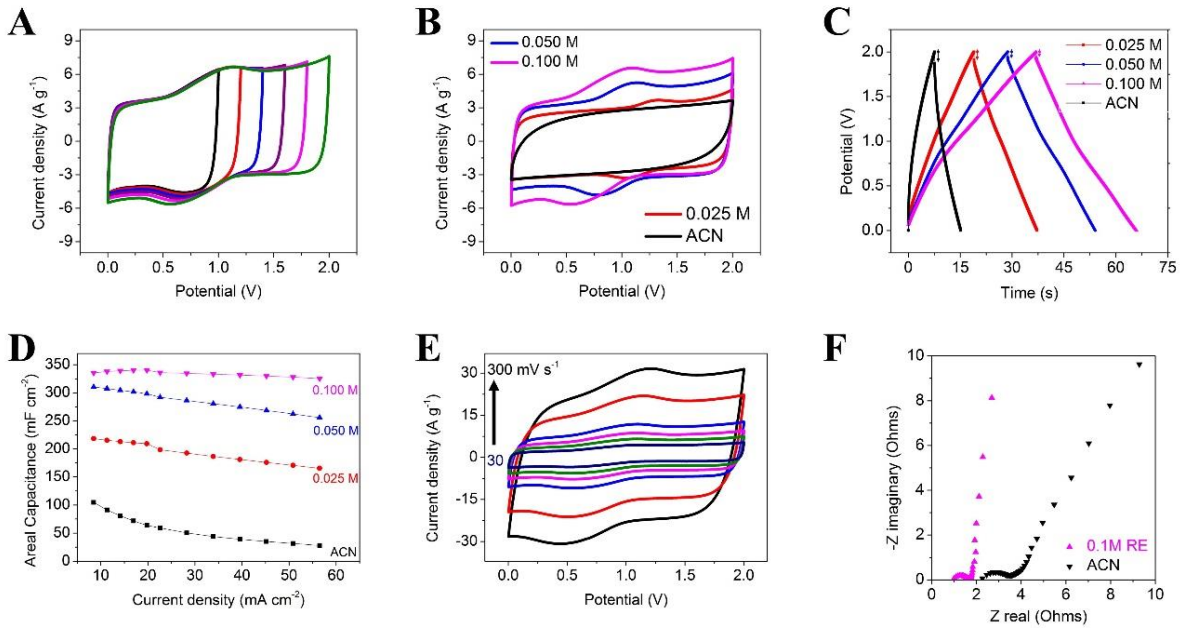

Figure 4.3. Electrochemical performance of a high voltage supercapacitor (SC) in a $[Fe(CN)_6^{3-}/Fe(CN)_6^{4-}]$ redox-active aqueous electrolyte (RE). (A) CV curves of the supercapacitor at an increasing voltage window from 1.0 V to 2.0 V in 0.1 M RE at 50 mV s^{-1}. (B) CV curves collected at increasing concentrations of the redox additive, tested at a scan rate of 50 mV s^{-1}, (C) the corresponding CC curves collected at a current density of 11.3 mA

cm^{-2}, (D) specific capacitance by area vs. current density for an activated carbon electrode in a 1.0 M Na_2SO_4 electrolyte containing different concentrations (0, 0.025, 0.050, and 0.100 M) of the redox additive. (E) CV profiles of 0.1M RE-SC at different scan rates of 30, 50, 70, 100, 200, and 300 mV s^{-1}. (F) Nyquist plots of the 0.1 M RE aqueous electrolyte and 1.0 M $TEABF_4$ in acetonitrile supercapacitors over a frequency range of 1.0 MHz to 0.1 Hz. All the electrochemical experiments were measured in a CR2032 coin cell.

Moreover, Fig 4.3A shows a reversible redox couple (between 0.6 V and 1.1 V) which can be attributed to the redox additive. This reaction is described in the following equation:

$$Fe(CN)_6^{4-} \leftrightarrow Fe(CN)_6^{3-} + e^-$$

At the positive electrode, the electrolyte undergoes an oxidation process from $Fe(CN)_6^{4-}$ to $Fe(CN)_6^{3-}$ during charging, i.e. Fe^{2+} going to Fe^{3+}, conversely at the negative electrode, the discharge process induces reduction from $Fe(CN)_6^{3-}$ to $Fe(CN)_6^{4-}$, i.e. Fe^{3+} going to Fe^{2+}.

We also studied the performance of the supercapacitor at various concentrations of RE, namely 0.025 M, 0.05 M, and 0.1 M and the results are presented in Figs. 4.3B and C, where the results of a traditional acetonitrile-based electrolyte is provided for comparison. With increasing concentration of RE ions, the area under the CV curves (Fig. 4.3B) and discharge time of the CC curves (Fig. 4.3C) increase, indicating that the specific capacitance increases. By increasing the concentration to 0.2 M, the cell exhibited a 1.2 times increase in capacitance compared to 0.1 M but the coulombic efficiency dropped to 58 % (Fig. S4.3). The high leakage current at this high concentration causes the device to take a longer time to reach 2.0 V during charging. Based on these results, the 0.1 M RE system was down selected for further optimization of the overall supercapacitor performance. Not only does the 0.1 M RE system show the highest capacitance, but also it exhibits the best rate capability. Fig. 4.3D shows the areal capacitance values extracted from the CC curves obtained at various

current densities in the different electrolytes. The 0.1 M RE system shows an ultrahigh areal capacitance of 335 mF cm^{-2} at 8.5 mA cm^{-2} and still retained 325.2 mF cm^{-2} at a higher current density of 56.5 mA cm^{-2}; this is 11.6 times larger than a standard activated carbon system with 1.0 M $TEABF_4$ in ACN electrolyte (Fig. 4.3D). Note in Fig 3E that the 0.1M RE device maintains a nearly ideal CV shape with increasing scan rate up to 300 mV s^{-1}. More importantly, the curves show distinct and reversible redox peaks at all scan rates, indicating rapid charge transfer between the electrodes and the redox electrolyte. In addition, this redox supercapacitor continues to provide high discharge currents with small IR drops (Fig S 4.4 (a, b)). These results imply that the 0.1 M RE electrolyte promotes rapid electron transfer and improved rate capability. This fast electron transfer was further confirmed by a Nyquist plot (Fig 4.2E), in the 0.1 M RE-SC system, where the ESR is much lower (1.61 Ω) than in an ACN electrolyte (3.52 Ω). One can conclude that the addition of the RE electrolyte brings about the following advantages: (1) It acts as a solution buffer to maintain neutral pH, allowing the operation of this electrolyte with widely used aluminum current collectors. (2) It extends the operating voltage window up to 2 V in an aqueous electrolyte and effectively increases the energy density. (3) It increases the areal capacitance of the device through fast and reversible Faradaic reactions. (4) It enables fast electron transfer and increased ion conductivity, allowing for higher rate capability and (5) It produces a low ESR.

4.3.4 Synergetic effects from combining laser scribed activated carbon with a redox-active electrolyte

Combining a macro patterned LSAC electrode with ferricyanide/ferrocyanide redox electrolyte produces a synergistic enhancement of the electrochemical performance. The macroporous structure of LSAC allows easy access of the RE ions to the surface of the

activated carbon particles and enables fast and reversible redox reactions as well as rapid absorption and desorption as illustrated in Fig. 4.4A. Therefore, the combination of a 0.1 M RE electrolyte with the LSAC electrodes is expected to not only boost the energy and power density, but also stabilize the cycle life allowing the operation of the device at a high voltage up to 2.0 V. Note that the 0.1 M RE system exhibits an essentially ideal CV profile with a rectangular shape and distinct redox peaks, whereas the ACN electrolyte system only shows EDLC properties as expected (Fig. 4.4B). Furthermore, compared with the 0.1 M RE with non-scribed activated electrodes, the 0.1 M RE-LSAC system shows about a 30% increase in the area of the CV. This suggests that the combination of LSAC electrode with RE can enhance the capacitance through the porous architecture of the electrode, allowing for better exposure of the active materials to the RE ions. Again, both CV and CC curves were collected with an increasing voltage window up to 2 V, tested at a scan rate of 50 mV s^{-1} for CV curves and a current density of 11.3 mA cm^{-2} for CC curves (Fig. S4.5a, b). This new hybrid (0.1 M RE-LSAC) system was also tested over a wide range of scan rates from 30 to 1000 mV s^{-1} (Fig. 4.4C and Fig. S4.5C) and current densities 8.5 to 56.5 mA cm^{-2} (Fig. 4.4D and Fig. S4.5D). This hybrid system shows very clear redox peaks up to a high scan rate of 1000 mV s^{-1}, indicating excellent charge storage through ultrafast redox reactions. Changes in the areal capacitances (Fig. 4.4E) and gravimetric capacitances (Fig. S4.5E) for all four systems were calculated as a function of the current density for comparison. Not only does the ACN with the non-scribed electrode system show lower capacitance, but the capacitance rapidly drops off at higher rates. Nevertheless, no significant changes can be observed in the capacitance of the hybrid system even at high charge-discharge rates. In order to get a glimpse of the difference between the two cases, the capacitance of the two devices are compared at a relatively high current density of 56.5 mA cm^{-2}. The hybrid system can deliver

364.6 mF cm^{-2}, which is 13 times larger than the capacitance of a traditional supercapacitor using non-scribed activated carbon electrodes and an acetonitrile-based electrolyte (28 mF cm^{-2}). Again, this confirms the improved ion diffusion kinetics within the laser scribed electrodes and the excellent Faradaic capacitance contribution from the redox electrolyte.

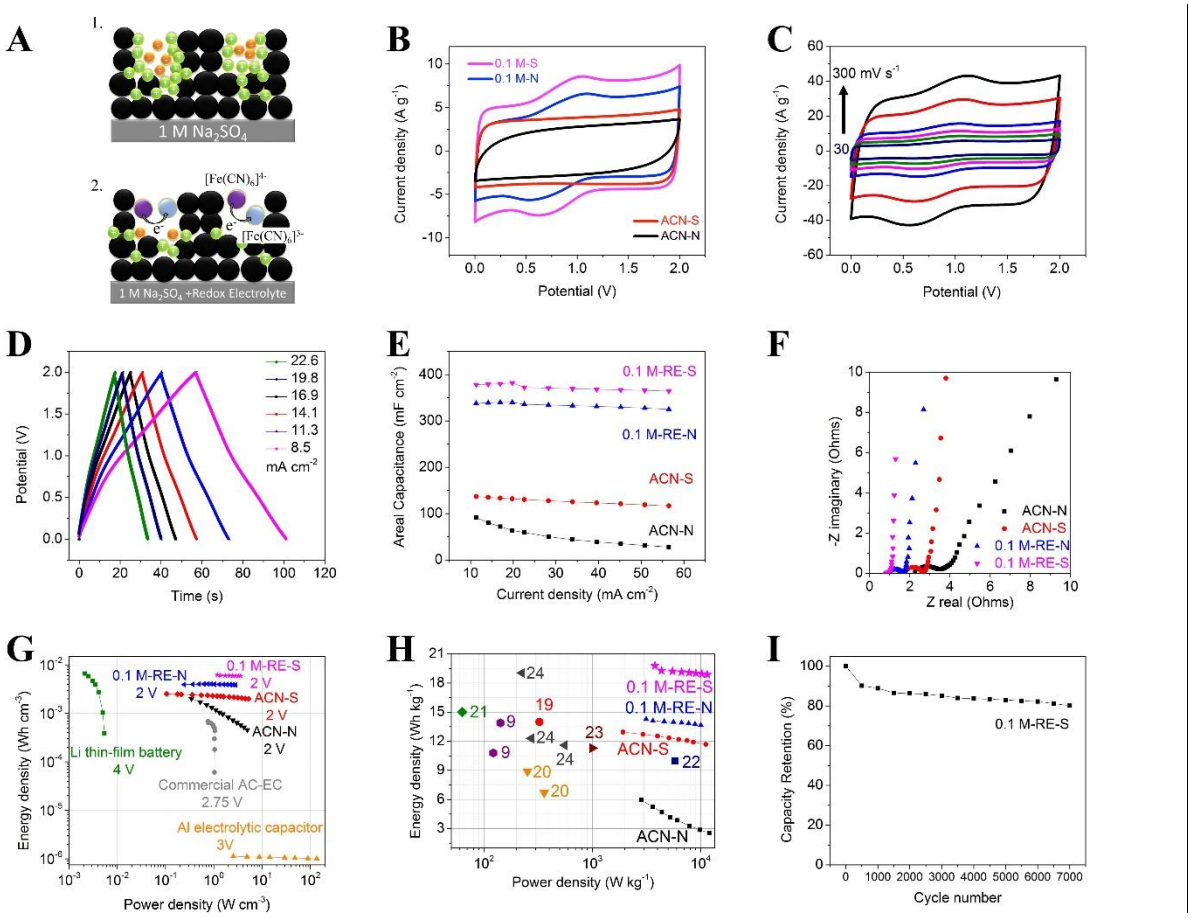

Figure 4.4. Electrochemical performance a supercapacitor combining laser scribed activated carbon (LSAC) electrodes and $[Fe(CN)_6^{3-}/Fe(CN)_6^{4-}]$ redox-active electrolyte (RE). (A) Illustration of the charge storage mechanism in an LSAC electrode using a 1.0 M Na_2SO_4 electrolyte (1) in the absence, and (2) in the presence of a redox additive. (B) CV profiles comparing the electrochemical performance of activated carbon electrodes before and after laser scribing tested in a traditional 1.0 M acetonitrile electrolyte and in a 0.1 M redox electrolyte with data collected at a scan rate of 50 mV s^{-1}. (C) Evolution of the electrochemical performance of an LSAC supercapacitor using 0.1 M RE at different CV scan rates at 30, 50, 70, 100, 200 and 300 mV s^{-1}, (D) corresponding CC curves at different current densities of 8.5, 11.3, 11.4, 16.9, 19.8, 22.6 mA cm^{-2}. (E) Areal capacitance vs. current density and (F) Nyquist plots comparing the performance of four different cases. (G) Ragone plot comparing the volumetric energy density and power density of the 0.1 M RE-LSAC supercapacitor with commercially available energy storage devices.[18, 25] (H) Another Ragone plot showing the gravimetric energy density and power density of the 0.1 M RE-LSAC system and other RE-based supercapacitors reported in the literature.[9, 19-24] (I) Long-term cycling stability of 0.1 M RE-LSAC supercapacitor at 2.0 V.

The superior synergetic interactions between the laser scribed macroporous electrodes and the 0.1 M RE was further confirmed from electrochemical impedance spectroscopy measurements, showing a low ESR of 0.9 Ω (Fig. 4.4F) and a short response time of 1.96 s (Fig. S4.5F) compared with 1.61 Ω and 3.33 s for a supercapacitor consisting of non-scribed AC electrodes and a 0.1 M RE and 2.6 Ω and 2.07 s for a supercapacitor consisting of laser scribed AC electrodes without a redox additive (not shown). Apparently, the laser scribed electrodes works together with the redox additive towards improving both the ESR of the cell and the response time, which is consistent with the CV and CC results.

Therefore, the 0.1 M RE-LSAC system shows excellent performance in a Ragone plot when compared with commercially available energy storage devices (Fig. 4.4G). This Ragone plot was normalized based on the volume of the full device that included the active material, current collector, separator, and electrolyte. The 0.1 M RE-LSAC supercapacitor can demonstrate 6.2 mWh cm^{-3}, which is about 9 times higher energy density than commercially available activated carbon electrochemical capacitors with an ACN electrolyte. Furthermore, the 0.1 M RE-LSAC can deliver ultrahigh power densities up to 3.6 W cm^{-3}, which is about 700 times faster than a lithium thin-film battery.[18] Therefore, the LSAC electrodes in combination with a 0.1 M RE electrolyte could be an ideal candidate for future energy storage applications.

Another Ragone plot based on the total mass of the active materials (Activated carbon and RE electrolyte) was made to compare with previously published RE-based electrolyte supercapacitors (Fig. 4.4H).[9,19-24] When compared to previously published data, our supercapacitors lie in the upper-right side of the plot, meaning that both power and energy density are outstanding. Even at a very high power density of 11.5 kW kg^{-1}, our 0.1 M RE-LSAC maintains 95 % (18.9 Wh kg^{-1}) of its original energy density measured at low rates

(19.8 Wh kg^{-1}). Since the redox electrolyte contributes to charge storage just like the active electrode material, the mass of the electrolyte was also considered in the calculations. Here, the specific power achieved for a 0.1 M RE-LSAC supercapacitor is 11,516 W kg^{-1} which is 70 times larger than previous reports for an RE-EC.[9] Table S4.1 provide a summary of the electrochemical data for previously published redox supercapacitors with aqueous electrolytes, the data indicate that the hybrid 0.1 M RE-LSAC system shows a higher voltage window as well.

Good cycle life is an important fundamental property of supercapacitors. In our case, we studied the cycle life of our 0.1 M RE-LSAC supercapacitor by charging and discharging at a current density 30 mA cm^{-2} for 7000 cycles (Fig. 4.4I). Compared with a supercapacitor utilizing 1.0 M Na_2SO_4 which loses most of its capacitance in the first 10 cycles, the 0.1 M RE-LSAC supercapacitor maintains 80 % of its original capacity after 7000 cycles at 2.0 V. This outstanding electrochemical stability can be attributed to the redox-electrolyte that not only adds Faradaic capacitance to the cell, but also stabilizes the cycle life of the cell even when operated at an ultrahigh voltage of 2.0 V. These results confirm the synergy between the macroporous activated carbon electrode made by laser scribing and the redox electrolyte through improved ion migration and fast and reversible redox reactions. The microscale channels act as electrolyte reservoirs and tend to reduce the inernal resistance and increase capacitance simultaneously.

4.4 Experimental

4.4.1 Preparation and Fabrication of LSAC electrode

Activated carbon electrodes were prepared by making a slurry consisting of activated carbon (MTI Corp, AB-520), a ratio of carboxymethyl cellulose/styrene-butadiene rubber

(MTI Corp) as a binder and carbon black (MTI Corp, *TIMICAL SUPER C65*) in deionized water with a weight ratio of 80:10:10, respectively. The slurry was then cast to carbon coated aluminum foil (Exopack, 16 µm), using a doctor blade. This film was dried for 12 h under ambient conditions. The dried film was then exposed to a 7-W CO_2 laser (Full Spectrum Laser H-series) to create an LSAC film. Etching the electrodes with a laser is very fast, reliable and reproducible process.

4.4.2 Fabrication of LSAC Supercapacitor Devices (CR 2032)

The electrodes were assembled in standard CR2032 coin cells using electrode discs (15 mm in diameter) and Celgard 3501 polymer separators. Two different types of electrolytes were utilized the standard 1.0 M tetraethylammonium tetrafluoroborate ($TEABF_4$) in acetonitrile (ACN) or variable concentrations of [$Fe(CN)_6^{3-}$/$Fe(CN)_6^{4-}$] in 1.0 M Na_2SO_4 solution. All the coin cells were assembled in air. The loading masses of the activated carbon film before and after scribing were 3.9 and 3.2 mg cm^{-2}, respectively.

4.5 Conclusions

A new method is described to produce macroporous electrodes using a simple laser scribing technique. These electrodes, when combined with an aqueous ferrocyanide/ferricyanide redox electrolyte, create supercapacitors with enhanced energy density enabled by both higher capacitance and a larger potential window. The LSAC has a macro-patterned architecture and improved ion diffusion pathways, which enable the efficient electric double layer capacitance from the active material and Faradaic capacitance from the electrolyte. The synergy between the laser scribed electrodes and the redox electrolyte produce supercapacitors with 8 times larger capacitance than traditional supercapacitors

utilizing non-scribed activated carbon electrodes with an acetonitrile-based electrolyte. In addition, the RE-LSAC system exhibits high rate capability, low ESR, and excellent cycling stability. The new supercapacitor utilizes commercial grade active materials, current collectors and separators and may, thus, have potential for real world applications.

4.6 Appendix to Chapter 4

Supplementary Table S4.1**:** Comparison of the Voltage Window of 0.1 M redox-active electrolyte (RE) with laser scribed activated carbon electrode (LSAC) with other published article using aqueous based redox-active electrolyte

Redox Couple	Based Electrolyte	Voltage	Reference
0.1 M Potassium ferrocyanide ($FeCN_6^{3+}$ /$FeCN_6^{4+}$)	1.0 M Na_2SO_4	2.0 V	This work
0.38 M hydroquinone (Q/HQ)	1.0 M H_2SO_4	1.0 V	26
0.3 g $VOSO_4$ (VO^{2+}/VO_2^{+})	1.0 M H_2SO_4	0.8 V	19
0.050 g p-phenylenediamine (p-phenylenediamine /p-phenylenediimine)	2.0 M KOH	1.0 V	16
0.08 M KI (I^-/I_3^-)	1.0 M H_2SO_4	1.0 V	24
0.08 M KI (I^-/I_3^-)	1.0 M Na_2SO_4	1.0 V	
0.08 M KBr (Br^- /Br_3^-)	1.0 M H_2SO_4	1.0 V	
0.06 M $CuCl_2$ (Cu^{2+}/Cu)	1.0 M HNO_3	1.35 V	17
0.4 M hydroquinone (Q/HQ)	1.0 M H_2SO_4	0.8 V	20
0.4 M $CuSO_4$ (Cu^{2+}/Cu)	1.0 M H_2SO_4	0.8 V	
1 M KI and 1 M $VOSO_4$ (I^-/I_3^- and VO^{2+}/VO_2^{+})		0.8 V	27
0.4 M KBr/0.1 M $HVBr_2$ (Br^- /Br_3^- and HV^{2+}/HV^{+})		1.2 V	9
1 M KBr/0.5 M $MVCl_2$ (Br^- /Br_3^- and MV^{2+}/MV^{+})		1.4 V	

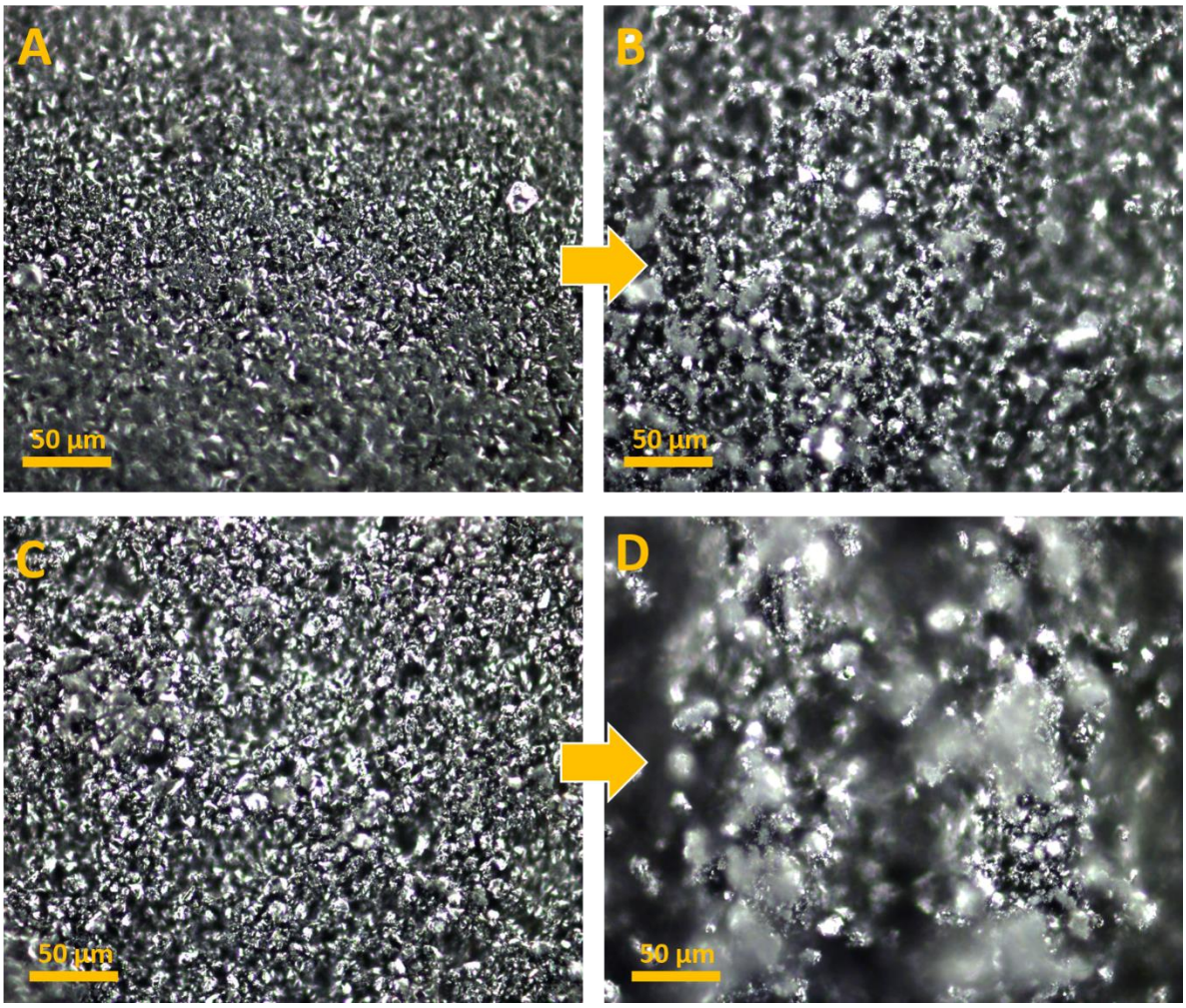

Supplementary Figure S4.1: Optical microscope images showing the microstructure of the electrode before and after laser scribing. Pictures on the left are for the as-made electrodes and on the right after laser irradiation. Electrodes in (A) and (B) are processed with a PVDF binder whereas electrodes in (C) and (D) use a CMC/SBR binder. The results reveal the appearance of macropores in the structure of the electrode following the laser treatment.

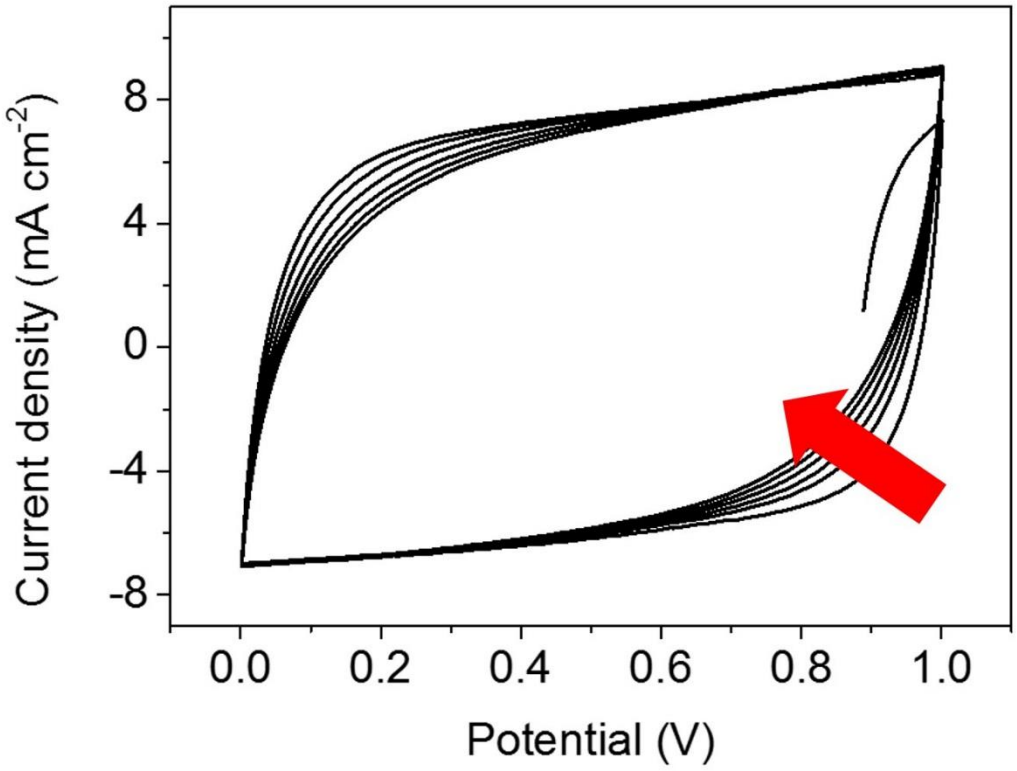

Supplementary Figure S4.2: Cyclic voltammetry (CV) of an activated carbon electrode (prepared on an aluminum current collector) in 1.0 M Na_2SO_4 measured at 50 mV s^{-1} and repeated for 6 cycles. The device was assembled and tested in a CR 2032 coin cell.

A

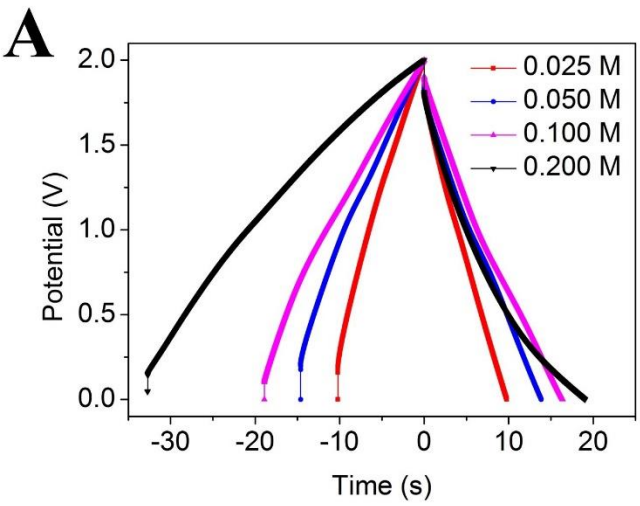

B

Concentration of RE	Areal capacitance mF cm^{-2}	Columbic efficiency %
0.025	105	96
0.050	149	95
0.100	170	87
0.200	207	58

Supplementary Figure S4.3. (A) Charge/discharge (CC) curves at 20 mA cm^{-2} of an activated carbon supercapacitor with 0.025 M (red), 0.050 M (blue), 0.100 M (pink) and 0.200 M (black) of the redox-active electrolyte [$Fe(CN)_6^{3-}$/$Fe(CN)_6^{4-}$] in 1.0 M Na_2SO_4. (B) Areal capacitance of the device and Coulombic efficiency as listed at different concentrations of redox-active electrolyte are calculated based on the CC results at 20 mA cm^{-2}.

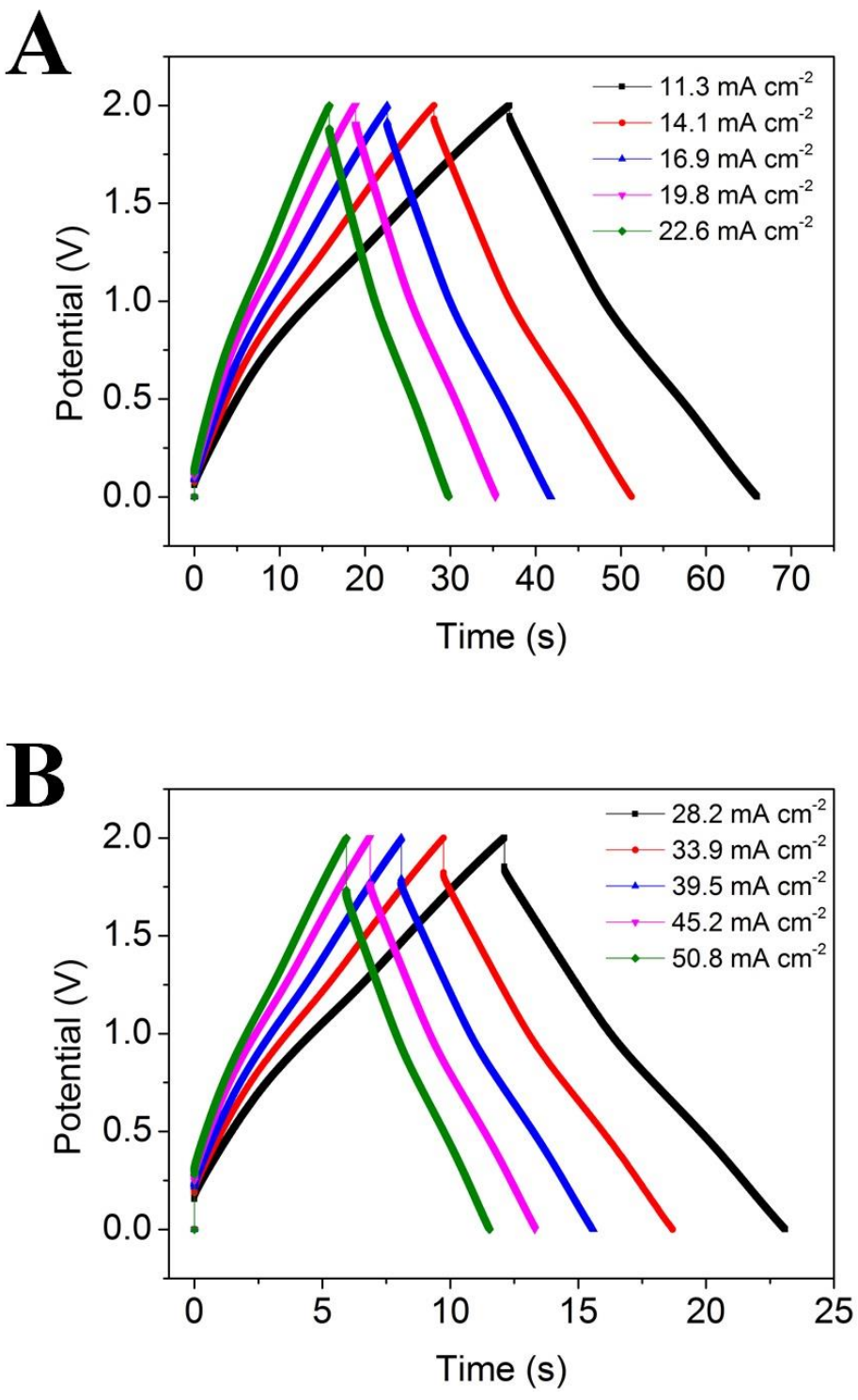

Supplementary Figure S4.4. CC curves of an activated carbon supercapacitor with 0.10 M redox-active electrolyte at current densities of (A) 11.3, 14.1, 16.9, 19.8 and 22.6 mA cm^{-2}, and (B) 22.8, 33.9, 39.5, 45.2 and 50.8 mA cm^{-2}.

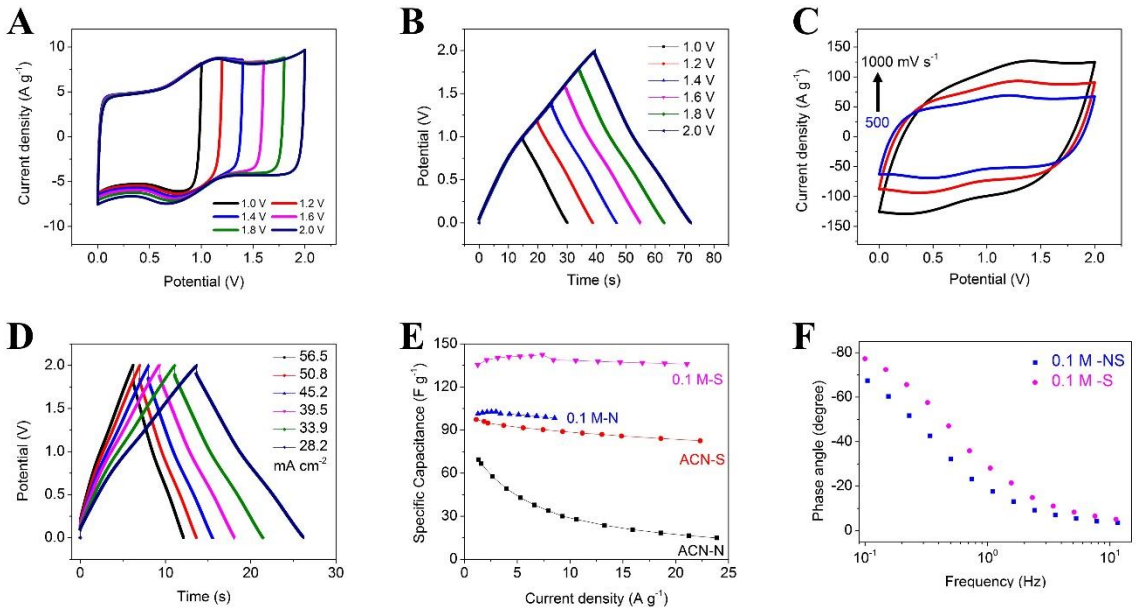

Supplementary Figure S4.5. Evaluation of the electrochemical performance of laser scribed activated carbon (LSAC) electrodes in a 0.10 M redox-active electrolyte (RE) (A) CV curves at 50 mV s^{-1}, (B) Galvanostatic charge/discharge (CC) curves at a current density of 11.3 mA cm^{-2} with an increasing voltage window from 1.0 V to 2 V. (C) CV curves at high scan rates of 500, 700, and 1000 mV s^{-1}. (D) CC curves at current densities of 11.3, 14.1, 16.9, 19.8 and 22.6 mA cm^{-2}. (E) Comparison of gravimetric capacitance per electrode for activated carbon before and after laser scribing, with and without a redox active electrolyte normalized by the active materials (activated carbon + 0.1 M RE). (F) Bode plots of the redox active electrolyte-based supercapacitors before and after laser scribing (i.e. RE-AC and RE-LSAC).

Calculations

The specific capacitance, energy density and power density of the full device were calculated from the charge/discharge curves at different current densities.

First, the specific capacitance of the device was calculated, and the time and the voltage were measured from the discharge curve:

$$\text{Specific C}_{\text{device}}\,(\text{F g}^{-1}) = \frac{2*\text{I (A)}*\int U(\text{t})\text{dt(Volt)(sec)}}{U^2*Mass(g)}$$

Mass refers to the mass of the active materials (activated carbon + 0.1 M potassium ferrocyanide)

$$\text{Specific C}_{\text{device}}\,(\text{F cm}^{-3}) = \frac{2*\text{I (A)}*\int U(\text{t})\text{dt(Volt)(sec)}}{U^2*Volume\ (cm^3)}$$

Volume refers to the volume of the stack device including the active materials, substrates and separator.

Second, the specific capacitance of the electrode was calculated from the full cell.

$$\text{Specific C}_{\text{electrode}}\,(\text{F g}^{-1}) = 4*\text{C}_{\text{device}}\,(\text{F g}^{-1})$$

Third, the specific energy density of the device was calculated from:

$$\text{Specific E}_{\text{device}}\,(\text{Wh kg}^{-1}) = \frac{\text{I(A)}\int U(\text{t})\text{dt(Volt)(hr)}}{Mass(kg)}$$

Mass refers to the mass of active materials (activated carbon + 0.1 M potassium ferrocyanide)

$$\text{Specific E}_{\text{device}}\,(\text{Wh cm}^{-3}) = \frac{\text{I(A)}\int U(\text{t})\text{dt(Volt)(hr)}}{volume(cm^3)}$$

Volume refers to the volume of the stack device including the active materials, substrates and separator.

Fourth, the specific power density of device was calculated from:

$$\text{Specific P}_{\text{device}}\,(\text{W kg}^{-1}) = \frac{\text{Energy density}(Wh/kg)}{Time(\text{hr})}$$

$$\text{Specific P}_{\text{device}}\,(\text{W cm}^{-3}) = \frac{\text{Energy density}(Wh/cm^3)}{Time(\text{hr})}$$

4.7 References

(1) El-Kady, M. F.; Shao, Y.; Kaner, R. B. *Nat. Rev. Mater.* **2016**, *1*, 16033.

(2) Weinstein, L.; Dash, R. *Mater. Today* **2013**, *16*, 356.

(3) Miller, J. R. *Science* **2012**, *335*, 1312.

(4) Dura, H.; Perry, J.; Lecacou, T.; Markoulidis, F.; Lei, C.; Khalil, S.; Decker, M.; Weil, M. International Conference on Clean Electrical Power (ICCEP), Alghero, Italy, June, **2013,** 516.

(5) Burke, A. *Electrochim. Acta* **2007**, *53*, 1083.

(6) He, M.; Fic, K.; Frckowiak, E.; Novak, P.; Berg, E. J. *Energ. Environ. Sci.* **2016**, *9*, 623.

(7) El-Kady, M. F.; Ihns, M.; Li, M.; Hwang, J. Y.; Mousavi, M. F.; Chaney, L.; Lech, A. T.; Kaner, R. B. *Proc. Natl. Acad. Sci. U.S.A.* **2015**, *112*, 4233.

(8) Hwang, J. Y.; El-Kady, M. F.; Wang, Y.; Wang, L.; Shao, Y.; Marsh, K.; Ko, J. M.; Kaner, R. B. *Nano Energy* **2015**, *18*, 57.

(9) Chun, S.-E.; Evanko, B.; Wang, X.; Vonlanthen, D.; Ji, X.; Stucky, G. D.; Boettcher, S. W. *Nat. Commun.* **2015**, *6*.

(10) Fic, K.; Lota, G.; Meller, M.; Frackowiak, E. *Energ. Environ. Sci.* **2012**, *5*, 5842.

(11) Lee, D.; Patwa, R.; Herfurth, H.; Mazumder, J. *J. Power Sources* **2013**, *240*, 368.

(12) El-Kady, M. F.; Kaner, R. B. *ACS Nano* **2014**, *8*, 8725.

(13) Maciá-Agulló, J. A.; Moore, B. C.; Cazorla-Amorós, D.; Linares-Solano, A. *Carbon* **2004**, *42*, 1367.

(14) Gogotsi, Y.; Simon, P. *Science* **2011**, *334*, 917.

(15) Yang, X.; Cheng, C.; Wang, Y.; Qiu, L.; Li, D. *Science* **2013**, *341*, 534.

(16) Wu, J.; Yu, H.; Fan, L.; Luo, G.; Lin, J.; Huang, M. *J. Mater. Chem.* **2012**, *22*, 19025.

(17) Mai, L.-Q.; Minhas-Khan, A.; Tian, X.; Hercule, K. M.; Zhao, Y.-L.; Lin, X.; Xu, X. *Nat. Commun.* **2013**, *4*.

(18) Pech, D.; Brunet, M.; Durou, H.; Huang, P.; Mochalin, V.; Gogotsi, Y.; Taberna, P.-L.; Simon, P. *Nat. Nanotechnol***. 2010**, *5*, 651.

(19) Senthilkumar, S. T.; Selvan, R. K.; Ponpandian, N.; Melo, J. S.; Lee, Y. S. *J. Mater. Chem. A* **2013**, *1*, 7913.

(20) Chen, L.; Bai, H.; Huang, Z.; Li, L. *Energ. Environ. Sci.* **2014**, *7*, 1750.

(21) Tomai, T.; Mitani, S.; Komatsu, D.; Kawaguchi, Y.; Honma, I. *Sci. Rep.* **2014**, *4*, 3591.

(22) Yu, H.; Fan, L.; Wu, J.; Lin, Y.; Huang, M.; Lin, J.; Lan, Z. *RSC Adv.* **2012**, *2*, 6736.

(23) Yu, H.; Wu, J.; Fan, L.; Lin, Y.; Xu, K.; Tang, Z.; Cheng, C.; Tang, S.; Lin, J.; Huang, M.; Lan, Z. *J. Power Sources* **2012**, *198*, 402.

(24) Senthilkumar, S. T.; Selvan, R. K.; Lee, Y. S.; Melo, J. S. *J. Mater. Chem. A* **2013**, *1*, 1086.

(25) El-Kady, M. F.; Strong, V.; Dubin, S.; Kaner, R. B. *Science* **2012**, *335*, 1326.

(26) Roldán, S.; Blanco, C.; Granda, M.; Menéndez, R.; Santamaría, R. *Angew. Chem. Int. Edit.* **2011**, *50*, 1699.

(27) Frackowiak, E.; Fic, K.; Meller, M.; Lota, G. *ChemSusChem.* **2012**, *5*, 1181.

Chapter 5. Flash Converted Graphene/Activated carbon supercapacitors for Potential Industrial Applications

5.1 Abstract

Electrochemical capacitors, well known as supercapacitors, are attractive energy storage devices with the ability to recharge in seconds. However, they are still limited by a low energy density and slow rate capability. State-of-the-art supercapacitors are manufactured with activated carbon (AC) electrodes. Unfortunately, activated carbons have a low specific capacitance and power density especially in organic electrolytes due to long ion diffusion pathway and low conductivity. Here, Flash Converted Graphene (FCG) is combined with AC to make novel architecture form that facilitates the rapid transport of the ions and electrons at the same time maintaining the high packing density. Devices made with these composite (FCG/AC) electrodes exhibit improved power, energy density, and rate capability. In addition, these devices have been made into a commercially viable coin cells form that holds promise for a wide range of applications.

5.2 Introduction

Supercapacitors, as energy storage devices exhibiting extremely high power density and excellent cyclic stability, have attracted tremendous attention due to the growing demand for power systems applications, such as smartphones, tablets, laptops and electric vehicles.[1-3] The primary type of supercapacitor is an electric double-layer capacitor (EDLC). EDLC's store energy by physical separation of charge at the interface between the electrode surface and the electrolyte, therefore, larger sized materials will store more charge.[4,5] Using activated carbon which has a large surface area (1000-3500 $m^2 g^{-1}$) for the active material, provides

more energy for EDLCs.[6] Up to now, activated carbon electrodes have been commercially used in the supercapacitor market due to their large surface areas, relatively high packing density, low cost and easy control over pore size.[7] There are two ways to prepare an AC – physical and chemical activation. Carbonaceous precursors (coconut shells, coal, etc.) can be physically activated in the presence of carbon dioxide at 900°C or chemically activated at 500 °C in the presence of chemical agents such as KOH, K_2CO_3, NaOH, Na_2CO_3, $AlCl_3$, $ZnCl_2$, $MgCl_2$ and H_3PO_4.[8, 9] The pore size and surface area can be controlled by regulating the carbonization time, temperature, or chemical agents.[10]

A high definite surface area, short ion diffusion pathway, and high electric conductivity of the materials are also crucial to ensure good overall performance of the supercapacitor in both categories of power and energy in the development of EDLCs. Unfortunately, AC particles usually have sizes up to several tens of micrometers, which result in a long diffusion pathway for ions as well as resulting in low electrical conductivity from weak inter-particle contact which leads to low power density compared to well-developed nanostructured materials like graphene, carbon aerogels, and carbon nanotubes. In the last decade, many carbonaceous materials have been studied as alternatives for AC in EDLC applications such as graphene,[11] carbon nanotubes,[12] carbon onions,[13] carbon fibers,[14, 15] carbon hydrogels,[16] carbide-derived carbons[17, 18] and templated carbons.[19] All these materials have been successfully applied as active materials and improve the overall performance of EDLCs. Nevertheless, almost all the materials suggested above are more expensive than AC and also suffer from low packing density which makes it difficult to make these materials commercially useful.[20] Therefore, AC is still the state-of-art material for commercial EDLCs.

To overcome the conductivity problem of activated carbon electrodes, current supercapacitors need carbon black added to achieve a reasonable conductivity (0.1 to 100 S cm^{-1})[21] with a weight percentage of ~10%. Carbon blacks are also commonly used in lithium-ion battery electrodes to improve conductivity. After adding the carbon black into activated carbon, the conductivity of the electrode will be enhanced, but the low surface area of the carbon black (~50 m^2 g^{-1}) makes it difficult to fully utilize the high surface area of the AC (Figure 5.1A).

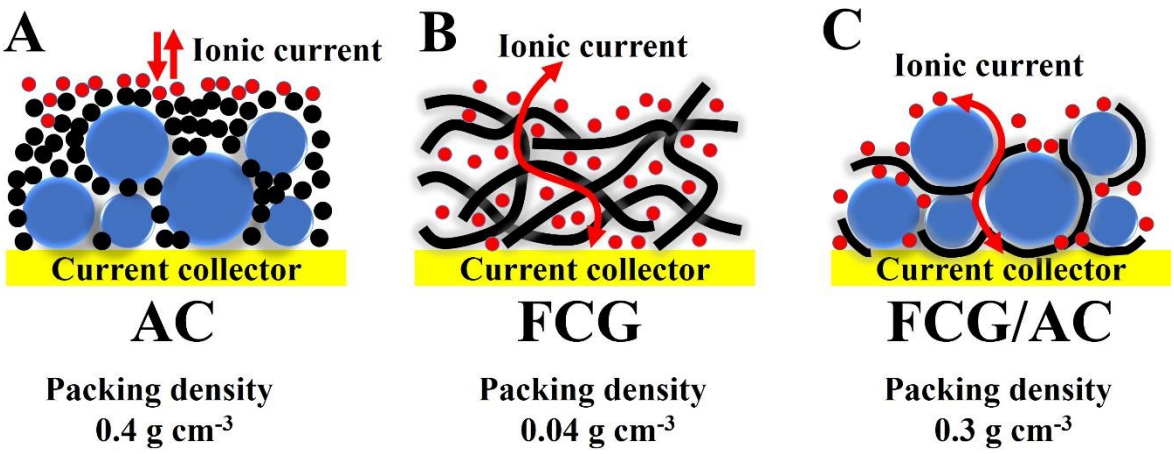

Figure 5.1. Schematic diagram of electrode architecture for activated carbon (AC), flash converted graphene (FCG) and FCG/AC hybrid materials. (A) In the composite electrode of AC and carbon black, the carbon black particles block all the porous sites, thus electrolyte can only be exposed to the top layer. (B) In contrast, the FCG electrode shows that electrolyte can be exposed throughout the whole active material due to its porous 3-dimensional architecture. (C) FCG connects the AC particles to each other and also to the current collector. FCG is partially wrapped around the AC particles and works as a conductive additive instead of blocking the pores. Therefore, electrolyte can be exposed to the entire amount of active material.

Due to its inappropriate architectural form that blocks the pores of AC, only the top active layer is exposed to the electrolyte slowing the ionic pathways, which results in low capacitance (~100 F g^{-1}). Therefore, for AC materials, enhancing the electrical conductivity

as well as maintaining high specific surface area remains a challenge. To improve the architecture of the AC electrode, the size of the AC particles, their pore shape, and connectivity between each particle have to be considered.

Graphene, as a new two-dimensional carbon material consisting of a single planar layer of sp^2 hybridized carbon atoms, has attracted much attention as an excellent candidate for supercapacitor applications. The attraction is due to the significant theoretical specific surface area of 2630 $m^2\ g^{-1}$ and excellent electrical conductivity.[22] Thus, the theoretical capacitance value of graphene is high (550 F g^{-1}); however, despite much research this theoretical value has not yet been achieved. The porous 3-dimensional graphene architecture can provide the needed short ion diffusion pathways while enabling all the electrolyte to wet the entire surface of the materials (Figure 1B). Unfortunately, due to their unique porous architecture, graphene-based electrodes have extremely low packing density (0.005 – 0.05 g cm^{-3}) that leads to very low areal capacitance (typically 21 μF cm^{-2}).[23] The areal capacitance value is much lower than that of an AC electrode, because only a limited amount of the graphene can be added to avoid the restacking problem between sheets.

A composite of graphene and AC have been investigated to solve the separate disadvantages of each. Zheng et al.[24] found that composite materials of graphene and AC can increase the capacitance by a factor of three and lower the series resistance (ESR) from 0.89 to 0.49 Ω. This significant improvement in the capacitance and ESR are impressive, but still the rate capability and power density could be increased further by using highly porous conductive graphene. Flash converted graphene (FCG) is an excellent candidate for a composite material with AC because FCG has a distinct high surface area structure comprised of nano-sheets and superior electrochemical performance has been observed.[25]

Here, we successfully increase the packing density of graphene at the same time maintaining the 3-dimensional open porous structure. The highly conductive FCG with a porous sheet morphology is well matched with the ideal architecture for connecting AC inter-particles without sacrificing the high particular surface area of the AC (Figure 5.1C). Unlike carbon black, graphene does not only provide the needed electrical conductivity, but also can store a significant amount of charge. In addition, this hybrid material can solve the restacking problem of graphene since the AC particles can act as spacers between graphene sheets. Thus, FCG/AC composite materials can overcome the disadvantages of both AC and graphene, and allow the advantages to be fully utilized. Electrochemical results indicate an ideal composite architecture with the FCG/AC composite exhibiting higher capacitance, higher power, lower ESR and shorter response times when compared to pure AC electrodes.

5.3 Results and Discussion

5.3.1 Characterization of FCG/AC electrodes

The structure and morphology of FCG/AC electrodes were investigated by scanning electron microscopy (SEM). A SEM image of FCG/AC composite materials is shown in Figure 5.2 with different scale bars. A homogeneous high packing density composite electrode was prepared by using probe sonication (Figure 5.2A).

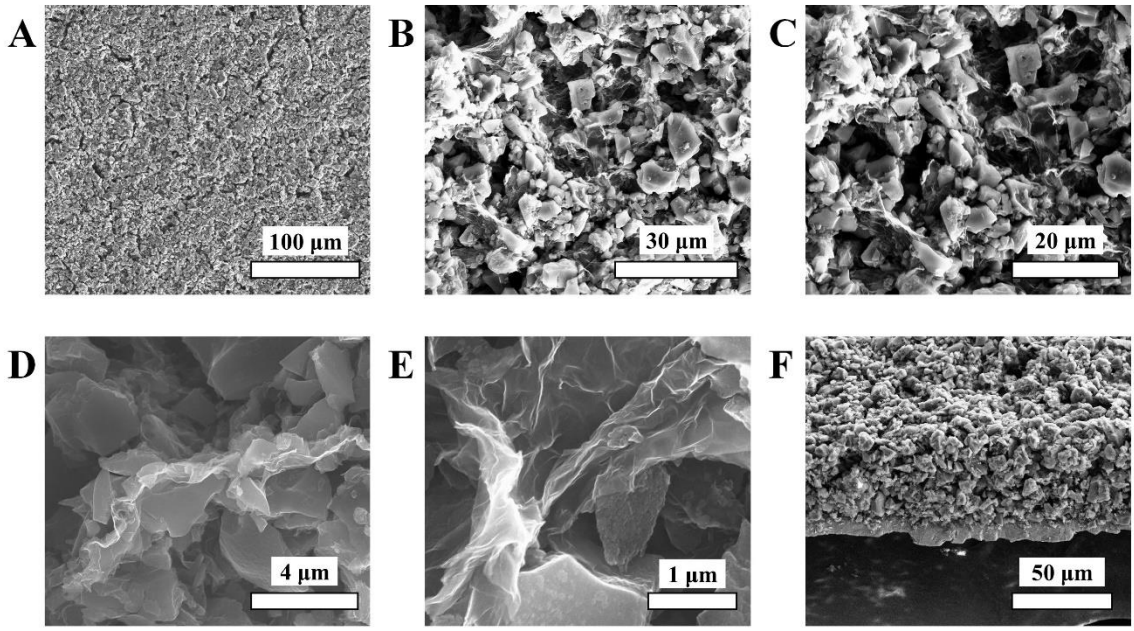

Figure 5.2. Microscopic characterization of an FCG/AC composite. (A) Top-view SEM image showing a homogeneous coated dense film (scale bar = 100 µm). SEM images showing FCG sheets are homogeneously interconnected with AC particles with (B) scale bar = 30 µm and (C) scale bar = 20 µm. (D) An SEM image under higher magnification illustrating that the AC particles are partially wrapped by the FCG sheets. (E) Image showing that AC particles work as spacers between FCG sheets and prevent restacking. (F) A cross-sectional view of an SEM image showing a homogeneous dense film coated on the current collector.

Figure 5.2B and C shows homogeneous films of AC particles uniformly connected on the FCG. The average AC particle size was found to be 10 µm. A zoomed in view SEM image of the composite electrode (Fig. 5.2 D) reveals that FCG sheets partially wrap around each AC particle. The FCG sheets do not restack and remain well connected to the AC (Fig. 5.2E). Figure 5.2F shows a cross-sectional SEM image of an FCG/AC film on a carbon coated current collector. The thickness of the FCG/AC layer is 45 µm.

5.3.2 Electrochemical properties of AC/FCG composite electrodes

To test the electrochemical performance of FCG/AC and AC electrodes, devices were assembled in CR2032 coin cell form with using a mixture of 1.0 M $TEABF_4$ in acetonitrile as the electrolyte. Both cyclic voltammetry (CV) and galvanostatic charge/discharge (CC) measurements were carried out to compare the charge storage behavior of FCG/AC and AC electrodes. Fig. 5.3A shows the CV of the AC device (black) and FCG/AC device (red).

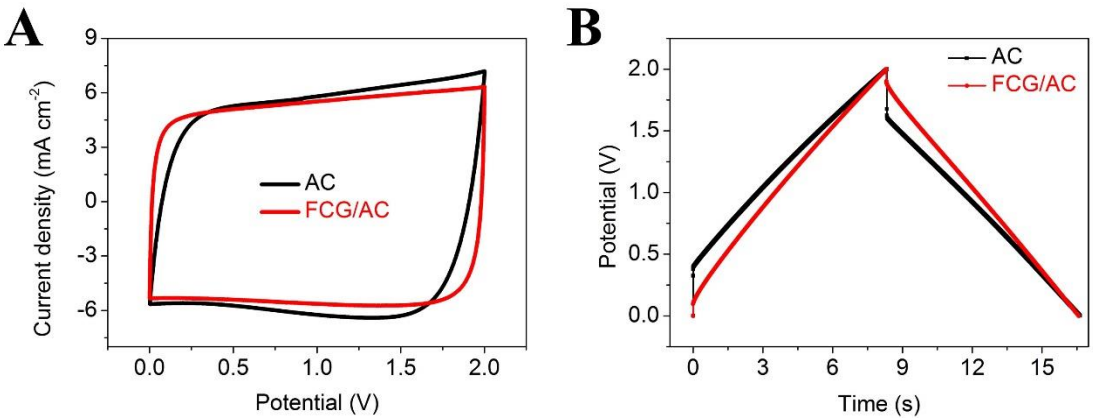

Figure 5.3. Evaluation of the electrochemical performance of flash converted graphene (FCG)/activated carbon (AC) supercapacitors in a traditional 1.0 M tetraethylammonium tetrafluoroborate ($TEABF_4$) in acetonitrile (ACN) electrolyte. (A) Cyclic voltammetry (CV) curves obtained at 100 mV s^{-1}, (B) Charge/discharge (CC) curves obtained at 20 mA for supercapacitors prepared with an AC (black) and an FCG/AC electrode (red).

In comparison with AC and FCG/AC, the FCG/AC shows a more rectangular CV curve at 100 mV s^{-1}, suggesting better ideal electrical double layer capacitance behavior compared to AC. In addition, the FCG/AC shows an ideal triangular shape to the CC curves with a much smaller IR drop (0.096 Ω) compared to AC (0.32 Ω (Fig. 5.3B). A lower equivalent series resistance (ESR) was also found via the intercept of the Nyquist plot (Fig. 5.4A) on the real

axis, which is 1.1 Ω in the FCG/AC and 6.07 Ω in the AC device. In addition, an FCG/AC Nyquist plot didn't show any semi-circle of resistance in the high-frequency region; however, a semi-circle is clearly observed in the AC device.

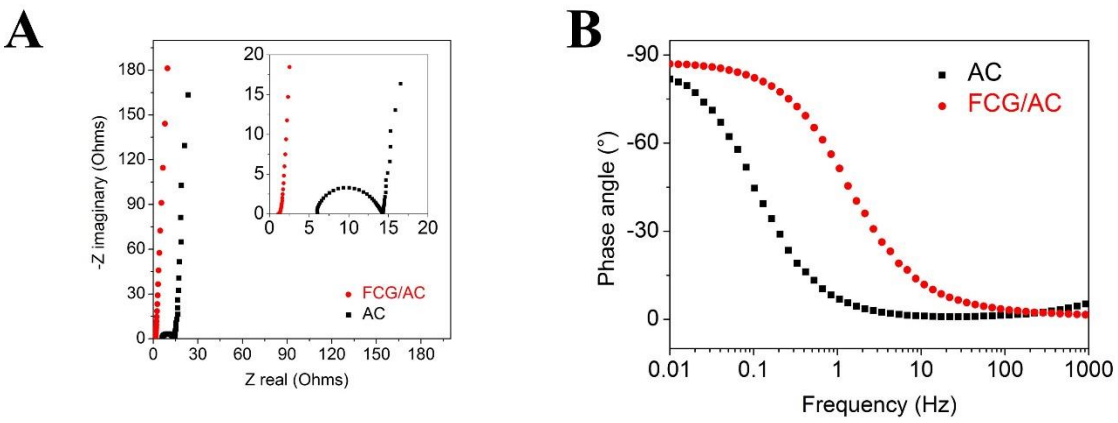

Figure 5.4. (A) a Nyquist plot, and (B) a Bode plot of the FCG/AC and AC supercapacitors over a frequency range from 1 kHz to 0.01 Hz. All the electrochemical measurements were carried out in a CR2032 coin cell.

These FCG/AC electrochemical performance results confirm low charge transfer resistance at the electrode/electrolyte interface because the electrolyte ions can easily diffuse into essentially all surfaces of the electrode through the ideal architecture of the FCG/AC and suggest rapid electron transfer along the highly conductive FCG sheets. The Bode plot displayed in Fig. 4B provides further evidence for the high rate capability of the FCG/AC electrochemical capacitor. The characteristic frequency f_0 for the FCG/AC at a phase angle of -45° is 1.3 Hz. At -45° (the Warburg region), the resistive and capacitive parts of the electrode should be equal.[26] The corresponding response time of 0.75 s is a much faster frequency response than AC (9.7 s). At the low-frequency region, the phase angle of the FCG/AC is close to -90° (-87°), while AC is -82°. This suggests that the FCG/AC supercapacitor functions more like a nearly ideal capacitor than AC.

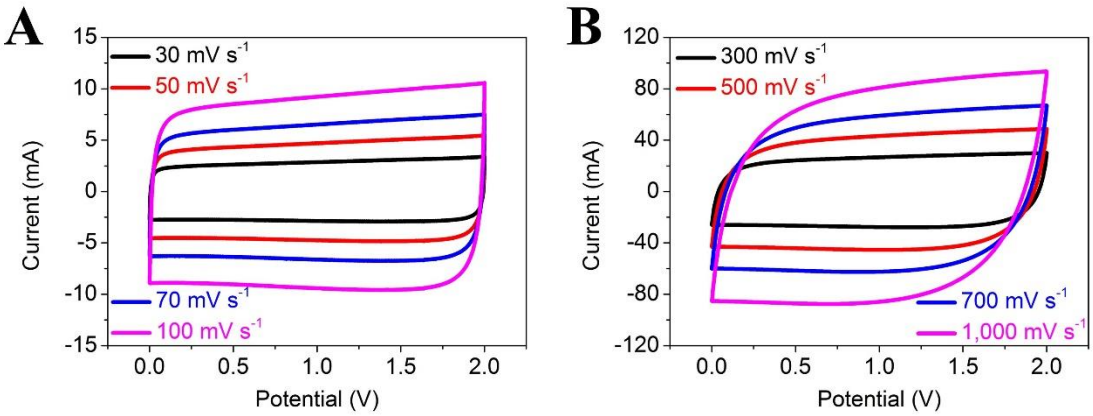

Figure 5.5. CV profiles of an FCG/AC supercapacitor at different scan rates of (A) 30, 50, 70, 100 and (B) 300, 500, 700 and 1,000 mV s^{-1}.

The manifest difference in the electrochemical performance agrees with the suggested FCG/AC architecture, which is confirmed through SEM images. Figures. 5.5A shows the rectangular CV shape of the FCG/AC electrode under different scan rates from 30 to 100 mV s^{-1}. The rectangular shape is also retained at high scan rates, up to 1,000 mVs^{-1} (Fig. 5.5B), suggesting that the FCG/AC supercapacitor performs with near ideal capacitive behavior with a high rate capability. The classic triangular shape of the CC curves under different currents from 5 mA to 80 mA provides further evidence for the ideal rate capability supercapacitor behavior of the FCG/AC electrode (Fig. 5.6A). The FCG/AC supercapacitor exhibits superior capacitance retention due to rapid transport of electrons through the conductive FCG and the highly porous electrode enabling fast ion diffusion (Figs. 5.5B and 5.6).

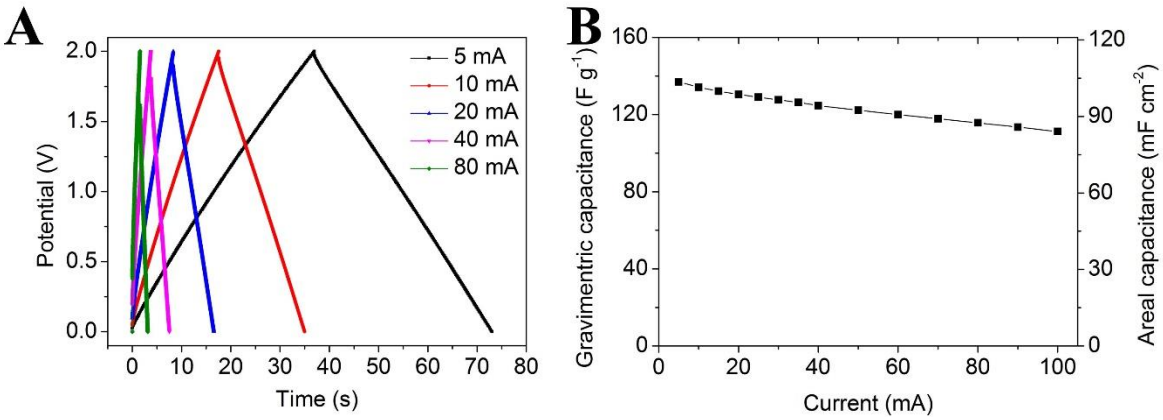

Figure 5.6. (A) Charge/discharge (CC) curves at different current densities of 5, 10, 20, 40 and 80 mA. (B) The gravimetric capacitance and areal capacitance retention of an FCG/AC supercapacitor as a function of the applied current.

The specific capacitance of the FCG/AC was calculated through the discharge part of the CC curve and was calculated to be 136 F g^{-1} (84.2 mF cm^{-2}) per electrode at 5 mA. Even at an ultrahigh current 100 mA, the FCG/AC supercapacitor can deliver 111 F g^{-1} (Fig. 5.6B).

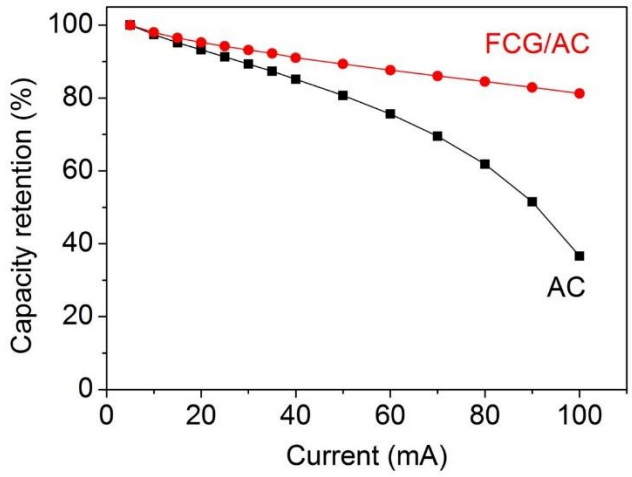

Figure 5.7. Comparison of rate capability potential of AC and FCG/AC supercapacitors.

When we compare the rate capability to a bare AC supercapacitor (Fig. 5.7), the composite electrode still can retain 80% of its capacitance at a high current of 100 mA, while the AC electrode can only retain 37% of its capacitance at a 100 mA current. The results imply that FCG/AC electrodes experience incredibly fast ionic and electronic diffusion due to the exceedingly porous structure of FCG/AC, which provides much-improved charge transfer pathways to the AC particles.

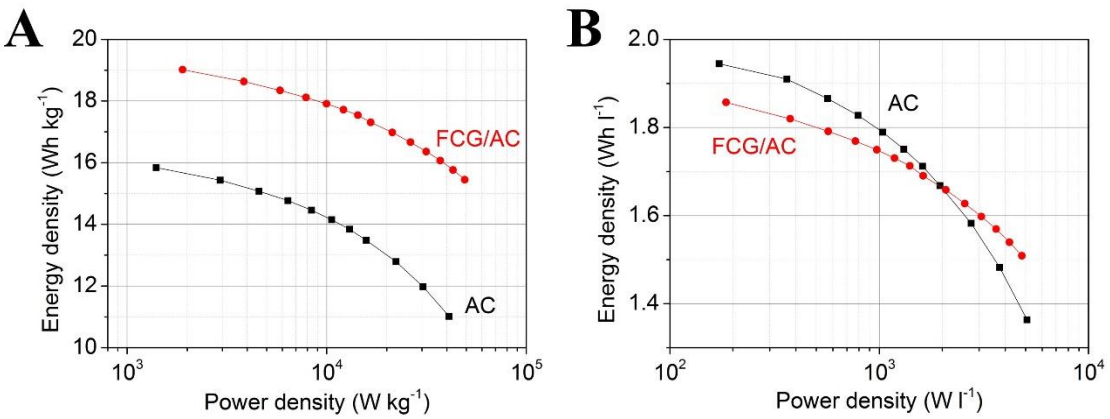

Figure 5.8. (A) A Ragone plot showing the gravimetric energy density vs. power density and (B) the volumetric energy density vs. power density for AC and FCG/AC supercapacitors.

In order to evaluate the device performance of the FCG/AC and AC electrodes, the energy density and power density were calculated from the CC curves and plotted on the Ragone plot by mass (Fig. 5.8A) and by volume (Fig. 5.8B). The specific gravimetric energy density of the FCG/AC (19 Wh kg^{-1}) is higher than that of the AC (15.8 Wh kg^{-1}) alone, but the volumetric energy density of the FCG/AC (18.6 Wh l^{-1}) is slightly lower than that of the AC (19.4 Wh l^{-1}). The volumetric energy density of the FCG/AC could be improved by using a calendering system. Once FCG/AC electrodes have been coated, the coated films can be pressed down through a roller in a process called calendering. The purpose of calendering is

to eliminate unnecessary volume from the electrode and this process facilitates an increase in the volumetric energy density. When we compare power densities to previously published composite electrodes of AC and graphene (33.2 W kg-1),[24] our FCG/AC device demonstrated about three orders of magnitude higher power density (21,300 W kg^{-1}). This result indicates that graphene prepared from our photo-thermal method[25,27] shows superior performance in electrochemical properties.

5.4 Experimental

5.4.1 Preparation of FCG

First, GO was prepared using a modified Hummers method and freeze dried with a lypholizer vacuum under 0.021 torr at a temperature of -45 °C. The freeze-dried GO was exposed to a commercial flash lamp (Alien Bees B1600) with 640 J of power and converted it into FCG.

5.4.2 Preparation of FCG/AC composite electrodes

A mixture of FCG powder, AC powder and a binder (carboxymetyl cellulose (CMC)/styrene-butadiene rubber (SBR)) in a ratio of 1:18:1 was stirred for 120 min then probe sonicated for 30 min. The homogeneous composite slurry was cast onto current collectors using a doctor blade. The films were dried in an oven at 60 °C for 12 hr.

5.4.3 Assembly of FCG/AC electrodes into CR2032 coin cell devices

Dried films were cut with a 15 mm-diameter round hole arch punch, and these discs were used as electrodes for the coin-cell devices. Once electrode, separator (polypropylene) and electrolyte (1.0 M $TEABF_4$ in acetonitrile) were ready, we assembled coin-cells by starting with the bottom cap, then adding one electrode, separator, 10 µL electrolyte, the

other electrode, a spacer, a spring and covering with the top cap. Each coin cell stack was crimped with a crimping machine.

5.4.4 Characterization of the FCG/AC supercapacitor

SEM characterization of the FCG/AC electrodes were performed using a Nova 600 SEM/FIB system. The mass of the active material was measured using an electronic balance (Mettler Toledo MX5), and found to be 1.33 mg. The effective thickness of the FCG/AC device was 155 μm including active material (45 μm), substrate (20 μm), and separator (25 μm). All electrochemical data were collected using a Biologic VMP3 electrochemical workstation equipped with a 10 A current booster (VMP3b-10), USA Science Instrument.

5.5 Conclusions

FCG/AC composite electrodes have been fabricated by photo-thermal carbonization and probe sonication as explained in this chapter. A commercially available flash lamp was used to produce FCG, while a probe sonication instrument was used to mix the FCG powder and the AC powder to achieve homogeneous films. SEM studies revealed that these composite electrodes are composed of a porous architecture in which homogeneously-dispersed AC particles are partially wrapped on conductive porous graphene. The AC serves as micro-spacers between graphene layers, which can prevent the graphene sheets from restacking. This results in enhanced packing density. Additionally, the graphene integrated into the AC connects the AC particles to each other and to the current collector which enhances the conductivity of the overall electrode. On the other hand, unlike carbon black particles, the nanosheet morphology of the graphene material provides short diffusion pathways without blocking pores, which facilitates the rapid transport of ions and electrons, thereby resulting in superior electrochemical performance. The specific capacitance based on

a composite material is 137 F g^{-1} in an acetonitrile electrolyte. The composite supercapacitor exhibits a low ESR, a short response time, and also shows excellent rate capability. The excellent electrochemical performance can be mainly attributed to the unique composite structure. Therefore, the FCG/AC composite prepared by a photo-thermal method is a promising electrode material for high performance supercapacitors. FCG/AC supercapacitors are readily made into commercially viable form factors such as coin cells that look promising for a sustainable energy future.

5.6 References

(1) El-Kady, M. F.; Shao, Y.; Kaner, R. B. *Nat. Rev. Mater.* **2016**, *1*, 16033.

(2) Winter, M.; Brodd, R. J. *Chem. Rev.* **2005**, *105*, 1021.

(3) González, A.; Goikolea, E.; Barrena, J. A.; Mysyk, R. *Renew. Sustainable Energy Rev.* **2016**, *58*, 1189.

(4) Shao, Y.; El-Kady, M. F.; Wang, L. J.; Zhang, Q.; Li, Y.; Wang, H.; Mousavi, M. F.; Kaner, R. B. *Chem. Soc. Rev.* **2015**, *44*, 3639.

(5) Simon, P.; Gogotsi, Y. *Nat. Mater.* **2008**, *7*, 845.

(6) Zhang, L. L.; Zhao, X. S. *Chem. Soc. Rev.* **2009**, *38*, 2520.

(7) Gamby, J.; Taberna, P. L.; Simon, P.; Fauvarque, J. F.; Chesneau, M. *J. Power Sources* **2001**, *101*, 109.

(8) Ahmadpour, A.; Do, D. D. *Carbon* **1996**, *34*, 471.

(9) Hulicova-Jurcakova, D.; Seredych, M.; Lu, G. Q.; Bandosz, T. J. *Adv. Funct. Mater.* **2009**, *19*, 438.

(10) Dastgheib, S. A.; Rockstraw, D. A. *Carbon* **2001**, *39*, 1849.

(11) Zhu, J.; Childress, A. S.; Karakaya, M.; Dandeliya, S.; Srivastava, A.; Lin, Y.; Rao, A. M.; Podila, R. *Adv. Mater.* **2016**, *28*, 7185.

(12) Yu, J.; Lu, W.; Pei, S.; Gong, K.; Wang, L.; Meng, L.; Huang, Y.; Smith, J. P.; Booksh, K. S.; Li, Q.; Byun, J.-H.; Oh, Y.; Yan, Y.; Chou, T.-W. *ACS Nano* **2016**, *10*, 5204.

(13) Zeiger, M.; Jackel, N.; Mochalin, V. N.; Presser, V. *J. Mater. Chem. A* **2016**, *4*, 3172.

(14) Le, V. T.; Kim, H.; Ghosh, A.; Kim, J.; Chang, J.; Vu, Q. A.; Pham, D. T.; Lee, J.-H.; Kim, S.-W.; Lee, Y. H. *ACS Nano* **2013**, *7*, 5940.

(15) Kim, C.; Choi, Y.-O.; Lee, W.-J.; Yang, K.-S. *Electrochim. Acta* **2004**, *50*, 883.

(16) You, B.; Kang, F.; Yin, P.; Zhang, Q. *Carbon* **2016**, *103*, 9.

(17) Chmiola, J.; Largeot, C.; Taberna, P.-L.; Simon, P.; Gogotsi, Y. *Science* **2010**, *328*, 480.

(18) Xu, J.; Tan, Z.; Zeng, W.; Chen, G.; Wu, S.; Zhao, Y.; Ni, K.; Tao, Z.; Ikram, M.; Ji, H.; Zhu, Y. *Adv. Mater.* **2016**, *28*, 5222.

(19) Fuertes, A. B.; Lota, G.; Centeno, T. A.; Frackowiak, E. *Electrochim. Acta* **2005**, *50*, 2799.

(20) Gogotsi, Y.; Simon, P. *Science* **2011**, *334*, 917.

(21) Schütter, C.; Ramirez-Castro, C.; Oljaca, M.; Passerini, S.; Winter, M.; Balducci, A. *J. Electrochem. Soc.* **2015**, *162*, A44.

(22) Chen, Y.; Zhang, X.; Zhang, H.; Sun, X.; Zhang, D.; Ma, Y. *RSC Adv.* **2012**, *2*, 7747.

(23) Xia, J.; Chen, F.; Li, J.; Tao, N. *Nat. Nanotechnol.* **2009**, *4*, 505.

(24) Zheng, C.; Zhou, X.; Cao, H.; Wang, G.; Liu, Z. *J. Power Sources* **2014**, *258*, 290.

(25) Wang, L. J.; El-Kady, M. F.; Dubin, S.; Hwang, J. Y.; Shao, Y.; Marsh, K.; McVerry, B.; Kowal, M. D.; Mousavi, M. F.; Kaner, R. B. *Adv. Energ. Mater.* **2015**, *5*.

(26) Liu, C. G.; Liu, M.; Li, F.; Cheng, H. M. *App. Phys. Lett.* **2008**, *92*, 143108.

(27) El-Kady, M. F.; Strong, V.; Dubin, S.; Kaner, R. B. *Science* **2012**, *335*, 1326.

Chapter 6.

A comparison of the electrochemical performance of different structures (1D, 2D, and 3D) based on Polyaniline/Graphene Micro-Supercapacitors

6.1 Abstract

Progress in micro-fabrication technology has enabled increasingly compact autonomous microsystems for applications ranging from distributed sensing and communications networks to implantable medical devices.[1, 2] Yet, power sources to enable their widespread adoption have not advanced nearly as rapidly. This is mainly due to the lack of energy dense materials and current fabrication techniques that rely on complicated and time-consuming processes. An efficient electron pathway and a short ionic diffusion distance can be achieved by the well-designed architecture of electrodes. As a result, a well-designed electrode structure can provide more electroactive sites and fast charge/discharge capability. According to nanostructured morphology, electrode materials can be classified as one-dimensional (1D) nanomaterials, two-dimensional (2D) nanomaterials, and three-dimensional (3D) nanomaterials. Here, we use a consumer grade LightScribe DVD burner for the direct fabrication of polyaniline micro-pseudo-capacitors (2D) on a large scale. The configuration of the device is based on polyaniline microelectrodes and welded polyaniline as a separator. This new design represents an important advance from current state-of-the-art micro-supercapacitors. Furthermore, we incorporated 1D-graphene fiber and 3D-laser scribed graphene with nanostructured polyaniline to produce hybrid micro-supercapacitors. The areal energy density and power density is further enhanced by utilizing the 1D structure of the fiber to reduce of the footprint of the entire system. Considering the ease of fabrication, flexibility,

and scalability, this technique could lead to the utilization of micro-supercapacitors as energy storage devices in future portable electronic and micro-electronic devices.

6.2 Introduction

The rapid development of wearable and portable electronics, wireless sensor networks and multifunctional microsystems drives an increasing demand for miniaturized energy storage.[1,2] At the same time, the desire to further miniaturize existing on-chip systems makes it attractive to develop power devices integrated with other elements.[3] Today, micro-power sources are essential for microelectronics, such as non-volatile memory, smart sensors, radio frequency identification tags, implantable medical devices and micro-electromechanical systems (MEMS).[4] While thin-film batteries have been considered as the prime candidates for these applications, they suffer from many limitations including limited cycle life, abrupt failure, poor low-temperature kinetics, and safety concerns associated with using lithium.[5] Supercapacitors can in principle solve these issues and provide a higher power density with maintenance-free operation.[5,6] The high surface-to-volume ratio of the active material creates the high energy and power densities of supercapacitors; this is even further enhanced in micro-supercapacitors.[7,8] Recently, notable advances have been achieved in the micro-supercapacitor field with most efforts focused on improving energy and power densities by investigating different electrode materials.[6] Generally, electric double layer capacitors (EDLCs), which store charge on the surfaces of high-surface area carbon materials, have been widely explored in the fabrication of micro-supercapacitors. Various nanostructured carbon materials have been utilized including activated carbons,[7] carbon nanotubes,[9] carbide-derived carbons,[5,10] onion-like carbon[8] and graphene.[11] Alternatively, pseudo-capacitive materials store charge through fast and reversible redox reactions and can offer higher

specific capacitance than EDLCs. This is particularly interesting because energy dense materials should enable further miniaturization of existing micro-supercapacitors (MSCs) and reduce the size of their footprint. Transition metal oxides such as ruthenium oxide[12] and manganese oxide,[13] and conducting polymers such as polypyrrole[14] and polyaniline[15-18] have been used as materials for pseudo-capacitive MSCs. Polyaniline can be considered as one of the most promising electrode materials, due to its unique ability to be doped/dedoped through acid/base interactions, and oxidation/reduction chemistry.[19] The conductivity of polyaniline increases reversibly with doping from the undoped insulating base form ($\sigma \leq 10^{-10}$ S cm^{-1}) to the fully doped, conducting salt form ($\sigma \geq 1$ S cm^{-1}). Conductivity can also be controlled either chemically or electrochemically by changing the oxidation state. These characteristics make polyaniline a promising material for many applications including sensors,[20] actuators,[21] electrochromic devices,[22] plastic nonvolatile memory,[23] water filtration membranes[24], and batteries.[25] Because of its high theoretical specific capacitance of around 2000 F g^{-1}, polyaniline is an ideal candidate for supercapacitors.[26,27] However, supercapacitors with conducting polymer electrodes generally suffer from limited stability during cycling. Previous research suggested that coupling nanostructured polyaniline to carbonaceous materials can improve the utilization of the pseudocapacitive properties of polyaniline and provide short transport pathways for ions and electrons.[28-32] It is believed that the excellent electrical and mechanical properties of graphene relieve the volume change of expansion and contraction of polyaniline during long-term charge/discharge processes.[33-36]

Recently, many researchers have focused on the concept that electrochemical performance may depend on electrode structures at varying dimensions. Herein, we synthesized polyaniline (PANI) and polyaniline/graphene-based materials for MSC electrodes, based on several macrostructures of varying dimensions, such as one-dimensional

(1D) fiber-type, two-dimensional (2D) films, and three-dimensional (3D) graphene foam. Laser scribed graphene/PANI (3D)-MSC exhibited the highest gravimetric energy (18.5 Wh kg^{-1}) and power (5,462 W kg^{-1}) densities compare to other 1D and 2D forms of MSCs. For the areal energy and power density, rGO-PANI fiber (1D)-MSC shows superior performance compare to the other MSCs. It can deliver a maximum areal energy and power density of 1.69 Wh cm^{-2} and 395 W cm^{-2}, respectively, which are the highest values among all MSCs reported to date.

6.3 Results and Discussion

6.3.1 Polyaniline micro-pseudo-capacitors

Recently, we have developed a simple technique for the patterning of polyaniline nanofiber films using a near infrared laser (780 nm) available in consumer grade LightScribe DVD burners.[37] Basically, a DVD disc is coated with a film of polyaniline nanofibers and then inserted into the drive for laser treatment. When light from the laser is absorbed by the nanostructured polyaniline, a photothermal effect occurs in which the absorbed light is converted into heat, leading to crosslinking of the molecular chains of polyaniline. This phenomenon is termed “laser welding” and is associated with a significant change in the electrical and optical properties of polyaniline. Since polyaniline nanofibers are poor heat conductors, the heat does not spread beyond the laser lines resulting in a well-defined separation between the welded and the non-welded areas. The high-resolution patterning along with a huge difference in electrical conductivity between pristine polyaniline (~1 S cm^{-1}) and welded polyaniline (10^{-8} S cm^{-1}) enables the direct fabrication of a new generation of polyaniline micro-pseudo-capacitors. These micro-pseudocapacitors employ the insulating properties of the welded polyaniline as a separator between pristine polyaniline

microelectrodes as shown in Figure 6.1A. This new and simplified architecture represents an important leap forward from current state-of-the-art micro-supercapacitors. In previous work, we showed that a LightScribe DVD burner can also be used for the direct writing of graphene MSCs from graphite oxide films.[11] Thus, it is important to clarify the differences between the laser scribing of graphene (LSG) and the laser welding of polyaniline, Figure 6.1B.

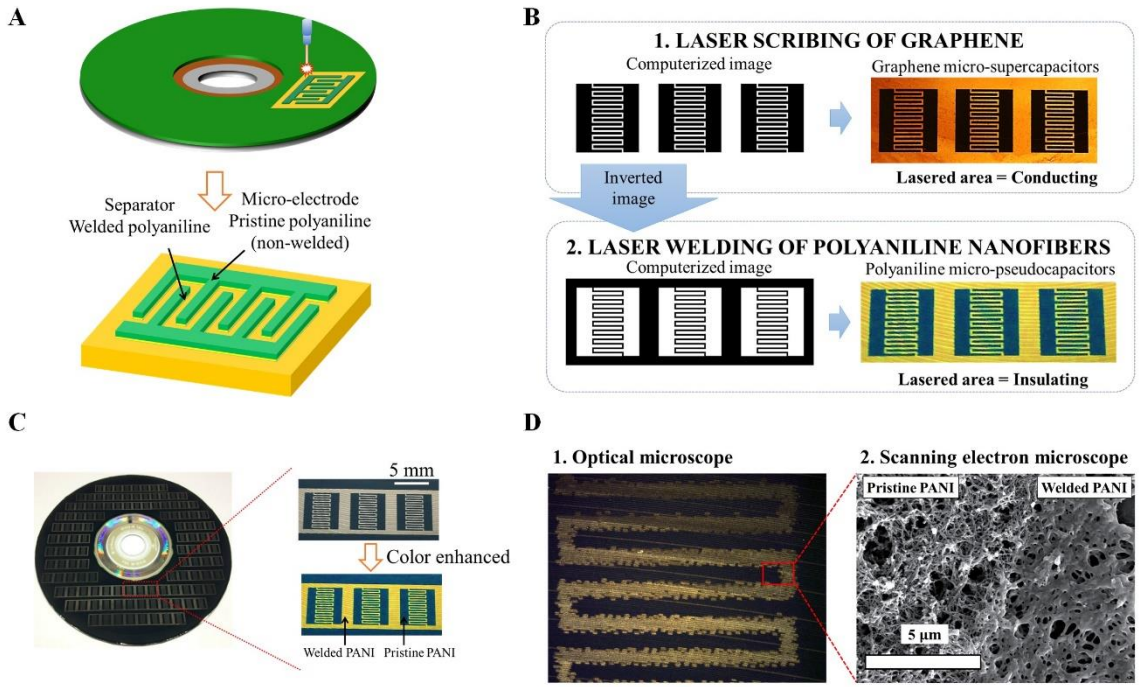

Figure 6.1. (A) Fabrication of polyaniline micro-pseudo-capacitors. Polyaniline film is coated on a DVD followed by laser patterning using a LightScribe DVD burner. (B) An explanation of the differences between the laser scribing of graphite oxide and the laser welding of polyaniline. The laser scribing process turns an electrically insulating graphite oxide golden brown film into an electrically conducting black 3D graphene film. In the laser welding process, non-welded electrically conductive, doped, green polyaniline nanofibers are converted to welded electrically insulating polyaniline represented by the yellow area. (C) The laser welding of polyaniline inside a DVD burner can be used for the fabrication of polyaniline micro-pseudo-capacitors on a large scale. (D) 1. An optical microscope image shows an interdigitated pattern of micro-pseudo-capacitors. 2. A scanning electron microscope (SEM) image of laser welded polyaniline nanofibers (right) in comparison to the pristine nanofibers before welding (left).

In the LSG process, wherever the laser hits the film, the graphite oxide becomes electrically conducting. For example, in LSG, a computerized image of an interdigitated pattern is printed on a graphite oxide film to produce graphene MSC. The inverse effect occurs during laser welding of polyaniline, i.e. wherever the laser hits the surface, it becomes electrically insulating. Although conventional microlithography processes are most commonly used in MSC fabrication, they are expensive and time-consuming and have thus limited the wide adoption of microscale supercapacitors. The present techniques avoid the difficulties associated with current lithographic processes: i.e. no need for templates, stamps, masks, thermal annealing, photoresists, clean rooms, and/or post-processing treatment of the polymer.[37] Furthermore, this technique can be used for the fabrication of planar polyaniline micro-pseudo-capacitors on a large scale. Figure 6.1C shows that over 100 well-defined micro-pseudo-capacitors can be produced on one DVD disc in less than 30 minutes.

The structure and morphology of laser welded polyaniline nanofibers electrodes have been investigated by optical and scanning electron microscopy (SEM). Fig. 6.1D (1) shows an optical microscope image demonstrating that the black area is pristine (non-welded) doped polyaniline nanofibers, whereas the yellow area is polyaniline after it has been laser welded. The detailed physical morphology of polyaniline nanofibers was analyzed by SEM, Fig. 1D (2). After the laser treatment, the morphology of fibers changed from the tangled nanofiber form (left) to the smooth melted form (right). Once polyaniline fibers absorb the laser light, the fiber chains start to cross-link leading to supramolecular fibers.

A flexible PANI micro-pseudo-capacitor made according to the laser welded method described above is shown in Figure 6.2A. For the electrolyte, gel-like polyvinyl alcohol (PVA)-H_2SO_4 was applied. Cyclic voltammetry (CV) of a typical PANI micro-pseudo-

capacitor are shown in Figure 6.2B and C. Two pairs of distinct peaks are observed at slow scan rates due to the redox transitions in PANI. The first pair can be ascribed to the redox transition of PANI between its leucoemeraldine form (semiconducting state) and its emeraldine (conducting) state, while the second pair is attributed to the emeraldine-pernigraniline transformation.[15]

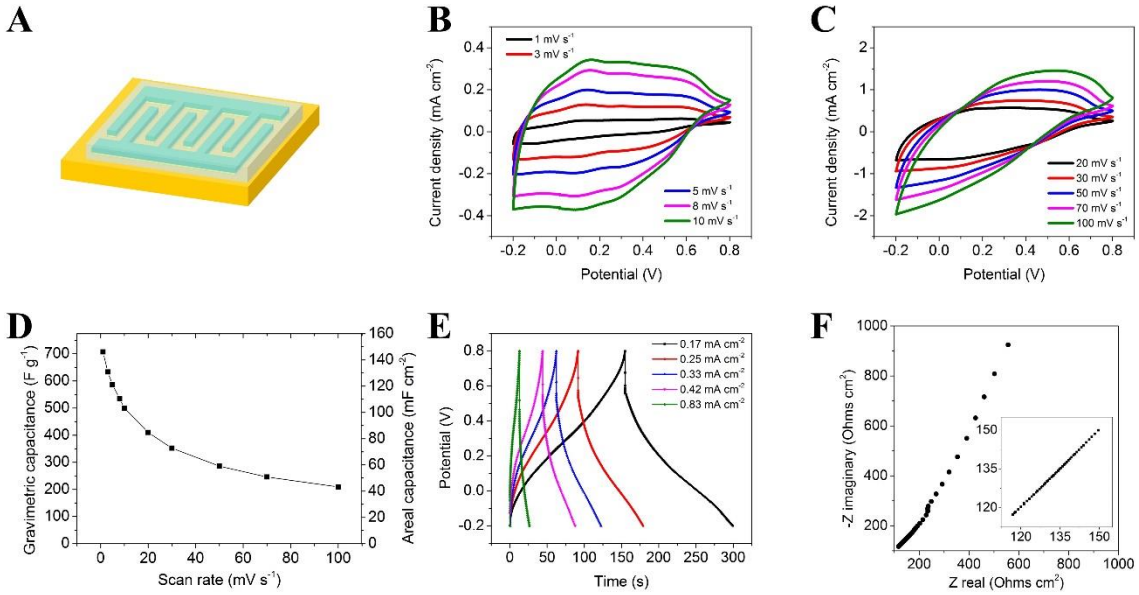

Figure 6.2. The electrochemical performance of a PANI-micro-pseudo-capacitor. (A) A schematic illustration showing the polyaniline interdigitated micro-pseudo-capacitor device after the addition of the electrolyte, polyvinyl alcohol (PVA)-H_2SO_4. CV profiles of the device at different scan rates of (B) 1, 3, 5, 8 and 10 mV s^{-1}, and (C) 20, 30, 50, 70, and 100 mV s^{-1}. (D) Gravimetric capacitance and areal capacitance of the device calculated based on the electrode with active materials only shown as a function of scan rate. (E) Galvanostatic charge/discharge (CC) curves at different current densities: 0.17, 0.25, 0.33, 0.42 and 0.83 mA cm^{-2}. (F) Nyquist plot with a magnified high-frequency region over a frequency range from 1 MHz to 0.01 Hz.

However, as the scan rate is increased to 100 mV s^{-1}, the redox peaks in the CV curve of the device become hard to find due to the large diffusion resistance. The PANI micro-pseudo-

capacitors exhibit extremely high specific capacitance up to 707 F g^{-1} which is about 40% of the theoretical specific capacitance of PANI (Figure 2D).[27] This is a direct result of the high surface area and electrochemical activity of the polyaniline nanofibers. The size reduction of the nanostructured PANI increases the contact surface area between the electrode and electrolyte and decreases the transport path length for both ions and electrons. This effect is even more pronounced when using a microstructured planar configuration. The detailed advantages of the interdigitated planar design with microstructured polyaniline will be discussed in Section 6.3. Another interesting aspect of these PANI micro-pseudo-capacitors is the high areal capacitance of up to 146 mF cm^{-2} which is much higher than the corresponding values for state-of-the-art EDLC micro-supercapacitors which range from 0.4 to 6 mF cm^{-2} (Figure 6.2D).[7,8,11,38-40] This high energy density per unit area is important for autonomous microsystems whose sizes are often determined by the size of the power supply. Increasing the areal capacity of the power source will reduce the size of the whole system, thus improving the efficiency of the design.[41] High specific capacitance per area is a critical requirement for practical supercapacitor electrodes and can be further improved by increasing the mass-loading of the active material. However, pursuing high mass-loading on conventional electrodes usually increases the ion and electron transport distance/resistance in the electrodes, thus preventing the full utilization of the active material and lower specific capacitances are often observed.[5,42,43] Interestingly, the areal capacitance of a PANI micro-pseudo-capacitor scales linearly with mass loading (Supplementary Figure S6.1). More importantly, the specific capacitance of PANI is not affected. The aggregation resistant properties of PANI nanofibers enable them to maintain their high accessible surface area and specific capacitance even upon increasing their film thickness. The representative charge/discharge (CC) curves for a PANI micro-pseudo-capacitor is shown in Figure 6.2E.

The discharge behavior of a PANI micro-pseudo-capacitor at a low scan rate of 0.17 mA cm^{-2} is nearly linear from 0.5 V to -0.2 V; however, the large IR drop of 0.3 V limits the power of this capacitor. As expected, electrochemical impedance spectroscopy (EIS) (Figure. 6.2F) shows a relatively high equivalent series resistance (ESR) of 117 Ω cm^2. This is possibly due to the relatively low electrical conductivity of polyaniline. The ESR can be reduced by using graphene substrates, the details of incorporating graphene substrates are discussed in the next section.

6.3.2 LSG/PANI micro-hybrid-supercapacitor

Making a hybrid capacitor by combing the pseudo-capacitive material polyaniline with the electric double layer capacitance of graphene is a proven solution that results in hybrid electrodes with lower ESR and improved capacity.[30-36] The high conductivity of LSG, its high electron transfer rate as well as its high surface area makes it an excellent substrate for growing polyaniline nanostructures.[37] Here, LSG interdigitated microelectrodes were produced directly on a graphite oxide coated DVD disc as described earlier. The LSG microelectrodes can be doped with polyaniline using the setup shown in Figure 6.3.

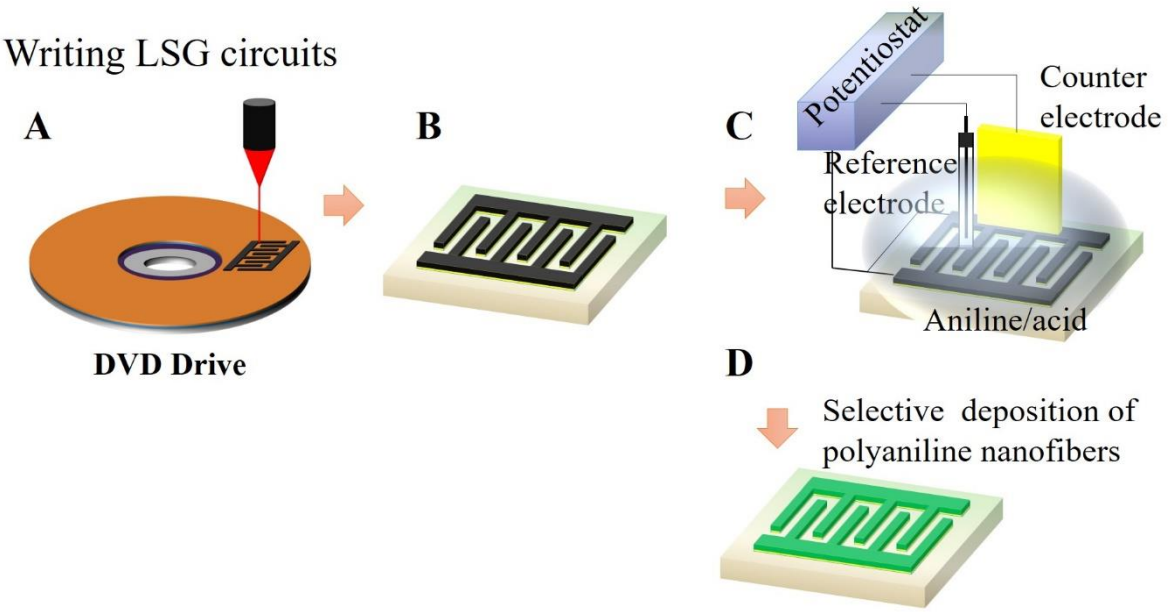

Figure 6.3. The fabrication process for LSG/PANI micro-supercapacitors: (A) First LSG micro-electrodes are printed on graphite oxide film. (B) The interdigitated micro-electrodes are then separated for the next steps. (C) Selective electro-deposition of PANI. (D) The produced LSG/PANI device.

Polyaniline is selectively electrodeposited on graphene using a three-electrode cell with graphene acting as the working electrode, an Ag/AgCl reference electrode, and a platinum foil counter electrode. Aniline monomers prefer to nucleate on the graphene surfaces, therefore nanostructured polyaniline (mainly nanofibers) appears to form no matter what acid dopant is used in the polymerization.

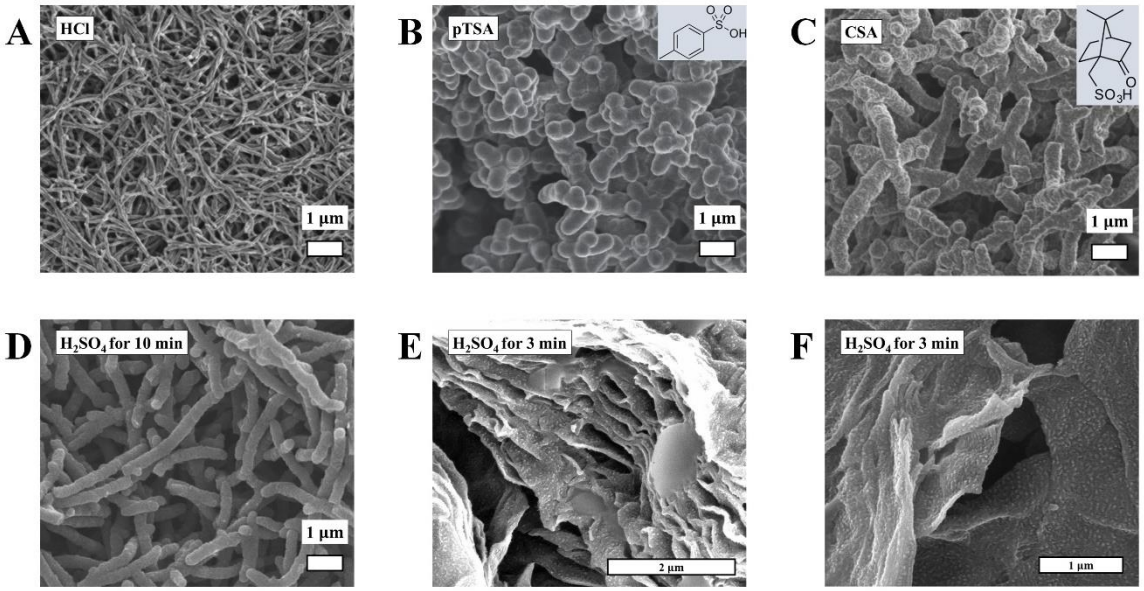

Figure 6.4. Scanning electron microscope (SEM) images of polyaniline films grown electrochemically on LSG from (A) HCl, (B) para-toluene sulfonic acid, p-TSA, (C) camphorsulfonic acid, CSA and (D, E and F) sulfuric acid, H_2SO_4 . (D) Polyaniline electrodeposited for 10 min and (E) for 3 min with a scale bar of 2 µm and (F) for 3 min with a scale bar of 1 µm.

However, the aspect ratio and the diameter of the formed nanofibers depend on the type of dopant, Figure 6.4 A-D. For example, very uniform and long nanofibers are observed in the SEM images after electropolymerization from mineral acids: HCl (Figure 6.4A) and H_2SO_4 (Figure 6.4D). The average diameter of the nanofibers is 500 nm when formed from H_2SO_4 and 100 nm for HCl. However, low aspect ratio nanofibers are produced when using organic acids dopants such as a p-toluene sulfonic acid (p-TSA) (Figure 6.4B) or camphor sulfonic acid (CSA) (Figure 6.4C). Moreover, the morphology of polyaniline corresponding to different deposition times was examined with an H_2SO_4 dopant. Figure 6.4D-F are the SEM images of LSG/PANI composites polymerized in H_2SO_4 at the reaction time for 10 min and 3 min. Figure 6.4E,F (3 min reaction) show homogeneous growth of polyaniline nanofibers on the surface of graphene, but the length of the fibers were short compared to 10 min (Fig

6.4D). We can conclude that most monomers tend to homogeneously nucleate after 3 min reaction time and start to form homogeneous nanofibers films.[44] With increasing the reaction time after 3 min, PANI molecular chains became longer and the nanofibers gradually grow, cover and block all the porous structures of LSG. However, Figure 6.4E,F (3 min disposition) maintain 3-dimensional porous architecture, which allows the electrolyte ions to enter the entire electroactive surface. Such a unique network structure is very attractive for an electrochemical electrode which allows for fast electron diffusion and provides short ion diffusion lengths.

CV and CC measurements (Figure S6.3A,B) were performed to explore the performance of the LSG/PANI hybrid electrodes made at different loadings of PANI. The mass loading of PANI to LSG is controlled by adjusting the deposition time. The current increases with PANI deposition time, leading to an increase in areal capacitance to ~1 F cm^{-2} obtained at a deposition time of 4 minutes, which is approximately 50 times higher than the value of bare LSG (Figure S6.3C). However, for the gravimetric capacitance, the 3 min-MSC shows the highest gravimetric capacitance up to 1200 F g^{-1} (Figure S6.3D). Moreover, the 3 min-MSC exhibits the fastest charge/discharge kinetics and high rate capability compared to the 4 min deposition MSC. For example, the 3 min MSC has a capacitance value of 1200 F g^{-1} (295 mF cm^{-2}) at a scan rate of 10 mV s^{-1}. This device maintains 70% of this value as the scan rate is increased to 100 mV s^{-1}, while the 4 min-MSC retains only 17% of the capacitance (150 F g^{-1} and 180 mF cm^{-2}) when tested under the same conditions. Figure 6.3E,F shows Ragone plots normalized by volume and mass; as expected, the 4 min-MSC delivered the highest volumetric energy density, but the lowest gravimetric power density. The 3 min-MSC exhibited the overall best electrochemical performance which is consistent

with the SEM images. Further detailed electrochemical measurements were carried out with the 3 min deposition MSC.

The electrochemical properties of 3 min deposition time of LSG/PANI –MSCs were assessed with PVA/H_2SO_4 gel electrolyte. Figure 6.5A shows the CV of the bare LSG-MSC and LSG/PANI-MSC, tested at a scan rate of 10 mV s^{-1}. The CV of the LSG/PANI exhibits two clear redox peaks with a significant increase in the capacitance compared to that of bare LSG, indicating that PANI contributes to the charge storage through reversible redox reactions. The specific capacitance of an LSG/PANI-MSC is about 6 times larger than the bare LSG-MSC. The increase of the capacitance of the LSG/PANI-MSC was also confirmed through the CC curves (Supplementary Figure S6.2A). Figure 6.5B shows thattwo redox peaks with rectangular CV shapes are maintained under different scan rates from 1 to 10 mV s^{-1}. Even at 100 mV s^{-1}, the CV retains a quasi-rectangular shape (Figure. S6.2B).

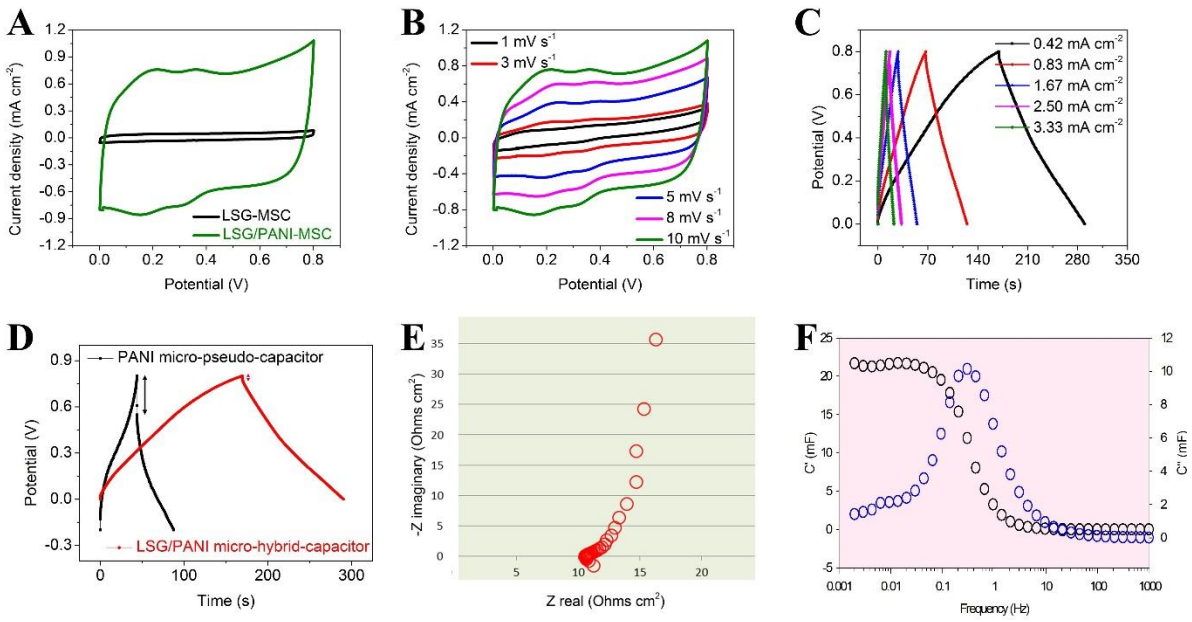

Figure 6.5. Evaluation of the electrochemical performance of an LSG/PANI micro-hybrid-capacitor (MSC). (A) CV curves of an LSG and an LSG/PANI MSC obtained at 10 mV s^{-1}. (B) CV profiles of an LSG/PANI MSC at different scan rates of 1, 3, 5, 8 and 10 mV s^{-1}. (C) CC curves at different current densities: 0.42, 0.83, 1.67, 2.50 and 3.33 mA cm^{-2}. (D) CC

curves of a PANI micro-pseudo-capacitor and an LSG/PANI micro-hybrid-capacitor tested at the same current density, 0.42 mA cm^{-2}. (E) Nyquist and (F) Bode plots of the PANI micro-pseudo-capacitor and LSG/PANI micro-hybrid-capacitor tested over a frequency range of 100 kHz to 0.01 Hz.

This can explain the excellent performance of the hybrid materials of LSG/PANI whose pseudo-capacitive properties from PANI can store charge through fast and reversible redox reactions along with surface charge storage on the conductive graphene. The specific capacitance of the LSG/PANI-MSC was calculated through its CV curves at 10 mV s^{-1} and determined to be 1248 F g^{-1} (295 mF cm^{-2}) per electrode based on the total active materials (LSG/PANI). The representative CC curves for the LSG/PANI micro-supercapacitor is shown in Figure 6.5D, the results for a PANI micro-pseudo-capacitor are also shown for comparison. The IR drop due to the internal resistance of the LSG/PANI micro-supercapacitor is hardly observed (0.009 V), which can be attributed to the improvement of the conductivity of the device by incorporating graphene. However, in a pure PANI micro-pseudo-capacitor a large 0.2 V IR drop was observed. The ideal shape of the CC curves under different current densities from 0.42 mA cm^{-2} to 16.7 mA cm^{-2} provides further evidence for the excellent electrochemical performance of the LSG/PANI-MSC (Figures 6.5C and Supplementary S6.2C). Further understanding of the fast ion diffusion/transfer kinetics of the LSG/PANI-MSC was gleaned from electrochemical impedance spectroscopy (EIS). The Nyquist Plot (Figure 6.5E) shows a nearly vertical line at low frequencies which reflects the excellent capacitive behavior of the LSG/PANI-MSC. From the extrapolation of the vertical portion of the Nyquist plot to the real axis, the ESR was estimated to be 10.3 Ω cm^2, which falls within the values expected for high power MSCs.[7,8,11,38-40] This contrasts with the PANI micro-pseudo-capacitor in which a very large (117 Ω cm^2) ESR was observed. A phase angle

of about −86.3° has been achieved which again confirms the good capacitive behavior of the LSG/PANI micro-supercapacitor (Figure 6.5F). The device is characterized by a relatively good relaxation time constant, τ_0 of 3.3 s with τ_0 being the minimum time needed to discharge all the energy from the device with an efficiency of greater than 50% .[45] The superior electrochemical performance of the LSG/PANI-MSC can be attributed to the favorable structure of the LSG/PANI for energy storage. Specifically, the high surface area along with the extremely high electron transfer rates on the surfaces of the LSG speeds up the charge/discharge kinetics. Also, the nanofiber structure of PANI provides a large number of electrochemically active sites that allows for fast and reversible surface redox reactions with high capacitance.

There have been two main types of micro-supercapacitors which differ by structure; the conventional sandwich structure in which two thin film electrodes are combined together to form the supercapacitor stack (Fig 6.6A). The other structure consists of interdigitated microelectrodes designed in a planar configuration (Fig 6.6B). In comparison, interdigitated MSCs have several advantages over the conventional stacked design.

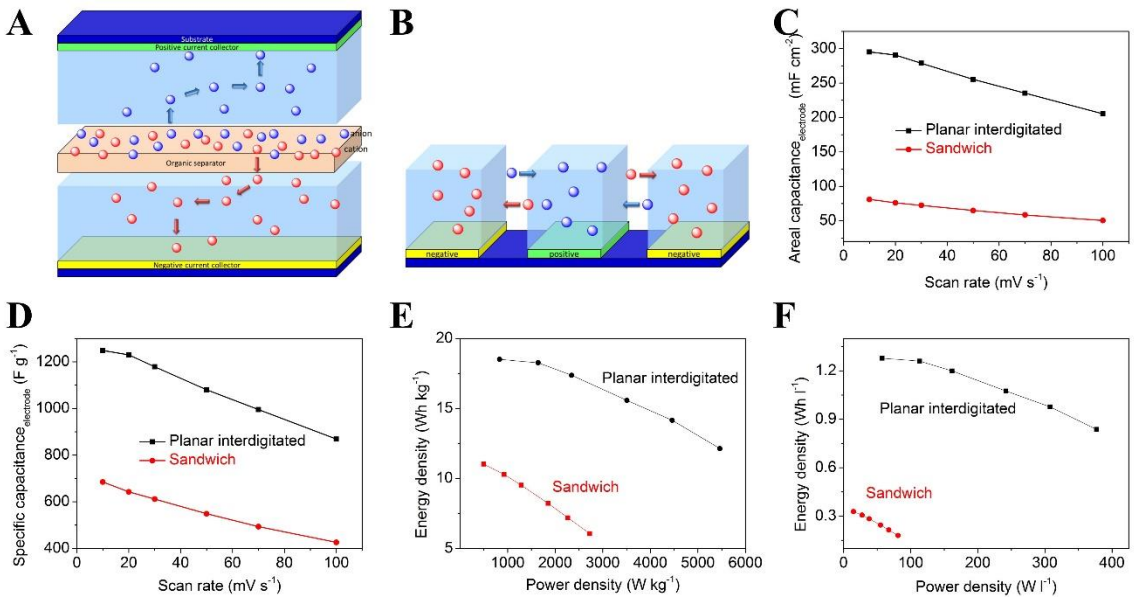

Figure 6.6. Schematic diagram showing the differences between the electrochemical properties of LSG/PANI-MSC in the (A) sandwich and (B) planar interdigitated structures. (C) Areal capacitance and (D) gravimetric capacitance of the sandwich type supercapacitor (SC) and planar interdigitated-MSC curves are shown as a function of scan rate. (E) A gravimetric Ragone plot and (F) a volumetric Ragone plot are shown to compare the energy density and power density of the sandwich type SC and the planar type MSC.

First, having both electrodes in the same plane is compatible with on-chip integration. Second, the traveling distance of the ions in the electrolyte, a major performance factor in supercapacitors, can be well controlled and shortened while eliminating the necessity of a separator, which is indispensable in the sandwich-type supercapacitors to prevent electrical shorting.[16] Third, the interdigitated structure can potentially be extended to three dimensions, which allows more materials to be loaded per unit area while leaving the mean ionic diffusion path unaffected. This architecture thus has the potential to achieve high power density and high energy density in a small footprint.[39,40] This theory finds support in Figures 6.6C-F. Figure 6C,D compare the specific capacitance between a sandwich and a planar structure. The planar design had an areal capacitance of 295 mF cm^{-2} which is 16 times larger than the

sandwich type value of 81 mF cm^{-2} (Figure 6.6C). Also the gravimetric capacitance of the planar design was about twice as large as the sandwich type (Figure 6.6D). Moreover, the energy and power density of these two types of supercapacitors can be compared through their gravimetric (Figure 6.6E) and volumetric (Figure 6.6F) Ragone plots. The planar design is superior in both energy and power density. Especially, in volumetric power density, the planar design can deliver up to 377 W l^{-1} which is about 5 times larger than the sandwich type.

6.3.3 rGO/PANI fiber hybrid-supercapacitor

In recent years, rapidly increasing research progress has been made in smart wearable electronics because of their potential applications in energy harvesting, micro-robotics, electronic textiles, epidermal and implantable medical devices.[46] One critical challenge is how to develop wearable energy storage devices, which are essential parts of powering the devices in a wearable system. Since the active materials in electrodes are the most important determinant of the performance of the energy storage system, it is crucial to study the rational design of macro-electrodes (1D fibers, 2D plates, and 3D foams) that can fit all the necessary requirements for a diverse design of flexible electronics.

One-dimensional flexible graphene fiber supercapacitors are of considerable interest for future wearable electronics due to their outstanding mechanical and electrical properties.[47-49] However, low energy density limits their development in the area of wearable high-energy density devices; therefore, enhancing their energy densities while retaining their high-power densities is critical. Herein, polyaniline (PANI) nanofibers are grown on reduced graphene oxide (rGO) fibers to improve the energy density. First, gel-

state GO fibers were made by wet-spinning into a coagulation bath of ethanol/water (1:1 v/v) solution with 25 wt% $CaCl_2$ (Figure 6.7A).

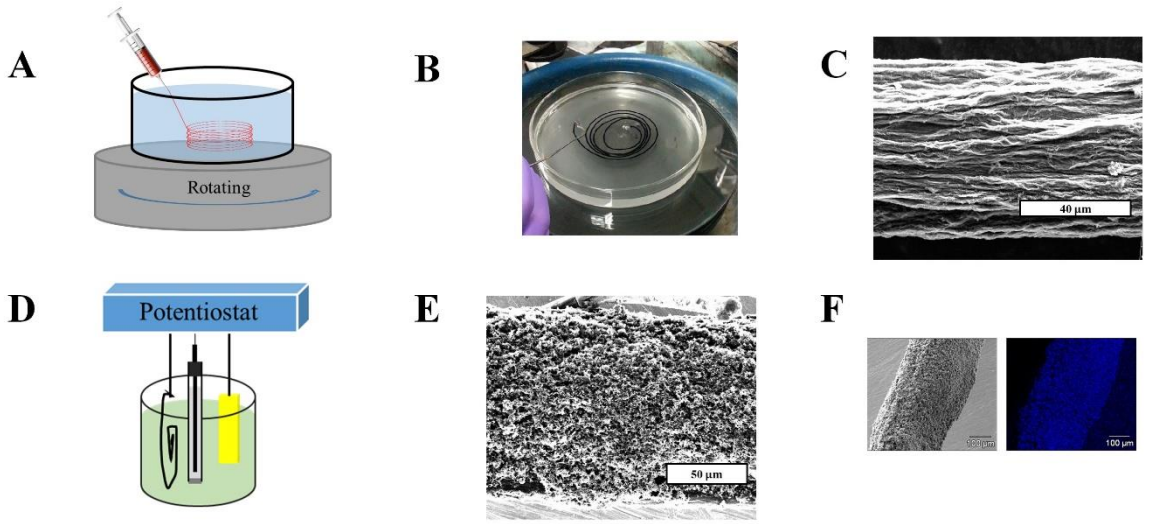

Figure 6.7. The fabrication process for rGO/PANI hybrid fibers: (A) Schematic of the apparatus used for wet-spinning of graphene oxide (GO) fibers. (B) Photograph of the as-spun GO fibers collected in the coagulation bath. (C) SEM images of reduced graphene oxide (rGO) fibers showing a corrugated surface; scale bar = 40 µm. (D) Schematic of the electrodeposition process for a rGO/polyaniline (PANI) hybrid fiber electrode. (E) SEM image of the outer surface of a rGO/PANI hybrid fiber with a 120.6 µm diameter. (F) SEM image of a rGO/PANI fiber (left), and an EDX nitrogen elemental map (right).

The photograph of the corresponding equipment is shown in Figure 6.7B. After drying, reduction of GO to rGO fibers was achieved by chemical reduction via hydrogen iodide (HI) at 80°C. The SEM images of the rGO fibers that were spun using the coagulation bath are shown in Figure 6.7C. Polyaniline is selectively electrodeposited on rGO fibers for 10 min at a constant potential of 0.78 V. The electrodeposition process is the same as that described in the previous section 6.3.2. Figure 6.7E shows the morphology of the composites of the rGO-PANI fiber, from which one can clearly distinguish the PANI nanofibers grown

on the rGO fibers. The diameter of the rGO/PANI fiber approximately doubled when compared to a bare rGO fiber (67.2 μm). The uniformity of the PANI nanofibers grown on the surfaces of the rGO fiber was confirmed through energy-dispersive X-ray spectroscopy (EDX) nitrogen mapping (Figure 6.7F).

We fabricated a rGO/PANI fiber-MSC using the obtained rGO/PANI hybrid fibers. Two rGO/PANI fibers were placed in parallel on a flexible polyester (PET) substrate and a polyvinyl alcohol (PVA)–H_2SO_4 gel electrolyte was spread on the top of the electrode (Figure 6.8A). The rGO/PANI fiber-MSC exhibits very distinct characteristic redox peaks and as expected, the bare rGO fiber-MSC shows an ideal rectangular CV shape (Figure 6.8B). The rGO/PANI fiber-MSC showed fast and reversible charge and discharge properties, as demonstrated by both variable scan rates of CV (Figure. 6.8C,D) and variable current densities of CC curves (Figure 6.8F). In recent time, Huang *et al*.[50] reported PANI nanoparticles grown on graphene fibers by an *in situ* chemical method, which demonstrated 66.6 mF cm^{-2} (compared to a theoretical expected value for a $C_{electrode}$ of 0.27 F cm^{-2}). While much better than this report, the capacitance of our hybrid supercapacitor using PANI could be improved. The highest capacitance of our rGO/PANI fiber-MSC electrode was 1414 F g^{-1} and 11.6 F cm^{-2} at a scan rate 10 mV s^{-1} which is a remarkable increase compared to a bare rGO fiber-MSC (455 F g^{-1} and 2.1 F cm^{-2}). This specific capacitance value is the best value reported so far in the literature for a fiber shaped supercapacitor.[51] This remarkable improvement indicates that our rGO/PANI fiber-MSC can provide efficient Faradaic processes for PANI combined with the rGO fiber framework. Figure 6.8E shows that the areal and gravimetric capacitance of the rGO/PANI fiber-MSC and bare rGO fiber-MSC is 1414 F g^{-1} at 10 mV s^{-1} and 798 F g^{-1} at 100 mV s^{-1}, corresponding to areal capacitances of 12 F cm^{-2} and 6.5 F cm^{-2}, respectively. The specific capacitance decayed to 56% of its

initial capacitance at 100 mV s^{-1}. With the incorporated the redox reaction, our system's rate capability was similar to previously reported EDLCs based on carbon nanotube-graphene fibers.[52]

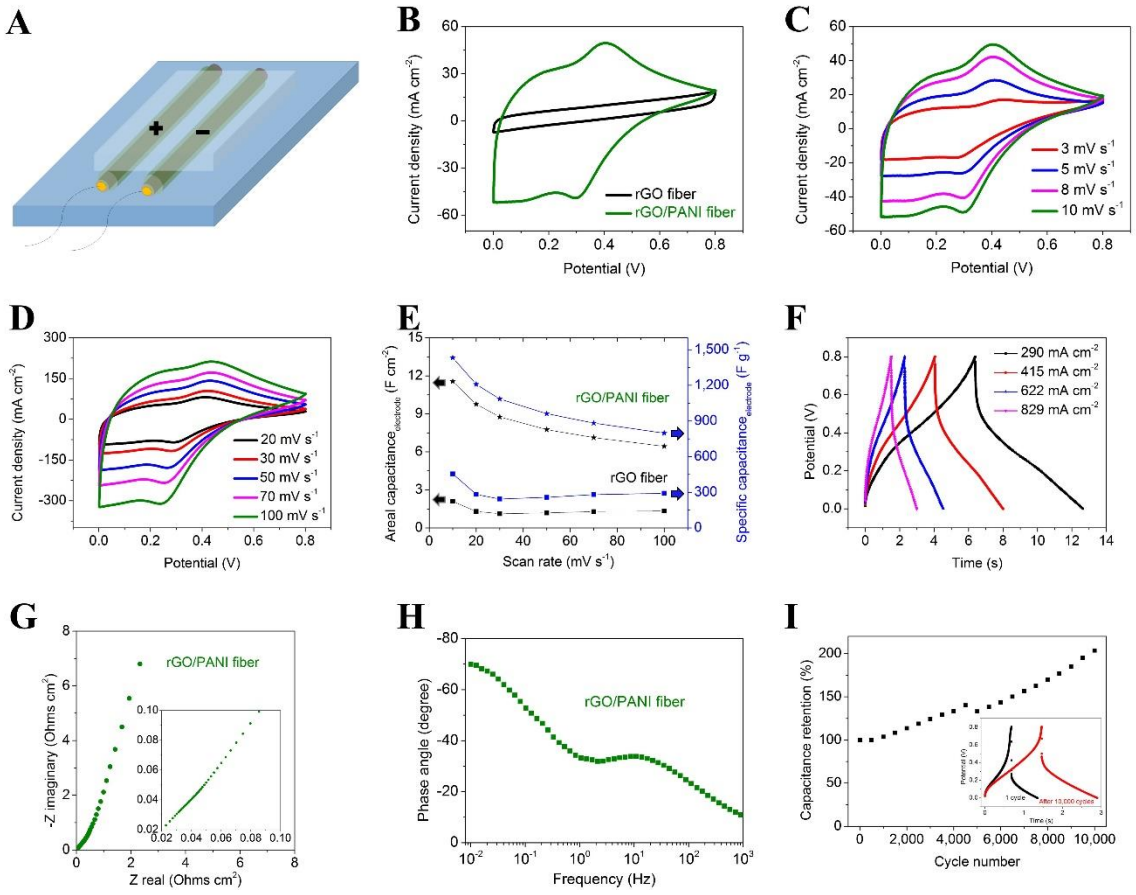

Figure 6.8. Evaluation of the electrochemical performance of a rGO/PANI fiber MSC. (A) Schematic of the fabrication of a rGO/PANI fiber-MSC based on the hybrid fiber electrodes. (B) CV curves of a bare rGO fiber and a rGO/PANI fiber-MSC obtained at 10 mV s^{-1}. (C) CV profiles of an rGO/PANI fiber-MSC at different scan rates of 3, 5, 8, 10, (D) 20, 30, 50, 70 and 100 mV s^{-1}. (E) The areal capacitance (left) and gravimetric capacitance (right) retention of bare rGO fibers and rGO/PANI fibers as a function of different scan rates. (F) CC curves at current densities of 290, 415, 622 and 829 mA cm^{-2}. (G) Nyquist and (H) Bode plots of the rGO/PANI fiber-MSC tested over a frequency range of 100 kHz to 0.01 Hz. (I) Long-term cycling stability of a rGO/PANI fiber-MSC.

EIS of the devices showed no semicircles in the high-frequency regions, which is due to small charge-transfer resistance (Figure 6.8G). The corresponding time constant τ_0 is 3.8 s (the inverse of the characteristic frequency f_0 (7 Hz) at a phase angle of -45° in the Bode phase plot, Figure 6.8F), also revealing an ideal capacitive behavior. The continuous electrochemical charge–discharge ability of the device has also been studied at 0.36 A cm^{-2} for 10,000 cycles. Figure 6.8I shows that our fiber MSC retains 200% of its initial capacitance after 10,000 cycles. An increase of capacitance to 200% from its initial value can be explained by the fiber nature of the nanostructure due to the high surface area and highly porous structure allowing electrolyte ions to continue to diffuse during electrochemical cycling thus enabling an activation process for pseudo-capacitance of PANI during cycling.

6.3.4 Summary of PANI/graphene materials for hybrid capacitors based on their structural complexity: one-dimensional (1D), two-dimensional (2D) and three-dimensional (3D)

In recent years, considerable efforts have been made on the understanding of the structural design of materials for supercapacitor electrodes.[53] Here, PANI-based materials in different forms i.e. 1D, 2D and 3D have been fabricated for performance evaluation as hybrid-capacitors. Table 6.1 summarizes the comparison of these three MSCs. Figure 6.9A,B,C compare the gravimetric (A), areal (B) and volumetric (C) specific capacitances among rGO/PANI fiber (1D), PANI (2D) and LSG/PANI (3D). The PANI micro-pseudo-capacitor shows a limited contribution to the capacitance of the 2D structure of PANI and performed with the lowest specific capacitances on all gravimetric, areal and volumetric categories. Compared to the 2D PANI pseudo-capacitor, the hybrid capacitors made of 1D

fibers and 3D foam structures possess higher electrical conductivities and superior overall electrochemical performances. A hybrid 3D interconnected network electrode can be achieved through the LSG substrate. The LSG/PANI-MSC can lead to high gravimetric capacitance at fast scan rates due to the porous structure which can allow for the effective diffusion of electrolyte ions.

Table 6.1. Comparison of Summarized Data for GO-PANI-Fiber-MSC (1D), PANI-MSC (2D) and LSG/PANI-MSC (3D)

Material	rGO/PANI-Fiber	PANI	LSG/PANI
Dimensionality	1D	2D	3D
Method	1. Wet-spinning 2. Electrodepositon	1. Chemical polymerization 2. Drop-cast	1. Laser-Scribing 2. Electrodeposition
Electrode capacitance (of polyaniline only)	1,887 F g^{-1}	500 F g^{-1}	1,711 F g^{-1}
Areal capacitance (electrode)	11,559 mF cm^{-2}	103 mF cm^{-2}	295 mF cm^{-2}
Volumetric capacitance	305 F cm^{-3}	25.3 F cm^{-3}	76.1 F cm^{-3}
Gravimetric energy (active material)	16.4 Wh kg^{-1}	6.58 Wh kg^{-1}	18.5 Wh kg^{-1}
Areal energy	1.69 Wh cm^{-2}	0.13 Wh cm^{-2}	0.43 Wh cm^{-2}
Volumetric energy (whole stack)	7.57 Wh l^{-1}	0.39 Wh l^{-1}	1.28 Wh l^{-1}
Gravimetric power (active material)	3.82 kW kg^{-1}	0.908 kW kg^{-1}	5.46 kW kg^{-1}
Areal power	395 W cm^{-2}	17.8 W cm^{-2}	127 W cm^{-2}
Volumetric power (whole stack)	1.77 W cm^{-3}	0.0538 W cm^{-3}	0.377 W cm^{-3}
Structure			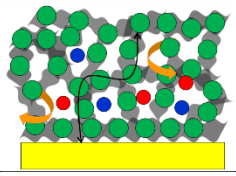

1D fiber based supercapacitors have great potential for wearable electronic applications due to their small volume and high flexibility. Therefore, the resultant rGO/1D-PANI-fiber exhibits the highest volumetric capacity of 305 F cm^{-3}, which is five times higher than the

3D-LSG/PANI-MSC. The power and energy density of the MSC is another important parameter for evaluating energy storage devices. Therefore, the final evaluation of the performance of PANI-based MSCs were carried out by comparisons done in Ragone plots (Figure 6.9D,E,F). Figure 6.9D show that LSG/PANI (3D)-MSC exhibited the highest gravimetric energy and power densities compared to two other forms of MSCs. The maximum energy density of 18.5 Wh kg^{-1} (with a power density of 833 W kg^{-1}) and power density of 5,462 W kg^{-1} (with an energy density of 12.1 Wh kg^{-1}) have been achieved using symmetric LSG/PANI-MSCs based on the total mass of active materials.

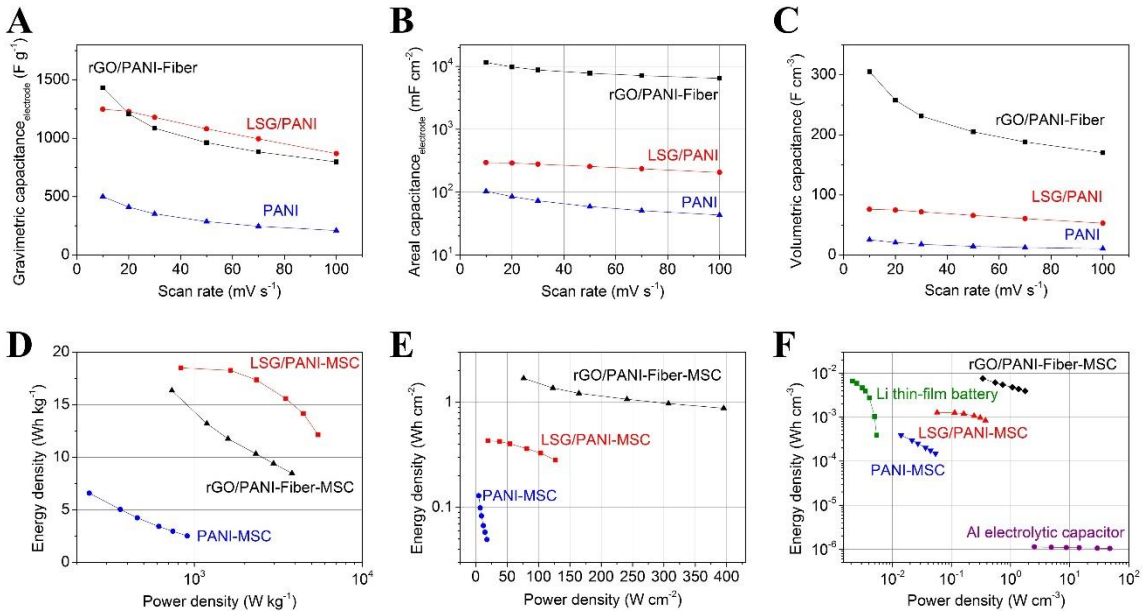

Figure 6.9. Comparison of the rGO-PANI-Fiber-MSC (1D), PANI-MSC (2D) and LSG/PANI-MSC (3D). The specific capacitances were normalized by (A) mass, (B) area and (C) volume. Power and energy densities were normalized by (D) mass, (E) area, and (F) volume.

A Ragone plot based on areal (Figure 6.9E) and volumetric (Figure 6.9F) densities are normalized by the whole device including electrodes, substrate, and gel electrolyte. Our rGO-PANI fiber MSC showed superior performance compared to other MSCs. The device

can deliver an areal energy density of 1.69 Wh cm^{-2} at 76.2 W cm^{-2} power density, which are much higher values than many recently reported SCs, such as a symmetric rGO-PANI nanofiber 3D based SC (0.13 mWh cm^{-2} and 2.1 mW cm^{-2})[54] and an RGO/ SWCNT fiber 1D based SC (0.016 mWh cm^{-2} and 2.84 mW cm^{-2})[52]. To our knowledge, the areal energy and power density in this work is the highest value among all MSCs reported to date. Also, our 1D fiber form MSC can deliver a high volumetric energy density of 7.57 mWh cm^{-3} at 0.34 W cm^{-3} power density, which is higher energy density than those of the reported rGO-PANI nanofibers 3D based SC (3.6 mWh cm^{-3} and 0.06 W cm^{-3})[54], LSG based SC in ionic liquid (1.36 mWh cm^{-3})[55] and RGO/ SWCNT fiber 1D based SC (6.3 mWh cm^{-3})[52]. Energy density is even comparable to a 4 V/500 lithium thin film batteries (0.3–10 mWh cm^{-3}); however, our fiber-based MSC can deliver two orders of magnitude higher power density.[8]

6.4 Experimental Section

6.4.1 Fabrication of polyaniline micro-pseudo-capacitors

Aniline (3.2 mmol) was dissolved in 1.0 M HCl (10 mL) and the oxidant ammonium peroxydisulfate (0.08 mmol) was also dissolved in 1.0 M HCl (10 mL) in another bottle: the two solutions were mixed and stirred for 30 s. The mixture was allowed to polymerize overnight. In order to remove the monomer and other impurities, dialysis tubing (wet cut-off between 12,000 and 14,000) were used. After the dialysis step, the polyaniline nanofiber solutions were diluted by a factor of 5 and drop-cast onto poly(ethylene terephthalate) (PET) substrates. The films were affixed onto LightScribe CD/DVD disks and then inserted into a DVD drive for laser patterning. Interdigitated micro-patterned designs were directly LightScribed on the polyaniline film. For electrochemical characterization of the polyaniline micro-pseudo-capacitors, copper tape was glued to the electrodes using silver paint and

polyimide tape was used to cover the copper tape. Finally, the gel electrolyte (PVA–H_2SO_4) was drop-cast onto the interdigitated electrode area (0.8 cm x 0.3 cm; 24.8 µg). The PVA-H_2SO_4 gel electrolyte was prepared by mixing 1.0 g PVA powder with 1.0 g H_2SO_4 in 10 ml DI water and subsequent heating under stirring to 80°C until the solution becomes clear.

6.4.2 Fabrication of LSG/PANI micro-supercapacitors

The LSG framework was also prepared by a LightScribe DVD burner with graphite oxide (GO). The GO solution (2 mg ml^{-1}) was drop-cast onto the PET covered DVD disk and left to dry overnight. Appropriate interdigitated patterns were printed onto GO films to make micro-supercapacitors. Once a LSG micro-supercapacitor was prepared, the polyaniline was electrodeposited from 0.3 M aniline in 1.0 M acid solutions such as HCl, p-toluene sulfonic acid (p-TSA), camphorsulfonic acid (CSA) and H_2SO_4 using a three-electrode setup. LSG was used as the working electrode, an Ag/AgCl as the reference electrode and a platinum foil was used as the counter electrode. The deposition was achieved by applying a constant voltage of 0.78 V for 3 min, 4 min, 5 min or 10 min. The 3 min electrodeposition with 1.0 M H_2SO_4 gave the best overall electrochemical performance. For electrochemical characterization of the LSG/PANI micro-hybrid-capacitors, copper tape and silver paint were applied to the electrode and the gel electrolyte was drop-cast onto the interdigitated electrode area (0.8 cm x 0.3 cm; 28.4 µg).

6.4.3 Fabrication of rGO/PANI fiber-supercapacitors

Preparation of rGO-fibers by wet-spinning: GO dispersion (7.5 mg ml^{-1}) was transferred to a syringe and injected at flow rates around 10 mL h^{-1} into a rotating Petri dish that contained the coagulation bath. The coagulation bath contained an ethanol/water (1:1

v/v) solution with 25 wt% $CaCl_2$. After coagulation, the GO fibers were immersed in 30 wt% HI solution for 24 h at 80°C for reduction. Dried rGO fibers were obtained by ethanol washing and then air-drying of the fibers under tension. Once the rGO fibers were prepared, the polyaniline was electrodeposited from 0.3 M aniline in 1.0 M H_2SO_4 for using a three-electrode setup by applying a constant voltage of 0.78 V for 10 min. The diameter of the rGO/PANI fibers was 120.6 µm and the supercapacitors were tested with a 1 cm length (97.4 µg). Two rGO/PANI fibers were put in parallel onto a flexible polyester (PET) substrate and gel electrolyte was spread on the top of the electrode. The 1 cm length of the rGO/PANI fibers were exposed to the electrolyte. The distance between the two electrodes was about 30 µm. The total volume of the rGO/PANI fiber-MSC, including the two fibers and the solid electrolyte, was estimated to be 4.2×10^{-4} cm^3. The total device area was 0.028 cm^2.

6.5 Conclusions

In summary, we compared the electrochemical performance of a 1D-rGO/PANI fiber-MSC, a 2D-PANI, and a 3D LSG/PANI MSCs. To make the 2D-PANI-MSC, a simple and scalable approach to fabricating interdigitated MSCs via coating a PANI nanofiber film and subsequent laser patterning was used. The 1D-MSC and the 3D-MSC were fabricated by electrodeposition on LSG fiber and 3D foam, respectively. The 1D-MSC showed an outstanding electrochemical performance with a specific areal capacitance of 12 F cm^{-2} which is much higher than current state-of-the-art EDL micro-supercapacitors. Such an efficient approach can drastically increase the density of micro-supercapacitors on a chip. This also reduces their complexity by removing intricate interconnects from bulky energy storage devices,[56] thus paving the way for efficient miniaturized flexible and portable electronic devices.

6.6 Appendix to Chapter 6

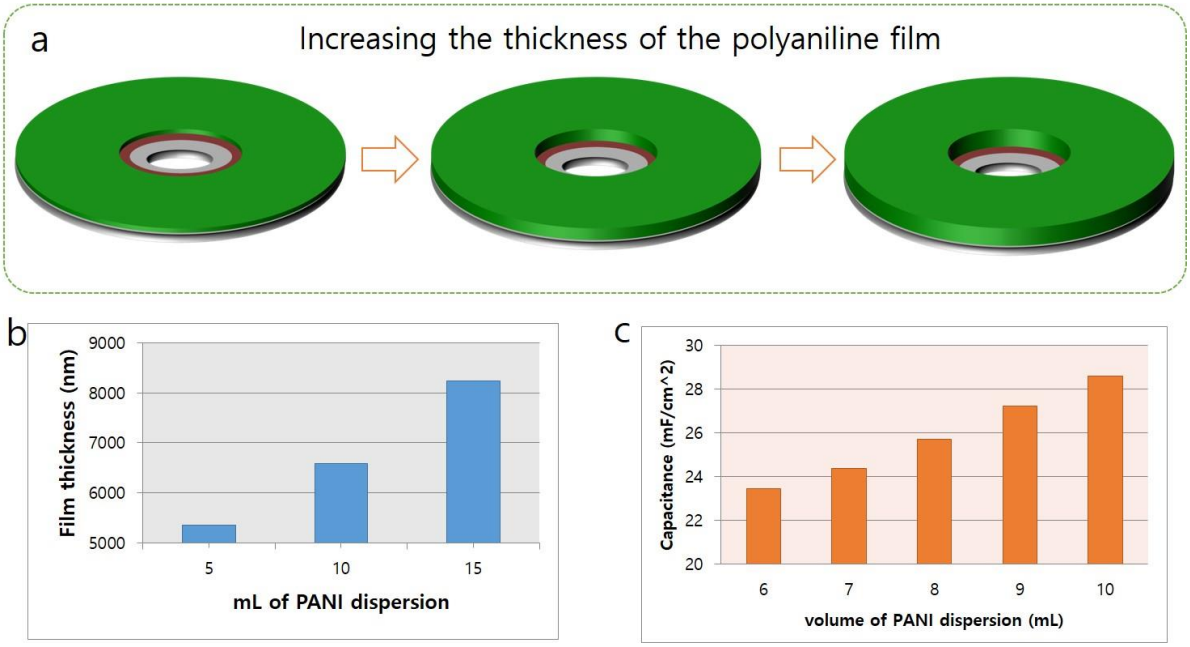

Supplementary Figure S6.1 Boosting the areal capacitance of PANI micro-pseudo-capacitors by increasing the mass loading of PANI. (a) Schematic diagram showing increased thickness of the PANI film. (b) The thickness of the PANI film as a function of the volume of the PANI nanofiber dispersion. (c) Areal capacitance of the PANI micro-pseudo-capacitor as a function of mass loading (represented by the volume of the dispersion).

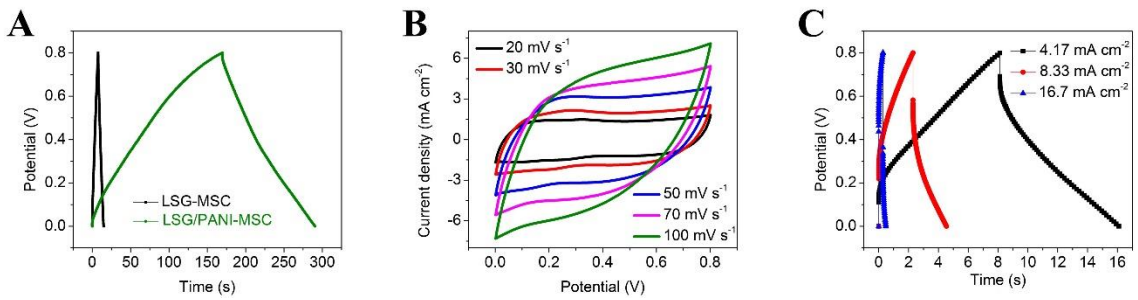

Supplementary Figure S6.2 Evaluation of the electrochemical performance of LSG/PANI-MSC. (A) CC curves of an LSG-MSC and LSG/PANI-MSC obtained at 0.42 mA cm^{-2}. (B) CV profiles of an LSG/PANI-MSC at different scan rates of 20, 30, 50, 70 and 100 mV s^{-1}. (C) CC curves at different current densities 4.17, 8.33 and 16.7 mA cm^{-2}.

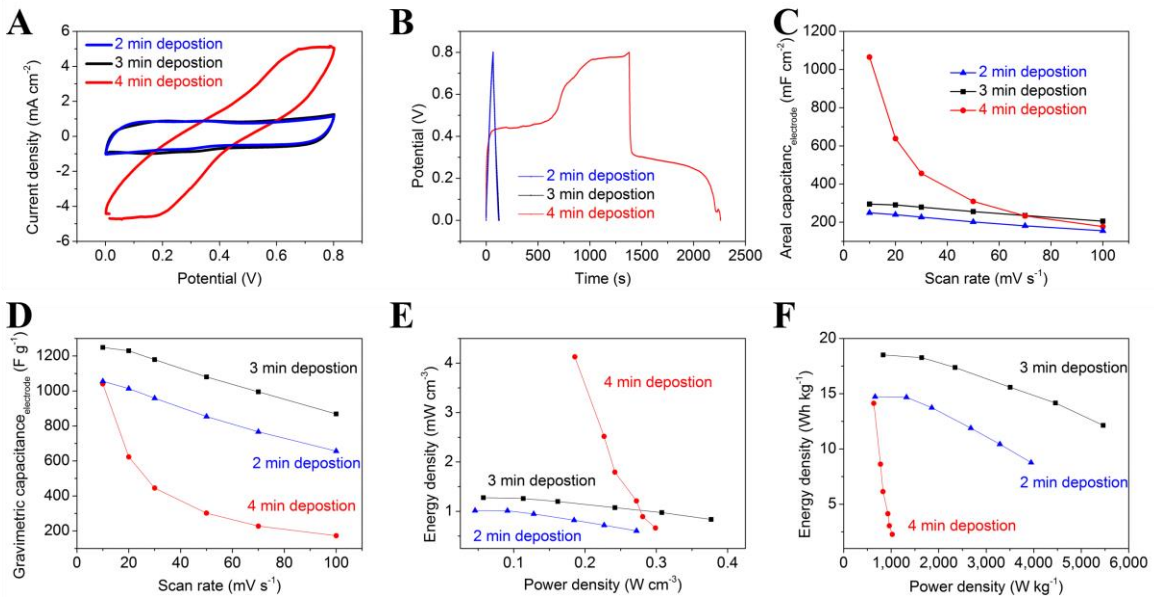

Supporting Figure S6.3 The electrochemical performance of an LSG/PANI micro-supercapacitor with different electropolymerization times (2, 3 and 4 min). (A) CV profiles for LSG/PANI for 2, 3 and 5 min depositions, tested at a scan rate of 10 mV s^{-1}. (B) CC curves for devices at a current density of 0.42 mA cm^{-2}. (C) Areal and (D) gravimetric capacitances of the three different devices as a function of scan rate. Ragone plots were normalized by (E) volume and (F) mass.

6.7 References

(1) Oudenhoven, J. F. M.; Vullers, R. J. M.; van Schaijk, R. *Internat. J. Energy Res.* **2012**, *36*, 1139

(2) Prescott, J. H.; Lipka, S.; Baldwin, S.; Sheppard, N. F.; Maloney, J. M.; Coppeta, J.; Yomtov, B.; Staples, M. A.; Santini, J. T. *Nature Biotechnol.* **2006**, *24*, 437.

(3) Shen, C.; Wang, X.; Zhang, W.; Kang, F. *J. Power Sources* **2011**, *196*, 10465.

(4) Lai, W.; Erdonmez, C. K.; Marinis, T. F.; Bjune, C. K.; Dudney, N. J.; Xu, F.; Wartena, R.; Chiang, Y.-M. *Adv. Mater.* **2010**, *22*, E139.

(5) Chmiola, J.; Largeot, C.; Taberna, P.-L.; Simon, P.; Gogotsi, Y. *Science* **2010**, *328*, 480.

(6) Beidaghi, M.; Wang,C. Proc. SPIE, **2012**, 837708.

(7) Pech, D.; Brunet, M.; Taberna, P.-L.; Simon, P.; Fabre, N.; Mesnilgrente, F.; Conédéra, V.; Durou, H. *J. Power Sources* **2010**, *195*, 1266

(8) Pech, D.; Brunet, M.; Durou, H.; Huang, P.; Mochalin, V.; Gogotsi, Y.; Taberna, P.-L.; Simon, P. *Nat. Nanotechnol.* **2010**, *5*, 651.

(9) Chen, W.; Beidaghi, M.; Penmatsa, V.; Bechtold, K.; Kumari, L.; Li, W. Z.; Wang, C. *IEEE Transactions on Nanotechnology* **2010**, *9*, 734.

(10) Heon, M.; Lofland, S.; Applegate, J.; Nolte, R.; Cortes, E.; Hettinger, J. D.; Taberna, P.-L.; Simon, P.; Huang, P.; Brunet, M.; Gogotsi, Y. *Energ. Environ. Sci.* **2011**, *4*, 135.

(11) El-Kady, M. F.; Kaner, R. B. *Nat. Commun.* **2013**, *4*, 1475.

(12) Liu, C.-C.; Tsai, D.-S.; Susanti, D.; Yeh, W.-C.; Huang, Y.-S.; Liu, F.-J. *Electrochim. Acta* **2010**, *55*, 5768.

(13) Xue, M.; Xie, Z.; Zhang, L.; Ma, X.; Wu, X.; Guo, Y.; Song, W.; Li, Z.; Cao, T. *Nanoscale* **2011**, *3*, 2703.

(14) Beidaghi, M.; Wang, C. *Electrochim. Acta* **2011**, *56*, 9508.

(15) Wang, K.; Zou, W.; Quan, B.; Yu, A.; Wu, H.; Jiang, P.; Wei, Z. *Adv. Energ. Mater.* **2011**, *1*, 1068.

(16) Xue, M.; Li, F.; Zhu, J.; Song, H.; Zhang, M.; Cao, T. *Adv. Funct. Mater.* **2012**, *22*, 1284.

(17) Wang, X.; Sumboja, A.; Foo, W. L.; Yan, C. Y.; Tsukagoshi, K.; Lee, P. S. *RSC Adv.* **2013**, *3*, 15827.

(18) Liu, W.; Yan, X.; Chen, J.; Feng, Y.; Xue, Q. *Nanoscale* **2013**, *5*, 6053.

(19) Li, D.; Huang, J.; Kaner, R. B. *Acc. Chem. Res.* **2009**, *42*, 135.

(20) Huang, J.; Virji, S.; Weiller, B. H.; Kaner, R. B. *J. Am. Chem. Soc.* **2003**, *125*, 314.

(21) Baker, C. O.; Shedd, B.; Innis, P. C.; Whitten, P. G.; Spinks, G. M.; Wallace, G. G.; Kaner, R. B. *Adv. Mater.* **2008**, *20*, 155.

(22) D'Arcy, J. M.; Tran, H. D.; Tung, V. C.; Tucker-Schwartz, A. K.; Wong, R. P.; Yang, Y.; Kaner, R. B. *Proc. Natl. Acad. Sci. U.S.A.* **2010**, *107*, 19673.

(23) Tseng, R. J.; Huang, J.; Ouyang, J.; Kaner, R. B.; Yang *Nano Lett.* **2005**, *5*, 1077.

(24) Guillen, G. R.; Farrell, T. P.; Kaner, R. B.; Hoek, E. M. V. *J. Mater. Chem.* **2010**, *20*, 4621.

(25) Nakajima, T.; Kawagoe, T. *Synth. Met.* **1989**, *28*, 629.

(26) Wang, K.; Wu, H.; Meng, Y.; Wei, Z. *Small* **2014**, *10*, 14.

(27) Li, H.; Wang, J.; Chu, Q.; Wang, Z.; Zhang, F.; Wang, S. *J. Power Sources* **2009**, *190*, 578.

(28) Wang, Y. G.; Li, H. Q.; Xia, Y. Y. *Adv. Mater.* **2006**, *18*, 2619.

(29) Wang, Y.; Yang, X.; Qiu, L.; Li, D. *Energ. Environ. Sci.* **2013**, *6*, 477.

(30) Wu, Q.; Xu, Y.; Yao, Z.; Liu, A.; Shi, G. *ACS Nano* **2010**, *4*, 1963.

(31) Wang, D.-W.; Li, F.; Zhao, J.; Ren, W.; Chen, Z.-G.; Tan, J.; Wu, Z.-S.; Gentle, I.; Lu, G. Q.; Cheng, H.-M. *ACS Nano* **2009**, *3*, 1745.

(32) Wang, H.; Hao, Q.; Yang, X.; Lu, L.; Wang, X. *Nanoscale* **2010**, *2*, 2164.

(33) Zhou, S.; Zhang, H.; Wang, X.; Li, J.; Wang, F. *RSC Adv.* **2013**, *3*, 1797.

(34) Huang, F.; Lou, F.; Chen, D. *ChemSusChem.* **2012**, *5*, 888.

(35) Yan, J.; Wei, T.; Shao, B.; Fan, Z.; Qian, W.; Zhang, M.; Wei, F. *Carbon* **2010**, *48*, 487.

(36) Peng, C.; Zhang, S.; Jewell, D.; Chen, G. Z. *Prog. Nat. Sci.* **2008**, *18*, 777.

(37) Strong, V.; Wang, Y.; Patatanyan, A.; Whitten, P. G.; Spinks, G. M.; Wallace, G. G.; Kaner, R. B. *Nano Lett.* **2011**, *11*, 3128.

(38) Miller, J. R.; Outlaw, R. A.; Holloway, B. C. *Science* **2010**, *329*, 1637.

(39) Beidaghi, M.; Wang, C. *Adv. Funct. Mater.* **2012**, *22*, 4501.

(40) Gao, W.; Singh, N.; Song, L.; Liu, Z.; Reddy, A. L. M.; Ci, L.; Vajtai, R.; Zhang, Q.; Wei, B.; Ajayan, P. M. *Nat. Nanotechnol.* **2011**, *6*, 496.

(41) Mao, Y.; Zhao, P.; McConohy, G.; Yang, H.; Tong, Y.; Wang, X. *Adv. Energ. Mater.* **2014**, *4*, 1301624.

(42) Luo, J.; Jang, H. D.; Huang, J. *ACS Nano* **2013**, *7*, 1464.

(43) Lu, Z.; Yang, Q.; Zhu, W.; Chang, Z.; Liu, J.; Sun, X.; Evans, D. G.; Duan, X. *Nano Research* **2012**, *5*, 369.

(44) Liu, X.; Shang, P.; Zhang, Y.; Wang, X.; Fan, Z.; Wang, B.; Zheng, Y. *J. Mater. Chem. A* **2014**, *2*, 15273.

(45) Taberna, P. L.; Simon, P.; Fauvarque , J. F. *J. Electrochem. Soc.* **2003**, *150*, A292.

(46) Liu, L.; Yu, Y.; Yan, C.; Li, K.; Zheng, Z. *Nat. Commun.* **2015**, *6*, 7260.

(47) Yoon, S. S.; Lee, K. E.; Cha, H.-J.; Seong, D. G.; Um, M.-K.; Byun, J.-H.; Oh, Y.; Oh, J. H.; Lee, W.; Lee, J. U. *Sci. Rep.* **2015**, *5*, 16366.

(48) Kou, L.; Huang, T.; Zheng, B.; Han, Y.; Zhao, X.; Gopalsamy, K.; Sun, H.; Gao, C. *Nat. Commun.* **2014**, *5*, 3754.

(49) Aboutalebi, S. H.; Jalili, R.; Esrafilzadeh, D.; Salari, M.; Gholamvand, Z.; Aminorroaya Yamini, S.; Konstantinov, K.; Shepherd, R. L.; Chen, J.; Moulton, S. E.; Innis, P. C.; Minett, A. I.; Razal, J. M.; Wallace, G. G. *ACS Nano* **2014**, *8*, 2456.

(50) Huang, T.; Zheng, B.; Kou, L.; Gopalsamy, K.; Xu, Z.; Gao, C.; Meng, Y.; Wei, Z. *RSC Adv.***2013**, *3*, 23957.

(51) Yu, D.; Qian, Q.; Wei, L.; Jiang, W.; Goh, K.; Wei, J.; Zhang, J.; Chen, Y. *Chem. Soc. Rev.* **2015**, *44*, 647.

(52) Yu, D.; Goh, K.; Wang, H.; Wei, L.; Jiang, W.; Zhang, Q.; Dai, L.; Chen, Y. *Nat. Nanotechnol.* **2014**, *9*, 555.

(53) Ke, Q.; Wang, J. *J. Materiomics* **2016**, *2*, 37.

(54) Hu, N.; Zhang, L.; Yang, C.; Zhao, J.; Yang, Z.; Wei, H.; Liao, H.; Feng, Z.; Fisher, A.; Zhang, Y.; Xu, Z. J. *Sci. Rep.* **2016**, *6*, 19777.

(55) El-Kady, M. F.; Strong, V.; Dubin, S.; Kaner, R. B. *Science* **2012**, *335*, 1326.

(56) Niu, Z.; Zhang, L.; Liu, L.; Zhu, B.; Dong, H.; Chen, X. *Adv. Mater.* **2013**, *25*, 4035.

Chapter 7. Conclusions and Future Work

7.1 Conclusions from the dissertation

This dissertation has explored and evaluated several alternative nanostructured materials electrodes for supercapacitor energy storage applications to improve the performance of state-of-the-art commercial supercapacitors. The following results have been obtained (Figure 7.1).

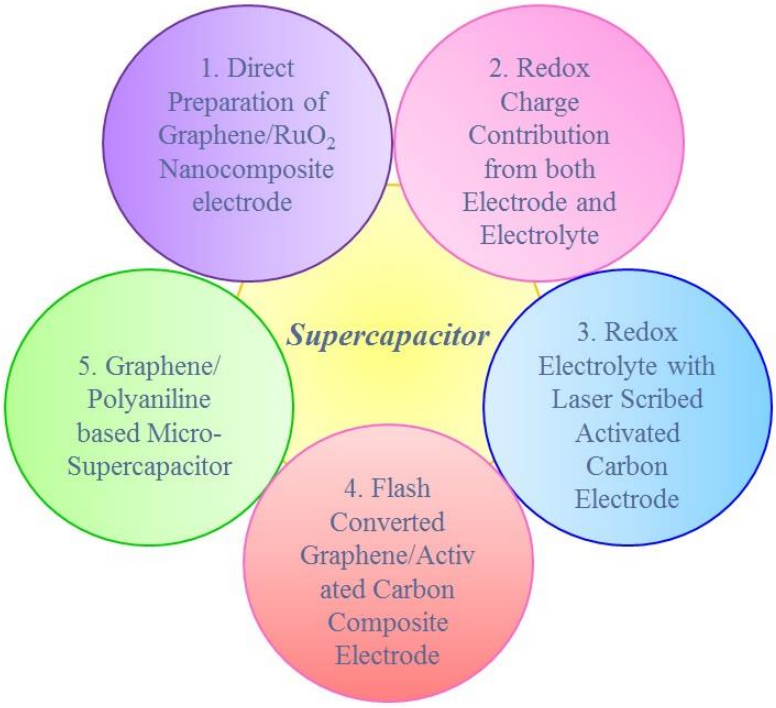

Figure 7.1 Five approaches to improve the electrochemical performance of a supercapacitor.

(1) Ruthenium oxide based nanocomposite hybrid electrodes were fabricated for high-performance supercapacitor devices. The nanocomposites of RuO_2-laser scribed graphene (LSG) showed better electrochemical performance than that of other reported

RuO_2/graphene composite electrodes due to the unique wrapping configuration of the RuO_2/LSG structure.

(i) This structure prevents the formation of agglomerated RuO_2, promoting low strain and stress that often results from volume changes and may thus improve the cycling performance of RuO_2; (ii) the LSG-wrapped structure allows a strong interaction with individual RuO_2 nanoparticles to induce efficient capacitance collection throughout the conductive LSG; and (iii) RuO_2 nanoparticles serve as nano-spacers to help maintain a high surface area, 3-dimensional porous structure within the LSG, allowing the electrolyte to interact with the entire surface of the electrode which in turn facilitates ion transport during redox reactions. Therefore, supercapacitors based on the novel electrodes of RuO_2/LSG showed excellent electrochemical performance with high energy and power density.

(2) We propose a symmetric supercapacitor consisting of magnetite nanoparticles that are carefully hybridized with a three-dimensional form of graphene and utilizing a redox mediator [$Fe(CN)_6^{3-}$/$Fe(CN)_6^{4-}$] with neutral Na_2SO_4 electrolyte. While Fe_3O_4/carbon hybrid electrodes can only operate at 1.0 V, the addition of a redox mediator extends the decomposition voltage of the electrolyte, resulting in a symmetric supercapacitor with an ultrahigh voltage of 1.8 V. This represents a conceptual advance in the field of aqueous supercapacitors and may enable a new generation of eco-friendly energy storage devices. This symmetric supercapacitor demonstrates excellent electrochemical performance with an energy density of 121 Wh kg^{-1}, placing it among the best performing hybrid supercapacitors.

(3) First, we demonstrated that laser treatment of activated carbon electrodes results in the formation of micro-channels that can connect the internal pores of activated carbon with the surrounding electrolyte. These micro-channels serve as electrolyte reservoirs that in turn shorten the ion diffusion distance and enable better interactions between the electrode

surfaces and electrolyte ions. Second, the capacitance can be further increased through fast and reversible redox reactions on the electrode surface using a redox active electrolyte, enabling the operation of a symmetric device at 2.0 V, much higher than the thermodynamic decomposition voltage of water (1.23 V). The synergy between the laser scribed electrodes and the redox electrolyte produces supercapacitors with 8 times larger capacitance than traditional supercapacitors utilizing non-scribed activated carbon electrodes with an acetonitrile-based electrolyte.

(4) Flash Converted Graphene (FCG) is combined with AC to make a novel architectural form that facilitates the rapid transport of ions and electrons at the same time maintaining the high packing density. A commercially available flash lamp was used to produce FCG, while a probe sonication instrument was used to mix the FCG powder and the AC powder to achieve homogeneous films. Devices made with these composite (FCG/AC) electrodes exhibited improved power, energy density, and rate capability due to the AC serving as micro-spacers between graphene layers, which can prevent the graphene sheets from restacking. This results in enhanced packing density. In addition, these devices have been made into a commercially viable coin cell form that holds promise for a wide range of applications.

(5) We synthesized polyaniline (PANI) and PANI/graphene-based materials for MSC electrodes, based on several macrostructural complexity dimensions, such as one-dimensional (1D) fiber-type, two-dimensional (2D) films, and three-dimensional (3D) graphene foam. To make a 2D-PANI-MSC, a simple and scalable approach to fabricating interdigitated MSCs was developed via coating a PANI nanofiber film and subsequent laser patterning. The 1D-MSC and 3D-MSC were fabricated by an electrodeposition method on fiber and 3D foam of

LSG, respectively. The laser scribed graphene/PANI (3D)-MSC exhibited the highest gravimetric energy and power densities compare to the other 1D and 2D forms of MSCs. For the areal energy and power density, rGO-PANI fiber (1D) - MSC showed the highest values among all the MSCs reported to date.

Overall, the work presented in this dissertation enhanced the energy storage performance of the supercapacitors and may enable a new generation of eco-friendly energy storage devices. Compared to the reported literature, our supercapacitors showed very promising electrochemical performance with much-improved energy and power densities as summarized in the Ragone plot in Figure 7.2. Thus, the current work provides an effective strategy for designing and fabricating aqueous supercapacitors and micro-supercapacitors that hold promise for a sustainable energy future.

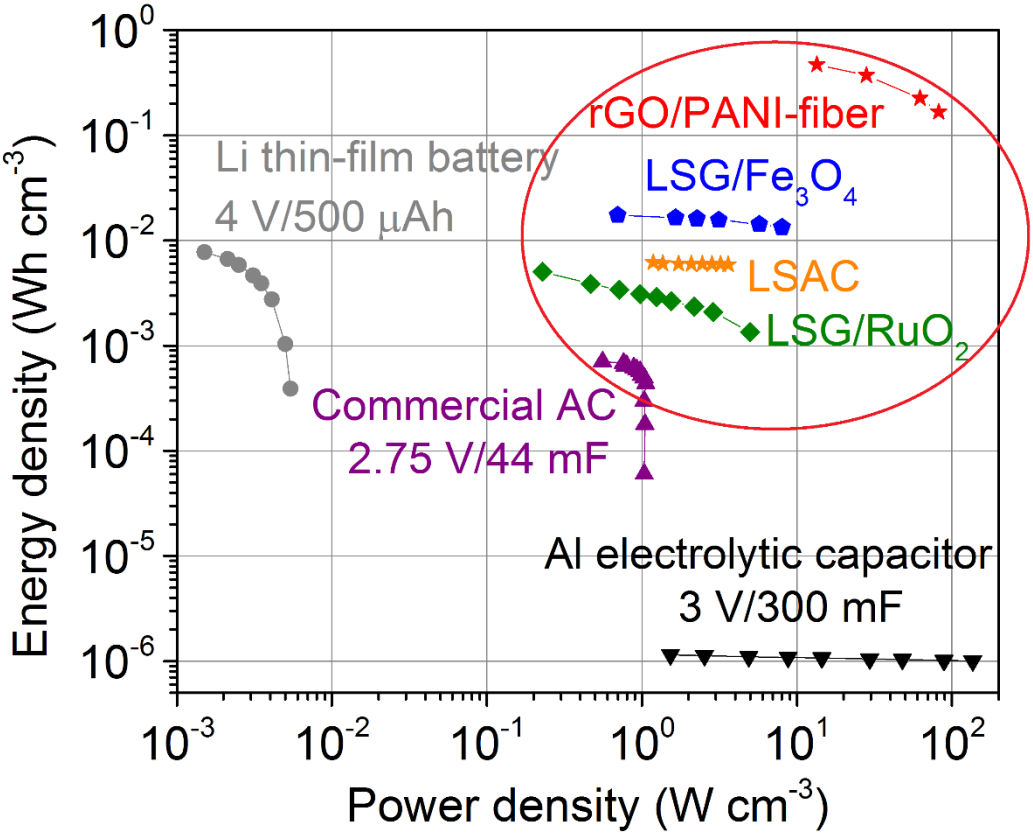

Figure 7.2 Ragone plot shows the achieved energy and power densities of our supercapacitors, including the supercapacitors of RuO_2/LSG, Fe_3O_4/LSG, and rGO/PANI fiber, as well as laser scribed activated carbon (LSAC) electrodes. All data were obtained from full cell supercapacitors with an aqueous based electrolyte.

7.2 Future Work

In order to further improve the energy storage capacity and fully exploit the potential of supercapacitors, the following directions should be taken into account.

7.2.1. CNT/LSG composite electrode

This dissertation has mainly discussed making hybrid electrodes based on laser scribed graphene (LSG). However, supercapacitors composed of LSG still suffer from a low density and low conductivity. To overcome these problems, we are investigating LSG-carbon nanotube (CNT) composite materials that can be easily processed using the original laser scribing technique.[1] High-performance supercapacitor electrodes can be produced *in situ* by coating graphite oxide/CNTs onto the required substrate and then laser scribed to produced LSG/CNT electrodes as illustrated in Figure 7.3.

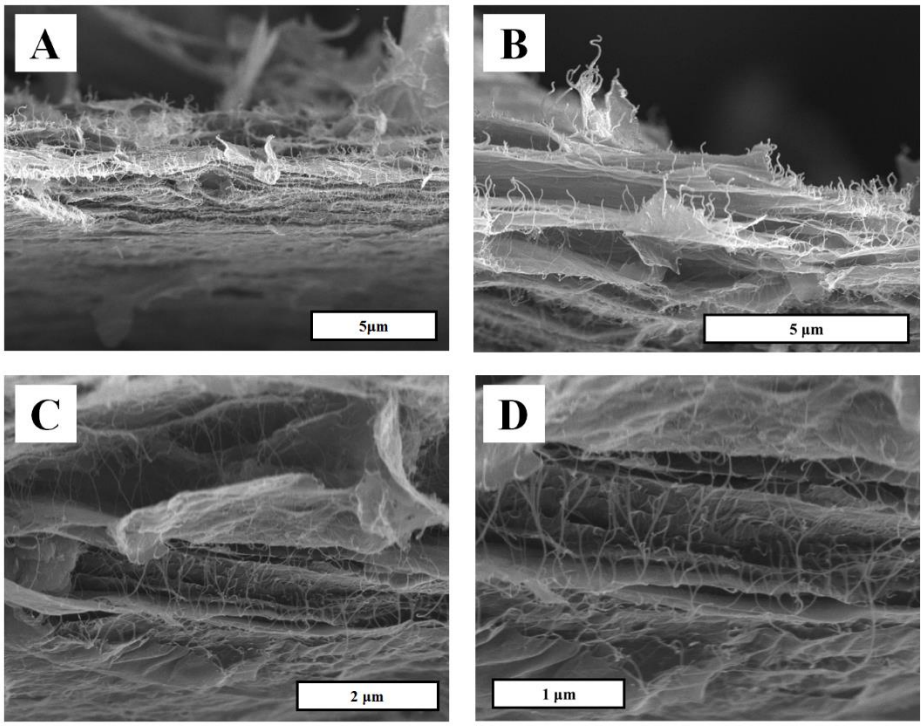

Figure 7.3 SEM images of an LSG/CNT composite electrode with different scale bars.

SEM confirmed that CNTs have successfully been grown in between the vermiculite-like layers. This structure is intended to prevent of restacking of LSG layers and thus increases the ion-accessible surface area. Additionally, the LSG/CNT nanostructured electrode showed low internal resistance due to the geometry proposed here which orients the conductivity pathways in the planar direction for graphene and the axial direction for the CNTs. Although CNT/graphene composites has been achieved recently,[2-4] our laser scribing method produces very high-quality graphene/CNT composites that can be easily processed into supercapacitors on a large scale. In the future, we will test the electrochemical performance of the CNT/LSG composite electrode.

7.2.2. Self-charging supercapacitor

Recently, researchers have been trying to develop a new type of hybrid system that integrates energy harvesting and energy storage in a single device. The Wang group introduced a self-charging supercapacitor power cell device, in which mechanical energy is converted to electrochemical energy via piezoelectric materials (polyvinylidene difluoride and ZnO) and is directly stored in a supercapacitor (using an MnO_2 electrode).[5] The authors introduce a novel idea of using PVDF-ZnO film as both the supercapacitor separator and the energy harvester, but the energy and power density of the device must be improved. In order to enhance the electrochemical performance, a piezoelectric film (as well as separator) should possess well-controlled porosity to increase the ionic diffusion. Herein, we have fabricated a mesoporous PVDF film to improve the performance of the supercapacitor. The mesoporous PVDF film was synthesized by casting a mixture of PVDF solution and ZnO particles onto a flat glass substrate, followed by acid etching to remove ZnO particles.[6] The mesoporous PVDF film with ZnO particles not only increases the ionic diffusion, but also enhances the piezoelectric performance. The two reasons for introducing ZnO particles are to create the porous film and to form of the piezoelectric β-phase. β-Phase PVDF is well-known as a piezoelectric material because of its high piezoelectric coefficient compared to other forms of the PVDF polymer.[7,8] Therefore, our β-phase PVDF film can increase the supercapacitor performance through the porous structure and also can increase the energy harvesting performance through creating the β-phase form of PVDF.

7.2.2.1 Characterization of Piezoelectric Materials

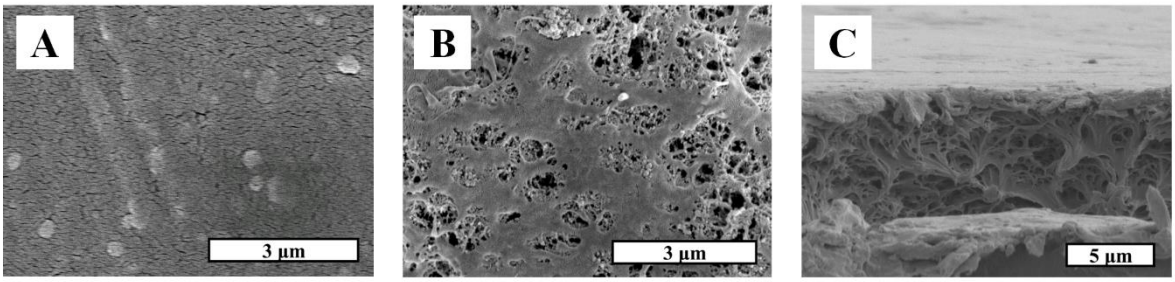

Figure 7.4 (A) SEM image of commercial PVDF film. (B) Top view, (C) cross-sectional view of the mesoporous PVDF thin film.

SEM images (Figure 7.4 B,C) show the mesoporous structure of the PVDF film compared to commercial PVDF film (Figure 7.4 A). It can be clearly seen that ZnO particles help to generate porous PVDF thin film.

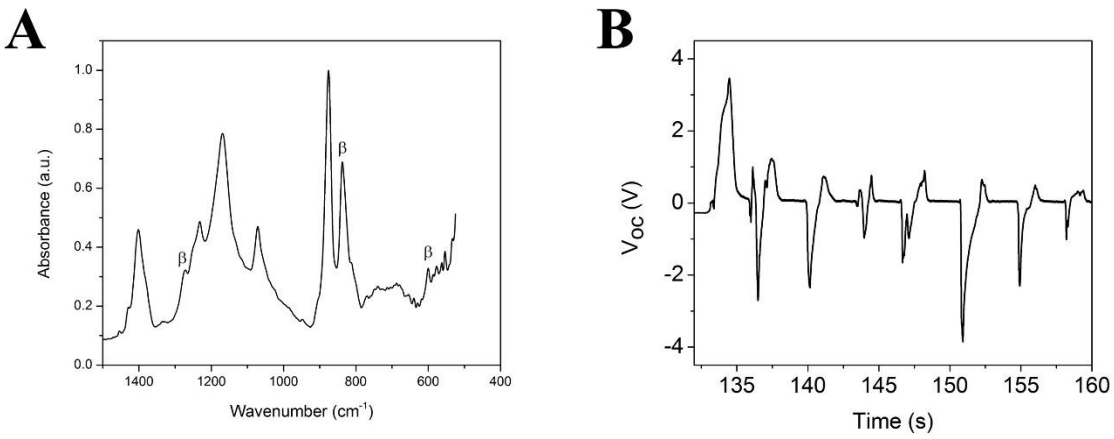

Figure 7.5 (A) FTIR spectrum of the mesoporous PVDF thin film. (B) The voltage outputs generated under human palm impact with a porous PVDF separator.

The Fourier transform infrared spectroscopy (FTIR) measurements performed in order to identify β-phase formation in the PVDF polymer is presented in Figure 7.5A. This

FTIR spectrum (Figure 7.5A) confirmed the presence of the β-phase of PVDF with peaks at 510, 840, and 1280 cm^{-1}.[9] Further, the piezoelectric electrode was fabricated using a porous PVDF film with copper tape as the top and bottom electrodes. Under the mechanical deformation through the human palm, the piezoelectric potential was generated on the surface of the PVDF film due to the polarization of the film. The generated output open circuit voltage was found to be about 2.5 V (Figure 7.5B). This output performance was higher than the recently reported values for other PVDF-based nanogenerators, such as single PVDF nanofiber (30 mV), PVDF nanofibers (20 mV),[10] PVDF film (0.4 V),[11] PVDF mats (1 V),[12] and porous PVDF film (1.3 V).[13] From these results, we conclude that our self-charging-supercapacitor fabricated with a porous PVDF separator can generate a piezopotential.

7.2.2.2 Electrochemical performance of the self-charging supercapacitor

We investigated the electrochemical properties of the self-charging device with the mesoporous PVDF separator using an activated carbon electrode.

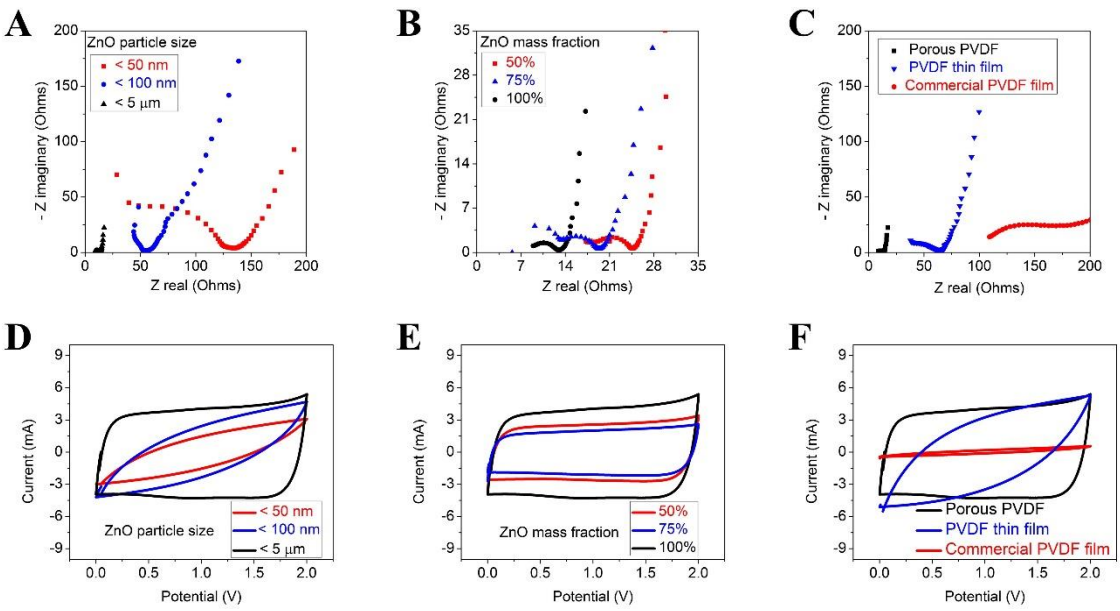

Figure 7.6 Electrochemical performance of the self-charging-supercapacitor with different types of piezoelectric PVDF separators. Nyquist plots comparing the performance of porous PVDF film fabricated (A) using different particle sizes of ZnO powder and (B) using different ZnO mass fraction mixtures: 50%, 75% and 100%. (C) Nyquist plots comparing the performance with a commercial PVDF film, a fabricated non-porous PVDF thin film and a porous PVDF film. CV profiles comparing the electrochemical performance of (D) using different particle sizes of ZnO powder and (E) using different ZnO mass fraction mixtures: 50%, 75% and 100%. (F) Comparing the performance with a commercial PVDF film, a non-porous PVDF thin film and a porous PVDF film.

Figure. 7.6 A shows the Nyquist plots of the mesoporous PVDF thin films prepared from mixtures with different particle size sof ZnO powder: 50 nm, 100 nm, and 5 µm, respectively. It can be clearly seen in the Nyquist plot, that the larger particle size of ZnO (<5 µm), produces an ESR that is much lower than that prepared with nanoparticles. In addition, when prepared with microparticle ZnO powder an enhanced capacitance with a nearly textbook rectangular CV curve is found (Figure 7.6 D), suggesting ideal electric double layer capacitance behavior. Figures 7.6 B,E show Nyquist plots and CVs of the porous PVDF thin

films prepared from mixtures with 50%, 75% and 100% ZnO mass fraction, respectively. It can be clearly seen that more ZnO in the mixture generates lower ESR and higher capacitance. As to the PVDF thin film prepared from 100% ZnO mass fraction mixture, much more pores were obtained in the matrix of the PVDF thin film after etching. When comparing our best prepared porous PVDF film with a commercial PVDF film and a prepared PVDF film without ZnO particle treatment, our porous PVDF film showed superior performance compared to those two films (Figure 7.6 C,F). These results imply that a porous PVDF film successfully enables rapid ion transport. This can be ascribed to the mesoporous structure of the separator that easily diffuses electrolyte ions. In the future, we will test the self-charging capability of the devices by using an oscilloscope.

7.3 References

(1) El-Kady, M. F.; Strong, V.; Dubin, S.; Kaner, R. B. Science 2012, 335, 1326.

(2) Fan, Z.; Yan, J.; Zhi, L.; Zhang, Q.; Wei, T.; Feng, J.; Zhang, M.; Qian, W.; Wei, F. Adv. Mater. 2010, 22, 3723.

(3) Lin, J.; Zhang, C.; Yan, Z.; Zhu, Y.; Peng, Z.; Hauge, R. H.; Natelson, D.; Tour, J. M. Nano Lett. 2013, 13, 72.

(4) Zhu, Y.; Li, L.; Zhang, C.; Casillas, G.; Sun, Z.; Yan, Z.; Ruan, G.; Peng, Z.; Raji, A.-R. O.; Kittrell, C.; Hauge, R. H.; Tour, J. M. Nat. Commun. 2012, 3, 1225.

(5) Ramadoss, A.; Saravanakumar, B.; Lee, S. W.; Kim, Y.-S.; Kim, S. J.; Wang, Z. L. ACS Nano 2015, 9, 4337.

(6) Mao, Y.; Zhao, P.; McConohy, G.; Yang, H.; Tong, Y.; Wang, X. Adv. Energ. Mater. 2014, 4, 1301624.

(7) Yu, L.; Cebe, P. Polymer 2009, 50, 2133(b) Martins, P.; Caparros, C.; Gonçalves, R.; Martins, P. M.; Benelmekki, M.; Botelho, G.; Lanceros-Mendez, S. J. Phys.Chem. C 2012, 116, 15790.

(8) Zheng, J.; He, A.; Li, J.; Han, C. C. Macromol. Rapid Commun. 2007, 28, 2159.

(9) Hansen, B. J.; Liu, Y.; Yang, R.; Wang, Z. L. ACS Nano 2010, 4, 3647.

(10) Dae-Yeong, L.; Hyunjin, K.; Hua-Min, L.; Jang, A. R.; Yeong-Dae, L.; Seung Nam, C.; Young Jun, P.; Dae Joon, K.; Won Jong, Y. Nanotechnology 2013, 24, 175402.

(11) Dhakras, D.; Borkar, V.; Ogale, S.; Jog, J. Nanoscale 2012, 4, 752.

(12) Cha, S.; Kim, S. M.; Kim, H.; Ku, J.; Sohn, J. I.; Park, Y. J.; Song, B. G.; Jung, M. H.; Lee, E. K.; Choi, B. L.; Park, J. J.; Wang, Z. L.; Kim, J. M.; Kim, K. Nano Lett. 2011, 11, 5142.